A Bioinspired Approach to Data Storage

By:

Scott Michael Bird

A thesis submitted in partial fulfilment of the requirements for the degree of
Doctor of Philosophy

The University of Sheffield
Faculty of Science
Department of Chemistry

March 2016

For Ann and Craig
Without their unwavering support and endless
sacrifices none of this would have been possible.

II

Abstract

Traditional magnetic data storage devices are reaching the limits of their capabilities, and new technologies must be sought if the remarkable pace of improvement in performance and storage capacity seen over the last 60 years is to continue. Bit-patterned media (BPM) has the potential to continue this development and significantly increase the storage densities of magnetic hard disks, but developing a cost-effective route to manufacture this technology has so far remained elusive. This work takes inspiration from nature, to develop a bioinspired and green approach to forming magnetic nanoparticles (MNPs) on surfaces, as a novel approach to BPM.

Magnetotactic bacteria (MTB) form highly uniform MNPs of the magnetic material of magnetite inside specialised lipid organelles called magnetosomes, under mild aqueous conditions. Control over the magnetite crystal formed is exerted through the use of biomineralisation proteins. One of these proteins from the MTB *Magnetospirillum magneticum* AMB-1, termed Mms6, has been shown to control the formation of magnetite nanoparticles *in vitro*. In this work, a modified version of the Mms6 protein, engineered to contain an *N*-terminal cysteine, is patterned and immobilised onto gold surfaces to biotemplate the growth of MNP arrays of magnetite.

Furthermore, different patterning methods are explored to control the location of Mms6, with the aim of producing MNP arrays that are suitable for BPM. Magnetite is a magnetically soft material that is unlikely to ever be used for data storage, but Mms6 has been shown to biotemplate the magnetically harder material of cobalt-doped magnetite and this is also explored as an alternative. This approach is also highly adaptable, and could be used for the production of a wide range of different nanomaterials on surfaces through the use of alternative biomolecules. The patterning approaches developed in this work are also used to pattern artificial biomolecules to biotemplate materials that are more technologically relevant and not found in nature, such as $L1_0$ phase CoPt, as a route to developing an environmentally friendly, scalable and bioinspired approach to the challenge of BPM.

Table of Contents

List of Figures

List of Tables

Bibliography

Galloway, J.M., Bird, S.M., Bramble, J.P., Critchley, K. & Staniland, S.S. *Biotemplating Magnetic Nanoparticles on Patterned Surfaces for Potential Use in Data Storage*. MRS Proceedings, 2013. 1569: p. 231-237.

Bird, S.M., Galloway, J.M., Rawlings, A.E., Bramble, J.P. & Staniland, S.S. *Taking a hard line with biotemplating: cobalt-doped magnetite magnetic nanoparticle arrays.* Nanoscale, 2015. 7: p. 7340 - 7351.

Bird, S.M., Rawlings, A.E., Galloway, J.M., & Staniland, S.S. *Using a biomimetic membrane surface experiment to investigate the activity of the magnetite biomineralisation protein Mms6.* RSC Advances, 2016. 6: p. 7356-7363.

Bird, S.M., El-Zubir, O., Rawlings, A.E., Leggett, G.J. & Staniland, S.S. *A novel design strategy for nanoparticles on nanopatterns: interferometric lithographic patterning of Mms6 biotemplated magnetic nanoparticles*. Journal of Materials Chemistry C, 2016. DOI: 10.1039/C5TC03895B.

Acknowledgements

So many people have contributed to this work in so many in different ways. So much so that it is impossible to list everyone and do justice to their efforts in these few small paragraphs. I will do my best to thank everyone, but I can only apologise to those I have forgotten. They should know that I am deeply grateful for their efforts, and that without their support this thesis might have never have been completed.

I will start with the directors, staff and everyone who was a part of the EPSRC Centre for Doctoral Training in Molecular Scale Engineering. The directors believed in me and gave me the chance to pursue a Ph.D. and the first master's year of the course made the transition from undergraduate to postgraduate so much smoother than it otherwise would have been. Most importantly it was the people who started this course with me that made it such a fantastic experience; Andy, Seybilla, Mark, Olly and Dave. Such different people, who all joined the course from different scientific backgrounds. I probably learnt more from them than I did in any lecture, especially about biology, and I now consider you all some of my best friends.

I would also like to thank my supervisor Sarah, who managed to create a positive and stress free environment during the course this project. At no point have I ever felt stressed or under pressure, and I have always felt like the project was moving in the right direction. I am also fully aware that when I first started the work presented in this thesis I was in the extremely fortunate position of having what were essentially three postdocs in the group, even more amazing considering there was only one other postgraduate. I do not think I can explain how much easier this made the start of this project. Jon, Jo and Andrea may not always see eye to eye, but I like to think I took a bit of experience from you all, and I definitely could not have done it without your help. I sometimes feel like you don't always realise how brilliant you all are, and I hope you all get to where you want to be.

This work was completed across three different institutions, and it is not possible to list everyone who I met and contributed. Everyone in the Staniland Group past and present; Jenny, Lori, Rosie, Zainab, Pavel, Naomi, Charlie and many more, everyone at the Molecular and Nanoscale Physics group in Leeds, Michael, Falco and everyone in the Dip-Pen Nanolithography Group in Karlsruhe and everyone in the Chemistry Department at Sheffield, you all contributed to this work and made the experience fulfilling. Special thanks go to Laurynas, the big dogs; Nath, Andy, Jack, Touch Cloth and Jarman (the butt of all jokes), the Wednesday night footballers, Otis and Luke and of course Sasha (who proof read most of this thesis) who made the work bearable and I hope will be friends for life.

Intellectual Property Statement

The candidate confirms that the work submitted is his own. The contribution of others to this work has been explicitly indicated below and throughout the thesis. The candidate also confirms that appropriate credit has been given within the thesis where reference has been made to the work of others.

Chapter 3: The Mms6 protein was synthesised in the Staniland group by Andrea Rawlings. XRD analysis was performed in collaboration with Nik Reeves-Mclaren at the X-ray Diffraction Small Research Centre based at the University of Sheffield. SIMS data was collected by Claire Hurley at the Sheffield Surface Analysis Centre (SSAC). TEM data was collected in collaboration with Jonathan Bramble at the University of Sheffield, with SEM and EDXA data collected in collaboration with Stuart Micklethwaite at the LENNF Centre based at the University of Leeds. VSM data was collected by Johanna Galloway at the University of Leeds. MFM data was collected in collaboration with Rebecca Savage at the University of Sheffield, and 3D plots were rendered in 'R' using a program written by Jonathan Bramble. Molecular modelling of the Mms6 protein was performed by Steve Baldwin and Andrea Rawlings.

Chapter 4: Stamp masters were produced with EBL in collaboration with Mark Rosamond at the University of Leeds. PPL and DPN were performed in collaboration with Michael Hirtz, Falko Brinkmann and Ravi Kapoor at The Karlsruhe Institute for Technology in Germany. IL and FFM was performed in collaboration with Osama El-Zubir at The Nanoscale Analytical Science Group at the University of Sheffield. TEM data was collected in collaboration with Jonathan Bramble at the University of Sheffield. SEM analysis was performed in collaboration with either Stuart Micklethwaite at the LENNF Centre based at the University of Leeds or Cheryl Shaw at the Sorby Centre based at the University of Sheffield. XRD analysis was performed in collaboration with Nik Reeves-Mclaren at the X-ray Diffraction Small Research Centre based at the University of Sheffield. MFM data was collected in collaboration with Rebecca Savage at the University of Sheffield, and 3D plots were rendered in 'R' using a program written by Jonathan Bramble.

Chapter 5: The MIA-1 protein was synthesised in the Staniland group by Andrea Rawlings. IL was performed in collaboration with Osama El-Zubir at The Nanoscale Analytical Science Group at the University of Sheffield. TEM data was collected in collaboration with Jennifer Bain at the University of Sheffield. SEM analysis was performed in collaboration with either Stuart Micklethwaite at the LENNF Centre based at the University of Leeds or Cheryl Shaw at the Sorby Centre based at the University of Sheffield. AFM was collected in

collaboration with Rebecca Savage at the University of Sheffield. XRD analysis was performed in collaboration with Nik Reeves-Mclaren at the X-ray Diffraction Small Research Centre based at the University of Sheffield.

Chapter 6: VSM was recorded by Johanna Galloway at the University of Leeds. ICP data was collected by Neil Bramall at the University of Sheffield. TEM data was collected in collaboration with Jonathan Bramble at the University of Sheffield. SEM and EDXA analysis was performed in collaboration with either Stuart Micklethwaite at the LENNF Centre based at the University of Leeds or Cheryl Shaw at the Sorby Centre based at the University of Sheffield. AFM and MFM was collected in collaboration with either Rebecca Savage at the University of Sheffield or with Johanna Galloway at the University of Leeds, and 3D plots were rendered in 'R' using a program written by Jonathan Bramble. XRD analysis was performed in collaboration with Nik Reeves-Mclaren at the X-ray Diffraction Small Research Centre based at the University of Sheffield. IL was performed in collaboration with Osama El-Zubir at The Nanoscale Analytical Science Group at the University of Sheffield.

Abbreviations and Definitions

μCP	micro-contact printing
AFM	atomic force microscopy
AMB-1	*Magnetospirillum magneticum* strain AMB-1, a magnetotactic bacterium
bcc	body centered cubic
BPM	bit-patterned media
BSA	bovine serum albumin
CD	compact disc
cgs	centimeter gram seconds, system of units
DNA	deoxyribonucleic acid
DPN	dip-pen nanolithography
DRAM	dynamic random access memory
DTM	discrete track media
EBL	electron beam lithography
EDC	ethyl(dimethylaminopropyl) carbodiimide
EDXA	energy dispersive X-ray analysis
fcc	face centered cubic
fct	face-centered tetragonal
Ga	gigaannum (1 billion years ago)
GB	gigabyte
G-L	glycine-leucine
HAMR	heat-assisted magnetic recording
HDD	hard disk drive
IC	integrated circuit
ICP-ES	inductively coupled plasma emission spectroscopy
IL	interferometric lithography
IMAC	immobilised metal affinity chromatography
LMR	longitudinal magnetic recording
Ma	megaannum (1 million years ago)
MAI	magnetosome island
Mam	magnetosome associated

MAMR	microwave-assisted magnetic recording
MBP	maltose-binding protein
MFM	magnetic force microscopy
MIA-1	magnetite interacting Adhiron 1
Mms	magnetosome membrane specific
Mms6	≈6kDa biomineralisation protein (magnetosome membrane specific 6)
Mms6$_{Peptide}$	peptide based on the *C*-terminal region of Mms6
MNP	magnetic nanoparticle
MSR-1	*Magnetospirillum gryphiswaldense* strain MSR-1, a magnetotactic bacterium
MTB	magnetotactic bacteria
NAND	a logic gate in digital electronics (negative-AND)
NHS	*N*-hydroxysuccinimide
NOR	a logic gate in digital electronics
OATZ	oxic-anoxic transition zone
PC	personal computer
PCR	polymerase chain reaction
PDMS	polydimethylsiloxane
PEG-F	1H, 1H, 2H, 2H-perflorodecanethiol
pI	isoelectric point (pH at which a particular molecule carries no net electrical charge)
PMR	perpendicular magnetic recording
POFHK	partial oxidation of ferrous hydroxide with potassium
PPL	polymer pen lithography
QCM-D	quartz crystal microbalance with dissipation
RAMAC	random access method of accounting and control
RIE	reactive ion etch
rpm	revolutions per minute
RTCP	room temperature co-precipitation
SAM	self-assembled monolayer
SEM	scanning electron microscopy
SI	système international d'unités (international system of units)

SIMS	secondary ion mass spectrometry
SRAM	static random access memory
T_B	blocking temperature
T_c	Curie temperature
TEM	transmission electron microscopy
T_N	Nèel temperature
T_V	Verwey transition temperature
UHV	ultra-high vacuum
UV	ultra-violet
VSM	vibrating sample magnetrometry
XRD	X-ray diffraction

Table I - Conversion from magnetic units in cgs to SI

		cgs	Conversion to SI
F	force between poles	1 dyne (dyn)	10^{-5} newton (N)
H	magnetising field	1 oersted (Oe)	79.58 ampere per meter (A m^{-1})
B	magnetic induction	1 gauss (G)	10^{-4} tesla (T)
E	energy	1 erg	10^{-7} joule (J)
Φ	magnetic flux	1 maxwell (Mx)	10^{-8} weber (Wb)
M	magnetisation	1 emu cm^{-3}	12.57×10^{-4} Wb m^{-2}
μ	magnetic permeability	1 G Oe^{-1}	1.257×10^{-6} henry per meter (H m^{-1})

Table II - Conversion of the SI units in Table I into their fundamental constituents; ampere (A), meter (m), kilogram (kg) and second (s).

newton (N)	kg m s^{-2}
tesla (T)	kg s^{-2} A^{-1}
joule (J)	kg m^{2} s^{-2}
weber (Wb)	kg m^{2} s^{-2} A^{-1}
henry (H)	kg m^{2} s^{-2} A^{-2}

1. Introduction

"After growing wildly for years, the field of computing appears to be reaching its infancy."

John R. Pierce

1.1 Overview

We now live in a technological world, driven by our ever expanding knowledge of the world we live in. Technology has also demanded miniaturisation, and the billions of transistors that are packed onto todays computer chips would have been unimaginable a few decades ago. Miniaturisation has also brought nanotechnology, a relatively new discipline, to the forefront of science. It is often stated that the field of nanotechnology began in 1959 with Richard Feynman's now infamous lecture entitled; "There's Plenty of Room at the Bottom", who discussed manipulating matter on the atomic scale [1]. However, at the time the talk remained rather unnoticed, and Feynman's role in fuelling the development of nanotechnology is now debated [2].

Nanotechnology really gathered momentum in the 1980's when tools such as the scanning probe and the electron microscope were invented, providing the tools for matter to be observed on the nanoscale [2]. Traditionally, materials have always been manipulated using top-down methods, modification by the removal of material. However, nanotechnology opens up the ability to manipulate matter on the atomic scale, to grow a material from the bottom-up. This bottom-up approach is what is used by nature, and as a result biology often looked to for inspiration within nanotechnology.

In this study inspiration is taken from nature, to develop a bioinspired approach to forming arrays of magnetic nanoparticles (MNPs) on surfaces. Magnetic materials have had a variety of uses throughout history and remain important to many of our modern technologies, so in Section 1.2 the theory of magnetism and nanomagnetism is introduced. MNP arrays form one approach to the challenging of forming bit-patterned media (BPM), potentially the next generation of ultra-high-density magnetic data storage devices. Therefore, in Section 1.3 the need and the challenge of BPM is outlined. Magnetotactic bacteria (MTB) are remarkable organisms that control the formation of MNPs of magnetite with the use of biomineralisation proteins inside specialised lipid organelles called magnetosomes, and are the inspiration behind this work. In Section 1.4 MTB, biomineralisation and how this can used or adapted for use *in vitro* to biotemplate the formation of MNPs is discussed. In this work biomolecules are combined with surface patterning, so Section 1.5 presents the techniques that are available and those that are used in this study. Finally, in Section 1.6 the previous work that this thesis is built upon is outlined, and the remainder of the thesis is introduced.

1.2 Magnetism

1.2.1 History of Magnetic Materials

The story of magnetism begins with the discovery of a mineral that is also the inspiration for this project. Legend has it that around 4000 years ago a Cretan shepherd called Magnes was herding sheep in Magnesia, an area of what is now modern day Turkey [3]. When standing on a large black rock he found the nails of his shoes and the metal tip of his staff suddenly became stuck. He is said to have dug up this rock to uncover lodestones[*] of the naturally occurring magnetic mineral magnetite, the same material that forms so precisely inside the magnetosomes of magnetotactic bacteria (MTB). This may just be a legend, but it is certainly true that there are a large number of magnetite deposits in the Magnesia region [4]. As far back as 2500 years ago, the Ancient Greeks knew that any piece of iron would become magnetic if rubbed with magnetite, and at some later date it was also discovered that a floating piece of magnetite would always align itself to point roughly north and south [4]. This formed the basis of the compass, which is believed to have been discovered independently in both the Ancient Chinese and Greek civilisations [4].

As recently as the 18th Century the only way a magnet could be made was by rubbing iron or steel with a lodestone, and further applications were only opened up with a deeper understanding of the origins and principles of magnetism. In 1820, the Danish scientist Hans Christian Oersted demonstrated that an electric current produces a magnetic field, leading to the development of the electromagnet [5]. 40 years later, the Scottish mathematician and physicist James Clerk Maxwell established the theory of electromagnetism in a series of beautifully simple equations [6]. Further discoveries such as that of the electron by the English Physicist J. J. Thomson at the end of the 19th century [7], the development of quantum mechanics at the beginning of the 20th century, and continued developments into the 21st century have expanded our knowledge of electromagnetism. It has become a major driving force in our technological age and is fundamental to many of our modern technologies [3].

1.2.2 Fundamental Principles of Magnetism

The theory of magnetism can be viewed in one of two ways, in terms of interactions between magnetic poles or in terms of circulating currents. This leads to two different sets of

---

[*] In Middle English this meant 'course stone' or 'leading stone' (deriving from the now obsolete definition of lode, which meant 'journey' or 'way').

units; centimetre-gram-second (csg) units for describing interactions between magnetic poles, and Système International d'Unités (SI) units when magnetism is viewed in terms of circulating currents [8]. Although on the face of it this seems like it confuses the issue, each viewpoint can be more useful in certain situations. In this work the cgs system of units are used, but these can be converted to SI units with the use of Table I (page XXI).

Most of us are familiar with a simple bar magnet (Figure 1.2.1). Forces emanate from poles at the ends of a bar magnet, and every magnet contains a north or north-seeking pole and a south or south-seeking pole. The north-seeking pole of a pivoted bar magnet will always point towards the magnetic north pole of the Earth, a direction close to the geographic north pole, and subsequently the south-seeking pole will point roughly in the direction of the geographic south pole. Like poles of a magnet always repel, whereas opposite poles attract, and magnetic poles always come in pairs. Cutting a bar magnet in half produces two smaller magnets, each of which still has a north and a south pole. Although the existence of magnetic monopoles is not forbidden by any known laws of nature [3], so far experimental evidence for their existence remains inconclusive [3].
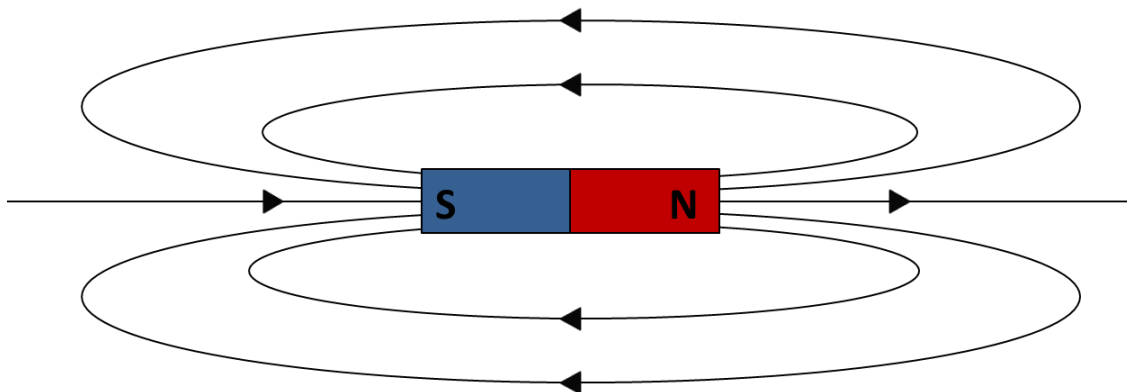
Figure 1.2.1 – Field lines around a bar magnet, flowing from the north to the south pole.

In 1750 the English scientist John Michell, and independently in France in 1785 Charles-Augustin de Coulomb, found that the strength of the force between two magnetic poles is proportional to the strength of these poles, and inversely proportional to the square of the distance between them[*] [9]. This provided a way of defining the strength of a magnetic pole, which in cgs units this force is measured in dynes (dyn), and hence a unit pole exerts a force of $1\,\mathrm{dyn}$ on another pole $1\,\mathrm{cm}$ away. A magnetic pole can be thought to form a magnetising field (H). A magnetic material can also become magnetised when in this field, so H is also known as the magnetising force. It was Michael Faraday who, in one of his many

---

[*] The inverse square law of magnetism, a law which is analogous to Coulombs law governing electric charges.

contributions to the field of electromagnetism, first suggested that this magnetising force could be represented by lines of force [10]. This can be envisaged, as shown in Figure 1.2.1, as the path taken by a magnetic force to flow from a north to a south pole. Therefore the force (*F*) between two interacting magnetic poles can be defined in terms of the two pole strengths (p_1, and p_2) and the distance between them (*d*), or in terms of a magnetising force (*H*) generated by a magnetic pole (p_1) that is exerted on a second pole (p_2) [11].

$$F = k\frac{p_1 p_2}{d^2} = p_2 H \qquad (1.2.1)$$

In cgs units the proportionality constant (*k*) is equal to 1. As a result, the magnetising force can be defined by the strength of the pole from which it emanates, over the square of the distance from the pole [11].

$$H = \frac{p_1}{d^2} \qquad (1.2.2)$$

In the cgs system of units the magnetising force is measured in oersteds (Oe), with 1 Oe equivalent to a field exerting a force of 1 dyn on a unit pole [11]. However, it can be easier to visualise the strength of the magnetising force in terms of the field lines first proposed by Faraday (Figure 1.2.1), with the field strength being equal to the number of field lines passing through a unit area perpendicular to the field. This concept is known as magnetic flux (*Φ*). In cgs units, magnetic flux is measured in maxwells (Mx), with 1 Oe cm^2 being equivalent to 1 Mx [11].

The discovery by Hans Christian Oersted in 1820 that electric currents generate magnetic fields led to the development of electromagnetism, unifying electricity and magnetism [5]. A straight current carrying wire forms a magnetising field circular around its axis, and the winding of a current carrying wire into a helical coil to form a solenoid produces a uniform field similar to that of a bar magnet (Figure 1.2.2) [3]. If the wire is curved into a complete loop then the field is produced along the centre of the axis. This magnetic field becomes closer and closer to that of a magnetic dipole, as the diameter of the current loop becomes smaller and smaller [3]. Based on this fact, the French physicist and mathematician André-Marie Ampère suggested the magnetism of a material can be viewed as a collection of circulating currents, now known as Amperian currents [12].
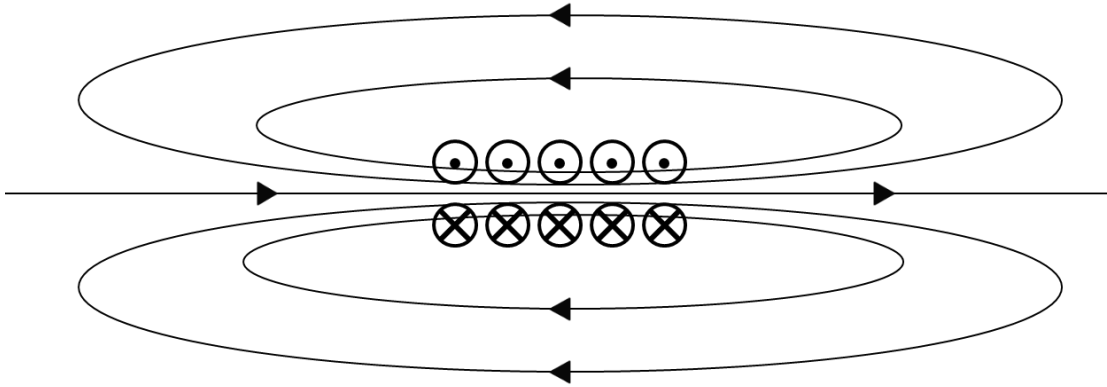
Figure 1.2.2 – Field lines around a current carrying solenoid (crosses represent the current traveling into the page, while the dots represent the current coming out of the page), flowing from the north to the south pole.

When a magnet or a current loop is placed into a magnetising field it will experience a torque [11]. For example, a pivoted bar magnet will turn to align itself parallel to an applied magnetising field. In cgs units the work done in turning a pivoted bar magnet through an angle is measured in ergs. As a result, the unit of the magnetic moment is erg Oe^{-1}, but it is convention for this unit to be defined as an electromagnetic unit (emu) [11]. A magnetic material will become magnetised when placed into a magnetising field, and the level of magnetisation is defined by the quantity *M* (occasionally written as *I* or *J*), which is known as the intensity of magnetisation or simply magnetisation [11]. If two identical bar magnets are placed side by side, then the magnetisation from the poles is summed and the magnetic moment is doubled. Although the magnetic moment has doubled so has the volume, hence the magnetic moment per volume has remained constant. As a result, magnetisation (*M*) can be defined as the magnetic moment (*m*) per unit volume (*v*), with a unit of emu cm^{-3} in the cgs system [11].

$$M = \frac{m}{v}$$
(1.2.3)

If a material is placed in a magnetising field, its magnetic response is measured in terms of magnetic induction (*B*). This is an archaic term derived from a time when magnetic poles were said to be induced in a piece of iron when it was rubbed with a lodestone to form a magnet [3]. The relationship between the magnetising field and magnetic induction is linear in free space (and in some materials), but for most materials this not the case. In cgs units this relationship is defined as [11]:

$$B = H + 4\pi M$$
(1.2.4)

Although magnetic induction and the magnetising field have the same units, it is convention to measure magnetic induction in gauss (G) and the magnetising field in oersteds (Oe) [11]. As shown previously, magnetisation is measured in terms of emu cm^{-3}, but 4πM is usually expressed in terms of gauss [11]. Furthermore, the magnetic properties of a material cannot only be defined by equation 1.2.4, but also by how magnetisation and magnetic induction vary when a material is placed into a magnetising field. Two other useful terms are known as magnetic susceptibility (χ) and magnetic permeability (μ). Magnetic susceptibility defines how responsive a material is to an applied field [11].

$$\chi = \frac{M}{H}$$

(1.2.5)

Whereas magnetic permeability defines how permeable a material is to a magnetic field [11].

$$\mu = \frac{B}{H}$$

(1.2.6)

1.2.3 Properties of Magnetic Materials

Ampère's postulation that the magnetism of a material can be viewed as a collection of circulating currents turned out to be far more insightful than anyone realised at the time, suggesting the existence of an "electrodynamic molecule" [12]. We now know this to be the electron, but remarkably Ampère made this claim prior to the discovery of the electron. Electrons have two kinds of motion, orbital and spin. Each of these has an associated magnetic moment, and as such the magnetic moment of an electron can be calculated [11]. The natural unit for expressing the magnetic moment of an electron is known as the Bohr magneton (μ_B) named after Niels Bohr, one of the key scientists in the quantum revolution of at the beginning of the 21st century [13]. Bohr's atomic model allowed this value to be calculated for the first time, and in the cgs system of units the Bohr magneton is defined by [11]:

$$\mu_B = \frac{e\hbar}{2m_e}$$

(1.2.7)

Where e is the charge of an electron, m_e is the mass of an electron and $\hbar$ is the reduced Plank constant.

Upon the application of a magnetic field all atoms experience diamagnetism, where the motions of orbiting electrons are altered to produce a magnetic moment opposing the

applied field. Purely diamagnetic materials have no net magnetic moment as a result of all of its constituent electron spins being paired [3]. Examples include; the noble gases (He, Ne, Ar, *etc*.) that have full electron shells, many diatomic gases (*e.g.* H_2, N_2) whose electrons pair up in molecular orbitals, and some ionic solids such as NaCl. Diamagnetism is a weak phenomenon that is overshadowed by other magnetic interactions if they take place within a material. Paramagnetic materials contain atoms or molecules that possess permanent magnetic dipoles as a result of the spin of unpaired electrons [3]. The application of a magnetic field causes these dipoles to align with the applied field direction. In purely paramagnetic materials, these dipoles are only weakly coupled, and as a result thermal energy causes these moments to randomly align in the absence of an applied field [3]. Examples of purely paramagnetic materials include many transition and rare-earth metal salts. These materials have a net magnetic moment due to incomplete electron shells, but the anion-cation spacing means that interactions between these magnetic moments are weak.

However, this is not always the case (Figure 1.2.3) and some materials are able to maintain their alignment when no field is applied. In the absence of an applied field, if all the magnetic dipoles in a material remain in parallel alignment then the material is classified as ferromagnetic. Ferromagnetic materials include Fe, Co, Ni and some rare-earth elements [3]. Some materials consist of atoms that have opposing magnetic moments, and usually these materials are made up of different materials or ions arranged into regular patterns on different sublattices [3]. If these differing moments are equal in magnitude, then after the removal of a magnetic field the moments present in the material will align so that exactly half are parallel and the other half are antiparallel. This results in the net magnetic moment remaining zero and the material is classified as antiferromagnetic. Examples of antiferromagnets include numerous transition metal compounds such as hematite (Fe_2O_3) and iron manganese (FeMn) [3]. On the other hand, if the opposing moments are unequal the dipoles will still align in an antiparallel fashion after an applied magnetic field is removed from the material, but the material will have a net magnetic moment [3]. These materials are termed ferrimagnetic, with examples including garnets such as YIG ($Y_3Fe_2(FeO_4)_3$) and ferrites such as the oldest known magnetic material magnetite (Fe_3O_4). Increasing temperature disrupts the magnetic ordering of ferromagnetic, ferrimagnetic and antiferromagnetic materials. Above a material specific blocking temperature (T_B)[*] the thermal energy becomes

---

[*] Also referred to as the Curie temperature (*Tc*) for ferromagnetic and ferrimagnetic materials, or Néel temperature (T_N) in the case of antiferromagnetic materials.

large enough to destroy the ordering of the magnetic moments, and all these materials become paramagnetic [3].
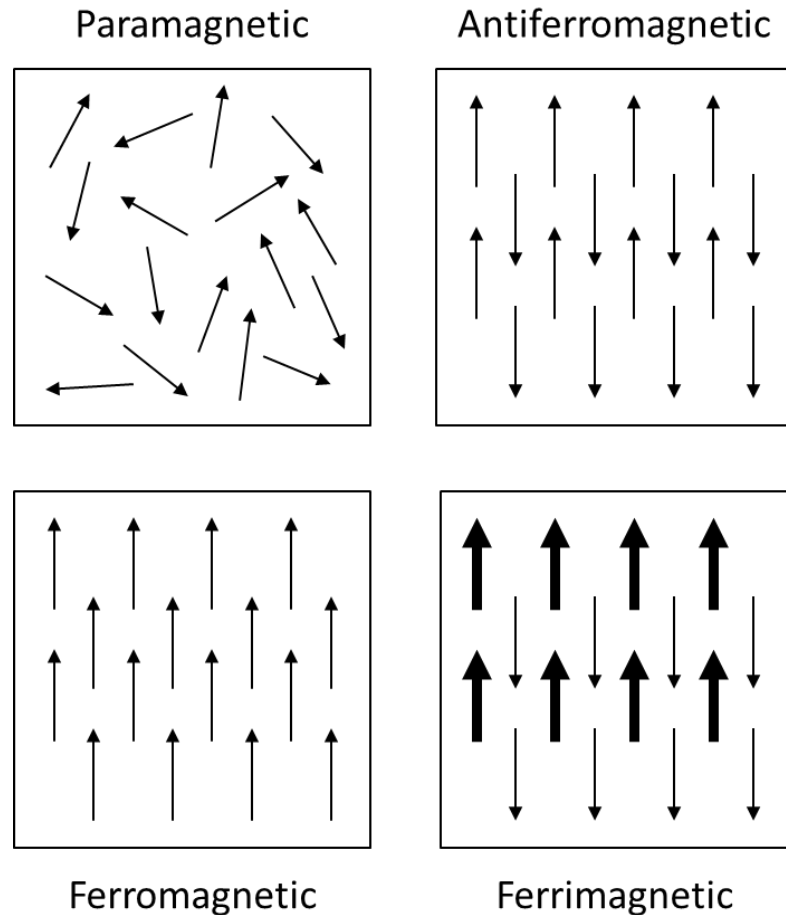
Figure 1.2.3 – Magnetic dipole ordering within different types of magnetic material.

1.2.4 Magnetic Domains

To explain why magnetic materials can exist in a demagnetised state, in 1907 the French physicist Pierre-Ernest Weiss was the first to formally introduce domain theory [14]. This theory suggests that bulk magnetic structures form small regions of uniform magnetisation known as magnetic domains. This allows a magnetic material with a domain structure to have no net magnetisation. Less than 30 years later the American physicist Francis Bitter observed these domains in a crystal of nickel [15]. Bitter covered his nickel sample with an aqueous solution of small magnetite particles, and in his microscope observed these particles collecting along the boundaries between domains.

Magnetic materials form magnetic domains to minimise the internal energy of the structure (Figure 1.2.4). The domains will form in such a way so that magnetic poles are not formed at the material surface, minimising the magnetostatic energy required for the material to generate a magnetic field [3]. Energy is also required to maintain the walls between domains, so domains form with a width that reduces the energy balance between magnetocrystalline energy and exchange energy [3]. As a result, magnetic domains will form in a way so that all these competing energy contributions will be minimised [3].
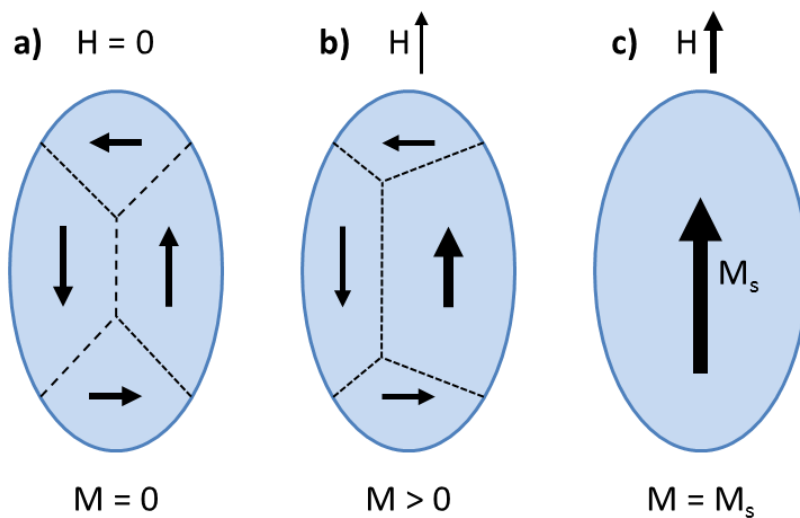
Figure 1.2.4 – Magnetisation (*M*) of a magnetic material. a) A magnetic material separated into magnetic domains (boundaries indicated with a dotted line) so that it has no net magnetisation. b) When a magnetising field (*H*) is applied, the domain aligned closest with the direction of the applied field grows via domain wall motion, and the material has a net magnetisation that is no longer non-zero. c) Through the application of a larger magnetising field the material becomes uniformly magnetised, and the magnetisation is saturated (M_s).

The application of a magnetising field to a demagnetised magnetic material causes the domains most closely aligned with the direction of the applied field to grow *via* domain wall motion [3]. Initially, this process is reversible and the material will return to its demagnetised state after the field is removed. Eventually domain growth will encounter imperfections such as dislocations and vacancies in the material that possess magnetostatic energy [3]. This energy can be eliminated with an intersection, but these defects fix the domain walls at these imperfections even after the external field is removed [3]. As a result the material retains its magnetisation after the field is removed, requiring the application of further energy to allow the domain to retreat back. In the case of large magnetising fields this process will continue until the whole material is saturated, and the material is uniformly magnetised in the direction of the applied field [3].

1.2.5 Magnetisation Curves and Magnetic Hysteresis

The ease in which different ferro- and ferrimagnetic materials can be demagnetised can vary with the material. As discussed in the previous section, the application of a magnetising field causes a magnetic material to become magnetised, with the application of a sufficiently large field resulting in saturation (as all the magnetic domains are aligned in the direction of the applied field). Magnetic materials are classified as either hard or soft, depending on the strength of the magnetising field that has to be applied before the magnetic domains can be reordered. Magnetically hard materials require the application of large magnetising fields, whereas in the opposite case magnetically soft materials require the application of much smaller fields. As a result magnetically hard materials are used when a material is required to have stable magnetic properties, such as the permanent magnets used in electric motors and generators. On the other hand magnetically soft materials are deployed when a change in magnetisation is beneficial or needs to be altered, such as in magnetic sensors or magnetic recording.

Ferro- and ferrimagnetic materials that do not return to a demagnetised state after an applied magnetic field is removed in fact display an interesting behaviour that can be modelled in a hysteresis loop (Figure 1.2.5) [3]. Increasing the strength of a magnetising field (H) that is applied to a demagnetised magnetic material increases the magnetisation of the material (red curve Figure 1.2.5). A magnetic induction (B) is also generated in the material, which also increases in a curve from the demagnetised state until saturation (dashed blue curve Figure 1.2.5). This is known as the normal induction curve. The slope of this curve is termed relative permeability (μ), and is a measure of how easy the material is to magnetise. The application of magnetising fields beyond the value required to reach saturation no longer increases the magnetisation of the material, and the magnetisation curve remains constant. On the other hand, magnetic induction continues to increase as the magnetising field forms part of magnetic induction (equation 1.2.4).
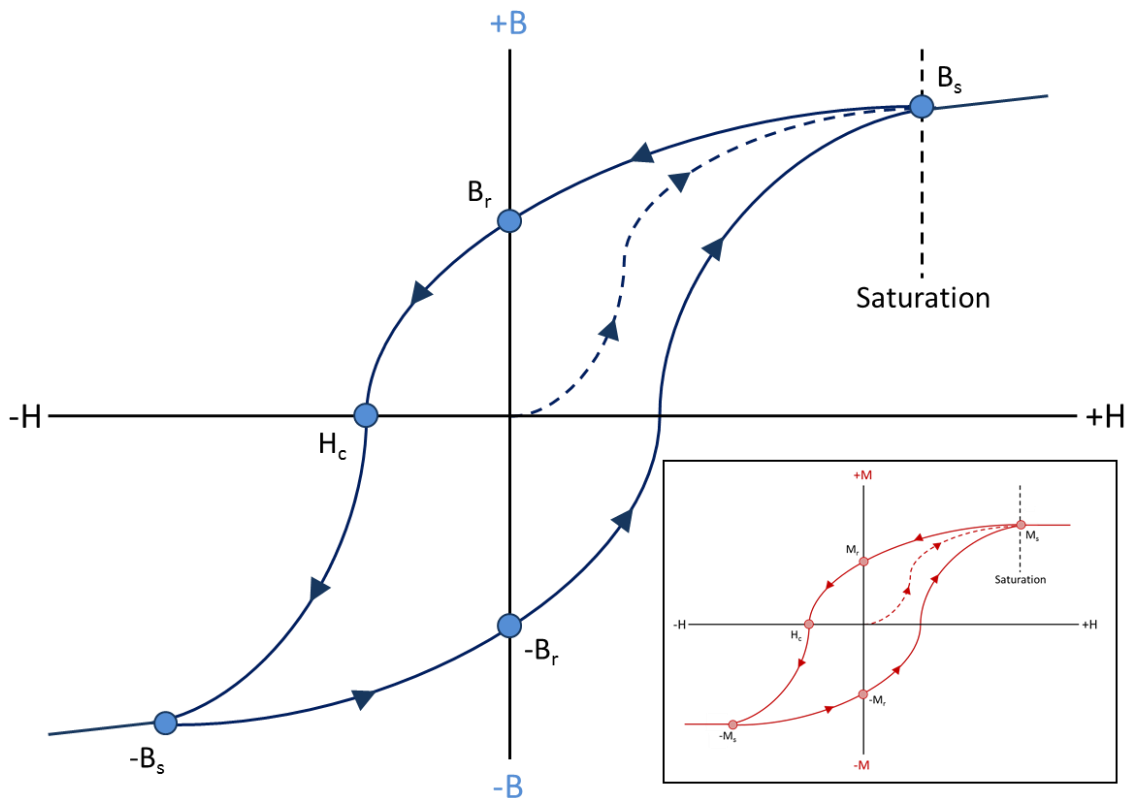
Figure 1.2.5 – Hysteresis (blue) and magnetisation (inset, red) curves of a ferro- or ferrimagnetic material. Symbols are as follows: H – applied magnetisation field, B – magnetic induction, M – magnetisation, B_s – magnetic induction saturation, M_s – magnetisation saturation, B_r – residual magnetic induction, M_r – residual magnetisation, H_c – coercivity.

When the applied field is removed, the material's magnetic induction decreases to a non-zero value known as the residual magnetic induction (B_r). The material also possesses residual magnetisation (M_r), shown in the red curve of Figure 1.2.5. The application of a reverse magnetic field reduces the value of the magnetic induction back to zero, the value of which is called the coercivity (H_c) (as the reverse field "coerces" the field back to zero induction) [3]. Magnetically hard materials have a large coercivity, whereas magnetically soft materials have a low coercivity. If the applied field is reversed further, saturation will be reached in the opposite direction. Reducing this field back to zero and applying it in the original direction results in the induction following the symmetrical hysteresis loop shown in Figure 1.2.5. Once magnetised, a ferro- or ferrimagnet will always have a non-zero value of magnetic induction and magnetisation once the magnetising field is reduced to zero. Demagnetisation can be achieved through the application of a series of alternating magnetising fields with decreasing amplitudes, or by heating the material above its Curie temperature [3].

1.2.6 Magnetic Anisotropy

Put simply, magnetic anisotropy is the directional dependence of the magnetic properties of a material. There are many kinds of anisotropy; magnetocrystalline, shape, stress, exchange, and those induced by processes such as annealing, irradiation, deformation, and so on [3]. In fact only magnetocrystalline anisotropy is a property of the material, all the other forms are induced [3]. The magnetisation of a magnetic crystal tends to align along specific crystal planes, called the easy axis. For example body centred cubic (bcc) iron has an easy axis in the <100> direction* along the edges of the cube (Figure 1.2.6) [3]. Also displayed in Figure 1.2.6 is the hard axis of bcc iron, which runs along the body diagonal <111>, and one of the intermediate axis running along the face diagonal <110> [3]. Magnetic materials such as bcc iron will reach the same saturation magnetisation with the application of a magnetising field when it is applied in any direction. However, it is easier to magnetise a material when the field is applied along the easy axis, as much smaller magnetising fields are required to achieve saturation magnetisation than when the field is applied along the hard axis.
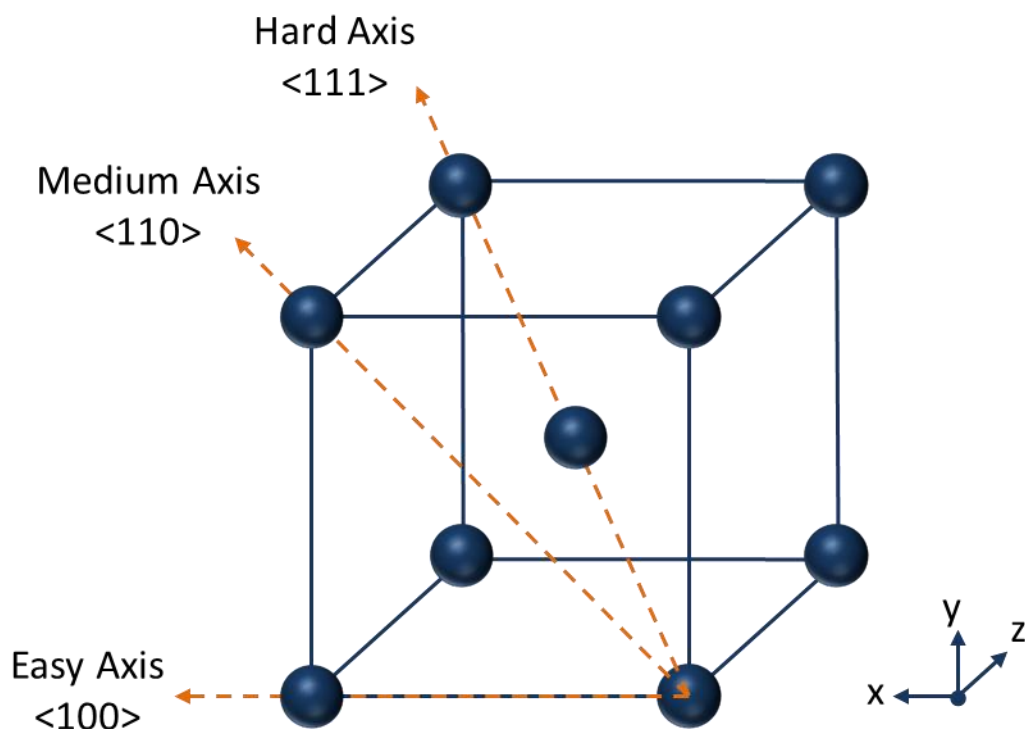
Figure 1.2.6 – The direction of the easy, medium and hard axis in the unit cell of bcc iron.

Different materials have an easy axis of magnetisation in different directions. For example, face centred cubic (fcc) nickel has an easy axis in the <111> direction [3]. This is a

---

* Miller indices are a useful notation system used in crystallography. There are in fact six cube edges directions ([100], [010], [001], [$\bar{1}$00], [0$\bar{1}$0], [00$\bar{1}$]), and it is convention to write these in square brackets. The notation written in chevron brackets (<100>) denotes this equivalent set of directions.

direct result of magnetocrystalline anisotropy, as a magnetic material exists in a higher energy state when magnetised along a hard axis as opposed to the easy axis [3]. As a result, magnetic domains form in materials so that their magnetisation points along an easy axis. Therefore, a demagnetised magnetic material will contain many domains, with their magnetisation orientated along an easy axis. Application of a magnetising field along an easy axis allows the domain aligned in that direction to grow *via* domain wall motion until all the other domains are eliminated and the material reaches saturation magnetisation (Figure 1.2.7a). On the other hand, when the magnetising field is applied in an alternate direction two domains will grow *via* domain wall motion so that the sum of their magnetisation points in the direction of the field (Figure 1.2.7b) [3]. The magnetisation of the material can only increase further by rotating the net magnetic moment of each atom in the domain, in a process known as domain rotation [3]. This only takes place with the application of large fields, hence it is much harder to magnetise a magnetic material in directions other than that of the easy axis.
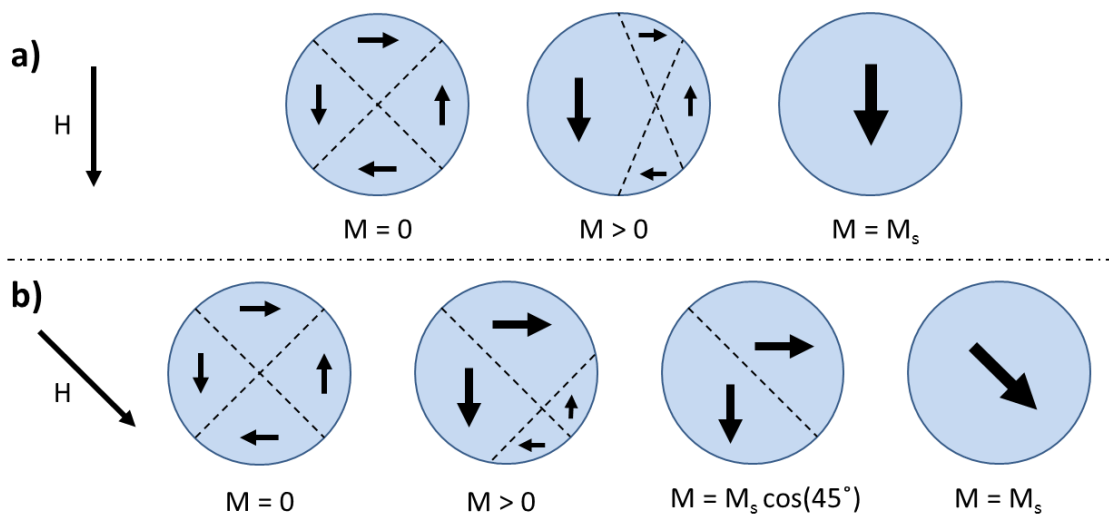
Figure 1.2.7 – Magnetisation (*M*) of a magnetic material as a magnetising field (*H*) is applied. a) Applying a magnetising field in an easy direction results in the domain aligned in this direction growing via domain wall motion until all the other domains are eliminated. b) Applying a magnetising field in a direction other than an easy axis results in domains growing via domain wall motion so that the net sum of the magnetisation points in the direction of the applied field. Magnetisation is only increased further *via* domain rotation, through the application of large fields.

1.2.7 Magnetic Materials

1.2.7.1 Magnetite

Magnetite (Fe_3O_4) is the most magnetic naturally occurring mineral on Earth, and is the mineral in which humanity first discovered the phenomenon of magnetism. In fact, magnetite has the highest saturation magnetisation of all the magnetic iron oxides, but is a soft magnetic material with a low coercivity [16]. It forms an inverse spinel structure (Figure

1.2.8), with ferrous (Fe^{2+}) and ferric (Fe^{3+}) ions arranged randomly at the octahedral sites, and ferrous iron at all the tetrahedral sites [16]. It is this $[Fe^{3+}]A[Fe^{2+}, Fe^{3+}]BO_4$ structure that generates the magnetic moment in magnetite, with electrons hopping between the ferrous and ferric sites at the octahedral sites as shown in equation 1.1.13 [16].

$$Fe^{2+} \rightleftharpoons Fe^{3+} + e^-$$ (1.1.13)
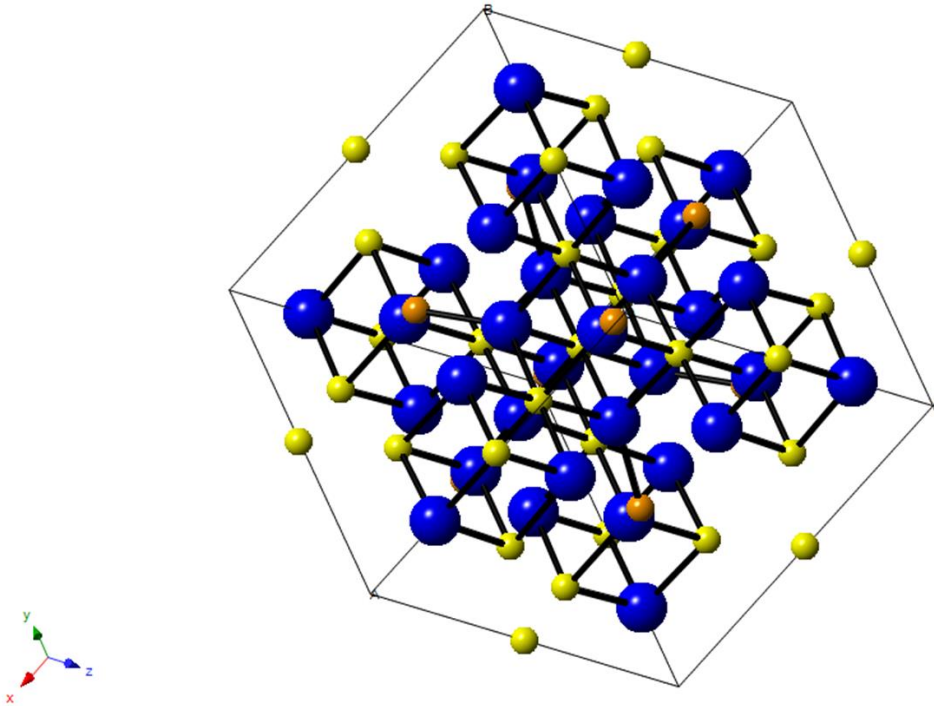
Figure 1.2.8[*] – A diagram of the inverse spinel structure of magnetite. The oxygen atoms are shown in blue, octahedral sites in yellow and the tetrahedral sites in orange.

Cooling magnetite below 120 K results in a phase transition, known as the Verwey transition (T_v) after the man who first discovered it [17]. Below 120 K there is a drop in the saturation magnetisation and the conductivity, along with an increase in resistivity and an elongation along certain crystallographic axes [18]. This is thought to be a result of magnetite restructuring from an inverse spinel structure to a monoclinic structure, creating order at the B sites [18].

---

[*] Produced by Jennifer Bain in CrystalMaker Software.

1.2.7.2 Cobalt Ferrite

Cobalt ferrite ($CoFe_2O_4$) can be formed by replacing the ferrous iron at the tetrahedral sites of magnetite with Co^{2+}. Cobalt ferrite has a low saturation magnetisation, but a high coercivity due to a preferred magnetic orientation being introduced. Magnetite has three easy axis of magnetisation, due to its isotropic crystal structure, resulting in its soft magnetic properties [16]. However, the introduction of Co^{2+} at the octahedral sites creates a preferred direction of magnetisation due to the inherent anisotropy of Co^{2+}. This reduces the saturation magnetisation and increases the coercivity as cobalt doping levels increase to form a harder magnetic material [16]. Additionally, the magnetic properties of cobalt-doped magnetite can be fine-tuned. As the level of Co^{2+} added into magnetite can be controlled between that of pure magnetite (Fe_3O_4, 0% Co, high magnetic saturation and low coercivity) and pure cobalt ferrite ($CoFe_2O_4$, 33% Co, low magnetic saturation and high coercivity) [19].

1.2.7.3 Cobalt Platinum (CoPt)

Binary and tertiary alloys of Fe, Co and Ni are ferromagnetic, but ferromagnetic alloys can also be generated when these elements are alloyed with materials that are not ferromagnetic [3]. Ferromagnetic cobalt-platinum (CoPt) alloys can be formed from a solid solution, usually with a disordered fcc structure, which is also known as the A1 phase [20]. For many years it has been known that the CoPt alloys in the 50:50 atomic range have distinct ferromagnetic properties with a high magnetocrystalline anisotropy energy after prolonged annealing at high temperatures (600-700˚C) [20, 21]. After this annealing, the fcc structure transforms into an ordered fct structure also known as the $L1_0$ phase, and the A1 and $L1_0$ phases of CoPt are displayed in Figure 1.2.9 [22]. In the case of the A1 phase (Figure 1.2.9a) the probability that each site is occupied by either a Co or Pt atom is the same, whereas the $L1_0$ phase (Figure 1.2.9b) is a derivative of the fcc structure with two faces occupied by one type of atom and the other face occupied with the other type of atom [22].
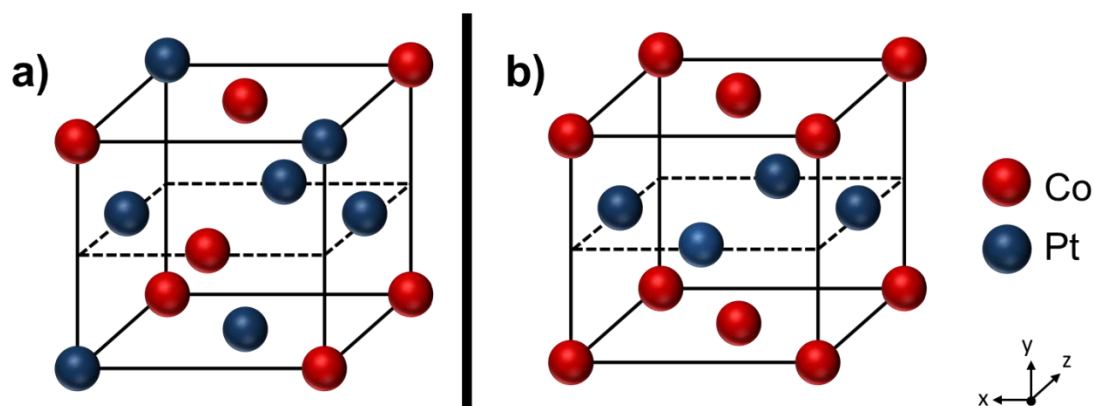
Figure 1.2.9 – The disordered A1 phase (a) and the ordered $L1_0$ phase (b) of CoPt.

The chemically ordered $L1_0$ phase of CoPt has a multilayer structure, consisting of alternating planes of pure Co and pure Pt. Spin-orbit coupling on the platinum and strong hybridization between the 5d electron sites of Pt and the 3d electron sites of Co result in the strong magnetic anisotropy and high coercivity of $L1_0$ CoPt [22]. The magnetic properties of $L1_0$ phase CoPt vary with the composition of Co to Pt, as well as the time and temperature of the heating and cooling processes that take place during annealing [21]. The high temperature annealing processes currently used are not only financially and environmentally expensive, but can lead to problems such as lattice deformation and particle agglomeration [23]. Increasingly technology demands miniaturisation, and the high magnetocrystalline anisotropy energy of alloys such as CoPt in the $L1_0$ phase mean that the magnetic properties remain stable at dimensions of a few nanometres (something that is discussed in more detail in the following Chapter 1.2.8 and Chapter 1.3) [24]. However, when small grains or nanoparticles of CoPt are used high temperature annealing can lead to grain growth, agglomeration and sintering [23].

1.2.8 Magnetism on the Nanoscale

A nanomaterial is often defined as a material with one or more dimensions in a size region between 1-100 nm. As the size of a material is reduced to this scale it often exhibits unique, or in some cases enhanced, properties that are different to those in the bulk state. The small size of nanoparticles results in a large surface area to volume ratio, meaning that unlike in the bulk, material properties are dominated by surface atom contributions [25]. The increase in surface area and surface free energy of a nanoparticle can have an effect on the structural properties of the material when compared to bulk materials, along with potential changes in other properties such as; thermal, chemical, mechanical, optical and magnetic properties [25].
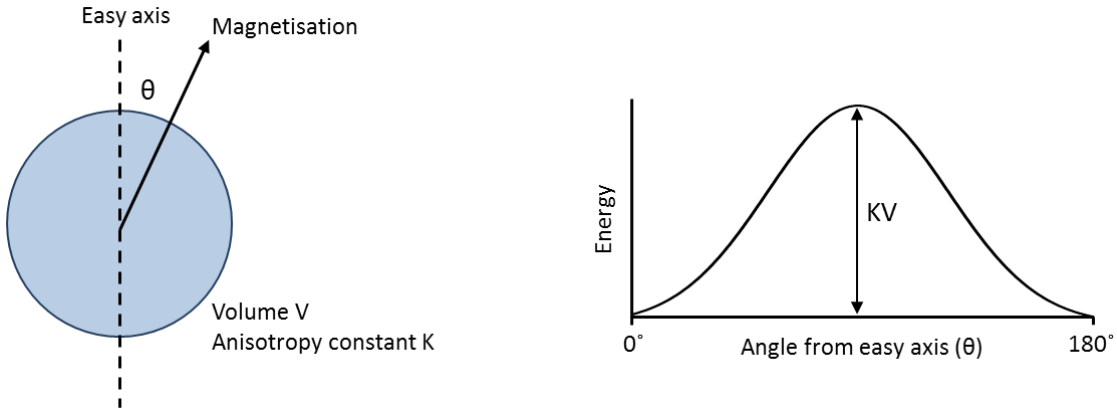
Figure 1.2.10 (adapted from Figure 1.6 in ref. [26]) – The dependence of anisotropy energy on the direction of magnetisation of a MNP with a uniaxial anisotropy.

As discussed previously, bulk magnetic structures form uniform domains of magnetisation separated by domain walls, forming a balance between magnetostatic energy and the energy required to form domain walls. As the size of a material is reduced, a critical volume is reached, where it costs more energy to create a domain wall than the total magnetostatic energy of the material. In this case, a uniformly magnetised single domain magnetic particle is formed. This can be seen if a particle with a uniaxial anisotropy is considered (Figure 1.2.10), whose anisotropy energy (E) is given by:

$$E = KV \, \sin^2 \theta \tag{1.2.8}$$

Where K is the anisotropy energy density, V is the particle volume and θ is the angle between the magnetisation vector and the easy axis. In the example shown in Figure 1.2.10 there are two minimum energy states separated by an energy barrier of KV. Therefore, the critical diameter (d_c) for the formation of a single domain particle (which is spherical and non-interacting) can be derived and is given approximately by [26]:

$$d_c \approx 18 \frac{\sqrt{AK}}{\mu_0 M_S{}^2} \tag{1.2.9}$$

Where A is the exchange constant, K is the anisotropy constant, μ_0 is the vacuum permeability, and M_s is the saturation magnetisation. Below d_c the MNP switches from approximately zero to approximately the full saturated value. Due to the fact that there are no domain walls to move, the magnetisation of a single domain particle is changed purely by domain rotation resulting in the high coercivities of small MNPs.

As shown in Figure 1.2.10, an energy barrier KV separates two easy directions of magnetisation. However, as the volume of a MNP is reduced, this energy approaches that of

the thermal energy k_BT (where k_B is the Boltzmann constant and T is the temperature). When in the case of [26]:

$$KV < k_BT \qquad (1.2.10)$$

The magnetization of the MNP is easily reversed. In this case, the particle can be viewed as having a large or 'super' moment, and behaves like a paramagnet. As a result this system is termed superparamagnetic and has no hysteresis. Therefore, for a MNP of a given size there is a temperature that marks a transition from a MNP with a permanent static magnetic moment, to a MNP with a continually fluctuating magnetic moment. The relaxation time of the moment of a particle (τ) is given by the Néel-Brown expression [26]:

$$\tau = \tau_0 exp\left(\frac{KV}{k_BT}\right) \qquad (1.2.11)$$

Where τ_0 is the relaxation time at the high temperature limit. If the magnetic moment of the particle reverses at times shorter than the experimental time scales, the system is in a superparamagnetic state, if not it is in a state which is known as the blocked state. The blocking temperature (T_B) is the temperature which separates these two regimes, and T_B can be calculated by considering the time window of any measurement performed. For example, if an experimental measuring time is arbitrarily chosen to be 100 seconds and $\tau_0 \approx 10^{-9}$ seconds, T_B is [27]:

$$T_B = \frac{KV}{30k_B} \qquad (1.2.12)$$

1.2.9 Magnetic Nanoparticles (MNPs)

1.2.9.1 Synthesis of MNPs

A great body of research now exists into the synthesis of MNPs, and many different routes to forming monodisperse and stable MNPs with tuneable sizes have been published [27, 28]. A wide range of different magnetic materials have been synthesised including; metals such as Fe and Co, iron oxides, spinel-type ferromagnets and useful magnetic alloys such as CoPt and FePt [27]. It is impossible to review all of these published methods, even for journal articles that are dedicated to this purpose [27]. However, whatever process is used has to be chosen with the application in mind. For example, if the MNPs are to be used for magnetic data storage it is paramount that they are of a uniform size, shape and crystallinity to ensure a reliable and predictable magnetic response, as well as offering long term stability [29].

Co-precipitation is a simple synthesis route for magnetic oxides (Fe_3O_4 or γ-Fe_2O_3) under mild aqueous reaction conditions, through the addition of a base to a mixed ferrous and ferric salt (Fe^{2+} and Fe^{3+}) solution [27, 28]. During this type of reaction the size, shape, and type of the iron oxide or iron oxyhydroxide that is formed is dependent on variables such as; the type and activity of the salts used (e.g. chlorides, sulphates, nitrates), the Fe^{2+} to Fe^{3+} ratio, the pH of the solution, the temperature of the reaction, the time taken and the level of oxygen [28]. For example, the synthesis of magnetite requires the reaction to be performed in a pH range of 8-10, with high ratio of Fe^{2+} to Fe^{3+} and in a low oxygen environment [28]. If these conditions are not met, other iron mineral phases are more likely to be produced. However, once suitable reaction conditions are established, co-precipitation forms a simple, cheap and environmentally friendly route for the formation of MNPs [27].

Thermal decomposition of organometallic compounds in organic solvents containing stabilising surfactants has been used to form consistent and monodisperse MNPs with narrow size distributions [27]. The size, shape and crystallinity of the final MNPs formed are all dependent on the experimental parameters such as; the reaction temperature, reaction time, maturation period, ratio of reactants, solvent used, and so on [27]. So, by adjusting these variables, the properties of the MNPs can be tuned. Although this approach produces extremely uniform MNPs, it is not the greenest approach, as it requires use of high temperatures (100-320°C) and harsh organic solvents.

MNPs have also been formed with the use of microemulsions, with this approach offering relatively good control over the shape and the size distribution of the particles formed [27]. A microemulsion is a stable dispersion of two liquids that cannot form a homogenous mixture, with one or both liquid stabilised by a surfactant [30]. For example, in a water-oil microemulsion microdroplets of water are stabilised by a monolayer of surfactant molecules. These microdroplets can form nanoreactors for the formation of MNPs if two microemulsions containing any reactants of choice are mixed [27]. The microdroplets continually collide, combine and mix their contents, leading to the formation of the MNPs inside the microdroplet [27].

Monodisperse MNPs with very narrow size distributions have also been synthesised under hydrothermal conditions in a liquid–solid–solution reaction [27]. This is a result of phase transfer and separation occurring at the interfaces between these different phases. For example Deng *et al*. [31] formed highly uniform MNPs of ferrite from a mixture of $FeCl_3$, ethylene glycol, sodium acetate, and polyethylene glycol. The mixture was stirred, sealed in an

autoclave and heated to 200˚C for 8-72 hours. However, although this approach produces excellent results, it does require the use of high temperatures and pressures [27].

Table 2.2.1 (information for table taken from ref.[27]) – Overview of the key properties of some of the different routes that are available for the synthesis of MNPs.

Method	Reaction Conditions	Solvent	Temperature (˚C)	Time	Size Distribution	Morphology
Co-Precipitation	Ambient	Water	20–90	Minutes-Hours	Fairly Narrow	Broad
Thermal Decomposition	Complicated	Organic	100–320	Hours-Days	Narrow	Good Control
Microemulsion	Complicated	Organic	20–50	Hours	Fairly Narrow	Some Control
Hydrothermal Synthesis	High Pressure	Water-ethanol	220	Hours-Days	Narrow	Good Control

1.2.9.2 Applications of MNPs

Due to the enhanced or unique properties that can be displayed by a nanomaterial, materials with one or more dimension in the nanoscale can now be found in an ever increasing number of applications. MNPs are no exception, and have been the subject of extensive research in a wide range of different fields. For many years colloidal liquids of MNPs suspended in a carrier fluid, termed a ferrofluid, have been used within technologies. Ferrofluids were first introduced by Steve Papell in the 1960's, who at the time was working for NASA during the space race, to form the basis of a rocket fuel that could be used in zero gravity [32]. Since then ferrofluids been have been used in many different technologies, such as magnetic seals, dampers and within loudspeakers [33].

It has also been proposed that due to their high surface to volume ratio, MNPs could form more efficient catalysts [34]. However, when used industrially nanoparticles cannot be separated by traditional means, leading to problems such as aggregation and the blocking of equipment [34]. One solution to this problem could be provided through the use of magnetic nanocatalysts, and the simple application of a magnetic field [34]. A great deal of research has also focussed on the use of MNPs for biomedical applications, especially for use as contrast agents in MRI, and as radical new cancer treatments such as mediators for targeting cancer cells with magnetic hyperthermia [35]. It has even been suggested that MNPs could be used for environmental contamination removal. For example, it has been proposed that carbon coated iron nanoparticles could be used to remove the contaminant hexavalent chromium

from waste water streams *via* carbon shell physical adsorption [36]. Furthermore, MNPs could also be used to form the basis of bit-patterned media, potentially the next generation of ultra-high density magnetic data storage devices, and this is something that will discussed in more detail in Chapter 1.3 [29].

1.3 Magnetic Data Storage

1.3.1 History and Basic Principles of Magnetic Data Storage

It is often overlooked, but the human brain can be viewed as a natural data storage device. Although our brain is perfectly designed for many tasks, it requires a great deal of effort to commit vast amounts of data to memory. The human memory is also prone to error, and ultimately after death, individual memories cannot be transferred from one person to another. Consequently, throughout history humans have used many different methods for storing and communicating information. Stone Age man may have decorated his cave for this reason, and writing, which throughout history has evolved in some form in every major civilisation on Earth, has certainly been used for this purpose. As we advance further into the information age, much of the world's information is now stored electronically, within the memories of computers.

Hard disk drives (HDDs), found within most personal computers (PCs), have come a long way since IBM introduced the 305 RAMAC (random access method of accounting and control) in 1956, the first magnetic hard disk [37]. These revolutionary HDDs were introduced more than 50 years after Valdemar Poulsen developed the first magnetic data storage device, which later became commercially available in the form of magnetic tape recorders [38, 39]. A magnetic tape recorder writes an electrical signal into a ferromagnetic tape with an electromagnetic head. The stored information can then be read at a later date by passing the tape over the electromagnetic head to produce the original electric signal. Once written, magnetic tapes can store data without the need for the input of energy, and data can be overwritten or replaced simply by the application of a different magnetic field pattern. Although magnetic tapes are well suited to applications such as sound recording, they do have one major drawback in the fact that they do not possess random access capability. Data can only be written or read serially, which can be explained with the analogy of a textbook such as an encyclopaedia. If you require information from an encyclopaedia you can read until you find the information you need in a serial process, but you also have the option to consult the index and simply turn to the page you require. You do not have to read the whole book to access the piece of information you require. The 305 RAMAC was the first magnetic storage device to combine the advantages of magnetic data recording with random access capability. Two read-write heads under servo control could be moved anywhere on the recording disk, making the RAMAC a landmark in the development of computers.

The magnetic HDDs available today contain many of the components that were a feature of the 305 RAMAC (Figure 1.3.1). Information is written by one or more flying read-write heads onto rotating magnetic disks, on which the information is stored. The recording medium is usually a thin granular layer of magnetic material, typically a Co-based alloy, sputter coated onto a supporting layer of glass or coated aluminium [40]. Data is stored digitally in binary code as a string of 1 and 0's, and can be encoded onto several disks stacked within the hard disk or even on both sides of the disks. The binary code is written onto circular tracks on the recording disks by a write head, which orientates the magnetic polarity of the magnetic grains on the disk.

Each of the grains on the magnetic disk can be considered an individual magnet, therefore orienting the magnetic polarity of a grain in a certain direction forms a bit of information. However, this is a more simplistic view than what occurs in reality. Although the polycrystalline magnetic materials that are sputter coated onto modern recording disks contain grains with diameters that are smaller than 10 nm, the smallest read-write heads are much larger with diameters in the range of 80 nm [41]. As well as this, the grains which make up the magnetic recording medium are not uniform, but instead form in a range of sizes and are randomly distributed. Therefore, it is necessary to couple the orientation of many grains to encode one bit of information, so that the data can be read with a significantly high signal to noise ratio and minimise errors [41]. As a result, each bit of information is written into several hundred grains on the magnetic hard disk.

In longitudinal magnetic recording (LMR, figure 1.3.1) the polarities of the magnetic grains lie along the circular tracks, parallel to the surface. For example, a 1 can be encoded by aligning like poles. This results in a large magnetic field emanating from the surface, and produces a large voltage when a read head is passed over this area. Alternatively, a zero can be encoded when opposite poles are next to each other, so that a voltage is not induced in the read head when it passes over this area. Recently LMR has been superseded by perpendicular magnetic recording (PMR, see figure 1.3.1). The basic principle is the same, except in the case of PMR the polarities of the magnetic domains lie perpendicular to the circular recording track (up and down in the z plane, as opposed to left and right in the x and y plane). The main driving factor behind this shift is that it has allowed for higher storage densities to be achieved, as the magnetic grains in PMR take up less space than in LMR [42].
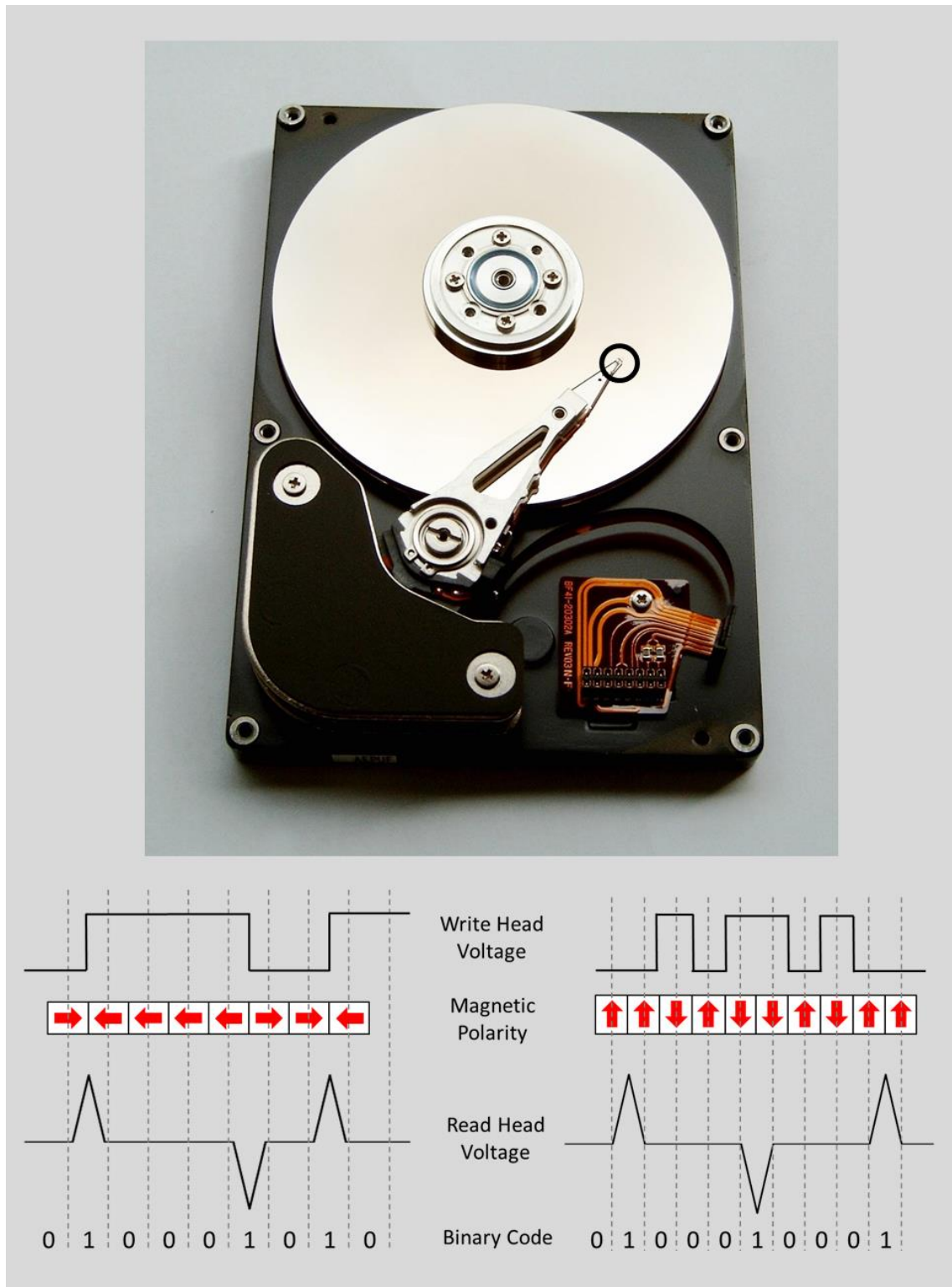
Figure 1.3.1 – A picture of a modern magnetic HDD (the read-write located on the recording disk is circled), and a simple illustration of the basic recording principle for longitudinal magnetic recording (LMR, left) and perpendicular magnetic recording (PMR, right).

Despite these issues the increase in the storage capacities and densities since IBM introduced the first commercial magnetic HDD has been remarkable, with today's devices having over 200 million times the storage capacity of the 305 RAMAC [29]. The number of bits

that can be stored on a magnetic recording disk (areal density) is usually measured in bits per square inch (b in^{-2}), and is determined by the number of tracks that can be packed onto the disk and the number of bits which can be written into a track. The 305 RAMAC boasted a total capacity of 5 MB, achieved with fifty 24 inch disks that each had an areal density of 2 kb in^{-2} [37]. Although this was revolutionary in 1956 it does not compare to modern standards, especially since the disk storage unit of the 305 RAMAC was approximately 1.5 m^2, weighed over a ton and cost US\$ 3200 per month (equivalent to approximately US\$ 160 000 today) to lease [43]. At the time it was unimaginable that the general public would have access to computers, even more so that people would be able to purchase their own. This is something that is reflected in the now infamous quote attributed to Thomas J. Watson (former chairman and CEO of IBM 1914-1956); "I think there is a world market for maybe five computers" [43].[*]
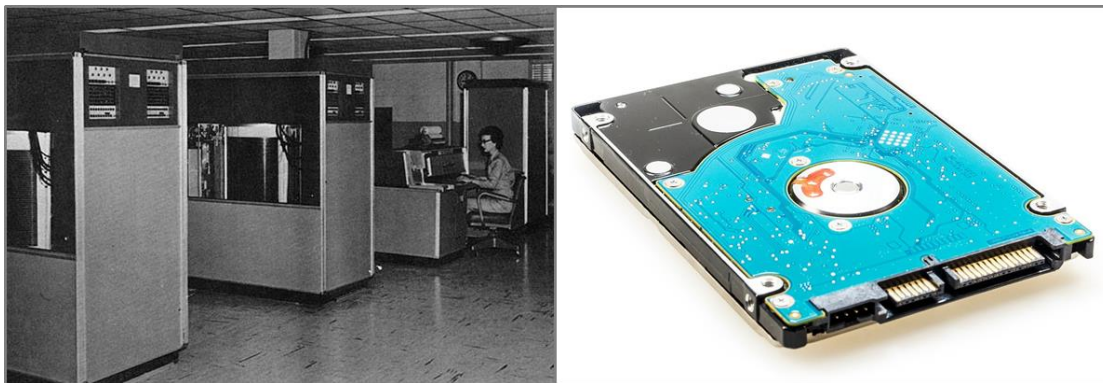
Figure 1.3.2 – In 1956 the 305 RAMAC (left) offered 5 MB of storage, would fill a room and cost you \$3200 per month to lease. Today modern HDDs (right) fit in the palm of your hand, with storage capacities in excess of 1 TB for less than \$50.

Yet in 2011 magnetic HDDs had capacities in excess of 1000 GB, with the use of only two 3.5 inch disks (or both sides of the same disk) with areal densities in the region of 500 Gb in^{-2} [29]. What is even more remarkable is these devices can now be purchased for less than US\$ 50. The great advances made in increasing storage capacities and densities have in the most part been achieved by continually scaling the components of magnetic HDDs to ever smaller dimensions. The grain size, track widths and read-write head sizes have been reduced, and the magnetic anisotropy of the recording medium and head fields have increased.

However, this trend cannot continue indefinitely, due to enhanced thermal effects and the onset of superparamagnetism as size reduces [29, 44]. The magnetic energy per grain KV, must remain larger than thermal energy k_BT (equation 1.2.10). If the volume V of the

---

[*] This quote is attributed to Thomas J. Watson, but there is no evidence he ever spoke these exact words. However, when the 305 RAMAC was released he did describe it as; "the greatest product day in the history of IBM".

grains in the magnetic recording medium becomes too small and equation 1.2.10 is not satisfied, then direction of magnetisation written by the write head into the grains on the recording medium will be thermally reoriented. Ultimately this results in the stored information being lost. *V* can be reduced as long as the magnetic anisotropy *K* of the recording medium is increased to satisfy equation 1.2.10. However, increasing *K* results in a larger field needing to be applied to orient the magnetisation of the grain, and is limited by the saturation magnetisation of the write head material. Current designs are approaching the limits imposed by equation 1.2.10, yet it is expected that the demand for data storage is unlikely to cease. If magnetic HDDs are to remain cutting edge, new technologies and materials must be sought to maintain the extraordinary progress made in increasing the performance, storage densities and capacities over the last 60 years.

1.3.2 Data Storage Technologies

As technology continues to become more of an important feature in our daily lives, data storage devices are not just found within PCs. Increasingly consumer products are becoming more user-friendly and intelligent or 'smart', and require the ability to access and store information. Although common in computer systems, magnetic HDDs are not the only technologies available, with optical and solid-state semiconductor drives now found in many products. Each of these memory technologies has its own unique set of advantages and disadvantages, and in the most part this results in each technology having its own place in the market [45].

Semiconductor memories are electronic data storage devices constructed on integrated circuit (IC) boards. Due to the lack of moving parts, these memories are extremely compact, and operate at very high speeds. As such these devices have become the primary internal memories within computers, with other classes of memory forming secondary memories. Semiconductor memories can be loosely organised into two classes; volatile devices which lose stored information without a power source, and non-volatile devices which will not lose stored information if power is lost. The two most common semiconductor memories, which fall into the volatile class, are dynamic random access memory (DRAM) and static random access memory (SRAM) [45]. DRAM stores bits of information inside capacitors, with each capacitor encoding a bit of information. A 1 or 0 can be formed by the capacitor being either charged or discharged, but these capacitors will discharge if the charge is not continually refreshed. Hence information stored on these devices will be lost if power is lost also. SRAM is similar in principle to DRAM, but in this case a bit of information is encoded into

four transistors. These transistors have two stable states that can encode a 1 or a 0, so like DRAM the stored data will be lost with the loss of power. However, the stored information does not need to be periodically refreshed, making SRAM faster and less power consuming than DRAM. Yet SRAM is much more complex, has lower optimum storage capacities, and is more expensive to produce [45]. As such, DRAM has become the dominant technology for internal computer memories, with SRAM reserved for niche applications where speed is most desired.

The recent trend towards portable computers, smartphones, as well as portable electronics, has fuelled the development of fast and compact non-volatile semiconductor data storage. One of the most successful technologies in this category is flash memory, which can store data for approximately ten years without power [45]. Flash stores data in arrays of floating gate transistors, which make up a memory cell. The most common types are named after NAND (negative-AND) or NOR (not-OR) logic gates, dependent on which gate the memory cells most closely resemble. As with magnetic data storage, flash memory has seen massive improvements in storage densities and capacities, by scaling the size of the floating gate transistors to smaller dimensions. Again this process cannot continue indefinitely, and it is believed that future improvements will be very challenging [45]. As a result many different technologies are currently being explored as alternatives to flash technology [45].

Despite the advances made with semiconductor data storage, magnetic HDDs can still be found within most modern PCs. They remain the most commercially viable choice for high volume data storage, something that may become more important if the current shift towards cloud computing continues. In the most part, this is due to the fact that magnetic HDDs use a continuous featureless recording medium. This requires far fewer processing steps to manufacture, having a dramatic effect on the price. Despite the more complicated mechanical structure and the complex processing required to manufacture read/write heads, in terms of cost per GB magnetic storage is significantly cheaper. In 2011 a magnetic HDD cost somewhere in the region of US$ 0.2 per GB, with flash drives costing approximately 20 times more around US$ 4 per GB [29]. To maintain this advantage it is vital that the storage capacities continue to increase without price being affected, or magnetic data storage technology will be replaced by alternatives such as semiconductor devices.

1.3.3 The Future of Magnetic Data Storage

Several new approaches to magnetic data storage are currently in development, with the aim of continuing the trend of increasing storage densities and capacities. These new approaches can be placed into one of two classes; energy assisted recording and lithographically patterned media [29]. Energy assisted recording applies some form of energy to the granular recording media, allowing the write head to orient the magnetic polarity of a higher anisotropy magnetic recording medium. This allows for smaller grain volumes to be used (see equation 1.2.10), and as a result higher areal densities can be achieved. The technology that has received the most attention in this class is heat-assisted magnetic recording (HAMR) [46], but there are alternatives such as microwave-assisted magnetic recording (MAMR) [47]. Although energy assisted recording promises to vastly improve the areal densities of magnetic hard disks, the development of this technology has been challenging and to date it is not commercially available [29].

Lithographically patterned media replaces the featureless granular recoding medium used in current magnetic hard disks with a magnetic medium that has been patterned by lithography (Figure 1.3.3). Two different classes of lithographically patterned media are currently under development, discrete track media (DTM) and bit-patterned media (BPM). DTM has the tracks into which information is written on the granular magnetic recording medium defined by lithography, either by filling the gaps between the tracks with a non-magnetic material or raising the tracks [29]. In conventional magnetic hard disks, which have a featureless granular recording medium, the write head defines the bit size. However, write errors occur as the head does not perfectly follow the track, resulting in a large amount of noise at the edges of the tracks [29]. To compensate for this the read head is often smaller than the write head, but defining the tracks on the recording medium means that this is no longer a problem [29]. This allows smaller read/write heads to be used, and track densities to be increased.
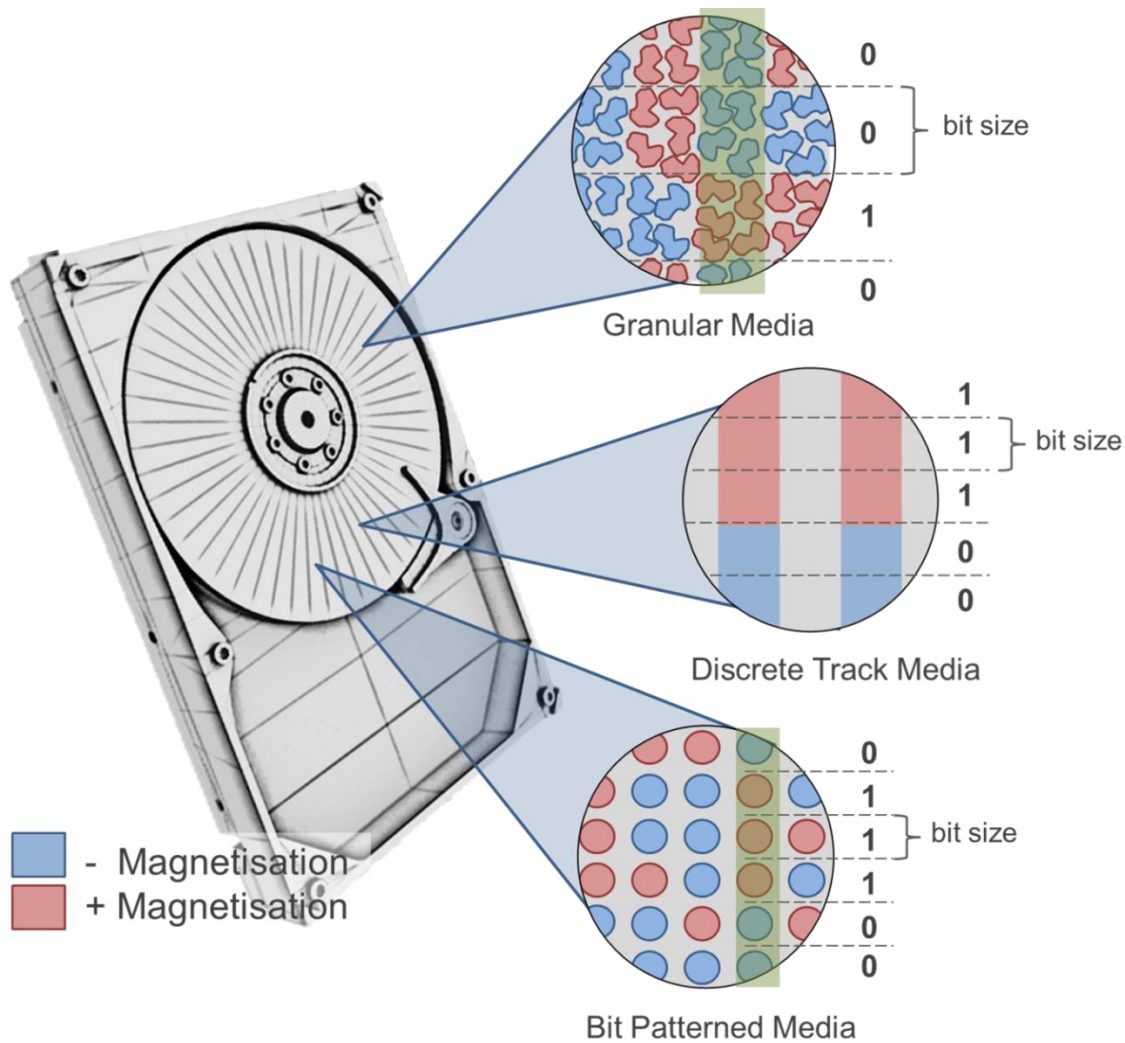
Figure 1.3.3 – A simple schematic of bits written into a traditional granular recording medium, and the proposed lithographically patterned mediums; discrete track media (DTM) and bit-patterned media (BPM).

Storage densities could be further improved with the use of BPM, where each bit of information is stored on an individual magnetic island as opposed to multiple grains on a granular recording medium. In this case the bit size is not defined by the write head, but is instead defined by the size of the magnetic island. It is likely that conventional granular recording media will soon reach storage capacities of approximately 1 Tbit in^{-2}, with bit sizes of approximately 625 nm^2 formed by aligning the polarities of multiple grains. With the use of current head materials, thermally stable magnetic islands suitable for BPM could be as small as 8 nm (for an island with equal diameter and thickness), and with the addition of spaces between the islands bit sizes could be as small as 12 nm^2 [29]. As a result it has been predicted that storage densities could be pushed beyond 50 Tbit in^{-2} [29]. Yet the development of a cost effective and industrially scalable manufacturing technique for BPM, as well as additional

challenges such as head design, mean that currently this technology is still very much in the development stage [29].

1.3.4 Fabrication of Bit-Patterned Media (BPM)

The development of a process capable of producing BPM is not only challenging, but for magnetic recording to remain commercially viable it must also be cost effective. It is not possible to adapt traditional lithographic methods, where a pattern is defined in a resist layer that is subsequently used to define a pattern on the magnetic recording medium, for the mass production of a recording medium suitable for BPM. Photolithography, which is widely used in the IC industry, forms a pattern in a light-sensitive resist material by exposure to light through a photomask, and could only achieve patterning resolutions suitable for the fabrication of bit-patterned media with the use of specialised resolution enhancement techniques [48]. Nanoscale patterns can be written into an electron-sensitive resist layer by a beam of electrons in electron-beam lithography (EBL). Although EBL is widely used for the production of sub-100 nm patterns, it is a high-cost and slow serial writing process that is unlikely to ever be scaled up for mass production [49]. Therefore, it is likely that new manufacturing methods must be sort before BPM becomes commercially viable.

One approach may be to replace the resist layers used in conventional lithography with a naturally occurring self-assembling structure. Hexagonally close packed anodised alumina has been used as a template for fabricating tall wires, through filling the pores *via* processes such as electrodeposition [50]. Although pore sizes can form in a size range suitable for BPM, templating low aspect ratio magnetic islands is challenging with this approach. Similarly, self-assembled layers of block co-polymers have been used to template the formation of magnetic structures [51]. These polymer chains comprising of two distinct monomers can form with periodicities in the range of 10-200 nm, yet achieving consistent ordering over the large areas required for BPM remains difficult. Similarly, inorganic particles may form close packed arrays on certain surfaces, which again can be used as a template. Layers of CoPt have been patterned in this way, but yet again maintaining long range ordering remains an issue [23].

Expensive and slow lithographic methods, such as EBL, may be impractical for the production of each individual magnetic disk, but could be used to fabricate an expensive master. This could then be used to manufacture many cheap replicas, in a similar way to which compact discs (CDs) are currently manufactured. Expensive moulds are fabricated by

direct laser writing, and the CDs themselves are manufactured cheaply through injection moulding. Likewise, it has been proposed that a similar technique could be used to manufacture magnetic hard disks. This could be done using nanoimprinting, which was pioneered by Chou *et al.* [52], and has received a great deal of interest [40]. In this approach a mould, produced by an expensive lithographic technique such as EBL, is used to emboss either a thermosetting or a photocuring resist layer. It has been suggested that this approach could form the next generation of lithography in the semiconductor industry, and has seen a lot of commercial interest [40].
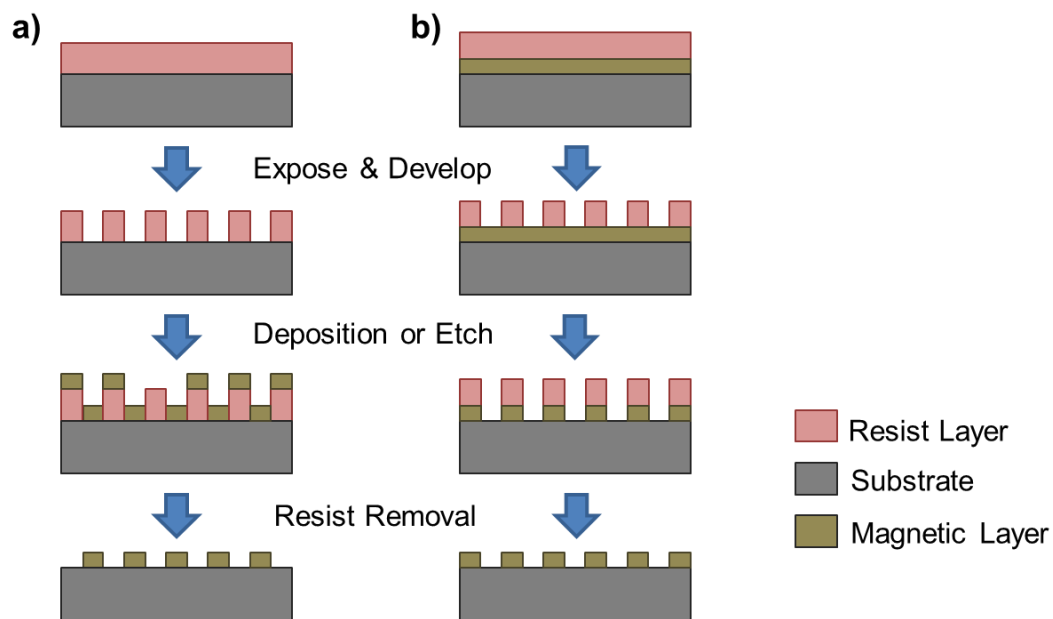
Figure 1.3.4 – A schematic of the traditional lithographic approaches available to form bit-pattered media. A resist layer can be patterned and used as a mask for depositing a magnetic material (a), or to protect a magnetic layer during an etch process (b).

Forming a pattern in a resist layer would only form the first step towards the production of BPM. This pattern must then be transferred onto a magnetic layer, which would form the recording medium of a HDD. The patterned resist could be used as a mask as a magnetic layer is deposited, sputter coated or electroplated [53]. This would leave behind the desired pattern after the resist is removed during a lift off process, usually by the resist being dissolved in a specific solvent (Figure 1.3.4 a). Alternatively, a resist can be deposited and patterned over a complete magnetic layer, and act as an etch mask [53]. This would allow a magnetic layer to be selectively removed in locales dictated by the overlying mask pattern by processes such as; chemical etching, by reactive ion etching (RIE) with the use of a chemically reactive plasma generated in an electromagnetic field under vacuum or by bombarding the surface with ions to sputter material away in a process known as ion milling (Figure 1.3.4 b) [53].

Yet producing magnetic features at the length scales required for BPM remains challenging. Although capable of generating high aspect ratio features in organic compounds, inorganic materials are degraded much less efficiently in a RIE etching process [53]. Therefore, RIE is not well suited for etching magnetic materials. Alternative etching techniques such as ion milling that sputter material away from the surface by bombarding it with high energy ions is not very selective [53]. In this case the whole surface is degraded at the same rate, making it difficult to form the nanoscale features required for BPM as the etch rate of the protective resist layers is similar to that of the magnetic layer [40]. This problem can be alleviated with the use of a focused ion beam (FIB), but like EBL this process is a slow serial writing process that is unlikely to ever be scaled up for mass production [53]. Depositing material to form nanoscale and low aspect ratio magnetic islands with nanoscale precision also remains challenging [40]. Many resists do not remain stable during the deposition process used and the uniformity of the deposited layer at the length scales required for BPM does not remain consistent [53]. This can lead to the formation of voids and of magnetic islands that are not uniform, leading to a magnetic response that would not be reliable and consistent over the whole surface if used as the recording media within a HDD. Additionally, any process used must produce an extremely smooth, clean and resist free surface without damaging the magnetic layer to avoid disastrous head crashes in a working magnetic HDD [40]. As a result of these problems, a process that is capable of producing a surface of magnetic islands with the uniformity and resolution required for BPM that can be scaled up for the mass production of HDDs cost-effectively has yet to be reported [40, 41].

An alternative approach could be to pattern MNPs by immobilising them onto surfaces. So far, $L1_0$ phase FePt, FePd and CoPt MNPs have received a lot of interest [29, 40]. Not only do they possess magnetic properties that are suitable for use in PMR magnetic data storage, but they are one of the few materials with high enough magnetocrystalline anisotropy to remain magnetically stable at MNP volumes of a few nanometres [24]. However, if MNPs are to be used for bit-patterned media, many challenges need to be overcome [40]. Not only is a patterning technique that will produce regular and uniform patterns required, but all the particles are required to be in the $L1_0$ phase and aligned with a common out-of-plane easy axis. To date a technique which overcomes all of these problems has yet to be developed [29, 40]. High-temperature annealing (> 600˚C) can be used to create the $L1_0$ phase, but this leads to agglomeration and sintering [29, 40]. Attempts have also been made to control the magnetic orientation of the MNPs through annealing in magnetic fields, but so far these remain unsuccessful [29, 40].

In summary, many challenges are still to be overcome if bit-patterned media is ever going to become a viable form of ultra-high density data storage. With the main obstacle remaining the development of a reliable, scalable and cost effective method to precisely and uniformly pattern billions of highly uniform magnetic islands with nanoscale precision over disks with diameters of a few inches. Yet if we look to nature, biology could offer an attractive and green approach for controlling the manufacture of materials with the nanoscale precision required. It is this bioinspired approach to the challenge that forms the basis of this thesis.

1.4 Biomineralisation Proteins

1.4.1 Biomineralisation

Biomineralisation is a phenomenon that is ubiquitous in nature, and can be defined in its most simple terms as the process used by living organisms to form minerals [54]. In some cases only limited control is exerted over the mineral that is formed, and the process is used to compartmentalise or store useful, rare or toxic minerals. Probably the most well-known example of this type of biomineralisation is the storage of essential iron in the form of ferrihydrate ($5Fe_2O_3 \cdot 9H_2O$). Ferrihydrate is formed by the accumulation of iron in the centre of cage-like proteins called ferritins [54]. In other cases of biomineral formation, the mineral structures formed have remarkable properties that can be superior to artificially synthesised minerals, but unlike most synthetic minerals, are normally produced under mild aqueous reaction conditions [55]. This type of biomineralisation is defined as the selective extraction of inorganic compounds from the local environment, and their deliberate incorporation into solid mineral structures under strict biological control [54]. As a result there has been a significant amount of research over many years with the aim of understanding and reproducing the mechanisms involved in biomineralisation for the development of advanced materials [56].

The evolution of biomineralisation has had far reaching consequences, not just for the development of life on earth, but also on the environment (an interesting topic which is unfortunately beyond the scope of that which can be discussed here) [54]. One of the remarkable benefits is that it has greatly aided our study of life, as unlike other biological transformations, hard biomaterials (such as bones and shells) leave a lasting impression in the fossil record. Although prokaryotic life on earth is thought to have appeared 3.5 billion years ago, evidence from the fossil record suggests that the major animal phyla only began biomineralising hard structures during the early Cambrian (about 525 Ma during the Cambrian explosion) [55]. It has been suggested that, coupled with a changing climate, the evolution of biomineralised teeth in predators led to an evolutionary arms race and an explosion in the development of protective hard tissues [55].

Today there exists a wide range of biominerals (over 60) used by organisms for functions beyond just protection and strength, such as motion, buoyancy, sensing and storage [54]. Probably the most well-known examples are calcium-based biominerals, which are deposited as calcium carbonate (in most cases calcite or aragonite) to form shells, or as hydroxyapatite (a calcium phosphate compound) and carbonated apatite to form bones and

teeth. Another common biomineral used mainly for structural purposes are amorphous silicates. Silica is able to not only provide support to the organism, but is also thought to have light guiding properties, which can be used for sensing and photosynthesis in organisms such as diatom frustules and sponges [57].

Bioinorganic iron oxides are another class of biomineral found in a wide range of organisms and used for a variety of functions, including the formation of teeth and for magnetic sensing [54]. Iron oxide has also been found to be mineralised extracellularly by a number of bacteria, such as *Geobacter metallireducens* [58]. These bacteria initiate the formation of magnetite particles through redox processes on the cell surface, in a process referred to as biologically induced mineralisation [59]. The biomineralisation of iron oxide intracellularly by prokaryotes is limited to a few remarkable magnetotactic bacteria (MTB), which form magnetite (or in some cases greigite) in specialised lipid vesicles called magnetosomes (Figure 1.4.1) [60]. Although biomineralisation is found throughout nature, MTB are the simplest organisms capable of this process [60]. In fact, MTB are believed to be the most ancient organisms capable of this process. There is evidence for the production of biomineralised magnetosomes from approximately 700 Ma, but could have developed even earlier around 2.0 Ga [55], which predates the Cambrian explosion (≈525 Ma) of biomineralised shells and teeth.

Figure 1.4.1[*] – TEM image of the MTB *Magnetospirillum gryphiswaldense* MSR-1 (scale bar 0.5µm). Magnetosomes containing magnetite crystals (dark cubes) are clearly visible inside the bacterium, as is the flagella at the right end of the bacterium.

---

[*] I would like to thank Sarah Staniland for providing this image.

1.4.2 Discovery of Magnetotactic Bacteria (MTB)

Salvatore Bellini, a medical doctor working at the University of Pavia in Italy, observed the unusual behaviour of bacteria in freshwater samples collected nearby (see recently translated references from 1963 [61, 62]). During microscopy studies, he noticed that a group of bacteria always accumulated at the edge of a water droplet, which corresponded to the magnetic north pole. Following a series of experiments observing the behaviour of the bacteria under the influence of various fields, he noted that the bacteria were magnetosensitive. However, these findings were never widely published. It was not until 1975, when Richard Blakemore published his findings after independently rediscovering MTB that these bacteria were first introduced to the scientific community at large [63, 64].

During his microscopy studies Blakemore observed a group of fast swimming bacteria in sediments collected near Woods Hole in Massachusetts. These bacteria were found not to be influenced by external stimuli such as light, but instead were always observed to swim in the same direction. However, Blakemore found that placing a magnet nearby altered the direction the bacteria swam. An explanation of this behaviour was provided when Blakemore showed that these 'magnetotactic bacteria' contained chains of iron crystals (shown in Figure 1.4.1), which would allow the bacteria to align with magnetic fields.

1.4.3 Magnetotaxis

Early research into MTB found that they responded to magnetic fields through the use of iron oxide magnetite or iron sulphide greigite nanoparticles contained within lipid vesicles termed magnetosomes [65]. Depending on the bacterial species, these magnetosomes vary in shape and size and are often arranged into one or more chains. However, what links all MTB discovered to date is that all they are all gram-negative, have the ability to sense and align with magnetic fields and are highly motile by means of long rotating filaments called flagella [60].

Most MTB are microaerophiles and are found in aquatic environments, where oxygen and other redox compounds are horizontally stratified. In these environments MTB are found in or close to an oxic anoxic transition zone (OATZ), formed due to the opposing gradients of sulphide from sediments and oxygen from the surface (as shown in Figure 1.4.2) [60]. Early research found that MTB existing in the northern hemisphere would predominantly swim northward, with the reverse case being found for MTB from the southern hemisphere [66]. This observation provided the basis of magnetotaxis, the first proposed theory that attempted

to explain the evolutionary advantage of magnetosomes. Other than at locations close to the equator, the Earth's magnetic field lines cut through the horizontally stratified environments (as shown in Figure 1.4.2), so MTB could follow these field lines as a guide to the OATZ [60].
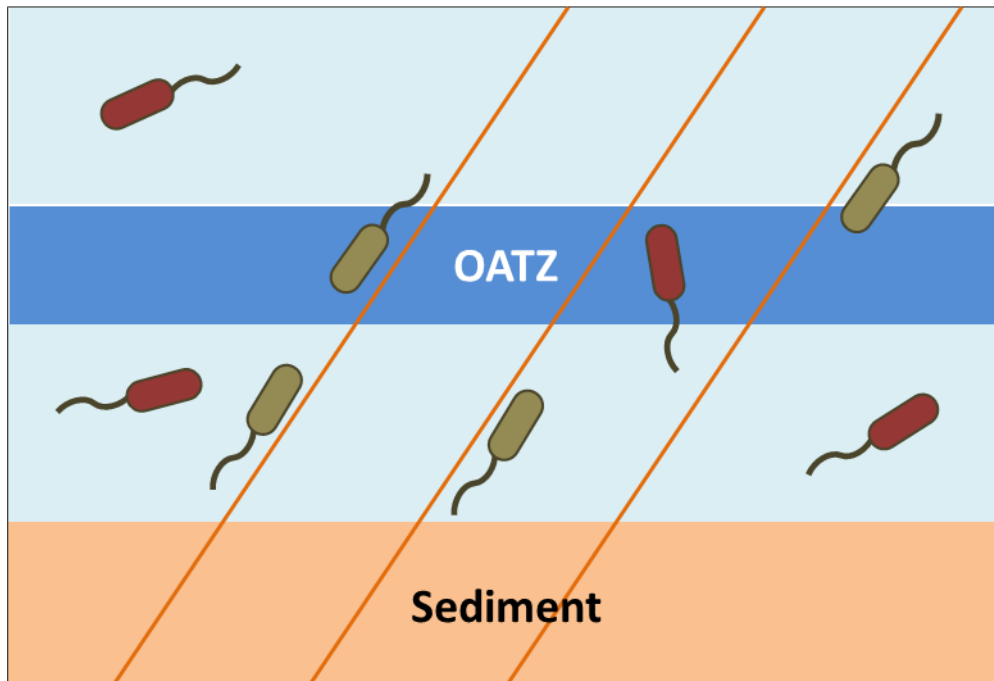
Figure 1.4.2 – Schematic of magnetotaxis (adapted from fig. 2 in ref. [60]). In many aquatic environments, an oxygen poor oxic anoxic transition zone (OATZ) is formed due to the opposing redox gradients of oxygen from the air-water surface and sulphides from the sediment floor. At locations distant to the equator, the Earth's magnetic field lines (orange lines) cut through this horizontally stratified environment. During magnetotaxis, MTB (green) align and swim along the Earth's magnetic field lines as a guide to the OATZ, whereas other organisms (red) must rely on other, potentially less efficient, methods for finding this zone.

Although MTB do display magnetotaxis and this could make the search for the OATZ more efficient (as shown in Figure 1.4.2), in reality this is probably an oversimplified view. MTB are likely to be able to respond to more than just magnetic fields, and numerous genetic studies have revealed that MTB have some of the highest numbers of signalling genes among all bacteria [67]. It is now more widely accepted that magneto-aerotaxis is a more accurate description of the mechanism used by MTB to locate the OATZ, as they are likely to also use aerotactic signalling to detect gradients in oxygen levels [66].

Although magneto-aerotaxis paints a simple picture for describing the evolutionary advantage of magnetosomes, many discoveries have cast doubt on this theory. These include; MTB found near the equator where the Earth's magnetic field lines run horizontally instead of vertically through the stratified environment shown in Figure 1.4.2, that MTB invest a lot of energy in creating more magnetosomes than necessary if their only purpose is to align with the Earth's magnetic field, and the fact that most MTB are only able to produce

magnetosomes when in their ideal OATZ environment and not outside of this environment when they would need them most [60]. Consequently, a number of alternative theories to explain the evolutionary advantage of magnetosomes have been suggested, and this remains a hot topic of debate.

One such theory proposes that magnetosomes act as an iron storage or detoxification mechanism [68], however several studies have since produced evidence that call this into question. For example, it has been found that MTB can live in low iron conditions, and the deletion of the ability to make magnetosomes in MTB living in high iron environments has also been found to have little effect [67]. Although currently not supported by any significant experimental data, another interesting theory is the 'magnetosome battery' hypothesis [69, 70]. This theory suggests that MTB can generate energy when redox changes trigger the reversible oxidation of magnetite contained within magnetosomes to maghemite, and would explain why MTB produce large numbers of magnetosomes. Finally, it is also possible that magnetosomes offer no significant evolutionary advantage, or may just be a relic from the past when they did provide some benefit [60]. In this case, as long as there is no selective pressure for MTB to lose their magnetosomes they will remain a part of the organism [60].

1.4.4 Phylogeny of MTB

Although the evolutionary advantage of magnetosomes remains unclear, all MTB discovered to date display magnetotaxis and are able to align with magnetic fields [60]. Since their discovery, many different MTB have been isolated from across the phylogenetic tree, and have been found to show a large diversity with respect to morphology (Figure 1.4.3) for example; cocci (round), sprilla (helical), bacillus (rod-shaped), vibrio (curved-rod) and multicellular bacteria [56]. Most MTB are found to biomineralise magnetite (although in some cases greigite) and although the size, shape and crystallinity of magnetosomes vary between different species, each strain usually produces magnetosomes with a well-defined morphology and size distribution (as shown in Figure 1.4.3).

MTB are known for being notoriously fastidious, and this has hampered studies that aimed to unravel the mechanisms behind the formation of magnetosomes. Only a few species have been successfully cultured, all of which belong to the phylum proteobacteria [71]. The first isolated and cultured MTB *Magnetospirillum magnetotacticum* MS-1 (originally known as *Aquaspirillum magnetotacticum* MS-1) certainly followed this trend, and was hard to cultivate and grow [60]. Most work since has focussed on two other species of MTB that are now

considered model organisms; *Magnetospirillum gryphiswaldense* MSR-1 (MSR-1) [72] and *Magnetospirillum magneticum* AMB-1 (AMB-1) [73].
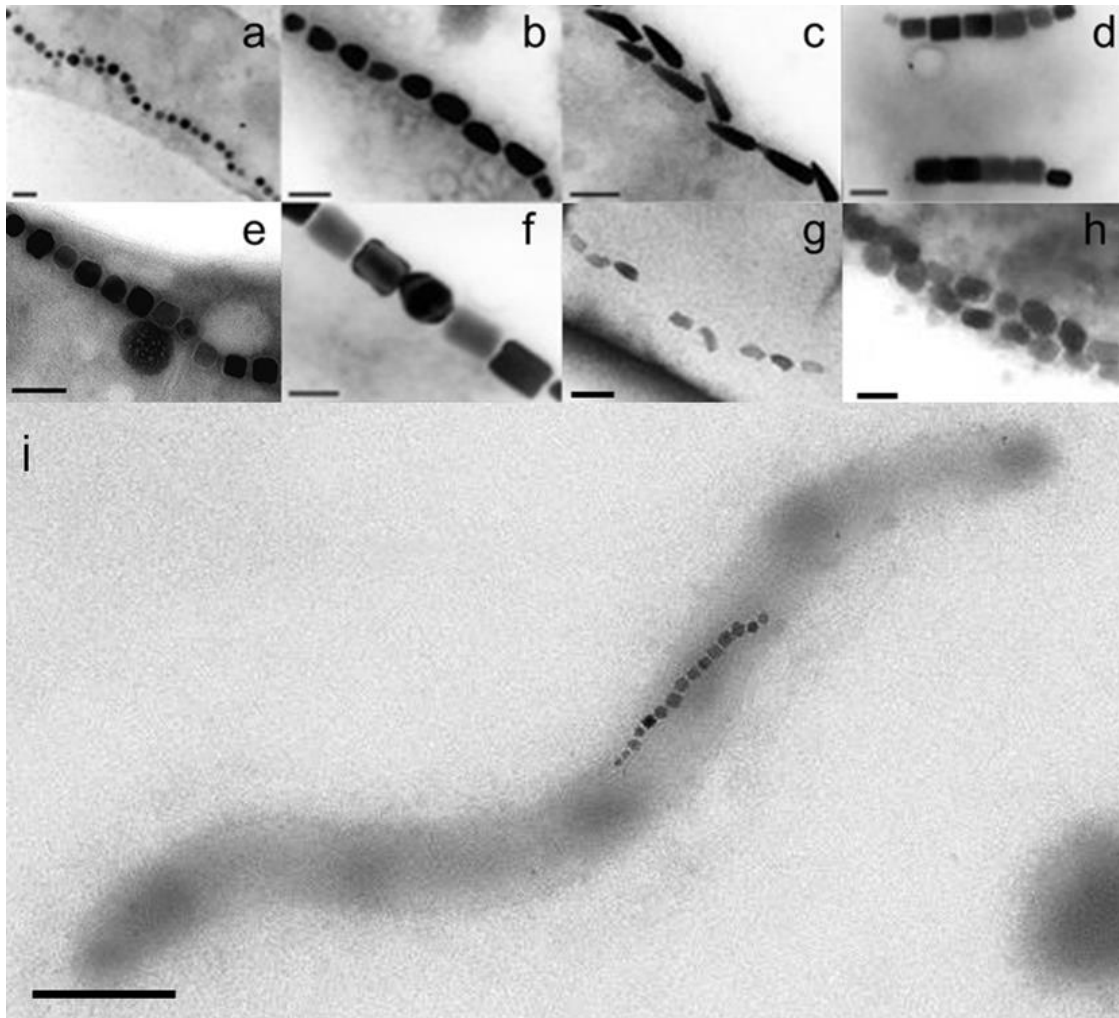
Figure 1.4.3 – TEM images of magnetosomes with different morphologies (published with permission from Figure 3.2 in ref. [74]). Magnetosomes containing; cubo-octahedral magnetite from *M. gryphiswaldense* MSR-1 (a), bullet shaped magnetite (b), saw-tooth shaped magnetite (c), elongated magnetite from *M. coccus* MC-1 (d), cubo-octahedral magnetite from *M. Magnetotacticum* MS-1 (e), elongated magnetite from *M. vibros* MV-1 (f), irregular bullet-shaped magnetite from *D. Magneticus* RS-1, irregular bullet-shaped particles from an uncharacterised greigite producing bacterium (h). Also shown is the whole cell of *M. Magnetotacticum* MS-1 (i). Scale bars; 100nm (a-h) and 500nm (i).

1.4.5 Magnetosome Formation

The fact that each species of MTB produce highly uniform MNPs within their magnetosomes suggests that these bacteria have strong genetic control over this process, exerted through the use of proteins. Two main approaches have been used (often in parallel) to study magnetosome formation; proteomic studies analysing the proteins associated with magnetosomes, and genetic studies. The separation of magnetosomes from a cell extract can be achieved fairly easily with the use of a magnet. Gorby *et al.* [75] made use of this and

pioneered proteomic studies of MTB, discovering a distinct set of proteins associated with purified magnetosomes. Other magnetosome-associated proteins were then discovered in later work, before Grünberg *et al.* [76, 77] published a comprehensive account of all the proteins associated with the magnetosome of MSR-1, showing that the majority of magnetosome-associated proteins were encoded in a few gene clusters. Later work by Richter *et al*. [78] comparing the genomic sequences of four species of MTB identified four conserved genomic regions encoding magnetosome-associated proteins, known as the *mamAB*, *mamGFDC*, *mms6* and *mamXY* gene clusters.

These studies have shown that most Mam (magnetosome associated) and Mms (magnetosome membrane specific) proteins are encoded within a genomic island, now commonly known as the magnetosome island (MAI). The MAI forms over 2% of the genetic material of AMB-1, is approximately 98kb in length and encodes over 100 proteins [79]. The MAI of MSR-1 is thought to be even larger, and comparisons between the two model species AMB-1 and MSR-1 have revealed their MAI share many characteristics [80]. Half the genes of the AMB-1 MAI have a homolog in MSR-1. However, it is unclear whether those genes that are not conserved play a role in determining factors that vary between species or are just 'junk' DNA [60]. It does however appear that the MAI is essential for magnetosome formation. Transposon mutagenesis is a process that allows genes to be transferred to the chromosome of an organism, disrupting the function of that gene and forming a mutant. Transposon insertions into the *mamAB* and the other gene clusters have been shown to have a serious effect on the formation of magnetosomes, and in some cases the loss of them entirely [81]. Recently, Kolinko *et al.* [82] confirmed the importance of the MAI for the synthesis of magnetosomes within bacteria. Expression of genes from the MIA of the magnetotactic bacterium *Magnetospirillum gryphiswaldense* in *Rhodospirillum rubrum*, a bacterial species not capable of producing magnetosomes in nature, conferred the genetic information necessary to enable these organisms to produce magnetosomes.

Studies performed so far have begun to reveal the mechanisms behind magnetosome formation in MTB. It appears that the first step (stage 1 Figure 1.4.4) is the biogenesis of the magnetosome membrane, probably from the invagination of the cell cytoplasmic membrane through the action of proteins such as MamY [83] and Mms16 [84]. Within most MTB, magnetosomes are ordered into chains, as a method of structuring the magnetosomes for efficient magnetotaxis. It is believed this is achieved through binding to the actin-like protein MamK, through activation by MamJ that anchors the magnetosome to the MamK filament [85]. Following this step, MamA and MamE are vitally important not just for mediating

interactions between the magnetosome and the cell, but also in recruiting and localising other magnetosome-associated proteins.
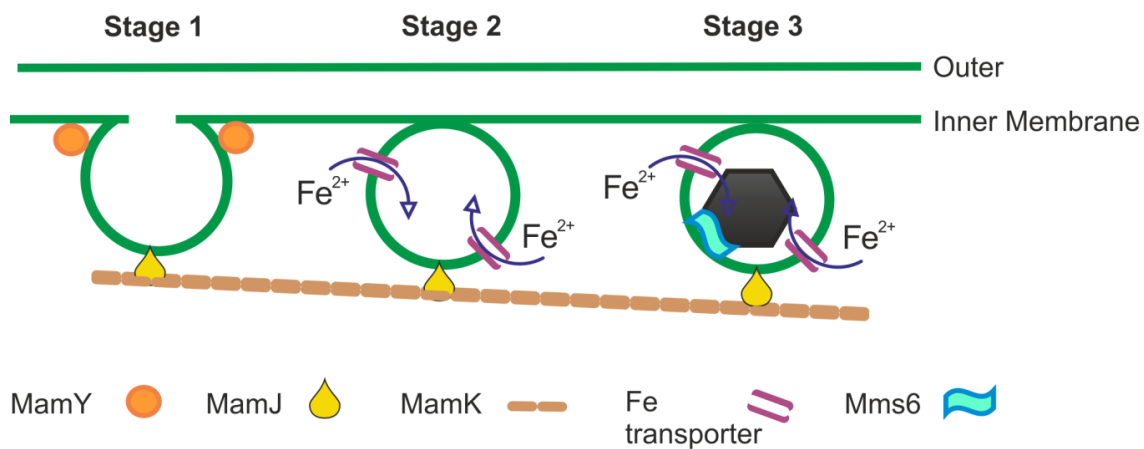
Figure 1.4.4 - A simplified schematic that highlights some of the key elements in the proposed method for magnetosome formation (adapted from Figure 3.3 in ref. [74]). Stage 1 involves the formation of a magnetosome membrane, probably from the inner cell membrane under the action of proteins such as MamY. This vesicle is then bound to the filamentous protein MamK *via* the protein MamJ. Stage 2 involves the transport of iron into the magnetosome through the use of iron transport proteins. In stage 3 iron is nucleated and crystal growth is controlled by proteins such as Mms6.

Before biomineralisation can take place, iron needs to be transported into the magnetosomes (stage 2 Figure 1.4.4). It appears that MagA, as well as other proteins such as MamB, M, N and O, may be important for this process, and for other factors such as initiating biomineralisation and controlling the chemical environment. It is clear that the mineralisation of magnetite within magnetosomes is not as simple as the accumulation of iron, and the chemical environment of the magnetosome needs to be controlled to lead to the formation of magnetite (or in some cases gregite). However, the exact mechanism for forming magnetite inside magnetosomes remains unknown [74]. Only a small number of experiments have ever been performed with the aim of unravelling this mystery, with results suggesting that the initial stages of biomineralisation take place outside of the magnetosome [74]. It is believed that iron, stored as ferrihydrate within a Ferritin-like protein, is co-precipitated with soluble ferrous iron to form magnetite crystallites, before being transported into the magnetosome through invaginations and matured into a magnetite crystal within the magnetosome. [74].

During biomineralisation, MTB produce nanoparticles of a highly consistent size, shape and crystallinity, and biomineralisation proteins are used to achieve this (stage 3 Figure 1.4.4). Arakaki *et al.* [86] identified four proteins; Mms5, 6, 7 and 13 (number based on the approximate molecular weight of the proteins in kDa) tightly bound to the magnetite crystals of AMB-1 after the magnetosome membrane was removed. Respectively, these proteins are

homologous to MamG, Mms6, MamD and MamC in MSR-1, and are found encoded in the *mam*CD and *mms*6 gene clusters of the MAI of both MSR-1 and AMB-1 [87]. A set of proteins such as MamE, P and T also appear to be important in promoting the development of biomineralised crystals to their final size [88]. Recent genetic studies have also discovered a new protein, MmsF, described as the master regulator for magnetite biomineralisation *in vivo* [89]. It is likely that this suite of Mms proteins play a crucial role in controlling the development of magnetite crystal growth, resulting in the high level of control MTB can exert over the size, shape and crystallinity of the MNPs formed.

1.4.6 The Biomineralisation Protein Mms6

Mms6 is one of many magnetosome associated proteins thought to control the formation of magnetite within the magnetosomes of MTB, which has also been used to control the formation of magnetite *in vitro*. The Mms6 protein itself is a small (≈6.4 kDa) protein, first found tightly bound to magnetite crystals from the magnetosomes of AMB-1 by Arakaki *et al*. [86]. Importantly it was also shown in the same work that when recombinant Mms6 was placed into a reaction designed to mineralise magnetite it not only bound iron, but also controlled the morphology and size of the crystals formed. Two identical iron oxide mineralisation reactions were performed, one with recombinant Mms6 added and one without. When the particles formed were compared, the biotemplating properties of recombinant Mms6 were revealed. The reaction completed without Mms6 produced particles with a range of different sizes, shapes and crystallinities. However, when the reaction was performed in the presence of Mms6, in most cases cubo-octahedral magnetite particles were formed with a much smaller size distribution. Subsequent studies where magnetite was formed *via* a partial oxidation reaction with the addition of Mms6 produced crystals with a uniform size, with a narrow size distribution and a mean size of ≈21 nm [90]. This suggests that Mms6 not only binds iron, but also templates the formation of cubo-octahedral magnetite particles outside of its usual setting within the magnetosomes of MTB.
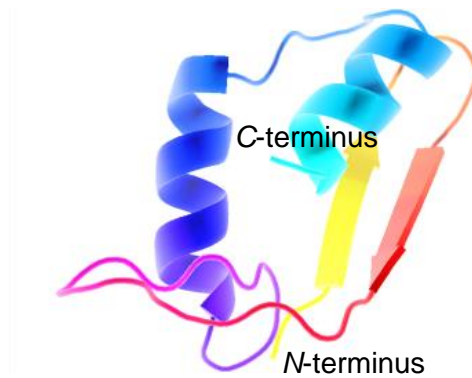
Figure 1.4.5 – Cartoon representation of Mms6 based on the amino sequence generated using Quark [91], and rendered using PyMOL [92]. β-sheet regions (represented by arrows) are located mainly at the *N*-terminal region, and helical regions (represented by coils) are found at the *C*-terminal region.[*]

The *N*-terminal region of Mms6 is hydrophobic, and it is believed that this allows for its integration into the lipid membrane of a magnetosome. This would then orientate the protein so that its *C*-terminus points into the interior of the magnetosome. The *C*-terminal region contains a large number of carboxyl and hydroxyl groups, which are capable of binding iron ions and could interact with the surface of magnetite [83, 86]. Although the precise role of Mms6 is still not fully known, it is thought to initiate the growth of magnetite crystals, and bind to specific crystal planes during this growth [83, 93]. The importance of Mms6 in controlling the morphology of biomineralised magnetite was highlighted further in a study by Tanaka *et al*. [94]. The deletion of the *mms6* gene in AMB-1 resulted in a *Δmms6* mutant that formed magnetite crystals half the size of those formed in the wild type. TEM analysis also showed distinct variations in the crystal structure formed, and the particles were no longer cubo-octahedral in shape.

Mms6 has been show to form cubo-octahedral magnetite nanoparticles *in vitro* [86, 94, 95], and short peptide sequences based on the *C*-terminal region of Mms6 have also been shown to have a similar function [96]. Mms6 has also been used to successfully biomineralise highly uniform MNPs of magnetite when immobilised onto patterned surfaces by Galloway *et al*. [97, 98], and in a further study also template the formation of the magnetically harder material cobalt-doped magnetite [99] (discussed in more detail in Chapter 5). The patterning of Mms6 onto surfaces presents a novel and green approach to aid the biomineralisation of MNP arrays of magnetite and cobalt-doped magnetite. This approach is also highly adaptable, and could form a new bioinspired approach for the formation of a wide range of different

---

[*] Model structure of Mms6 discussed in more detail in Section 3.2 of ref. [153].

technologically relevant nanomaterials through the use of alternative biomineralising biomolecules.

1.4.7 Recombinant Protein Synthesis

Recombinant protein synthesis is a process that allows for the production of proteins through recombinant DNA techniques, and is the technique which is used to produce Mms6 for use in this work. Organisms polymerise amino acids into proteins by following information encoded in sections of DNA called genes. Most bacteria have a DNA chromosome that contain the information it needs to function and survive in the form of a closed loop, but many also contain DNA plasmids that encode other information. These plasmids can be passed between bacterial strains *via* transformation, transduction or conjugation, and recombinant protein synthesis (Figure 1.4.6) makes use of this ability to produce proteins.
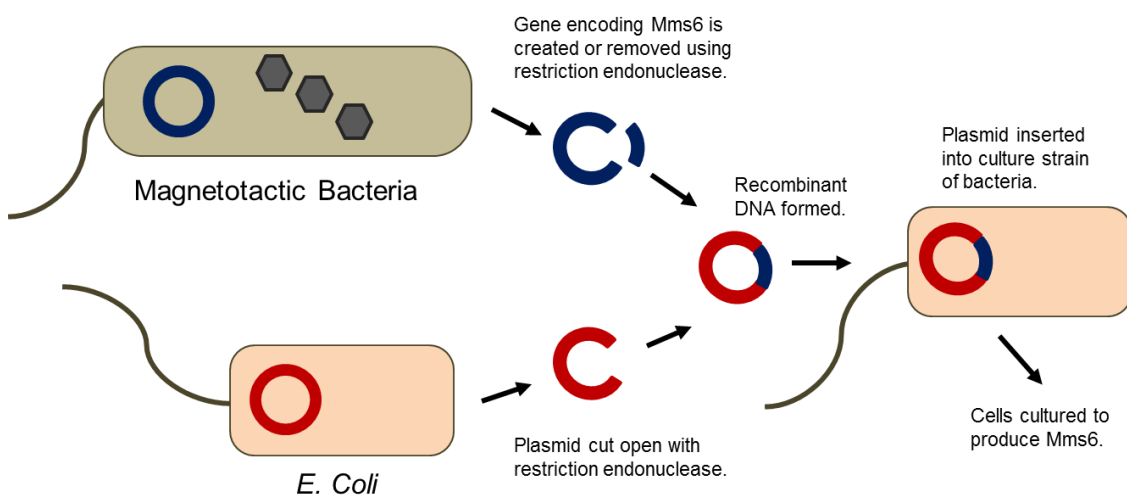
Figure 1.4.6 - A simplified overview of recombinant protein synthesis to produce Mms6. The gene encoding for Mms6 is inserted into a vector plasmid from *E.coli* to form recombinant DNA. Instructions for antibiotic resistance, affinity tag production and expression promoters can also be inserted into the recombinant DNA. The recombinant DNA is then transformed into culture strains of bacteria, which are then cultured to produce Mms6.

In recombinant protein synthesis, the gene encoding the genetic information of the protein of interest (for example Mms6 from the MTB AMB-1) is located or synthetically manufactured, and the process of polymerase chain reaction (PCR) is used to amplify it. These sections of DNA encoding for Mms6 can then be inserted into a plasmid cut open with restriction endonuclease, which are then inserted into a culture strain of bacteria. The plasmids are also designed to contain other instructions (e.g. that encode for antibiotic-resistance, for the production of an affinity tag at the *N*-terminus, enzymatic cleavage sites and expression promoters). The culture strain of bacteria will, due to the expression

promoters, over-express Mms6 when triggered by a specific chemical stimulus. The production can also be aided by culturing the bacteria in an antibiotic solution so that only the bacteria containing plasmids with the antibiotic resistance, and therefore also encoding the Mms6 gene, will survive.

The inclusion of an affinity tag allows the desired protein to be isolated from the rest of proteins and any other material in the bacterial culture [100]. Many different affinity tags have been developed and used successfully for protein purification, some commonly used examples include polyhistidine-tags [101], small ubiquitin-like modifier (SUMO) [102], strep II and the maltose binding protein (MBP) [103]. The tag used can also modify the properties of an overexpressed protein, for example MBP and SUMO can improve its solubility and as a result the final yield [102].

As an example, in this study Mms6 was purified with the use of an *N*-terminal polyhistidine-tag, which allows it to be extracted from the other proteins produced by the culture bacteria by immobilised metal-ion affinity chromatography (IMAC). IMAC involves filtering of the cell material through a column containing nickel or cobalt [101]. Any untagged material (*i.e.* that is of no interest) will flow through the column, but histidine tagged proteins will bind to the nickel or cobalt. The immobilized protein can then be extracted by an imidazole rinse that will outcompete the histidine binding, displacing the tagged protein from column [81]. Often affinity tags are no longer required after purification steps and they can be separated from a protein chain if enzymatic cleavage sites are included, as some enzymes such as thrombin will only cleave a specific sequence of residues [104].

1.4.8 Designing New Biomolecules for Biomineralisation

Although many naturally occurring biomineralisation proteins and peptides, such as Mms6, have been used to control the formation of a wide range of different biominerals *in vitro*, the materials which they can target are not exhaustive. Many materials that would be well suited to forming bit-patterned media, such as CoPt and FePt, are not found within nature. However, a process known as biopanning has uncovered many new peptides and proteins, with the ability to interact with a material of choice [105, 106].

Biopanning (Figure 1.4.7) makes use of large peptide or protein libraries, containing a wide range of random sequences. In traditional biopanning, gene sequences were inserted into bacterial cells or a bacteriophage virus so that peptide sequences were expressed on the surface of the bacterial cells (cell display) or the bacteriophage (phage display) [107]. This

peptide library can then be screened against a substrate material and amplified, mimicking natural selection in a laboratory environment. After the peptide library is exposed to a substrate, the sequences that do not bind can be washed away. On the other hand the sequences that do bind can then be amplified, and re-exposed to the substrate. This process can be repeated many times, resulting in the peptide sequences which show the greatest affinity to the substrate being enriched. This approach has been used successfully to identify novel peptide sequences with an affinity for materials that even nature does not make use of including; gold [108, 109], titanium oxide [110], platinum [111] and platinum alloys [112, 113].
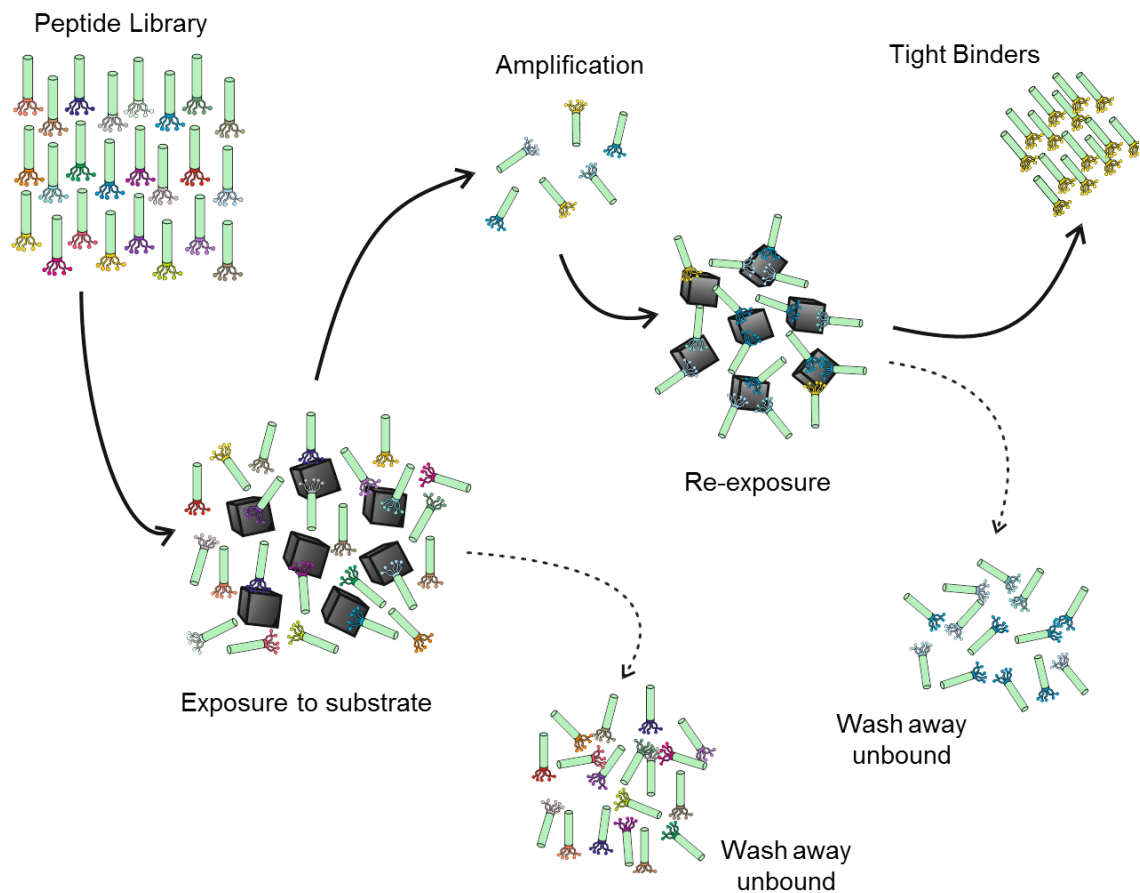
Figure 1.4.7 - An overview of the biopanning process (adapted from Figure 1 in ref. [114]). A large library of different peptide sequences is exposed to a substrate material of choice, and those which do not interact strongly with the substrate can then be washed away. The peptide sequences that are found to interact with the substrate can then be amplified and re-exposed to the substrate. The enrichment of sequences that show the greatest affinity to the substrate can be obtained through continued washing, amplifying and re-exposure. This allows peptide sequences with a large affinity for a substrate material to be identified.

Recently Rawlings *et al.* [114] took the biopanning process one step further, by displaying peptide sequences on a protein scaffold known as an Adhiron (commercially known as an Affimer) [115]. The Adhiron forms a robust scaffold that displays two nine amino acid loop regions on its surface, and can be produced easily in large quantities by bacterial

expression. This protein was then put through a biopanning process to identify the peptide loops that had the strongest affinity for the [100] face of magnetite. The artificial protein that was engineered is termed 'Magnetite Interacting Adhiron 1' (MIA-1, Figure 1.4.8), and was found to control the formation of magnetite nanoparticles during a room temperature precipitation to produce magnetite nanoparticles with a cubic morphology. This highlights how we are no longer reliant on using naturally occurring proteins to control biomineralisation. Instead we are beginning to be able to develop the capability to move beyond what nature can provide to design our own biomolecules, with properties that are more suitable for our needs.
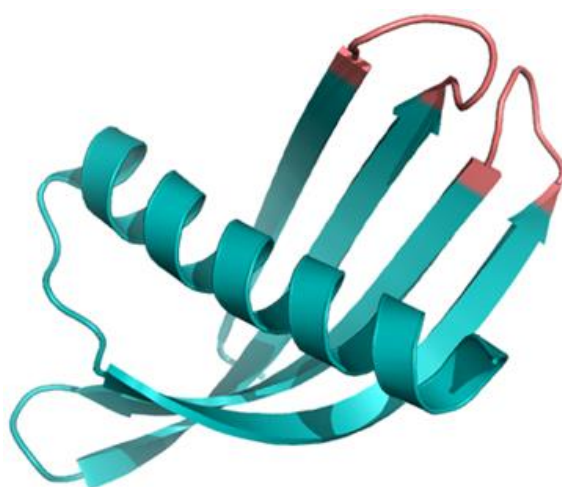
Figure 1.4.8[*] **-** Cartoon representation of the magnetite interacting Adhiron 1 (MIA-1) based on the amino sequence generated using Quark [91], and rendered using PyMOL [92]. The Adhiron scaffold is shown in blue, and the magnetite binding peptide regions in red (β-sheet regions are represented by arrows and helical regions are represented by coils).

1.4.9 Immobilising Proteins on Surfaces

Proteins can be immobilised through hydrophobic interactions with residues such as leucine, isoleucine and alanine, with a hydrophobic surface, such as that formed by the self-assembly of –CH_3 terminated molecules onto a surface. Although this type of physisorpsion can inactivate proteins, Mms6 has been shown to have some degree of magnetite templating ability when immobilised in this way [93]. However, this method is not ideal. Attaching Mms6 by the *N*-terminus to expose the active biotemplating *C*-terminal region during MNP mineralisation is the preferred approach, as this should result in better functionality and increased mineralisation control.

---

[*] Thank you to Andrea Rawlings for kindly providing this image.

Proteins can be bound to species *via* their *N*-terminus through covalent binding. Ethyl(dimethylaminopropyl) carbodiimide (EDC) and N-hydroxysuccinimide (NHS), form an activated ester on a carboxylic acid surface. This will preferentially bind to the *N*-terminal amine of a protein, when the protein is buffered to ≈1 pH point below its isoelectric point (pI) [116]. This approach was used successfully by Galloway *et al*. [97, 98], who showed that Mms6 immobilised in this way could be used to biotemplate consistent MNPs of magnetite. However, achieving consistency in the patterning and orientation of proteins such as Mms6 can be challenging with this approach. The EDC/NHS attachment is not specific for the *N*-terminal amine group, and could also bind to other accessible lysine residues, resulting in protein that is not oriented correctly that could impair functionality.

The affinity tags used in the purification of proteins can be also be used to attach them to surfaces. For example, polyhistidine tagged proteins have been shown to bind to gold and other metals, but only a weak bond is formed [101]. Therefore, it is unlikely that this process would be suitable for biomineralisation proteins, which need to remain stable during a mineralisation reaction. Alternatively, other tags can be introduced to the *N*-terminus. The introduction of a sulphur containing cysteine at the *N*-terminus allows the protein to bind directly to gold surfaces *via* a thiol-gold bond, whilst in the case of Mms6 also correctly orientating the protein so that the active *C*-terminal region is available for biomineralisation.

In the case of forming biotemplated arrays of MNPs on surfaces, immobilising the biomineralisation protein is only part of the story. Areas need to also be patterned to resist protein attachment. Bovine serum albumin (BSA) sticky proteins can be used, but these have been shown to also mineralise particles themselves, and as a result are unsuitable for use in this work [117]. However, it should be noted that BSA proteins cannot be used for efficient biomineralisation. In the case of magnetite formation they have not been reported to exert any control over particle formation, but instead only have iron binding properties. As a result, a surface pattered with BSA proteins could not be used to form highly organised surfaces of MNPs for applications such as data storage, but instead are likely to produce surfaces containing many different iron oxide particles, with a wide range of sizes, crystallinities and magnetic properties. Poly-ethylene glycol (PEG) terminated thiol molecules form a self-assembled monolayer (SAM) on gold surfaces, and have been shown to resist protein binding [118]. Again this approach was used successfully by Galloway *et al*. [97, 98] as a means to pattern areas that would resist the attachment of Mms6, and a significantly smaller amount of magnetite MNPs were found to mineralise in these areas when compared to the protein attachment sites.

1.5 Self-Assembled Monolayers (SAMs)

1.5.1 Overview

Self-assembly is commonly defined as the spontaneous self-organisation, or self-association of molecular subunits to form more complex secondary structures with functional properties that are not found within individual molecules. Nature can be considered to have developed highly sophisticated versions of this process to form structures such as membranes, viruses and even cells [119], however the simplest example of a self-assembly process has been termed a self-assembled monolayer (SAM) [120]. This class of organic thin film can be described in simple terms as ordered molecular assemblies spontaneously formed when a surfactant is absorbed onto a solid substrate from a liquid or gas phase [121].

Organic thin films are not a new area of scientific study. Franklin documented the calming influence of oil on water over 200 years ago [122]. Later work by Langmuir [123] who studied monolayers of amphiphilic molecules on water and Blodgett [124] who deposited carboxylic acid chains onto solid substrates laid the foundations of surface chemistry, clarifying the existence of monolayers. The notion of a SAM is often credited to Zisman [125], but it was not until the work of Nuzzo and Allara [126] and Moaz and Sagiv [127] in the 1980's who introduced the two most popular SAMs (thiols on gold and trichlorosilanes on silicon oxide respectfully) that SAMs became widely studied. This work coincided with the development of surface-sensitive instruments within nanotechnology, such as scanning probe, diffraction and spectroscopy techniques, which allowed for the study of SAMs on the molecular scale [128]. Without these tools, most of the early work on thin films and SAMs was focussed on the macroscopic properties of the systems. However, since the 1980's the interest in SAMs has continued to grow, with the continued development of nanotechnology and the tools it provides.

1.5.2 Basics of SAM Formation

In general the molecules involved in the formation of a SAM have three key components (Figure 1.5.1). A head-group with a specific affinity to a substrate drives the process, and is chemisorbed or interacts strongly [129]. The backbones of the SAM molecules can stabilise the system and ensure efficient packing, or can deliberately promote disorder through interactions including Van der Waals and hydrophobic forces [129]. Finally the end-group (active-group) allows for the design and formation of specific or desired properties in the SAM. For example, in alkanethiol-based SAMs a -CH$_3$ or -CF$_3$ end-group results in a

hydrophobic SAM surface, and polar -OH, -NH$_2$ or -COOH end-groups result in hydrophilic SAM surfaces [120].
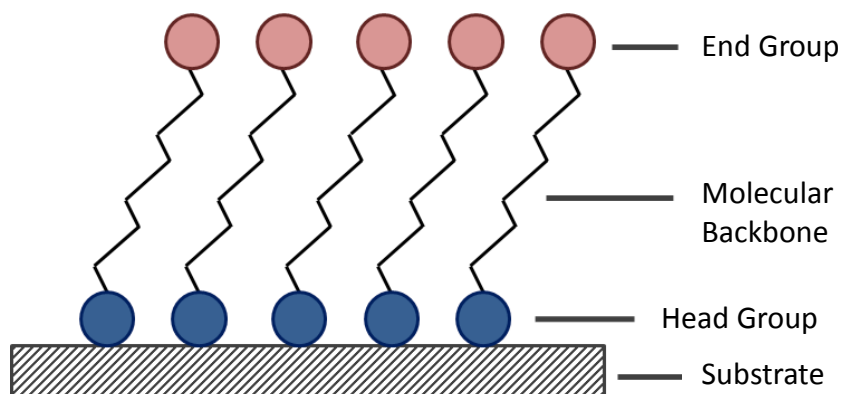
Figure 1.5.1 - Simplified diagram of a SAM (adapted from [129]). A head-group (blue circle) is chemisorbed onto a substrate and connected *via* a molecular backbone to an end-group (red circle).

SAM formation is enthalpically driven by the formation of a strong head group-substrate bond, and can be created simply both from a solution or a gas [129]. They have become one of the most important strategies in bottom-up fabrication within nanotechnology, with the ability to bind to surfaces of all orientations and possessing the scope for modifying the surface characteristics. By using SAMs one can form a building block for more complicated structures by being able to link materials of significantly different chemical properties, thus leading to great interest within a wide range of current and potential applications [120]. The most popular and well-studied SAMs are thiols, dithiols and other sulphur head-group molecules on metal surfaces (Au, Ag, Fe, Mg, *etc*.) and some semiconductors (Ga/As, *etc*.) [119]. However, SAMs have also been constructed from other material systems including; silanes such as octade-cyltrichlorosilane on hydroxylated surfaces (SiO$_2$/Si, mica, glass, *etc*.), fatty acids on metal oxides and hydrocarbons on silicon [130].

1.5.3 Alkanethiol SAMs

Alkanethiols on Au (111) have been by far the most studied SAM system. The inertness of Au and the accessibility of evaporated Au films (with the Au (111) surface being the lowest energy surface and preferred in growth of thin films by evaporation) may explain why this system has been so popular [130]. *n*-alkanethiols, where *n* represents the number of carbons in the hydrocarbon chain (a 10-alkanethiol is shown in Figure 1.5.2) are relatively simple molecules with all the features necessary to form a SAM [130]. Hence alkanethiols are considered the simplest SAM system, and as a result are the most studied and well understood. The formation of an alkanethiol SAM on Au (111) is still a complex process with

many competing interactions and degrees of freedom, leading to different growth phases on multiple time scales. This can be further complicated with the addition of different end-group molecules.

Figure 1.5.2 – Structure of 10-alkanethiol**.**

SAMs of n-alkanethiols on Au (111) are usually grown from a liquid solution by immersing the Au substrate in hexane or ethanol solutions, with thiol concentrations in the region of milli to micromolar [119]. It was expected that the coverage of chemisorbed alkanethiols onto Au would follow a simple Langmuir uptake curve, which is proportional to the number of available sites. However, studies continuously found multiple time scales that suggest a more complicated growth process, with a first absorption step of 80-90% coverage within minutes followed by a period of much slower growth [131, 132]. An initial lying-down phase has been observed in a number of scanning tunnelling microscopy (STM) and atomic force microscopy (AFM) studies, followed by a final standing-up phase [133]. This lying-down phase was defined as physisorption, with a different time constant to the standing-up phase known as chemisorption [133].

The physisorption and chemisorption processes can be modelled simply as equations 1.5.1 and 1.5.2 respectively [120].

$$CH_3(CH_2)_nSH + Au \rightarrow [CH_3(CH_2)_nSH]_{phys}Au \qquad (1.5.1)$$

$$[CH_3(CH_2)_nSH]_{phys}Au \rightarrow CH_3(CH_2)_nS\text{-}Au + \tfrac{1}{2}H_2 \qquad (1.5.2)$$

The molecular energies involved in the formation of an alkanethiol-Au SAM *via* chemisorption (equation 1.5.2) are the cleavage of the S-H bond (87 kcal mol^{-1}), the formation of the S-Au bond (40 kcal mol^{-1}) and the removal of hydrogen to H_2 (104 kcal mol^{-1}) [130]. For a SAM system to form it must result in a reduction in free energy (*ΔG*). From the energies involved, the chemisorption reaction is exothermic and fits these criteria, with a *ΔG* value of approximately -5 kcal mol^{-1} [130]. This is related to entropy *ΔS via* equation 1.5.3.

$$\Delta G = \Delta H - T\Delta S \qquad (1.5.3)$$

The enthalpy (H) of the chemisorption process has been measured to be 28 kcal mol^{-1} [134], and results in a large and negative ΔS value. Thus providing an explanation as to why the chemisorbed alkanethiols are driven to form a highly ordered SAM system on Au.

1.5.4 Patterning SAMs

There are currently a wide range of techniques available for pattering SAMs [119]. It is impossible to review all of these techniques in this chapter (for more examples see reference [119]). Therefore, some of the more commonly used approaches are discussed here, along with those which were used in this work.

1.5.4.1 Photolithography or Particle Beam Lithography

Photolithography, which is common within the IC industry, can also be used to form patterns in SAMs (Figure 1.5.3). A SAM can be photo-oxidised by exposure to ultra-violet (UV) light, and removed simply by rinsing with a solvent [135]. The minimum resolution that can be achieved is determined by the optics of the system, and the wavelength of the light used. For example, UV light from a mercury arc lamp focussed through a projection microscope and a pattern definition mask can form features with sizes approaching ≈0.3 μm [135]. However, this approach requires expensive equipment and cleanroom facilities, and there are cheaper and more accessible approaches to forming patterns of SAM with feature sizes that are achievable with photolithography.
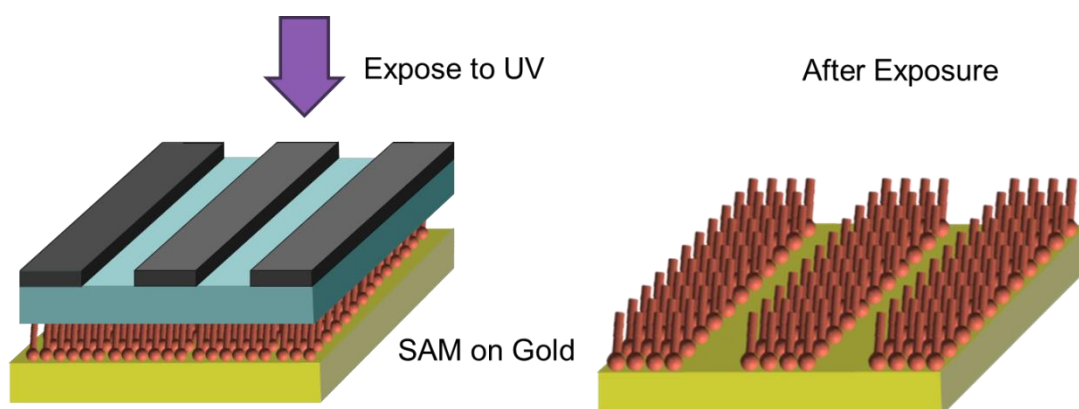
Figure 1.5.3 – An overview of SAM patterning by exposure to UV light. A complete alkanethiol SAM layer (red balls and sticks) formed on a gold surface is exposed to UV light through a photomask. Areas of the SAM surface that are not covered by the mask are photo-oxidised, and can be removed by washing with a solvent to form a pattern.

A low energy (10-100 eV) beam of electrons can have a number of effects on a SAM (e-beam lithography). In the case of an alkanethiol SAM on gold certain bonds can be broken (*e.g.* C-S, C-H), bonds can be formed (*e.g.* C=C), the SAM molecules can be cross-linked, or it can even lead to disordering of the monolayer [136]. Although through these modifications SAM features of <10 nm have been formed with this approach, it does require the use of expensive equipment in an ultra-high vacuum environment [136]. Additionally, this is a slow serial process that is not well suited to forming patterns over wide areas. Also, alkanethiol SAMs can also be damaged by ion beams of rare gases (≈8-20 eV) [137]. This approach has also been shown to achieve patterns with feature sizes comparable to what can be achieved with e-beam, but suffers from the same drawbacks.

1.5.4.2 Micro-contact Printing (µCP)

Micro-contact printing (µCP) is a simple and cost effective approach to produce reliable microscale patterns of SAMs [138]. Flexible elastomer stamps can be repeatability formed from a stamp master, which can be manufactured by optical or electron beam lithography. For example, stamps inked with a alkanethiol SAM solution (Figure 1.5.4) will then transfer onto a gold surface when placed in conformal contact with a clean gold surface [138]. This approach can be used to pattern SAMs over wide areas, without the use of expensive equipment or a clean room environment (the production of the stamp master is the only part of the process that requires the use of a clean room, and once made can be used repeatedly). However, the stamp has to be laid onto the surface by hand, and this can lead to problems in achieving patterning consistency.
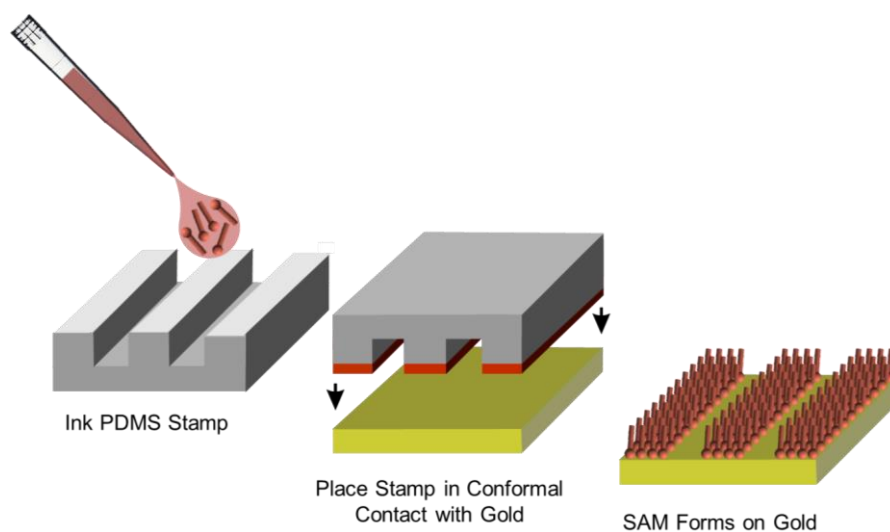
Figure 1.5.4 – An overview of µCP. A flexible polymer stamp is inked with an alkanethiol solution (red). This stamp is placed in conformal contact with a gold surface, allowing an ordered SAM to form at the places where the stamp meets the surface.

µCP has in the most part been developed with the use of poly(dimethylsiloxane) (PDMS) polymer stamps in the low elastic modulus form of Sylgard 184 PDMS. This soft-PDMS (or s-PDMS), allows patterns with feature sizes >500 nm to be routinely produced [139]. The high compressibility of Sylgard 184 PDMS leads to stamps made from this material with nanoscale features collapsing during preparation or patterning [139]. To extend the resolution of µCP, alternative siloxane polymers based on vinyl and hydrosilane end-linked polymers (hard-PDMS or h-PDMS) have been used to form stamps [138]. Stamps that contain a thin layer of h-PDMS, supported by a thicker layer of another material such as s-PDMS or glass have been used successfully to achieve patterns with features <100 nm [138].

1.5.4.3 Patterning with a Scanning Probe

Since its first introduction by Piner *et al.* [140] in 1999, dip-pen nanolithography (DPN) has become a versatile technique for the fabrication of nanostructures on surfaces (Figure 1.5.5). It has the been shown to routinely pattern alkanethiols onto gold surfaces with nanoscale resolution and even has the capability to pattern multiple chemical species with separation distances less than 100 nm [141].
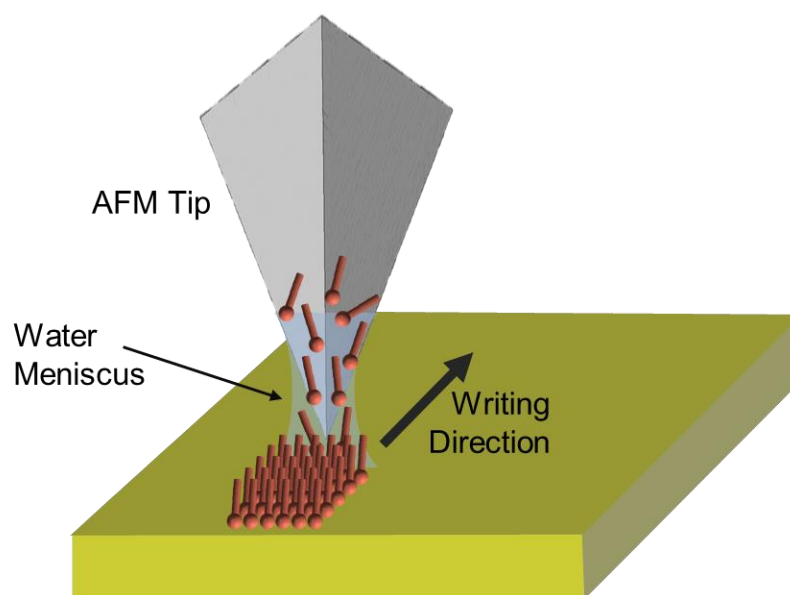
Figure 1.5.5 – An overview of DPN. An AFM tip delivers alkanethiol molecules to a gold surface *via* capillary action, writing an ordered SAM onto the surface.

DPN is a scanning probe patterning technique, analogous to quill and ink writing. An atomic force microscope (AFM) tip is coated with a molecular species of interest, and is used to directly write these molecules onto the surface (Figure 1.5.5). AFM is a technique that has become common for characterising surfaces with nanoscale precision, (see Chapter 2.5.6)

[142]. The surface of a sample can be imaged during AFM by scanning an atomically sharp tip attached to the free end of a cantilever over the surface, or scanning the surface under the tip. Van der Waals forces act on the tip when it is between 10-100 Å from the surface, and repulsive electrostatic forces when the tip is <2 Å from the surface causing the cantilever to deflect [142]. The location of the tip on the surface can be maintained and controlled through measurements of the cantilevers position, usually achieved with a laser beam that is reflected off the back of the cantilever and detected with a position-sensitive photodetector [142].

During DPN, a water meniscus forms between the AFM tip and the surface, leading to the capillary transport of the ink molecules from the tip to the surface [141]. The size of the meniscus can be adjusted with careful control of the humidity, which determines the rate of molecular transport and the patterning resolution that is achieved [141]. DPN is not a parallel lithographic method like μCP that can pattern large surface areas making it costly and time consuming, but it offers the capability to extend the resolution that is achievable with μCP. Multiple tip arrays can also be used to improve the speed of patterning [143].

Alternatively SAMs have been patterned by physically removing the molecules with an AFM probe [144]. In this case a complete SAM is formed on a surface, and regions are selectively removed by the tip to form a pattern. This approach, which has been termed nanoshaving, works in the opposite way to DPN, and has been used to form patterns with features <100 nm by literally shaving SAM molecules off the surface. However, like DPN it is also a costly and slow serial patterning technique.

1.5.4.4 Polymer-Pen Lithography (PPL)

Recently polymer-pen lithography (PPL) has been developed, building on the patterning techniques of μCP and DPN (occasionally referred to as controlled μCP) [145]. PPL controls an elastomer stamp, which like μCP is formed from a silicon master, with the use of a piezoelectric system (Figure 1.5.6) [145]. Certain materials generate an electric charge when under an applied mechanical stress, or conversely the generation of a mechanical strain when under an applied electric field [142]. These changes are reversible, so through careful control of the applied electric field the position of the stamp in a PPL system can be precisely adjusted. The stamp usually contains an array of pyramids, which is inked with a molecule of interest, and brought into contact with a surface [145]. Through careful control of the pen-surface contact area through the use of the piezoelectrics, this system can be used to pattern surfaces with micro (up to 10 μm) or nanoscale (<100 nm) features [146]. Although more

complex than µCP, PPL is classified as being a parallel patterning technique that is able to pattern wide areas unlike the serial technique of DPN.

Stamp Controlled with
Piezoelectric System

SAM Forms on Gold
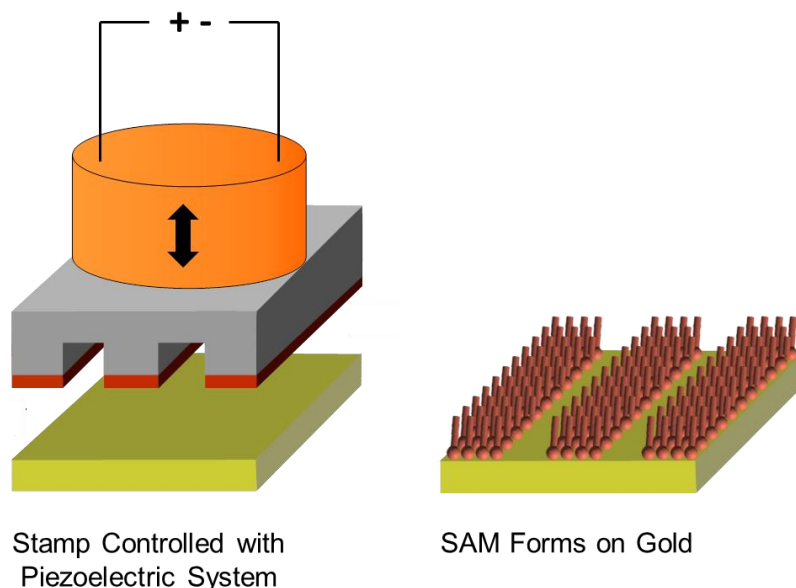
Figure 1.5.6 – An overview of PPL. Similar in principle to µCP, but in this case the stamp is controlled with a piezoelectric system (represented by the orange cylinder), and not placed on the gold surface by hand.

1.5.4.5 Interferometric Lithography (IL)

SAMs can be modified and patterned by exposure to UV light. Alkylthiolate SAMs are photo-oxidised on exposure to light with a wavelength of 244 nm, converting the strongly bound alkylthiolate to a weakly bound alkylsulfonate that may be displaced by a contrasting adsorbate in a simple solution-phase exchange process [147-149]. Patterns can be formed over wide areas through the use of a benchtop laser in a Lloyd's mirror arrangement, a process that is known as interferometric lithography (IL), in which two coherent beams of light are caused to interfere to create an interferogram (with sinusoidal cross-section and a period of $\lambda/2nsin\Theta$) over the sample surface (Figure 1.5.7) [150, 151]. Such approaches have been used to pattern SAMs [152, 153]. In regions of the monolayer exposed to a maximum in the interferogram, the adsorbates are photo-oxidised, while in regions exposed to minima, the extent of oxidation is minimal. This approach has enabled dimensions as small as 30 nm to be achieved under ambient conditions, and over wide areas (cm^2 and above) [152, 153]. Multiple exposures at different angles can also be used to form patterns beyond just lines, but the types of pattern that can be formed is limited to one consistent array [152, 153].

a) Complete SAM layer exposed to laser light in a Lloyd's mirror configuration

c) Regions exposed to a high intensity band can be removed

Mirror

Laser Beam

θ
θ

Sample on Vacuum

b) Diffraction pattern formed over SAM surface

Real Source

Diffraction Pattern

Mirror

Reflection
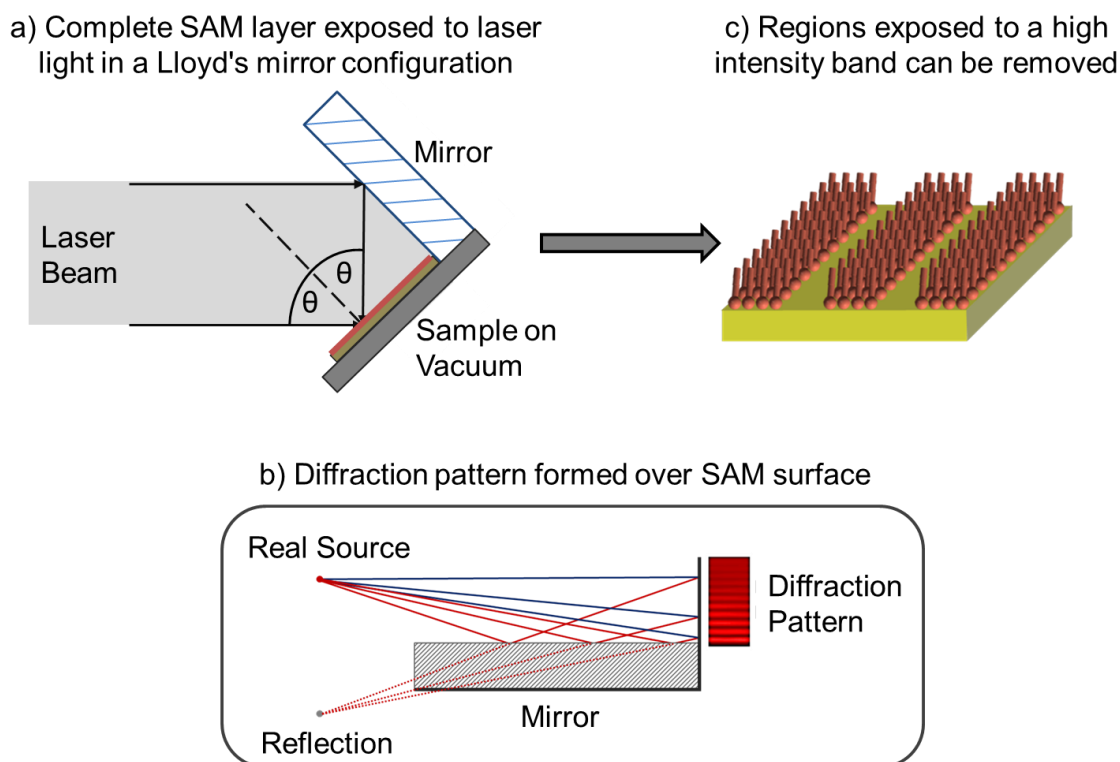
Figure 1.5.7 – An overview of IL. a) Laser light is directed at a SAM surface in a Lloyd's mirror configuration. b) A diffraction pattern of light and dark fringes is formed over the SAM surface. c) The SAM regions exposed to the bright fringes degrade more quickly; hence a pattern can be formed.

Table 1.5.1 – An overview of some of the techniques available for patterning SAMs onto surfaces.

Technique	Resolution	Advantages	Disadvantages
Photolithography	≈0.3 µm	Established, pattern wide areas, fast.	Expensive, clean room facilities required.
Particle beam	<10 nm	Nanoscale resolution, reliable.	Slow serial process, expensive equipment, UHV.
µCP	s-PDMS: >500 nm h-PDMS: <100 nm	Cheap, quick, can pattern wide areas.	Reproducibility and consistency issues.
Scanning Probe	<10 nm	Nanoscale resolution, reliable.	Slow serial process.
PPL	<100 nm	Precise µCP, can pattern wide areas.	Specialist equipment required.
IL	<50 nm	Relatively fast, can pattern wide areas.	Specialist equipment, limited patterns available.

1.6 Project Outline

1.6.1 Biomineralised MNP Arrays

Science is a progression, and this project is no exception.[*] This study builds directly on the work done by Johanna Galloway, whose results are published in numerous journal articles [97-99] and the complete body of work in a thesis [154], with the aim of developing a new bioinspired approach for the formation of nanomaterials on surfaces for technologies such as BPM. Much of the groundwork had already been completed, and as a result did not need to be repeated here. Therefore, the reader is directed to the relevant reference wherever necessary.
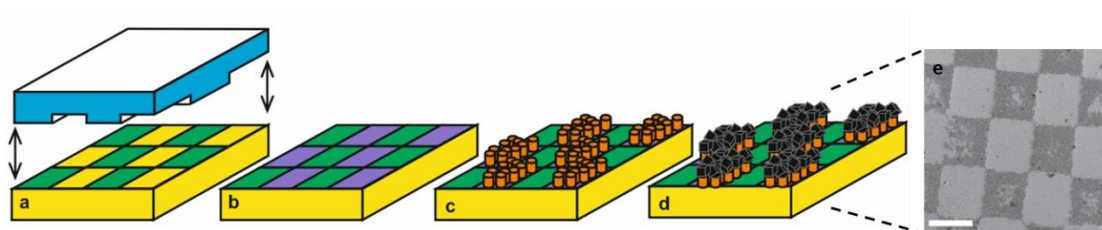
Figure 1.6.1[†] – Overview of the process used to form MNP arrays of magnetite. a) μCP is used to pattern a gold surface with a protein resistant PEG SAM (green). b) The remaining clean gold space is then backfilled with a PEG SAM containing carboxylic acid residues (purple). c) Mms6 (orange cylinders) binds to these residues *via* its *N*-terminal amine when activated by EDC/NHS. d) MNPs of magnetite (black cubes) form on the protein patterned areas when the surface is immersed into a mineralisation reaction. e) SEM image of a mineralised surface (scale bar 20 μm).

The main focus of the previous work was to develop a route to biomineralising MNPs on surfaces. This was successfully achieved through the combination of surface patterning and the biomineralisation protein Mms6 (Figure 1.6.1). A new, green, integrated and adaptive approach for forming microscale patterns of magnetite MNP arrays was developed (summarised in [97, 98]). The soft-lithographic approach of μCP was used to pattern a protein resistant PEG SAM onto a gold surface, before the remaining space was backfilled with a SAM containing carboxylic acid residues. These residues bound to the *N*-terminal amine of Mms6, when activated by EDC/NHS, forming a method that would not only pattern Mms6 on the microscale, but also correctly orientate it for efficient biomineralisation. These patterned surfaces were then immersed into a mineralisation reaction, allowing the immobilised Mms6 to template the formation of MNPs with a consistent cubic morphology under mild aqueous

---

[*] In 1676 Sir Isaac Newton famously wrote "If I have seen further it is by standing on the sholders of Giants" in a letter to Robert Hooke, a metaphor for the progression of science that is still relevant today (ironically this quote is not an original and is first attributed to Bernard of Chartres, a twelfth-century French Neo-Platonist philosopher, scholar and administrator).
[†] Adapted from Figure 1 in ref. [94].

reaction conditions. The Mms6 protein itself is dual purpose; not only controlling the morphology of the magnetite particles, but also tethering them to the gold surface.

However, this approach is not without its drawbacks, and the microscale patterns are as long way from being a surface that would be suitable for BPM. Although leading to the formation of MNPs of magnetite onto the immobilised Mms6 protein, achieving consistency in the patterning and orientation of Mms6 could be challenging as the EDC/NHS attachment is not specific for the *N*-terminal amine group. Other accessible lysine residues can also be targeted, resulting in the protein not being orientated correctly for biomineralisation. Coupled with this, magnetite is a magnetically soft material, which would not be well suited for data storage, and the microscale patterns need to be significantly reduced into the nanoscale before this approach becomes technologically relevant. This project aimed to address these and further issues, and an outline of the work is summarised below.

1.6.2 Summary of Chapters

In the subsequent chapters the theory and ideas introduced in this chapter are built upon, with the aim of developing a bioinspired approach to data storage. Firstly, in the following chapter the methods used throughout this study are outlined. Chapter 3 builds on the previous work done with Mms6, to understand and optimise the synthesis of biotemplated microscale MNP arrays of magnetite on gold surfaces. Chapter 4 then looks at the use of a number of different patterning techniques that are capable of patterning Mms6 with nanoscale precision, something which is required for the data storage technology of BPM. Following this MNP arrays formed with the artificial magnetite binding protein MIA-1 are analysed in Chapter 5, before the strategies developed in this thesis are employed in Chapter 6 to biotemplate arrays of MNPs of cobalt-doped magnetite and cobalt platinum that are more suitable for use in technologies such as magnetic data storage. Finally, conclusions are drawn and potential routes to developing an industrially viable route to forming a truly bioinspired magnetic hard disk are outlined.

2. Methods

"'Data! Data! Data!' he cried impatiently. 'I can't make bricks without clay.'"

Sherlock Holmes - The Adventure of the Abbey Grange

2.1 Biomolecules for Biomineralisation

Four different biomolecules were explored in this thesis for biotemplating the formation of MNP arrays. These were either synthesised within the Staniland Group or purchased. The biomolecules are introduced below, and the key properties are summarised in Table 2.1.1.

2.1.1 Cysteine-Tagged Mms6

As discussed in Section 1.4.6 Mms6 was first identified by Arakaki *et al.* [86] from the magnetosomes of the MTB AMB-1, and in the same study recombinant Mms6 was shown to control the size and shape of magnetite MNPs during a magnetite mineralisation reaction. Mms6 has since been shown to biotemplate the formation of consistent MNP arrays of magnetite when immobilised by its *N*-terminus to a SAM containing carboxylic acid moieties, after activation *via* EDC and NHS [97, 98, 154]. Here, Mms6 was engineered to contain an *N*-terminal cysteine, allowing it to be ordered directly onto a gold surface without the need for an attachment SAM.

2.1.2 Peptide Based on the *C*-terminal Region of Mms6 (Mms6_{Peptide})

Short peptide sequences based on the biotemplating *C*-terminal region of Mms6 have been shown to exert some control over forming MNPs of magnetite [96]. A synthetic peptide is cheaper and easier to produce than the full Mms6 protein, so in this thesis is explored as an alternative. The peptide sequence was designed to include an *N*-terminal cysteine and a glycine linker, which should allow the peptide to order onto gold surfaces whilst spacing it for efficient biomineralisation.

2.1.3 Magnetite Interacting Adhiron 1 (MIA-1)

Biopanning has identified many novel peptide sequences capable of interacting with materials, including those not found in nature [105, 106]. Recently, Rawlings *et al.* [114] built on this approach, by displaying two peptide loops on a robust protein scaffold termed an Adhiron [115]. The protein was then put through a biopanning process to identify the peptide loop sequences with the strongest affinity for the [100] face of magnetite. The protein was also engineered to contain a *C*-terminal cysteine, which should allow it to assemble directly onto a gold surface. Therefore, in this thesis the magnetite interacting Adhiron 1 (MIA-1)

protein that was developed is explored as an alternative to the naturally occurring Mms6 protein.

2.1.4 CoPt Binding Peptide

A peptide sequence, identified through biopanning, has been shown previously to be able to template the formation of CoPt [155] when immobilised onto a patterned surface [156]. Here, the peptide was designed to contain an *N*-terminal cysteine and a flexible glycine linker. These features should allow the peptide to self-assemble onto gold surfaces without affecting its biotemplating capability.

Table 2.1.1 – Key properties of the biomolecules used in this thesis.

Mms6	**Amino acid sequence:** MGSHHHHHHHHGSTENLYFQGCPRMGGTIWTGKG LGLGLGLGLGAWGPIILGVVGAGAVYAYMKSRDIESAQSDEEVELRDALA
	C : Cysteine
	H : Histidine purification tag
	N : Tobacco etch virus (TEV) cleavage site
	G : Wild type Mms6
	Number of amino acids: 87
	Molecular weight: 8.92 kDa **pI:** 6.2
	Synthesis: Produced in the Staniland Group by Andrea Rawlings
	Reference: [157]
Mms6~Peptide~	**Amino Acid Sequence:** CGGSKSRDIESAQSDEEVELRDAL
	C : Cysteine
	G: Flexible glycine linker
	D : Biotemplating region based on the *C*-terminal region of Mms6
	Number of amino acids: 24
	Molecular weight: 2.6 kDa **pI:** 4.2
	Synthesis: Purchased from GenScript (USA)
Magnetite Interacting Adhiron 1 (MIA-1)	**Amino Acid Sequence:** MKKIWLALAGLVLAFSASASAATGVRAVPGNENSL EIEELARFAVDEHNKKENALLEFVRVVKAKEQQKFVPKSTNTMYYLTLEAKDG GKKKLYEAKVWVKPKKSKIELKNFKELQEFKPVGDAAAASAWSHPQFEKC
	C : Cysteine
	H : Strep II purification tag
	K : Magnetite binding loop regions
	Number of amino acids: 138
	Molecular weight: 15.43 kDa **pI:** 9.6
	Synthesis: Produced in the Staniland Group by Andrea Rawlings
	Reference: Adhiron scaffold protein [115], MIA-1 [114]

CoPt Binding Peptide	**Amino acid sequence:** CGSGKTHEIHSPLLHK
	C : Cysteine
	G: Flexible glycine linker
	H : CoPt binding region
	Number of amino acids: 16
	Molecular weight: 1.74 kDa **pI:** 8.2
	Synthesis: Sequence designed by Johanna Galloway and purchased from GenScript (USA)
	Reference: Sequence based on a biopanned peptide sequence shown previously to template the formation of CoPt [155]

2.2 Patterning Biomolecules on Gold Surfaces

2.2.1 Overview of Patterning Biomolecules on Gold Surfaces

Polyethylene glycol (PEG) SAMs have been shown to form an antibiofouling surface [118], and have been used in previous work to resist the attachment of Mms6 so that it can be patterned with microscale precision to form a biomineralising surface [97, 98, 154]. Therefore, in this study various techniques were used to pattern a PEG alkanethiol (11-mercaptoundecyl tetra(ethylene glycol), $HS(CH_2)_{11}(OCH_2CH_2)_4OH$) (Sigma-Aldrich), the structure of which is shown in Figure 2.2.1. This formed protein resistant areas on gold surfaces. Conversely, this left areas of clean gold available so that another desired biomolecule could be attached, forming a route that would allow biomolecules to be patterned onto gold surfaces.
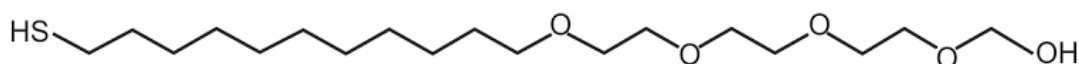
Figure 2.2.1 – Structure of the PEG molecule used to form the protein resistant SAMs in this work.

In some cases, the patterning technique could not be used to pattern the PEG SAM, but instead was used to pattern the biomolecule directly onto the surface. In this case, the surface was then backfilled with PEG alkanethiol after the biomolecule was patterned onto the surface.

2.2.2 Preparation of Gold Surfaces

Gold surfaces with a thickness of ≈50-200 nm were formed on clean glass microscope slides. The glass slides were sonicated in 1% Decon 90 and then Milli-Q water for 10 minutes each, before being dried in a nitrogen stream. The slides were then sonicated in isopropanol for a further 10 minutes, before being dried again with nitrogen. Following this, the slides

were immersed in a piranha solution (H_2SO_4 70%: H_2O_2 30% v/v) before thorough rinsing in Milli-Q water and drying with nitrogen. The clean slides were then mounted inside an Edwards Auto 360 thermal evaporator. The chamber was sealed and pumped to $<2\times10^{-6}$ mbar, before ≈5 nm of chromium was evaporated onto the glass at 0.1 nm s^{-1} to form an adhesion layer. Gold was then evaporated under the same conditions until the desired film thickness (50-200 nm) was reached, and the slides were removed and stored until required.

Prior to use, the gold coated glass slides were sectioned with a diamond tipped scribe, and broken into ≈1 cm^2 substrates. The gold substrates were then subjected to further cleaning before SAMs were formed. The gold surfaces were rinsed in Milli-Q water to remove any debris or dust that collected on the surfaces during the scribing process, before being dried in nitrogen and immersed into a piranha solution (H_2SO_4 70%: H_2O_2 30% v/v) for 2 minutes. The substrates were then thoroughly rinsed in Milli-Q water once more, and were once again dried with nitrogen. The gold substrates were then given one final rinse in ethanol and drying with nitrogen, before protein resistant SAMs were formed.

2.2.3 Microcontact Printing (μCP) of Microscale Patterns

2.2.3.1 Microscale Stamp Master Manufacture

Microscale stamp masters with feature sizes >1 μm were formed by the UV-photolithography of the epoxy type negative tone photoresist SU-8 2002 (Microchem. Corp and Chestech) in a class 100 cleanroom (the process is outlined in Figure 2.2.2). Silicon was cut into ≈1 cm^2 substrates with a diamond tip scribe and cleaned with 5 minute sonications in acetone, Milli-Q water, isopropanol and again in Milli-Q water. The substrates were then dried in nitrogen and dehydrated on a hot plate at 150°C for 2 minutes, before being piranha etched (H_2SO_4 70% : H_2O_2 30% v/v) for 5 minutes, with a final rinse in Milli-Q water and drying in nitrogen. SU-8 2002 was then applied to the clean silicon substrates so as to completely cover the surface, before being spun at 2000 rpm for 100 seconds and soft baked at 95°C for 2 minutes to form an average resist thickness of 1.6 μm [158]. The edge bead was removed,[*] as these raised edges of resist that form on the wafers after spin coating were found to lead to the centre of the substrate not contacting the mask during the next exposure step. This could

---

[*] I am indebted to Li Chen at the University of Leeds who first suggested removing the edge bead, and for his help in designing this protocol.

lead to diffraction of the light used to expose the resist between the substrate and the mask, blurring the final patterns that were formed.

Soft UV (365 µm)
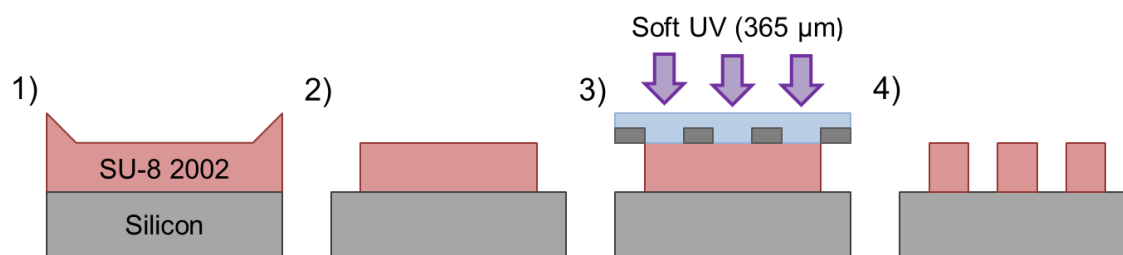
Figure 2.2.2 - Schematic of the photolithography process used to form microscale stamp masters for µCP. 1) SU-8 2002 is spin coated onto clean silicon substrates and soft baked at 95°C for 2 minutes. 2) The edge bead is removed. 3) The SU8 resist is exposed to soft UV light at 365 µm in contact with a pattern definition mask in a mask aligner, and post baked at 95°C for 2 minutes. 4) The resist is developed in an EC11 solution, before an isopropanol rinse, being dried in nitrogen and hard baked at 150°C for 10 minutes to form microscale patterns on the silicon surface.

SU-8 was patterned by exposure to soft UV light (365 nm) in contact mode through a pattern definition mask using a Karl Suss MJB-3 UV mask aligner. The lamp power of the mask aligner was measured before exposure and the exposure time was adjusted so an optimal dose of 21 mJ cm^{-2} was applied to the ≈1.6 µm thick SU-8. The mask was aligned with the substrates using an optical microscope, and after exposure the cross-linking was completed with a post bake at 95°C for 2 minutes. The substrates were then cooled to room temperature, developed in an EC11 solution for 1 minute, rinsed in isopropanol to halt the development process, dried in nitrogen and underwent a final hard bake at 150°C for 10 minutes.

2.2.3.2 Silanisation

All of the stamp masters were silanised immediately after being manufactured, and before being used to produce elastomer stamps for µCP. The silicon masters were rinsed in isopropanol and dried in nitrogen, before being loaded into the top of an evaporation column. A 1H, 1H, 2H, 2H-Perfluorodecyldimethylchlorosilane ($CF_3(CF_2)_7(CH)_2Si(CH_3)_2Cl$) solution (Alfa Aesar) was added to the base of the column, which was then purged with nitrogen and sealed. The silane solution was then heated to 150°C for one hour, after which the column was allowed to cool to room temperature. The evaporated silane solution condensed onto the stamp masters forming a hydrophobic SAM that helps prevent the elastomer sticking to the mould when forming stamps for µCP.

2.2.3.4 Micro-Contact Printing (μCP) with soft-PDMS (s-PDMS) Stamps

Polydimethylsiloxane (PDMS) stamps were formed through the curing of Sylgard 184 Silicone Elastomer and Silicone Elastomer Curing Agent (Dow Corning) over silicon masters to form flexible polymer stamps containing the desired pattern. The elastomer and curing agent were thoroughly mixed in a 10:1 ratio, then vacuum desiccated until all the trapped air bubbles that were visible were removed. Silicon masters were rinsed in isopropanol, dried with nitrogen and covered with a thin layer of the desiccated elastomer mixture. The covered masters were then desiccated for a second time to remove any further air bubbles introduced by this process, and cured for >24 hours at 60˚C. The stamps were then cut from the silicon masters and soaked in ethanol for >16 hours before being used, to remove any uncured polymer.

PDMS stamps that had been soaked in ethanol were dried in a nitrogen stream, before being inked with PEG. The dried PDMS stamps were covered with a 5 mM solution of PEG in ethanol, and incubated for 4 minutes. The excess SAM solution was removed *via* pipette and the inked stamps were then dried carefully in a nitrogen stream. The dried stamps were placed in conformal contact with a clean gold substrate for 4 minutes. The stamp was then removed forming an ordered PEG SAM where the stamp met the gold surface, leaving areas of clean gold not contacted by the stamp suitable for backfilling.

2.2.3.5 Assessing the SAM Quality with Secondary Ion Mass Spectroscopy (SIMS)

Many properties of the PEG SAM system, and its effectiveness as anti-biofouling surface, had previously been characterised by Johanna Galloway [154],[*] so this work was not repeated. However, it remained unclear whether the PDMS stamps were contaminating the gold surface surfaces during the μCP process (something that has been reported as an issue when forming SAM surfaces with μCP [159]). Thus, a secondary ion mass spectrometry (SIMS) study was used to probe the quality of the SAM surfaces produced, with the main aim of confirming that the μCP process used did not lead to any significant PDMS contamination.

SIMS provides chemical and structural information of surfaces by sputtering ionised particles from a surface of interest for analysis with mass spectrometry. Usually SIMS operates under high vacuum conditions and sputters material from a surface by bombarding it with a primary beam of ions or atoms. This results in ejection of clusters of atoms located close to

---

[*] Sections 3.3.1.1, 3.3.1.2 and 3.3.1.3 (p. 118-129) of ref. [113].

the surface (≈1-2 nm from the surface) [142]. Most of the clusters released are neutral, but some are ionised and can be extracted with the application of electric or magnetic fields for analysis in a mass spectrometer to determine the atomic species present [142]. As a result, SIMS is not a directly quantitative technique, but can be semi-quantitative with the use of calibration samples (although sputtered neutral mass spectrometry (SNMS) is a variation of SIMS that attempts to ionise and then detect the neutral clusters sputtered [160]).

SIMS can analyse a sample in two modes; time-of-flight SIMS (ToF-SIMS) where the primary beam is pulsed and ionised atom clusters that are sputtered from the surface are analysed with a ToF mass spectrometer, and Dynamic SIMS where a constant primary beam is used and certain ions are detected with a magnetic sector mass spectrometer [142]. SIMS can also image a sample by scanning the primary beam across a surface to provide a spectrum of the different sputtered clusters and hence detecting the elemental species present, routinely achieving <100 nm lateral resolution [142]. In this study, SIMS was carried out on a TOF.SIMS[5] (IONTOF Inc., Germany) with a bismuth source to probe the PEG SAM surfaces formed by μCP, and to confirm that it did not lead to significant PDMS contamination.[*] Spectra were obtained for 7 samples (numbered 1-7) mounted in a back mounted SIMS holder in both the positive and negative ion modes, and maps were also obtained for samples 4-7 (Table 2.2.2). For this experiment, gold surfaces were prepared in exactly the same way as described in section 2.2.1.3, and a control spectrum was obtained for a clean gold surface that underwent no further processing (sample 1, Table 2.2.2).

In this experiment samples were stamped with a PEG SAM, before being backfilled with a fluorine terminated thiol, which provides good contrast with the PEG SAM in a SIMs experiment. Samples 1-3 formed the controls in the SIMS experiment, with sample 1 being a clean gold surface. Sample 2 contained a complete PEG SAM and sample 3 a complete fluorinated thiol SAM, formed through immersing clean gold surfaces in either a 1 mM solution of PEG or a 1 mM 1H, 1H, 2H, 2H-perfluorodecanethiol ($CF_3(CF_2)7CH_2CH_2SH$) (Sigma-Aldrich, PEG-F) in ethanol for <16 hours respectively. These control samples allowed the fragments that were most characteristic for the gold substrate, PEG and PEG-F to be identified. Samples 4-7 were printed with PEG in the same way as described in Section 2.2.1.4, with the exception that the polymer stamp underwent a different cleaning process for each sample. Sample 4 was stamped with a stamp that underwent no cleaning protocols, the stamp

used for sample 5 was soaked in ethanol for >24 hours, sample 6 was patterned with a stamp that had been ozone cleaned for 20 minutes then soaked in ethanol for >24 hours and sample 7 was stamped with a stamp that had been left in ethanol for >4 weeks. After stamping, samples 4-7 were all backfilled with a PEG-F SAM by immersion in a 1 mM PEG-F in ethanol solution for >16 hours.

Table 2.2.2 - The different samples imaged during the SIMS experiment.

Sample	Sample Details
1	Clean gold substrate.
2	PEG SAM formed on a gold substrate.
3	PEG-F SAM formed on a gold substrate.
4	Gold substrate that was patterned with PEG *via* μCP using a polymer stamp that underwent no cleaning protocols, and was then backfilled with PEG-F.
5	Gold substrate that was patterned with PEG *via* μCP using a polymer stamp that was soaked in ethanol for >24 hours, and was then backfilled with PEG-F.
6	Gold substrate that was patterned with PEG *via* μCP using a polymer stamp that was ozone cleaned for 20 minutes, soaked in ethanol for >24 hours, and was then backfilled with PEG-F.
7	Gold substrate that was patterned with PEG *via* μCP using a polymer stamp that was soaked in ethanol for >4 weeks, and then backfilled with PEG-F.

2.2.4 Microcontact Printing (μCP) of Nanoscale Patterns

2.2.4.1 Nanoscale Stamp Master Manufacture

Nanoscale stamp masters with feature sizes in the 100-500 nm were manufactured by EBL of ZEP520A (Zeonex, Japan) resist to form a mask for reactive ion etching (RIE) of silicon with 1 μm of thermally grown oxide, with all processing performed in a class 100 cleanroom (process outlined in figure 2.2.3).[*] The oxide coated silicon was cut into ≈1 cm^2 substrates with a diamond tip scribe, which was then cleaned in the same way as described in the previous section (2.2.3.1) for the silicon wafers. ZEP520A was then applied to the clean silicon oxide substrates to completely cover the surface, before being spun at 3000 rpm for 100 seconds and soft baked at 95°C for 2 minutes forming an average resist thickness of 420 nm [161].

---

[*] I would like to thank Mark Rosamond at the University of Leeds for all his hard work in helping to develop this protocol, and for operating the EBL system.
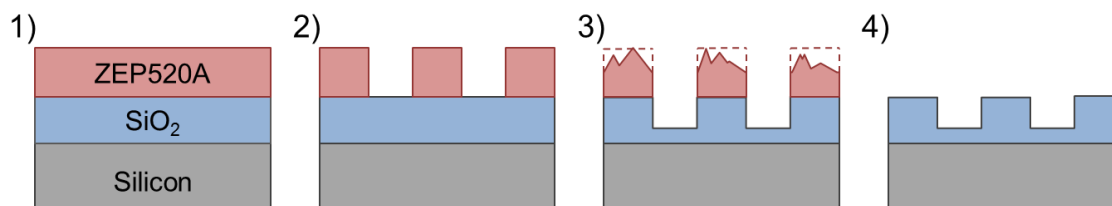
Figure 2.2.3 - Schematic of the lithography process used to form nanoscale stamp masters for µCP. 1) ZEP520A resist is spin coated onto clean silicon substrates with 1 µm of thermally grown oxide, and soft baked at 95°C for 2 minutes. 2) The resist is patterned by EBL and developed in ZED-N50. 3) The substrates then underwent reactive ion etching in a CHF$_3$ + Ar gas for varying lengths of time. 4) The resist was removed in a ZDMAC solution, before an isopropanol rinse and being dried in nitrogen to reveal nanoscale patterns in the silicon oxide surface.

Patterns for EBL were designed with Wavemaker software (Barnard Microsystems Ltd) in the industry standard GDS11 format and programmed onto a Joel JBX-6300FS EBL system (exposure was performed using recommended conditions; accelerating voltage 75 keV, electron current 5×10^{-11}A and 0.7 micro second per dot [161]). After exposure, the resist was developed in a solution of ZED-N50, before being rinsed in isopropanol, dried in nitrogen and undergoing a reactive ion etch in a CHF$_3$ + Ar gas. Unfortunately, after relocating to the University of Sheffield (and due to many problems with the EBL system) access to this equipment was lost. So only a few preliminary experiments were performed, and this process was never optimised. Only three samples were ever produced, all etched at different times; 150 seconds, 270 seconds and 540 seconds. Following the etching process the resist was removed in ZDMAC solution, before being rinsed in isopropanol and dried in nitrogen.

2.2.4.3 Micro-Contact Printing (µCP) with hard-PDMS (h-PDMS) Stamps

Traditional Sylgard 184 Silicone Elastomer cannot be used to form stamps with nanoscale features for µCP (section 2.2.3.4) as it is too soft, so the patterns usually collapse. So in this study a layer of hard-PDMS (h-PDMS), supported by a glass back panel, was used.[*] 3.4 g of vinyl-compound-rich prepolymer (abcr, Germany) 18 µl of 2,4,6,8-tetramethyltetravinylcyclotetrasiloxane (Sigma-Aldrich) and one drop of a platinum catalyst (platinumdivinyltetramethyldisiloxane complex in xylene, abcr, Germany) were mixed in a falcon tube, and degassed to remove all the trapped air bubbles. 1 g of a hydrosilane-rich crosslinker ((25-35% Methylhydrosiloxane) - dimethylsiloxane copolymer, abcr, Germany) was then added to the mixture, which then mixed and degassed once more. This mixture was then

---

[*] I am grateful to the Dip-Pen Nanolithography Group at the Karlsruhe Institute of Technology for providing me with this protocol.

poured over the silicon masters patterned with EBL, and a cut glass microscope slide was pressed over the top so that any trapped air bubbles were forced out. Stamps were then cured by baking on a hot plate at 70˚C overnight. Finally, the cured stamps were removed from the masters with a scalpel.

2.2.5 Polymer Pen Lithography (PPL)

A short collaboration with the Dip-Pen Nanolithography Group at the Karlsruhe Institute of Technology (KIT) in Germany allowed access to a polymer pen lithography (PPL) NLP 2000 instrument (NanoInk, USA). The PPL process described here is adapted from the method described in Brinkmann *et al*. [146]. PDMS stamps are manufactured as described in section 2.2.4.3, so that a layer of h-PDMS with a regular pattern of pyramid shaped tips is supported by a glass back panel (an example of which is displayed in Figure 2.2.4).
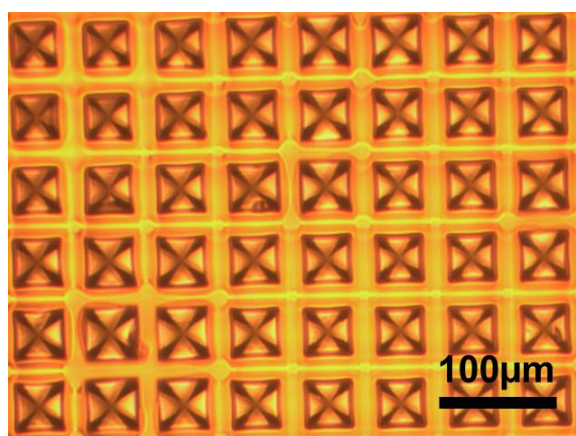
Figure 2.2.4 – Optical microscopy image of an example PDMS stamp containing an array of pyramid shaped tips, which was used in the PPL process.

The array of tips on the stamps used (Figure 2.2.4) lends itself well to patterning arrays of dots, like those required for use as bit-patterned media [41]. However, to achieve this patterning the biomolecules had to be inked onto the stamp, and not the PEG SAM. The PDMS stamps were first plasma cleaned in an Oxford Instruments Plasmalab 80 Plus at 100 mTorr and with 30 W for 2 minutes. The stamps were then spin coated for 2 minutes at 3000 rpm with a mixture of phosphate buffered saline (PBS) and glycerol (70:30 %, v/v) containing the desired biomolecule at a concentration 10 µg mL^{-1} to ensure an even spread of the ink across the stamp. The glass back panel of the stamp was then glued to a glass microscope slide, and secured to the stamp holder that was then fixed into the PPL machine. A clean silicon and gold substrate was secured on the substrate holder under the PDMS

stamp. The stamping chamber was then sealed, and the relative humidity set to 80% and the stamp incubated for 1 hour.

The PDMS stamp was first brought into contact with the clean silicon substrate, with the use of a piezoelectric stage controlled by NLP 2000 software. This allowed the stamp to be levelled, to ensure a uniform stamping process when placed in contact with the gold substrate. Once levelled, the stamp was raised away from the silicon substrate and placed in contact with the gold substrate. An array of dots were stamped onto the gold surface by continually raising and lowering the PDMS stamp, while moving the gold substrate to the desired distance with control of the piezoelectric stage. After the patterning process, the humidity control was stopped, the stamping chamber was opened and the patterned substrate was removed. The substrate was then rinsed with PBS, dried in nitrogen, and placed into a PBS solution overnight. The substrates were then rinsed in ethanol, dried once more in nitrogen and placed into a 1 mM solution of PEG in ethanol for 1 hour to backfill the remaining unpatterned and clean gold on substrate with a PEG SAM.

2.2.6 Dip-Pen Nanolithography (DPN)

The collaboration with the Dip-Pen Nanolithography Group at KIT also allowed for access to a dip-pen nanolithography (DPN) system. The DPN process described here is adapted from the method described in Chen *et al.* [162] and was carried out using a DPN 5000 system (NanoInk, USA). A 1-D cantilever array containing 26 Si_3N_4 tips were first cleaned in an Oxford Instruments Plasmalab 80 Plus 10 at 100 mTorr and with 30 W for 5 minutes. As with PPL, DPN has to be used to write the biomineralisation proteins or peptides directly onto the gold surface, *i.e.* the protein is the ink and not the backfill. Therefore, the tips were coated in with a mixture of PBS and glycerol (70:30%, v/v) containing the biomolecule at a concentration 10 µg mL^{-1} and dried in a nitrogen stream. The coated tips were then used to write onto clean gold surfaces with the use of NLP 2000 software, in a sealed environment set to a humidity of ≈80%. Following DPN patterning, the gold substrates were rinsed in PBS, dried in nitrogen, rinsed in ethanol and placed into a 1 mM solution of PEG in ethanol to backfill the remaining clean gold on substrate with a PEG SAM.

2.2.7 Interferometric Lithography (IL)*

Collaboration with The Nanoscale Analytical Science Group at the University of Sheffield allowed for access to an interferometric lithography (IL) system, and patterns of protein resistant PEG SAMs to be formed with nanoscale resolution. The IL process was modelled on the protocol described in Tizazu *et al.* [150]. A complete PEG SAM layer was formed on clean gold surfaces by immersion in a 1 mM PEG (11-mercaptoundecyl tetra(ethylene)glycol, Sigma Aldrich) in ethanol solution for <24 hours. The surfaces were then removed from the solution, rinsed in ethanol and dried in a nitrogen stream. IL was carried out by exposing the surfaces to a Coherent Innova 300C FreD frequency-doubled argon ion laser beam ($\lambda \approx 244$ nm, maximum power 100 mW) in a Lloyd's mirror arrangement (Figure 2.2.5).
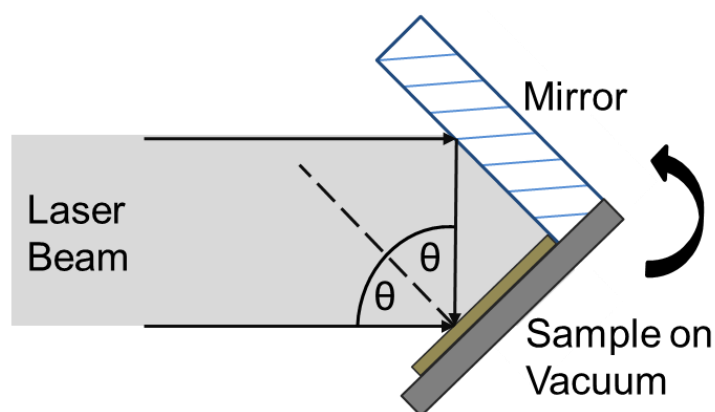
Figure 2.2.5 – The Lloyd's arrangement used during the IL patterning.

The laser beam was expanded so that an area of ≈ 1 cm^2 was illuminated, and was directed towards the surface that was held in place by a vacuum and fixed at an angle 2θ to a mirror. The laser beam was positioned so that half of the beam interacted directly with the sample surface, while the other half reflected off the mirror onto the sample. The reflected beam interferes with the first half of the beam, resulting in an interference pattern of bright and dark fringes forming over the sample surface with a period defined by the following equation:

$$period = \frac{\lambda}{2n \sin \theta} \qquad (2.2.1)$$

The laser power at the sample surface was recorded before samples were exposed, so that the exposure could be adjusted to ensure that the samples received the optimum dose of

---

* I am grateful to Osama El-Zubir for his support in developing this protocol.

20 mJ cm^{-2}. After exposure, the samples were removed from the Lloyd's mirror arrangement, rinsed with ethanol and dried with nitrogen.

2.3 Attaching Biomolecules to Surfaces

2.3.1 Quartz Crystal Microbalance with Dissipation (QCM-D)

A quartz crystal microbalance (QCM) system makes use of the stable properties of a piezoelectric quartz crystal resonator. The application of an electric field to a piezoelectric material induces a mechanical strain, so a QCM system oscillates a quartz crystal at its resonant frequency with the application of an AC voltage [163]. Most QCM systems monitor the frequency of thin circular quartz crystals cut in the AT form,[*] with any change in mass of the quartz crystal resonator resulting in a change in the frequency of oscillation [163]. QCMs allow for the real-time measurement of elastic mass adsorbed or desorbed onto a quartz crystal resonator with nm cm^{-2} accuracy through the application of the Sauerbrey equation. This reveals a simple linear relationship between the change in mass of a quartz crystal resonator (Δm) and an associated frequency shift (Δf) [164, 165]:

$$\Delta m = -\frac{\Delta f \rho_q v_q}{2n\sqrt{f_{fun}}} = -\frac{\Delta f \rho_q t_q}{n f_{fun}} \qquad (2.3.1)$$

Where ρ_q is the density of quartz (2648 kg m^{-2}), v_q is the speed of sound in quartz (3340 m s^{-1}), t_q is the thickness of the quartz crystal resonator and f_{fun} is the resonant frequency of quartz (4.95 MHz). QCMs have been widely used as mass balances since the theory of a quartz crystal resonator was first published by Sauerbrey in 1959 [165], particularly for the measurement of a deposited film thickness during vacuum deposition techniques such as evaporation and sputtering. However, it must be noted that the Sauerbrey equation is only valid for the addition of small masses[†] [163]. It has also been demonstrated that QCMs can be used to monitor the adsorption or desorption of mass from a liquid phase, and has been used successfully as a technique for monitoring protein adsorption [164].

The Sauerbrey equation assumes that mass deposited onto a quartz crystal resonator forms a rigid overlayer that can be treated as an increase in the quartz thickness.

---

[*] A cut at 35° to the z-axis. This provides a stable oscillation with little thermal fluctuation in frequency at room temperature.
[†] < 2% of the mass of the quartz crystal.

Unfortunately, this assumption becomes invalid for the adsorption of soft thin films such as protein layers that are not always rigid [164]. However, as well as the simplest QCM systems, two further QCM techniques are currently commercially available, and these can be used to obtain useful information such as the viscoelastic properties of any soft thin films absorbed. These systems combine a technique that measures the frequency of a quartz crystal resonator with a network analyser or impulse excitation technology, for impedance or dissipation measurement respectively [164].

Impulse excitation QCM systems switch the power used to drive the oscillation frequency of a quartz crystal resonator on and off, to determine the dissipation of the oscillation. The energy dissipation (D) of the quartz crystal resonator can be determined by application of equation 2.3.2 [164]:

$$D = \frac{1}{2\pi f \tau} = \frac{1}{Q} = \frac{E_{Dissipated}}{2\pi E_{Stored}} \qquad (2.3.2)$$

Where f is frequency, τ is the relaxation time, Q is the quality factor, E_{Stored} is the total energy stored in the oscillator and $E_{Dissipated}$ is the energy lost during one oscillation cycle. Measurements of dissipation allow for the analysis of different layers adsorbed onto a quartz crystal, to establish whether the Sauerbrey equation is valid for approximating any absorbed mass [166]. These impulse excitation QCM systems are commercially available from Q-Sense (Q-Sense, Gothenburg, Sweden) with the name quartz crystal microbalance with dissipation (QCM-D), and can be used for monitoring the adsorption of mass from both a gaseous or liquid phase [166].
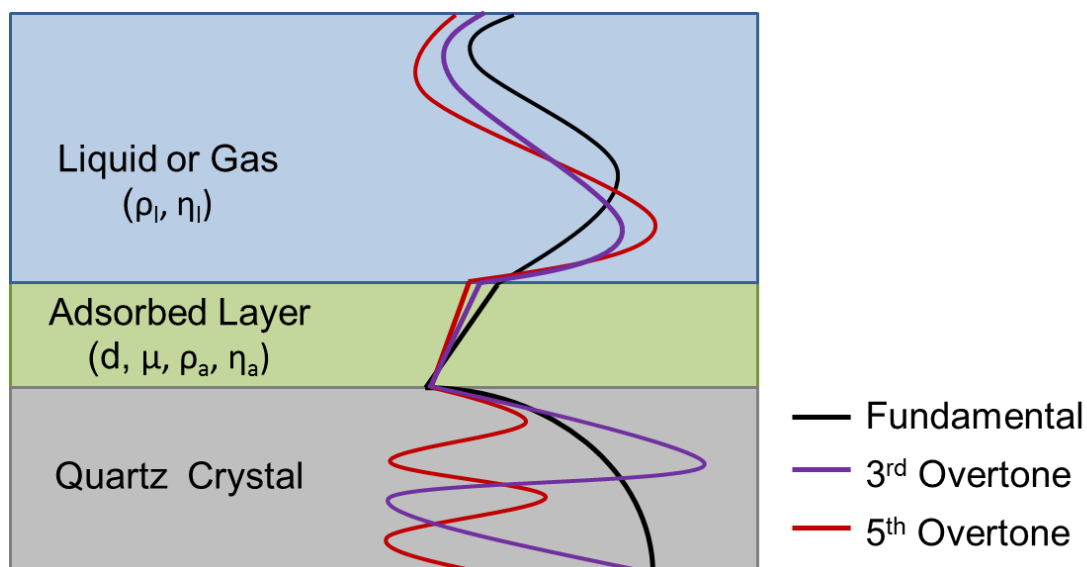
Figure 2.3.1 - Schematic of Voight viscoelastic model applied by Q-tools software. The model assumes the adsorbed layer has uniform thickness, and that frequency (f) and dissipation (D) can be modelled as functions of the overtone (n), thickness (d) and elasticity (μ) of the adsorbed layer, and the density and viscosity of both the bulk fluid or gas (ρ_l, η_l) and the adsorbed layer (ρ_a, η_a).

As absorbed layers are not always rigid, Voight based viscoelastic modelling can be used to estimate properties such as thickness, shear elastic modulus and viscosity of layers absorbed onto quartz crystal resonators [167]. For the Q-Sense systems, this modelling can be done through the application of Voight modelling using the Q-tools software (Q-Sense, Gothenburg, Sweden) [166]. Q-tools combines the frequency and dissipation measurements from the 3rd - 13th overtones during adsorption, with the adsorbed film assumed to have a uniform thickness and density. The measured frequency (f) and dissipation (D) are modelled as functions of overtone (n), thickness (d) and elasticity (μ) of the adsorbed layer, and the density (ρ) and viscosity (η) of both the bulk fluid or gas and the adsorbed layer (as shown in Figure 2.3.1). Fitting with multiple overtones allows these unknown parameters to be extracted by the software.

In this work, a Qsense E4 Multifrequency QCM-D (Q-Sense, Gothenburg, Sweden) was used to monitor the binding of biomolecules to gold-coated quartz crystals (Q-Sense, Gothenburg, Sweden) with and without a PEG SAM coating, and an overview of the system is shown in Figure 2.3.2. The gold-coated quartz crystals were rinsed in isopropanol, dried in nitrogen, ozone cleaned for 20 minutes, soaked in ethanol for 40 minutes and then either loaded straight into one of the four 40 µL flow cells of the QCM-D system or placed into an ethanol solution containing 1 mM PEG for 1 hour before loading. Crystals immersed in the PEG SAM solution are rinsed in ethanol and dried with N_2 prior to loading into the QCM-D. To check the setup for errors, the frequency and dissipation of the 3rd-13th overtones of all four

crystals are remeasured and recorded with Q-Sense Acquisition software (Q-Sense, Gothenburg, Sweden) and checked against standard values in air. Degassed Milli-Q water was then flowed through at a rate of 100 µL s^{-1} with a peristaltic pump, and the overtones checked again under liquid flow.
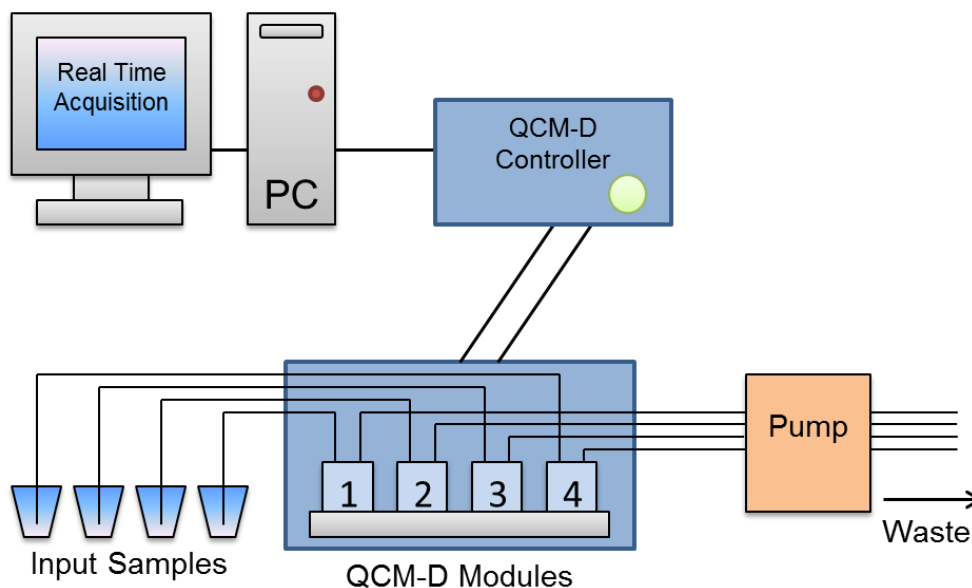
Figure 2.3.2 - Simplified overview of the Q-Sense E4 QCM-D System. A QCM-D controller programmed by Q-Sense acquisition software is connected to a peltier temperature controlled box containing the QCM-D modules. Liquid samples can be flowed through the modules containing gold-coated quartz crystals with a peristaltic pump in parallel as shown.

Degassed Milli-Q water was pumped through the four cells at a rate of 50 µL min^{-1}, and the frequency and dissipation of the 3rd-13th overtones was monitored until these values stabilised. After stabilisation, the water flow forms a base-line measurement for each crystal. A PBS buffer containing the biomolecule of interest was then pumped through the cells at 50 µL min^{-1} at a concentration of 10 µg mL^{-1} for 1 hour, with the same resonances recorded. The cells were then transferred back to degassed Milli-Q water at 50 µL min^{-1} until once again the measured values stabilise at a level that now reflects the amount and type of material that is adsorbed to the crystal surface. All data was modelled with the Qtools software (Qsense, Gothenburg, Sweden). If the adsorbed layer is thin and rigid (*i.e.* the change in energy dissipation is small), the added mass due to adsorption can be calculated with the Sauerbrey equation (equation 2.3.1). The added Sauerbrey mass (Δm) can then be used to estimate the total coverage of the biomolecule bound to the gold-coated quartz crystals:

$$pmol\ cm^{-2} = \frac{\Delta m}{M_p} \tag{2.3.3}$$

Where the mass of the biomolecule in its hydrated state in kDa is denoted by M_p. This coverage can then be compared to the expected coverage of the ideal, hydrated biomolecule, which depends on the space the peptide is expected to take up on the surface[*]:

$$mol\ cm^{-2} = \frac{\frac{1 \times 10^7}{l} \times \frac{1 \times 10^7}{w}}{N_A} \qquad (2.3.4)$$

Where *l* and *w* are the length and width of the hydrated biomolecule in nanometres, and N_A is Avogadro's number. The assumption that any biomolecule binding is rigid is not always valid, so viscoelastic Voight-based modelling can also be performed with Qtools. The modelling was performed following the methods used in the work done by Krzemiński *et al* [168], where the layer density, fluid density and viscosity were fixed at 1200 kg m^{-3}, 1000 kg m^{-3} and 0.00089 kg m s^{-1} respectively. The layer fitting was performed in 6 steps within ranges for the adsorbed layer; shear of 1x10^{-4}-1x10^{-8} Pa, viscosity of 0.001-0.02 kg m^{-1} and thickness of 1x10^{-7}-1x10^{-10} m.

2.4 Synthesis of Magnetic Nanoparticles (MNPs)

2.4.1 Formation of Magnetite using Partial Oxidation of Ferrous Hydroxide with Potassium Hydroxide (POFHK)

Although there are many methods available, in this study MNPs of magnetite were formed on surfaces patterned with Mms6 using partial oxidation of ferrous hydroxide with potassium hydroxide as the base (POFHK) [169]. This route was chosen in part because biomineralisation offers a greener, low temperature alternative for the production of high quality nanomaterials, eliminating some of the other synthesis methods discussed in Section 1.2.9.1, such as thermal decomposition. In addition, Mms6 has also been shown to biotemplate MNPs for both room temperature co-precipitation (RTCP) [86, 90, 99] and partial oxidation of ferrous hydroxide (POFH) [90, 99]. However, when Mms6 was immobilised onto a surface, RTCP was found to be unsuitable for the formation of MNP arrays, probably because the nanoparticles form too quickly when the reactants mix [98, 154]. As the Mms6 patterned surfaces are placed at the bottom of a reaction vessel in a large volume of solution containing

---

[*] The dimensions of the biomolecule can be taken directly from a crystal structure if one is available. Alternatively, a computational model can be used to calculate the expected dimensions of the protein or peptide. In either case, the values should be multiplied by 1.25 to allow for the increase in size caused by hydration by water as described in ref. [167].

a mixture of the reactants, this may prevent Mms6 from interacting with the MNPs that form quickly at the surface.[*]

Many variables can alter the type of iron mineral formed during a POFHK reaction, as discussed in Section 1.2.9.1. Therefore, I am grateful to Johanna Galloway for determining the optimum conditions used in this work.[†] During a POFHK reaction, ferrous hydroxide is formed through the mixing of a ferrous iron salt and potassium hydroxide. This is then partially oxidised by potassium nitrate, as shown below [169]:

$$3Fe^{2+} + 6OH^- \rightarrow 3Fe(OH)_2$$
$$2Fe(OH)_2 + NO_3^- + H_2O \rightarrow 2Fe(OH)_3 + NO_2^- \qquad (2.4.1)$$
$$Fe(OH)_2 + 2Fe(OH)_3 \rightarrow Fe_3O_4 + 4H_2O$$
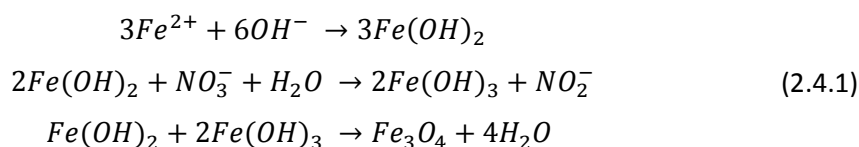
If used, substrates patterned with the desired biomolecules were rinsed in Milli-Q water, and added to a glass reaction vessel prior to the addition of the reactants. 24.75 mL of anaerobic Milli-Q water, which had been vacuum degassed for >1 hour and sparged with nitrogen for >1 hour to remove oxygen, was then pipetted into the vessel. The vessel was sealed against air, with a nitrogen flow maintained that passes through the water in the vessel. The pH could also be monitored during the course of the reaction. If this was the case, a pH probe attached to a Mettler Toledo Seven Multi controller was inserted into the reaction vessel, and the pH was recorded at 5 second intervals.

Reactants were dissolved in anaerobic Milli-Q water to form stock solutions of 0.5 M $FeSO_4 \cdot 7H_2O$ (1.39 g in 10 mL), 1 M KOH (0.56 g in 10 mL) and 0.5 M KNO_3 (1.52 g in 30 mL). 2.5 mL of the $FeSO_4$ solution was then pipetted into the reaction vessel, followed by 2.75 mL of the KOH solution. 20 mL of the KNO_3 solution was then added drop-wise over ≈5 minutes. The vessel was heated to 80°C and held at this temperature for 4 hours whilst under an inert atmosphere. Over this maturation period, MNPs of magnetite form in the reaction solution, and onto the patterned and immobilised biomolecules. After 4 hours, the biomineralised surfaces (if used) were removed, rinsed in Milli-Q water to remove any unbound nanoparticles, and dried in nitrogen. The MNPs that form from the bulk solution that are not attached to the surfaces were collected magnetically, rinsed with degassed Milli-Q water at least 5 times, and sealed in glass vials for further use or analysis.

---

[*] For more details see Section 5.2 p.175-177 in ref. [153].
[†] For more information see Section 5.3 p.177-182 in ref. [153].

2.4.2 Formation of Magnetite with Room Temperature Co-Precipitation (RTCP)

Although it had previously been established that RTCP was not very effective for the production of surfaces patterned with immobilised Mms6 [98, 154], it remained unclear whether this was the case for the MIA-1 protein also explored in this thesis. Therefore, surfaces patterned with MIA-1 were also subjected to a RTCP reaction. In this case, ferrous and ferric iron salts were mixed, and then a base was added under an inert atmosphere to form magnetite, as shown below [169]:

$$Fe^{2+} + 2Fe^{3+} + 8OH^- \rightarrow Fe_3O_4 + 4H_2O \hspace{2cm} (2.4.2)$$
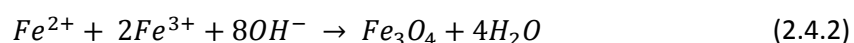
Although, in reality equation 2.4.2 is an oversimplified view of the reaction scheme, as many other iron oxides and (oxy)hydroxide intermediates and impurities may also form during co-precipitation [16].

If used, MIA-1 patterned surfaces were rinsed with Milli-Q water, and placed into a glass reaction vessel before the addition of the mineralisation reactants. The pH could also be monitored during the course of the reaction. If this was the case, a pH probe attached to a Mettler Toledo Seven Multi controller was inserted into the reaction vessel, and the pH was recorded at 5 second intervals. 47.75 mg of $Fe_2(SO_4)_3$ and 106.35 mg of $FeSO_4$ were both dissolved separately in 10 mL of anaerobic Milli-Q water (to form 12 mM and 70 mM solutions respectively), which had been degassed for >1 hour and nitrogen sparged for >1 hour. These were then both added to the reaction vessel, after which the vessel was sealed except for a flow of nitrogen that was bubbled through the reactant solution. NaOH was dissolved into anaerobic Milli-Q water to form a 500 mM stock solution (2 g in 100 mL). 4 mL of this solution was then injected into the reaction at a rate of 20 μL min^{-1} through the use of a syringe pump driver, whilst nitrogen purging was maintained. After the reaction was complete, the biomineralised surfaces (if present) were removed, rinsed in Milli-Q water to remove any unbound particles and dried with nitrogen. The MNPs that form from the bulk solution that are not bound to the surfaces were collected magnetically, rinsed with Milli-Q water at least 5 times and sealed in glass vials for further use or analysis.

2.4.3 6% Cobalt-Doped Magnetite Formation using Partial Oxidation of Ferrous Hydroxide with Potassium Hydroxide (POFHK)

Mms6 has been shown previously to template the formation of magnetically harder cobalt-doped magnetite, potentially providing a way to fine tune the magnetic properties of biomineralised MNP arrays of magnetite [99, 154]. The introduction of cobalt results in an increase in coercivity and a decrease in magnetic saturation, with a doping level of 6% found previously to result in the largest increase in coercivity with only a minor decrease in magnetic saturation [99, 154].[*] As a result MNP arrays of 6% cobalt-doped magnetite, which were biomineralised by patterned and immobilised Mms6, were compared to undoped arrays as a route to forming a system with tuneable magnetic properties.

Biomineralised 6% cobalt-doped arrays were formed following the process described in Section 2.4.1, with the addition of the correct ratio of cobalt to iron. Gold surfaces patterned with immobilised Mms6 were rinsed in Milli-Q water, and added to a glass reaction vessel. 24.75 mL of anaerobic Milli-Q water was added, the reaction vessel was closed and the water was purged with nitrogen. Reactants were dissolved in anaerobic Milli-Q water to form stock solutions of 0.5 M $FeSO_4 \cdot 7H_2O$ (1.39 g in 10 mL), 0.5 M $CoSO_4 \cdot 7H_2O$ (77.5 mg in 1 mL), 1 M KOH (0.56 g in 10 mL) and 0.5 M KNO_3 (1.52 g in 30 mL). 2.35 mL of the $FeSO_4$ solution followed by 0.15 mL of the $CoSO_4$ solution were added in place of the 2.5 mL of $FeSO_4$ as described previously in section 2.4.1. The rest of the reaction was then performed as described in Section 2.4.1.

2.4.4 Washing Pre-formed Magnetite Nanoparticles over Surfaces

A key aim of this project is to establish whether Mms6 (and other biomolecules used in this study) act more efficiently as a nucleator of iron ions or as a binder to magnetite once it formed. Therefore, surfaces patterned with Mms6, peptides based on Mms6 and MIA-1 have been produced to see which biomolecule (if any) is able to bind to pre-formed MNPs of magnetite by simply washing the particles over the surfaces.

Surfaces patterned with these biomolecules were added to 50 mL glass flasks. MNPs were collected magnetically after the POFHK and RTCP reactions were performed as described above in Sections 2.4.1 and 2.4.2, but without the addition of any protein patterned surfaces.

---

[*] See Section 4.2 p.149-154 in ref. [153] for more information.

These MNPs were then dispersed in 20 mL of anaerobic Milli-Q water and added to the flask containing the protein decorated surfaces. The flasks were then sealed, and placed on a tilt stirrer so that the particles gently flowed over the surfaces and did not just settle at the bottom of the flask. Surfaces were left in the nanoparticle suspension for >24 hours, as this length of incubation was found to result in more particles binding to the patterned biomolecules, and thus the best MNP patterns forming. After the incubation period, the surfaces were removed from the nanoparticle suspension, rinsed in Milli-Q water to remove any unbound particles and dried with nitrogen.

2.4.5 Formation of CoPt

MNPs of CoPt were synthesised following the procedure outlined in Galloway *et al*. [156], but using a different method of attaching the CoPt biotemplating peptide to the surface that allows for patterning of the surfaces. In Galloway *et al*. [156], a dual affinity peptide, designed to bind to silicon at one end and to biotemplate CoPt at the other, is coated onto a silicon substrate without patterning. A cysteine containing version of the CoPt templating sequence (see Table 2.1.1 in Section 2.1) is combined with patterning of PEG SAMs on gold to create CoPt biotemplating patterns. Substrates patterned with the CoPt binding peptide, using any of the methods outlined in section 2.2 for patterning Mms6, were rinsed in Milli-Q water, and added to a glass reaction vessel. Reactants were dissolved in anaerobic Milli-Q water (vacuum degassed for >1 hour and nitrogen sparged for >1 hour), to form stock solutions of 30 mM $CoSO_4 \cdot 7H_2O$ (126.5 mg in 15 mL), 15 mM Na_2PtCl_4 (57.4 mg in 15 mL) and 25 mM $NaBH_4$ (28.4 mg in 30 mL). 15 mL of each of the $CoSO_4 \cdot 7H_2O$ and Na_2PtCl_4 stock solutions were then added to the reaction vessel, which was then closed under an inert atmosphere. After 5 minutes, 30 mL of $NaBH_4$ was injected into the reaction vessel to reduce the metal salts, and nitrogen flow was maintained. After 45 minutes, the surfaces were removed from the reactants, rinsed in Milli-Q water to remove any unbound particles and dried with nitrogen.

2.5 Characterisation

2.5.1 Scanning Electron Microscopy (SEM)

Scanning electron microscopy (SEM) has become one of the most important and widely used techniques for the characterisation of surfaces displaying nanoscale features. Accelerated electrons have a wavelength much smaller than that of visible or ultra-violet light,

resulting in electron microscopy being able to image with a much greater resolution than is possible using conventional light microscopy.[*] Additionally, electrons interact more strongly with matter than with photons, so a stronger signal can be obtained from samples with reduced dimensions [142]. However, this does mean that all optical paths in an electron microscope have to be held under high vacuum, to prevent attenuation of the electrons by collision with atoms of the air.

Electrons are produced in an SEM by either thermionic or field emission from a solid source, which in the majority of microscopes is a tungsten filament [142]. During thermionic emission, the solid source is heated, releasing electrons by providing enough thermal energy for the potential energy barrier for electrons to leave the material to be overcome. Alternatively, during field emission, a strong electric field is applied to the solid source, reducing the surface potential barrier and allowing for the quantum tunnelling of electrons out of the source. These electrons form the primary electron beam. The primary beam is controlled using electromagnetic optics, which use electrically generated magnetic fields to collimate, accelerate, and focus the electrons. This beam is then raster scanned across a sample of interest by another system of electromagnetic lenses.

Primary electrons are focussed onto a solid sample, and interact with a volume that is dependent on the energy of the primary beam, and the atomic number of the sample [142]. After electron-surface interactions, secondary electrons escape from the sample with a kinetic energy <50 eV. Secondary electrons are most likely ionised electrons from atoms close to the sample surface, or primary electrons that have lost almost all their energy through scattering processes [142]. Backscattered electrons are also produced as a result of primary electrons undergoing large deflections, leaving the surface with only small changes to their initial kinetic energy [142]. Furthermore, atoms within the sample can undergo inner shell ionisation. Higher energy electrons will then drop into the vacant energy levels, releasing the excess energy as an auger electron, X-ray or visible photon (Figure 2.5.1) [142].

---

[*] The resolution of a conventional light (*i.e.* diffraction-limited) microscope can be approximated with the Abbe diffraction limit, and is inversely proportional to the wavelength of the light being observed, which is ≈250 nm for green light.
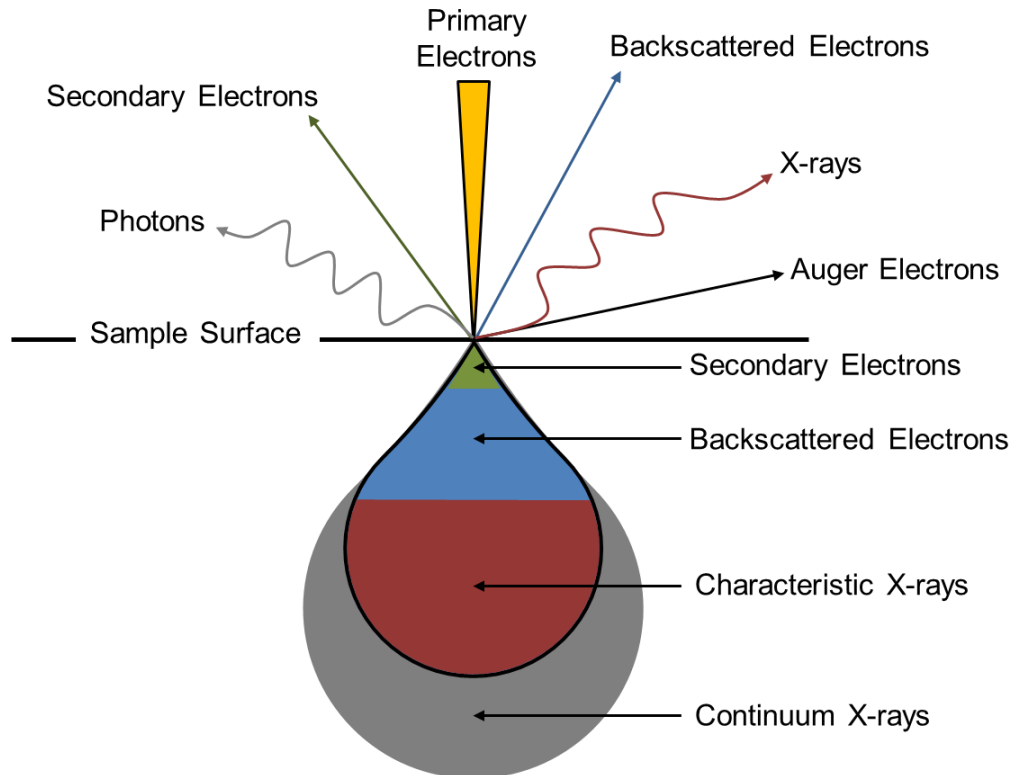
Figure 2.5.1 (produced with information from ref. [142]) - The interactions of primary electrons focused onto a sample during SEM, forming a teardrop shaped interaction volume. Backscattered electrons undergo one or more scattering events before exiting the sample. The primary beam or backscattered electrons produce secondary electrons, but these only leave the sample when produced <1 nm from the surface. Auger electrons are easily attenuated and have to be produced <10 nm from the sample surface to escape. X-rays exit the sample surface when produced from anywhere within the interaction volume.

Samples can be imaged in a variety of different modes, but topographic images of the biomineralised MNP arrays formed in this study were obtained through the detection of the high number of secondary electrons produced as the primary beam is scanned over a surface. These are normally detected with a scintillator-photo-multiplier system placed at a shallow angle to the side of the imaged sample. In most cases, a Faraday cage with a small positive bias surrounds the detector to attract the low energy secondary electrons that leave the sample in all directions. Higher energy backscattered electrons traveling directly towards the detector will also be detected, but due to the shallow angle of the detector, this signal is significantly smaller than that produced by the secondary electrons.

As this work was completed over four years, and across three different institutions, the SEM images included in the results chapters were recorded with many different instruments. Although different SEMs were used, the sample preparation always remained the same. In every case samples were mounted onto aluminium stubs with double sided carbon tape, and earthed with the application of silver paint at the edge of the sample.

When this work began at the University of Leeds, SEM images were recorded with a Hitachi SU8230 SEM, which was operated with Zeiss SmartSEM software.[*] The SEM chamber wass pumped to $<2x10^{-5}$ mbar and the samples imaged at a working distance (WD) of approximately 15 mm, with a primary beam accelerating voltage of 15 keV. Digital micrographs were produced by the Ziess SmartSEM software through the detection of secondary electrons with the in lens secondary electron detector. After relocating to the University of Sheffield, SEM images were instead recorded on an FEI Inspect F50, operated with xT microscope Control software.[†] In this case, the SEM chamber was pumped to $<5x10^{-5}$ mbar, with the samples imaged at a WD of 10 mm and at an accelerating voltage of 5-10 keV. The digital micrographs were produced through the use of the xT software, after detection of secondary electrons with an in lens secondary electron detector.

2.5.2 Energy Dispersive X-ray Analysis (EDXA)[‡]

Atoms can undergo the process of inner shell ionisation when impacted by an electron beam, as discussed in Section 2.5.1 above and shown in Figure 2.5.1. Electrons in higher energy levels will then drop into the vacant lower energy states, potentially emitting an X-ray as part of the de-excitation process [142]. Energy dispersive X-ray analysis (EDXA) measures the energy of X-rays emitted from a sample probed by an electron beam, and can be used to determine the atomic species that are present. This is possible due to the well-defined quantised nature of atomic energy levels, and the fact that a set of dipole selection rules determines the de-excitation processes that are allowed [142]. As a result, the X-rays that are produced have characteristic energies and wavelengths depending on the atomic species that are present.

EDXA spectroscopy can be used in an SEM system to provide elemental information on a sample in a spatially defined manner. EDXA is used in this study to provide information on the elements present in the biomineralised MNP arrays that are formed. EDXA detectors detect the energy of X-rays produced from a sample irradiated with a primary electron beam *via* the creation of electron-hole pairs in biased silicon, with the number of electron-hole pairs

being directly proportional to the energy of the detected X-ray [142]. Hence an EDX system can be used within a SEM to detect the atomic species present over the whole sample surface, or to map the location of atomic species as the primary beam is raster scanned over the surface.
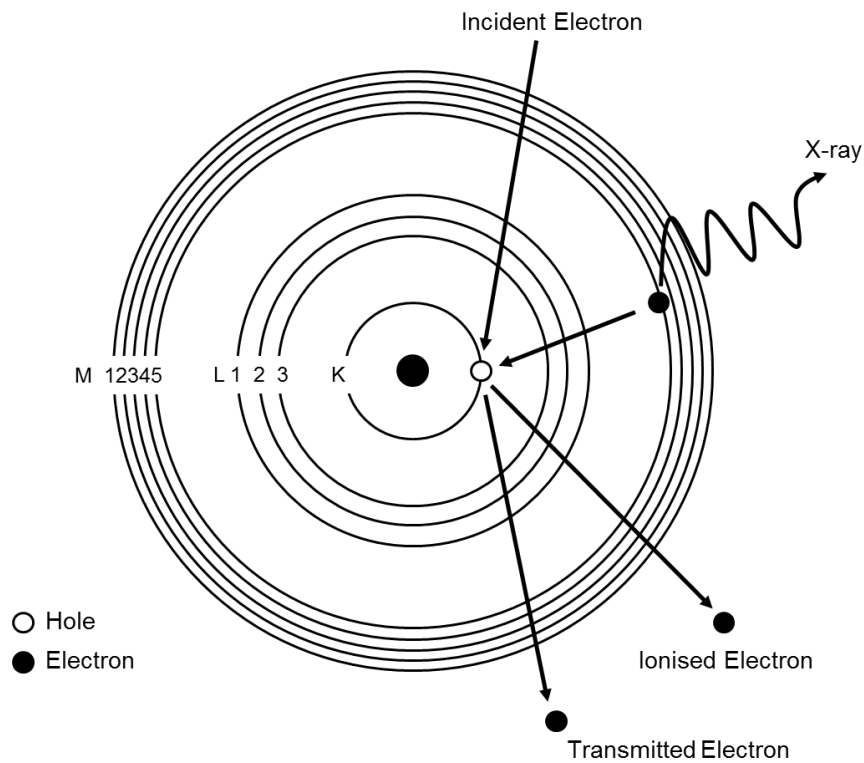
Figure 2.5.2 - Schematic of an X-ray emission process due to the de-excitation of an atom that has undergone K-shell ionisation.

Unfortunately, EDXA was only available at the University of Leeds, so after moving to the University of Sheffield this facility was no longer available.[*] In this work, an Oxford Instruments AztecEnergy EDX detector system attached to the Hitachi SU8230 SEM was used to obtain X-ray spectra of the biomineralised MNP arrays, and elemental maps of gold, oxygen, iron and cobalt. Data was collected at a WD of approximately 15 mm, with an accelerating voltage of 7 keV and processed with INCA software.

---

[*] EDXA is due to be installed on the FEI Inspect F at the University of Sheffield, but sadly too late for this work.

2.5.3 Transmission Electron Microscopy (TEM)[*]

Transmission electron microscopy (TEM) is similar in principle to SEM, and has become one of the key techniques available for imaging ultrathin structures on the nanoscale. TEM operates at much higher accelerating voltages than SEM (typically 100-400 keV, but some instruments can operate up to and above 1 MeV), ultimately leading to greater resolution. Traditionally most TEMs generate electrons *via* field emission from a tungsten filament, but it is more common to find a Schottky style field emission gun (FEG) in modern instruments. As with SEM, TEM focuses electrons through the application of electromagnetic fields onto a sample under high vacuum conditions. This sample must be thin (no more than a few 10s of nanometres), as the electrons must penetrate the sample to be detected underneath. The transmitted electrons are usually detected with a phosphor screen or a charged coupled device (CCD) to form a two dimensional projection of the sample.

A TEM can image in a number of different modes. A bright field image can be generated as electrons undergo a number of different scattering processes when interacting with the sample. Regions that are more dense or thicker will lead to greater scattering, which means that electrons will not be detected from these areas, and thus lead to these regions appearing darker on the final image. Crystalline samples also diffract the electron beam, which can be used to form a dark field image if the transmitted beam is excluded. In dark-field, dark areas of the image correspond to areas where no diffraction takes place in the sample. Chemical information can also be obtained through techniques such as electron energy loss spectroscopy (EELS), or by the detection of X-rays with EDXA if these detection systems are fitted to a TEM.
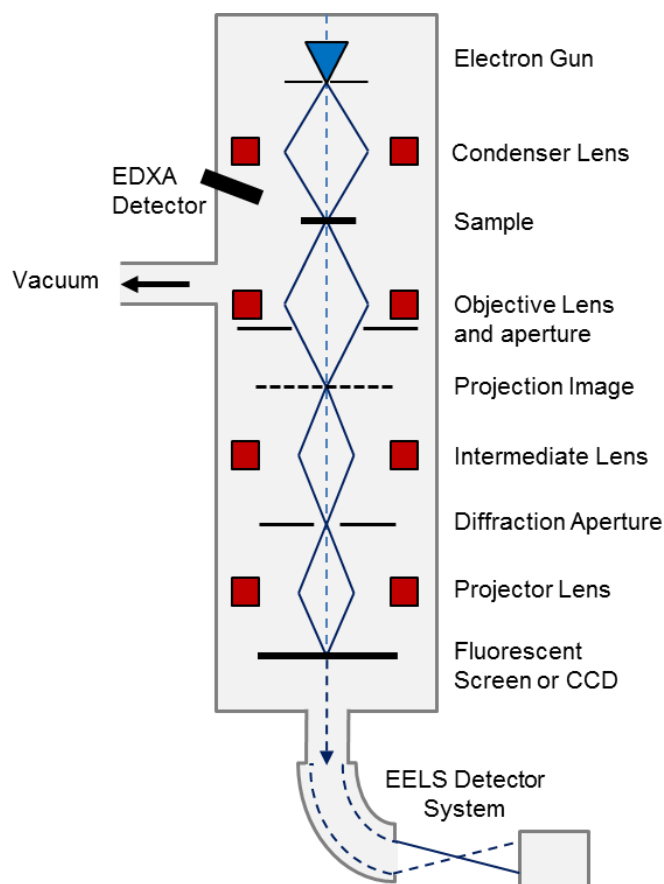
Figure 2.5.3 – Schematic showing the typical layout of a TEM (adapted from Figure 2.8 in ref [142]). Electrons are focussed onto a sample through the use of electromagnetic lens systems (red boxes) under high vacuum conditions. After passing through the sample, the electron beam (blue lines) is then focused to form an image. The typical locations for EDXA and EELS detection systems are also shown.

In this study, TEM was used to image any MNPs that were formed. The MNPs were collected magnetically, rinsed in Milli-Q water at least 5 times, before being dispersed in Milli-Q water. 10 µL of this suspension was pipetted onto carbon coated copper TEM grids (S162-3, Agar), and the grids were allowed to dry in air. Grids were imaged with a FEI Tecnai G2 Spirit operating at 80 keV, and processed with Gatan DigitalMicrograph software.

2.5.4 Grain Size Analysis

The grain size of the nanoparticles imaged with SEM and TEM was recorded along the longest axes of the projection using ImageJ software [170]. ≈100 particles per sample were measured, and these data were fitted with a Gaussian distribution in GraphPad Prism software.[*] To compare the morphology of the particles, the length of the longest axis of the projection of the nanoparticles was compared to the shortest axis in Image J. The size

---

[*] *GraphPad Prism*, version 6.01, Graphpad Software Inc., San Diego, CA, USA, 2013.

recorded for the shortest axis was then divided by that recorded for the longest axis, giving a value for an aspect ratio in range of 0-1. These data was then fitted in GraphPad Prism, with aspect ratios closer to 1 indicating the particles had a more equidimensional morphology.

2.5.5 Particle Density Counts

The density of particles biotemplated onto surfaces was determined following the procedure outlined by Galloway *et al*. [156].[*] The number of particles per unit area in five different representative SEM images for each sample were counted and averaged. These areas were chosen to be on the regions patterned with biomolecules where the formation of nanoparticles was expected, and not on the regions of the surface patterned by PEG.

2.5.6 Atomic Force Microscopy (AFM) and Magnetic Force Microscopy (MFM)

Along with electron microscopy, scanning probe techniques have become one of the most well used methods for characterising surfaces with nanoscale resolution [142]. Atomic force microscopy (AFM) has the ability to image materials without the need for high vacuum conditions, and has become one of the most versatile tools in nanotechnology. AFM can be used to image the topography of a sample by scanning a sharp tip[†] attached to the free end of a cantilever over the surface, or alternatively by scanning the surface under the tip with the use of a piezoelectric system. Several forces act between the tip and the surface, causing the cantilever to deflect. The most common are attractive Van der Waals forces, when the tip is between 10-100 Å from the surface, and repulsive electrostatic forces when the tip is <2 Å from the surface [142].

A topographical image of the scanned sample is built from measurements of the cantilevers position, usually achieved with a laser beam that is reflected off the back of the cantilever and detected with a position-sensitive photodetector (as shown in figure 2.5.4). AFM can be operated in a variety of different modes including. For example constant-height, where the scanner height is fixed and an image is built from measurements of the cantilever deflection, and constant-force, where measurements of the cantilever deflection are used in a feedback loop to maintain it at a constant force by moving the scanner over the surface

---

[*] I would also like to thank Johanna Galloway for suggesting this useful approach.
[†] With dimensions on the nanoscale, the sharper the tip the greater the potential resolution.

topology. AFM can also be operated in other modes, such as tapping mode where a stiff cantilever is vibrated at close to its resonant frequency so that the tip just touches the sample surface at the bottom of its movement. When the tip approaches the surface, it causes a shift in the frequency of vibration, but with the aid of a feedback system the AFM vibrates the cantilever at a constant frequency by moving the scanner up and down. This provides a method of recording surface topography, but due to the fact the tip is not dragged laterally across the surface it causes less damage than contact mode AFM.

In this study, magnetic force microscopy (MFM), which uses a tapping mode cantilever with a magnetised tip, is used to not only image the topography of biomineralised MNP arrays, but to also obtain magnetic information. Firstly, samples are imaged with tapping mode AFM, before being retraced in lift mode at a constant lift height of 50-200 nm above the surface (figure 2.5.4). Magnetic interactions between the magnetised tip and the sample cause vertical frequency and hence phase shifts in the cantilevers oscillation, which can be used to map repulsive and attractive magnetic interactions over the sample surface.
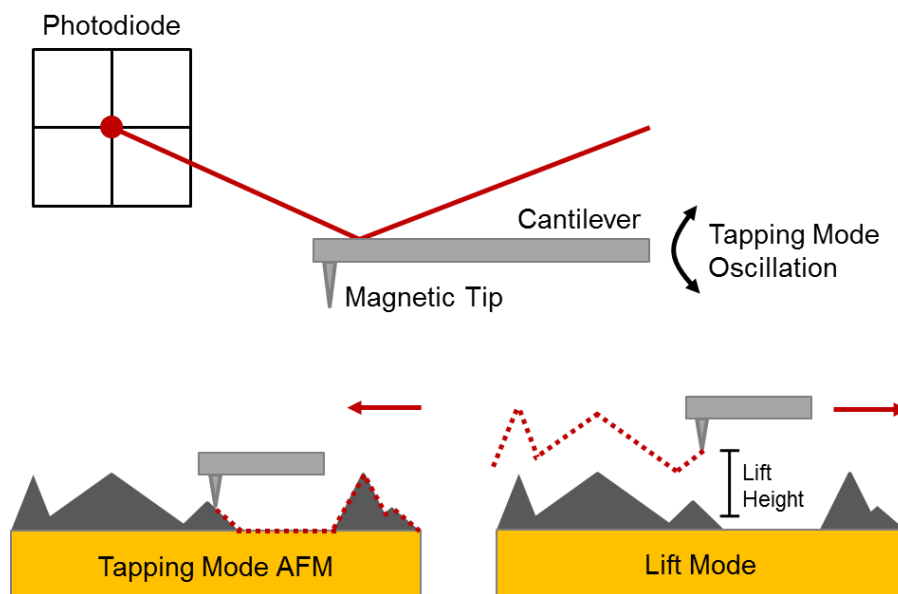
Figure 2.5.4 - Schematic of AFM and MFM (adapted from the excellent fig. 2.14 in ref [154]). The defection of an AFM cantilever is detected by the reflection of a laser off the cantilever and onto a photodetector. The surface is first imaged with tapping mode AFM, before the cantilever is raised a certain lift height and the surface is retraced to record magnetic information.

Again, due to this study being carried out over multiple institutions, two different AFMs were used to produce the AFM and MFM images included in this work. In both cases, silicon AFM cantilevers with Cr/Co coated MFM tips were used (MESP probe, Veeco), and all

the data was processed with WSxM software [171] and 3D data maps were produced in "R" using the rgl package.[*]

At the University of Leeds, a Multimode Nanoscope III AFM was used to image the topography of biomineralised MNP arrays in tapping mode, and MFM was used to obtain magnetic information.[†] The AFM tips were fixed into a tip holder, magnetised with a permanent magnet and attached to the AFM head. The cantilever was then tuned to resonant frequency in air (typically ≈70 kHz for MESP probes) using the Nanoscope software. Initially, the cantilever was vibrated over the surface at its resonant frequency in tapping mode to form a good topographic image. Once the tip is engaged with the surface, the amplitude set point was reduced so that the tip lightly contacted the surface, and the cantilever was maintained at a constant frequency by a feedback circuit controlled with the Nanoscope software. The feedback controls (integral gain and proportional gain) were also adjusted to ensure the best possible image was obtained. MFM was performed in interleave mode, where after a tapping mode pass, the sample was retraced at a constant lift height of between 50 and 200 nm above the surface in a lift pass. Magnetic interactions between the magnetised AFM tip and the sample were then used to map repulsive and attractive magnetic interactions.

Data obtained at the University of Sheffield was collected on a Bruker Multimode 8 AFM, following a similar procedure to what was performed at Leeds.[‡] Again a Cr/Co coated MFM tip (MESP probe, Veeco) was fixed into a tip holder and magnetised with a permanent magnet before being fixed onto the AFM head. The Nanoscope software was then used to tune the cantilever, and an image was formed in tapping mode. The cantilever was maintained at a constant frequency with the Nanoscope software, with the amplitude and the gains adjusted so that the best possible image was obtained. To record magnetic information, interleave mode was enabled. After a tapping mode scan, the sample was retraced at a lift height of between 50 and 200 nm, so that any interactions can be used to plot repulsive and attractive magnetic interactions independently of the topography of the surface.

---

[*] Program used to render the MFM images in 3D is available here: https://github.com/jonbramble/MFMPlot.

[†] I would like to thank Johanna Galloway for assisting with the AFM and MFM measurements performed at Leeds.

[‡] I would like to thank Rebecca Savage for assisting with the AFM and MFM measurements performed at Sheffield.

2.5.7 Friction Force Microscopy (FFM)[*]

Friction force microscopy (FFM) is a variation of AFM derived from contact mode imaging, which measures frictional forces on surfaces [172]. In this case an AFM probe is brought into repulsive contact with a sample surface, resulting in the bending of the cantilever that supports it. The tip is then scanned over the top of the surface, with lateral forces acting to deflect and twist the cantilever. Areas with a higher coefficient of friction cause greater deflections and twists on the cantilever, and this can be measured using the laser beam that is reflected off the back of the cantilever that is detected with a position-sensitive photodetector (as shown in Figure 2.5.4). Therefore, FFM is a useful approach for measuring surfaces with a lack of homogeneity in materials.

In this work Friction force microscopy images were acquired in air using a Bruker MultiMode 8 NanoScope V AFM following a method adapted from the process described in Ul-Haq *et al.* [173]. The probes used for FFM were silicon nitride probes (NP series, Bruker) with spring constant $k = 0.12$ N m^{-1}, and images were processed with WSxM software [171].

2.5.8 X-ray Diffraction (XRD)[†]

Since the pioneering work by the two Braggs, for which William Laurence and his father William Henry shared the 1915 Nobel Prize in Physics, X-ray diffraction (XRD) has been one of the most important techniques within the field of science, involving in some of the most significant and well-known discoveries [174].[‡] Powder X-ray diffraction works on the principle of the constructive interference of monochromated X-rays with a crystalline lattice. An X-ray beam striking a crystalline solid at an angle (θ) results in the production of secondary spherical waves through the atoms electrons [142]. In most directions, these waves will cancel out due to destructive interference. However, they will add *via* constructive interference in certain directions given by Bragg's Law [175]:

$$2d \sin \theta = n\lambda \qquad (2.5.1)$$

---

[*] All FFM was performed by Osama El-Zubir.
[†] I am grateful to Nik Reeves-Mclaren at the X-ray Diffraction Small Research Centre based at the University of Sheffield for his support in setting up XRD measurements.
[‡] Probably the most notable being the work done by Watson, Crick, Franklin and Wilkins who used XRD to determine the helical structure of DNA.

Where *d* is the crystal lattice spacing, *λ* the wavelength of the incident X-ray and *n* is the order (as shown in Figure 2.5.5 below).
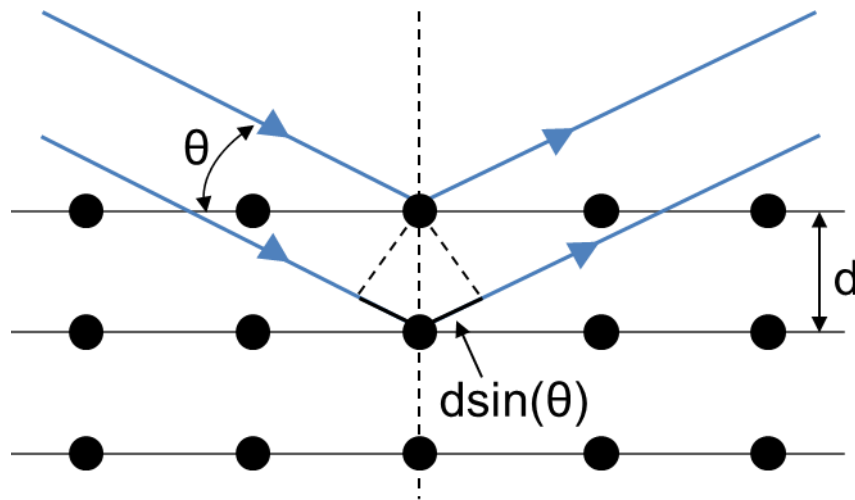
Figure 2.5.5 – An X-ray beam incident on a symmetrical plane of atoms will result in reradiated secondary waves adding constructively when their path-length difference (2dsinθ) is equal to an integer number of the incident wavelength (nλ).

Therefore a powder X-ray diffractometer records the intensity of the secondary reflected waves over a range of angles, either by rotating the specimen and detector while keeping the incident beam fixed or by keeping the specimen fixed while rotating the detector and the incident beam [142]. Crystallographic planes produce characteristic peaks in the recorded spectrum at precise angles, which can be converted back to a *d*-spacing with the use of equation 2.5.1. The full spectrum can then be compared to a database to identify the sample.

Biomineralised MNP surfaces were analysed with XRD using a Siemens D5000 diffractometer in reflection mode. X-rays were generated at 40 kV and 40 mA using a Cu Kα source (average *λ* = 1.54178 Å). X-rays were directed onto surfaces that were mounted on non-elastic Apiezon Q Sealing Compound putty in glancing angle geometry, taking special care to ensure that only the sample would be exposed to the X-rays and not the putty. X-ray intensities were then collected between $2\theta = 15°$ and 70° with a position sensitive detector (in 0.025° steps and 2.5 seconds per step).

MNPs that formed from the bulk solution during mineralisation reactions were dried and mixed with Elmer's glue onto acetate disks, and loaded into a STOE STADI P diffractometer. X-rays were generated at 40 keV and 35 mA using a Cu Kα1 source, with X-ray intensities collected between $2\theta = 15°$ and 70° (in 0.03° steps and 2.5 seconds per step). Data

analysis was performed with Diffrac.Plus TOPAS software, and compared to *d*-spacings in the JCPDS crystallographic database [176].

The grain size of the MNPs analysed with XRD was calculated with the use of the Debye-Scherrer Equation [177]:

$$D = \frac{k\lambda}{\beta \cos\theta} \qquad (2.5.2)$$

Where *D* is the grainsize, *k* is the shape constant (0.89), and β the full width half maximum (FWHM) of the peak at the angle of θ in radians. In the case of MNPs of magnetite and cobalt-doped magnetite, this analysis was performed on the dominant 311 peak for magnetite (at *2θ* = 35.75˚) [176].

2.5.9 Vibrating Sample Magnetometry (VSM)

Vibrating sample magnetometry (VSM) is a technique that can record the magnetic properties of a sample, as a function of an applied field, temperature and/or time [142]. As such, a VSM can be used to record the magnetisation of a magnetic sample as a function of an applied magnetising field. In a typical set up, a sample is placed into a uniform magnetising field. If the sample is magnetic, this field will magnetise the sample, with stronger fields inducing a larger magnetisation. VSM records the magnetisation of the sample through the use of Faraday's law of induction, by vibrating the sample perpendicular to the applied field and next to a set of pick up coils [142]. If the sample is magnetised, its magnetic moment will generate a magnetic field.[*] As the sample is vibrated, this alternating magnetic field generates an electric field in the pick-up coils that is proportional to the magnetic moment of the sample. By recording the magnetic moment of the sample over a range of applied magnetising fields, a magnetic hysteresis loop can be constructed for a sample material.

---

[*] Also known as the magnetic stray field.
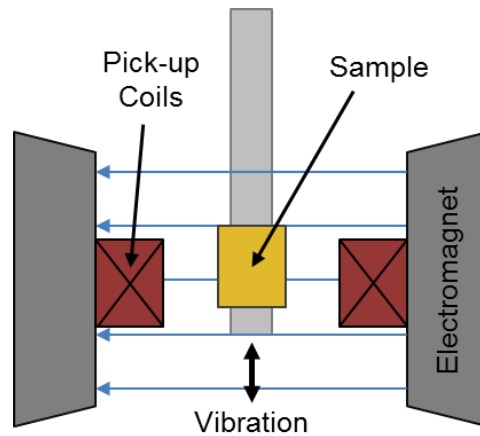
Figure 2.5.6 – Schematic of a VSM. The magnetisation of a sample (yellow box) is recorded by vibrating it next to a set of pick-up coils (red boxes), as the voltage induced in the coils is proportional to the magnetic moment of the sample. This magnetisation can be recorded over a range of different magnetising fields, applied with an electromagnet, to construct a magnetic hysteresis loop for the sample.

VSM was performed to characterise the bulk magnetic properties of the biomineralised MNP arrays, and of any bulk MNPs precipitated. Bulk MNPs were dried in a vacuum desiccator, before being weighed into a gelatine capsule. This capsule, or a biomineralised surface, was then mounted onto the end of a rigid carbon rod and loaded into an Oxford Instruments Maglab VSM. The samples were vibrated at 55 Hz, and the magnetic response of the samples was recorded over a field range of −10 to 10 kOe at 295 K (in the case of the biomineralised surfaces the magnetic response was recorded perpendicular to the sample surface).

2.5.9 Inductively Coupled Plasma Emission Spectrometry (ICP-ES)*

Inductively coupled plasma emission spectroscopy (ICP-ES) is a technique that uses a plasma source produced by electromagnetic induction to excite atoms and ions within a sample so that they emit electromagnetic radiation [142]. This radiation is dependent upon the emitting element, and analysis of this emitted radiation with the use of an optical spectrometer allows these elements to be determined [142]. ICP-ES is commonly used for the detection of metals and in this study was used to analyse the elements present in the MNPs produced.

---

* I would like to thank Neil Bramall for collecting all ICP-ES data.

Biomineralised MNP arrays formed on gold surfaces were washed in anaerobic Milli-Q water, dried in a nitrogen stream and dissolved in 2 mL of aqua regia (HCl 50% : HNO_3 50% v/v) under sonication for 30 minutes. This dissolves the biotemplated MNPs and the gold film, and the remaining glass surface can then be removed. 3 mL of Milli-Q water was added to the solution. Excess MNPs formed in solution during the mineralisation reactions were also dissolved in a 2 mL solution of aqua regia, and dissolved by sonication for 30 minutes. Again 3 mL of Mill-Q water was then added.

MNP solutions were analysed with ICP-ES, along with a blank reference solution (2 mL of aqua regia plus 3 mL of Milli-Q water that did not contain any dissolved nanoparticles). In the case of magnetite and cobalt-doped magnetite nanoparticles, the amount of iron and cobalt present in the MNPs solutions was quantified using a Spectro Ciros Vision ICP-ES. Iron and cobalt were measured at the 238.204 nm and 228.616 nm emission lines respectively, following calibration with suitable standards.

3. Magnetic Nanoparticle Arrays Biotemplated with the Biomineralisation Protein Mms6

"What I cannot create, I do not understand."

Richard Feynman

3.1 Overview: Creating Biotemplated Arrays of Magnetite MNPs

In this chapter the use of a cysteine-tag to attach Mms6 and its derivatives to gold surfaces is explored, as a route to developing simpler methods of synthesising biomineralised arrays of magnetite nanoparticles. When immobilised *via* its *N*-terminus to a PEG SAM containing carboxylic acid moieties, Mms6 was shown to biotemplate consistent magnetic nanoparticles of magnetite with a cubic-like morphology and a narrow size distribution onto gold surfaces [97, 98, 154]. Here, this approach is simplified through the engineering of Mms6 to contain an *N*-terminal cysteine (see Section 2.1.1). Micro-contact printing (μCP) is used to pattern a gold surface with a protein resistant PEG SAM, before the remaining space is backfilled with cysteine-tagged Mms6. In this case, Mms6 binds directly to the gold surface without the need for an attachment SAM, through the strong gold-cysteine interaction at the *N*-terminal region. Therefore, Mms6 should be orientated correctly to form an efficient biomineralising surface.

It also remains unclear whether Mms6 is able to bind to pre-formed MNPs of magnetite, or can only bind to magnetite MNPs through the nucleation of iron ions during a mineralisation reaction. If Mms6 binds strongly to magnetite MNPs, a MNP array could be formed by simply supplying an Mms6 patterned surface with pre-formed magnetite nanoparticles. As a result, the surfaces and the protein would not have to be subjected to a mineralisation reaction. Therefore, the feasibility of this approach is also assessed in this chapter. Gold surfaces patterned with Mms6 were placed into a solution of magnetite nanoparticles, which were pre-made in a POFHK reaction, with gentle mixing.

In addition, short peptide sequences based on Mms6 have also been shown to exert some degree of control over the formation of magnetite MNPs [96]. A synthetic peptide has the advantages of being cheaper and easier to produce than a full-length protein, which would make this process more scalable. Therefore, a peptide sequence based on the *C*-terminal region of Mms6 (see Section 2.1.2, hereby referred to as Mms6$_{Peptide}$) was patterned in the same way as the full Mms6 protein and subjected to the same two schemes (placed into a mineralisation reaction and supplied with pre-formed magnetite MNPs) to form arrays of MNPs of magnetite. These schemes are summarised in Figure 3.1.1, and this chapter compares the use of these two different schemes with the full Mms6 protein and Mms6$_{Peptide}$.

This chapter begins by exploring a number of controls, before assessing the MNP arrays biotemplated by cysteine-tagged Mms6, when patterned onto gold surfaces and placed into a POFHK reaction, with a number of different characterisation techniques. The second part of this

chapter compares these results to MNP arrays generated by supplying Mms6 patterned surfaces with pre-formed MNPs and with the use of Mms6$_{Peptide}$, with the aim of establishing the simplest and most effective route to forming high quality arrays of biotemplated magnetite MNPs.
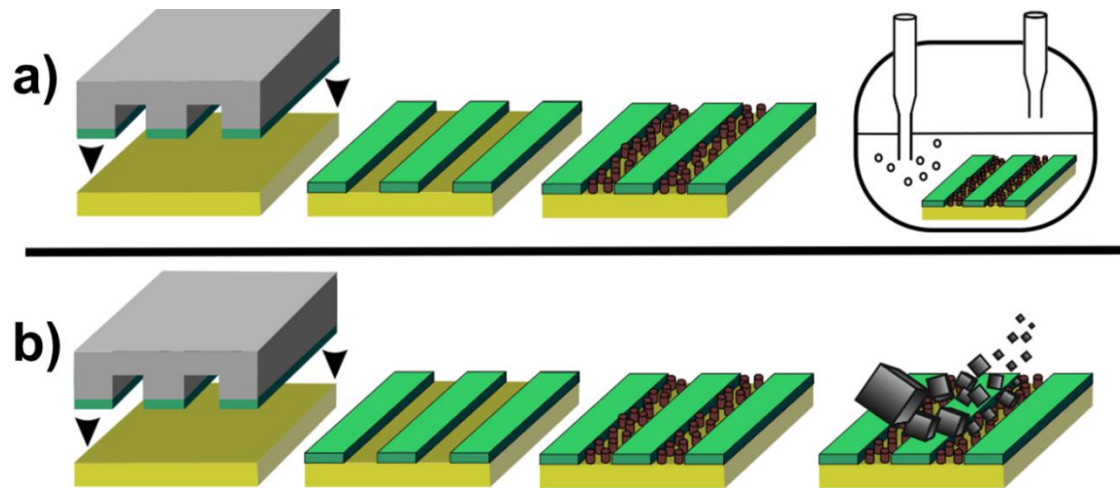
Figure 3.1.1 – Schematic of the experimental schemes. In both schemes a PEG SAM (green) is printed onto a gold surface with the use of µCP. The remaining space is then backfilled with cysteine-tagged Mms6 or Mms6$_{Peptide}$ (represented by brown cylinders). These patterned surfaces are then either subjected to a POFHK reaction (a), or pre-made MNPs of magnetite are washed over them (b).

3.2 MNP Synthesis with POFHK

MNPs were synthesised in a POFHK reaction, and these control particles were analysed with TEM (Figure 3.2.1a). Grainsize analysis was performed on ≈100 MNPs (Figure 3.2.1b), by measuring the longest and shortest axes of the projection of the MNPs in Image J. The aspect ratio of the MNPs was also determined by dividing the longest axis by the shortest axis of the MNP (Figure 3.2.1c). Both of these data were plotted in GraphPad Prism and fitted with a Gaussian distribution.

These analyses reveal that the nanoparticles formed in the POFHK reaction have broad distributions as regards to size and morphology, with a mean size of ≈60±21 nm. The majority of the nanoparticles were found to be synthesised in the 40-80 nm range, with many smaller particles and some much larger particles also forming. Larger acicular (needle shaped) structures can also be seen, these are unlikely to be magnetite (α-Fe$_3$O$_4$) as it does not usually form particles with an acicular morphology [16]. The reaction conditions were chosen to form the optimum conditions for the formation of magnetite, but it is more likely that these needles are another form of iron mineral that is able to form acicular crystals (such as maghemite (γ-Fe$_2$O$_3$) or goethite (α-FeOOH), which are the most likely iron minerals to have formed under the POFHK

reaction conditions) [16]. This is reflected in the aspect ratio recorded for the MNPs, which appears to result in two populations. As a result, two Gaussian distributions were fitted to these data, resulting in mean aspect ratios of 0.08±0.14 (long needle shaped particles) and 0.90±0.21 (more cubic shaped MNPs).
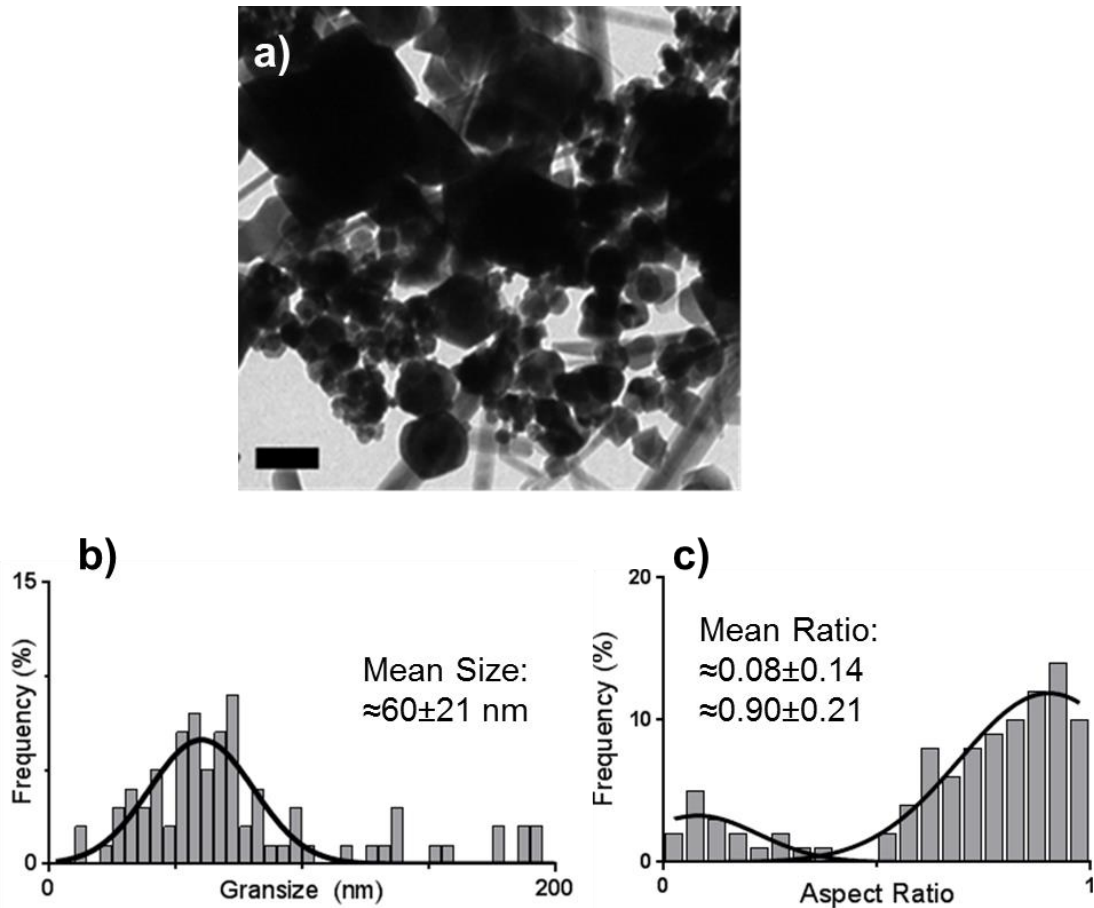
Figure 3.2.1 – TEM image (a, scale bar 100 nm), grainsize analysis (b) and aspect ratio (c) of MNPs formed during a POFHK reaction.

The results presented Figure 3.2.1 can be compared with the grainsize and aspect ratio measured for MNPs formed in six other separate POFHK reactions (Appendix 1), with the comparison revealing that the POFHK reaction performed consistently produces MNPs with a size distribution that is comparable to that shown in Figure 3.2.1 and a mean size around 60 nm. The measured aspect ratio also produced two distinct populations in every case, suggesting that the needle shaped nanoparticles seen in Figure 3.2.1a are also formed consistently.

Crystallographic analysis of the MNPs synthesised with a POFHK reaction was performed using XRD (Figure 3.2.2), and the position of the peaks were converted to interplanar distances (*d*-spacings) using Equation 2.5.1 (Table 3.2.1). The MNP samples were compared to the known values (from the JCPDS crystallographic database) for magnetite, maghemite (that has as a very

similar crystal structure to magnetite) and goethite. The XRD data (Figure 3.2.2) shows peaks at 2θ = 30.09°, 35.45°, 36.98°, 43.11°, 53.46°, 56.98°, 62.57° and 74.00°, which are all a good fit to the *d*-spacings of magnetite: (220), (311), (222), (400), (422), (511), (440) and (533) respectively, and a better fit than for maghemite or goethite (Table 3.2.1). These data strongly support that the crystal structure of the majority of the nanoparticles formed is magnetite, and that these nanoparticles are stable against oxidation as there is no strong indication of maghemite or significant quantities of other oxidation products.
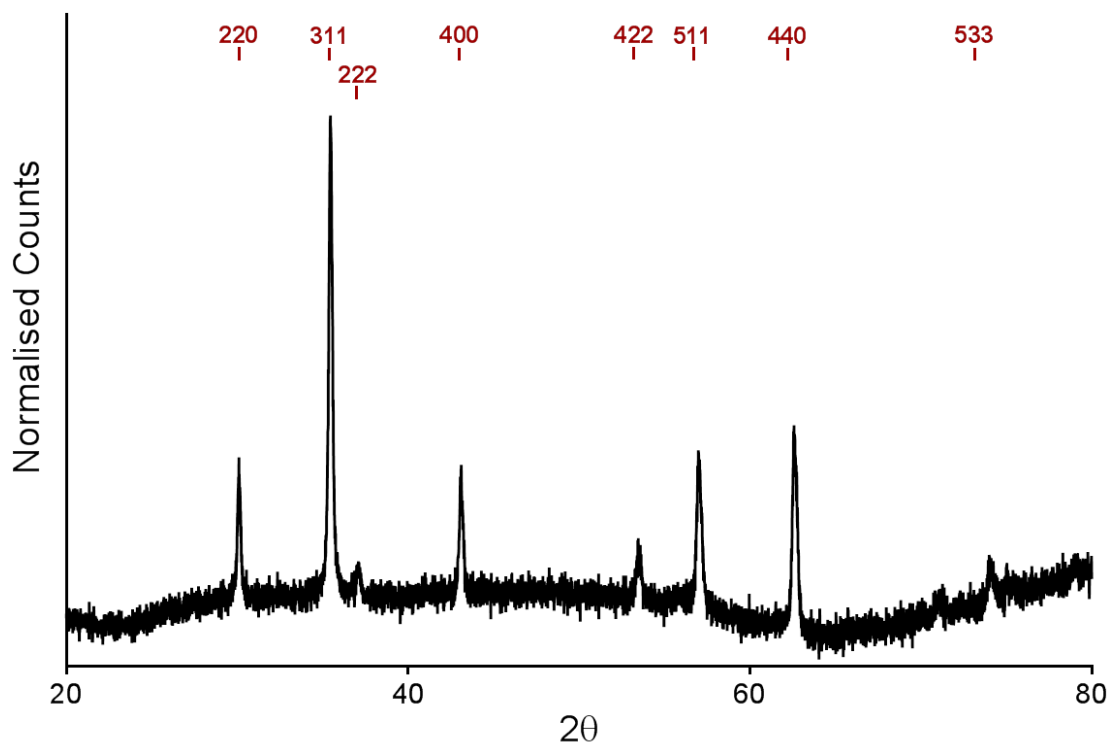
Figure 3.2.2 – XRD data of MNPs synthesised in a POFHK reaction. The expected peak positions for magnetite are highlighted.

Table 3.2.1 – Summary of the *d*-spacings for maghemite, goethite and magnetite, and the MNPs formed in a POFHK reaction shown in Figure 3.2.2 (all measured in Å). Maghemite values are from JCPDS card 00-039-1346, magnetite from 00-019-0629 and goethite from 01-081-0464. The value which is the closest match to the POFHK peak is highlighted in green, and only those plains on the JCPDS card that are the nearest to the peak are shown.

Peak	Maghemite	Magnetite	Goethite	POFHK
(220)	2.950	2.966		2.970
(130)			2.693	
(311)	2.520	2.530		2.532
(101)			2.527	
(111)			2.449	2.431
(222)	2.410	2.419		
(220)			2.190	2.098
(400)	2.080	2.096		
(221)			1.719	1.714

(422)	1.700	1.712		
(511)	1.610	1.614		1.616
(231)			1.603	
(440)	1.480	1.483		1.484
(241)			1.475	
(042)			1.292	1.281
(533)	1.270	1.279		

Based on the standard spectrum for magnetite and these XRD data, the (311) peak is the most intense and distinguishable. Therefore, this peak was fitted to the Debye-Scherrer equation (Equation 2.5.2) to estimate the grainsize of the particles [178]. This fitting suggests that the nanoparticles have a mean size of ≈32 nm, approximately half the value that is measured from the TEM images. However, the Debye-Scherrer analysis assumes that the particles are perfectly crystalline and have a narrow grainsize distribution [179]. The discrepancy between these two values may due to the nanoparticles actually having a broader size distribution, as can be seen in the TEM images shown in Figure 3.2.1. It may also be that these non-biotemplated control particles are not perfectly crystalline. Either of these reasons, or a combination of both, could lead to the Debye-Scherrer formula underestimating the particle sizes.

TEM analysis reveals that the MNPs form in a POFHK reaction with a large size distribution and a range of morphologies. However, it is anticipated that when surfaces patterned with the biotemplating biomolecules of Mms6 and Mms6$_{Peptide}$ were placed into this reaction, these biomolecules would control the growth of MNPs of magnetite on the surface. Similarly, when the surfaces patterned with Mms6 and Mms6$_{Peptide}$ were exposed to pre-formed MNPs, it is thought that these biomolecules may be able to selectively bind to a particular size or shape of MNP within the population. For example, this could take place if Mms6 selectively binds to a specific crystallographic face of magnetite, thus the Mms6 may be able to selectively bind to and filter out magnetite MNPs with certain properties. This would lead to MNPs with much more uniform properties being filtered out of the mixed control population onto the surfaces by binding to the immobilised biomolecule.

3.3 The Formation of Protein Resistant PEG SAMs

PEG SAMs are known to form an anti-biofouling surface [118], and have been used to resist the attachment of Mms6 to gold surfaces [97, 98, 154]. To be used successfully for the

formation of biomineralised MNP arrays, the PEG SAM surfaces are required to not only resist the attachment of biomolecules, but also not bind magnetite nanoparticles. MNPs of magnetite were found to bind to clean gold surfaces as shown in Figure 3.3.1, which displays the state of an unmodified gold surface after it was subjected to a POFHK reaction (as described in Chapter 2.4.1). Grainsize analysis of the particles formed shows that these MNPs have a similarly large size distribution to those formed from a bulk solution. However, they have a smaller mean size of 46±25 nm when compared to the MNPs that formed in the control POFHK reaction (Figure 3.2.1, mean size of 60±25 nm). This is a result of many smaller particles (<50 nm) being found to bind to the clean gold surface. The PEG SAMs used in this study have been shown previously (and in this study, Figure 3.3.2) to be stable in water, in a POFHK reaction [97, 98, 154], up to 80°C[*] and resistant to the binding of magnetite nanoparticles. Therefore, this protein resistant SAM forms an excellent mineralisation resistant background, and its patterning should allow the location of biomolecules such as Mms6 and Mms6$_{Peptide}$ to be controlled. These combined SAM-Mms6 surfaces can then be used to make biomineralised arrays of magnetite.
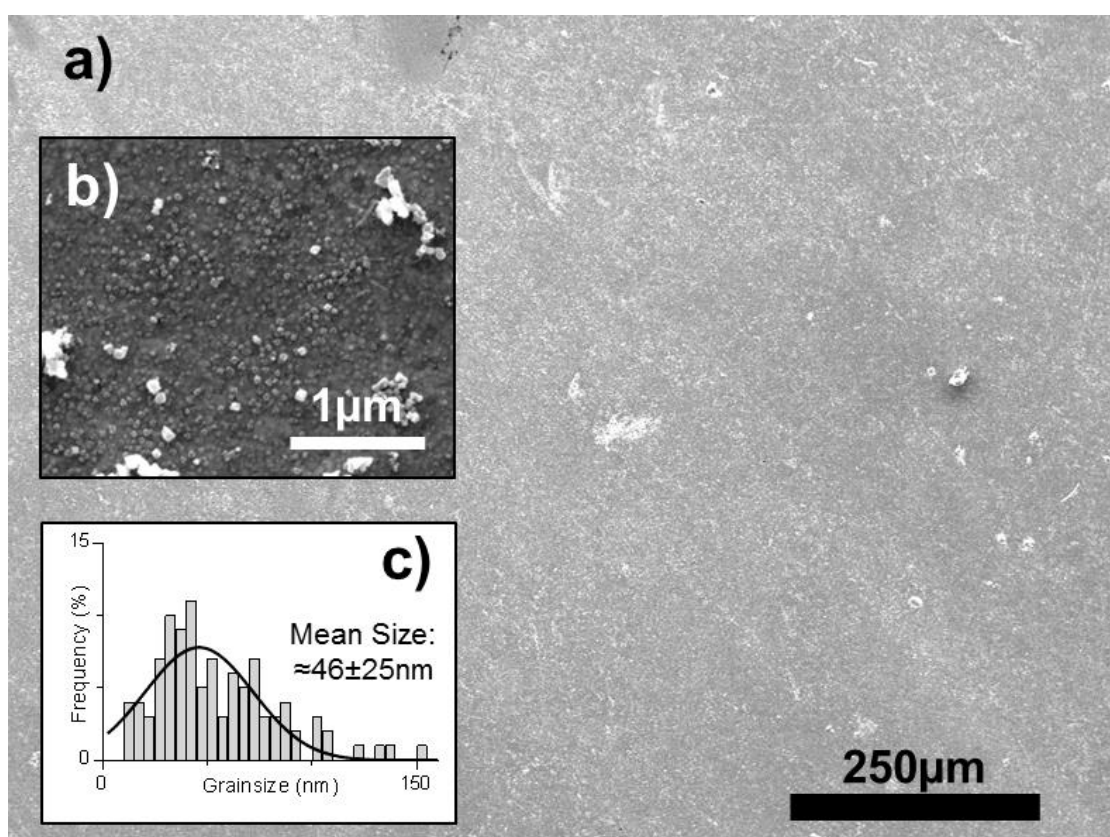
Figure 3.3.1 - SEM images (a and b) and grain size analysis (c) of a clean gold surface (which underwent no surface patterning) that was subject to a POFHK reaction.

---

[*] Section 3.3.1.3 p.126-129 of ref. [153].
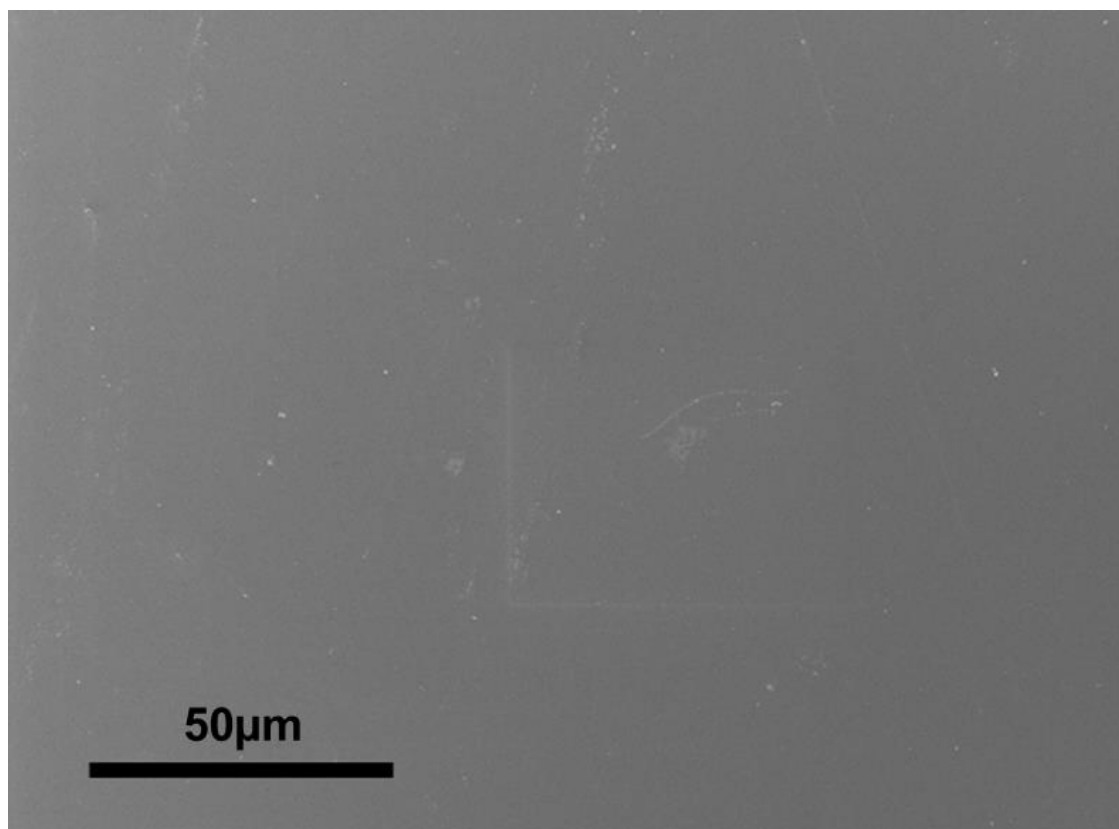
Figure 3.3.2 - SEM image of a gold surface completely covered in PEG (which underwent no surface patterning) that was subject to a POFHK reaction.

PEG SAMs were patterned onto gold surfaces *via* μCP with the use of PDMS stamps, as described in Section 2.2.3.4. However, it has been reported that this process can contaminate surfaces, this in turn could affect the final SAM layer and thus the attachment of the biomolecules [180]. Therefore, four SAM surfaces patterned with μCP were probed with SIMS (full experimental details are outlined in Section 2.2.3.5) to see if contamination by the PDMS stamp could be detected. These included surfaces that were patterned with PDMS stamps that; underwent no cleaning protocols, were soaked in ethanol, were soaked in ethanol and ozone cleaned, and a stamp that was a few months old. These surfaces were then backfilled with a fluorinated PEG-F SAM (for details see Section 2.2.3.5), which provides good contrast with the PEG SAM in a SIMS experiment as it contains fluorine.

Firstly, three control samples were analysed; a clean gold surface, a gold surface with a complete PEG layer and a gold surface with a complete PEG-F layer (Figure 3.3.1). This allowed for the peaks that were characteristic for the PEG SAM or PEG-F surfaces to be identified, so that these regions could be located when the surfaces containing both PEG and PEG-F were analysed. The peaks that were found to be the most characteristic for the PEG and PEG-F surfaces are labelled in Figure 3.3.3.
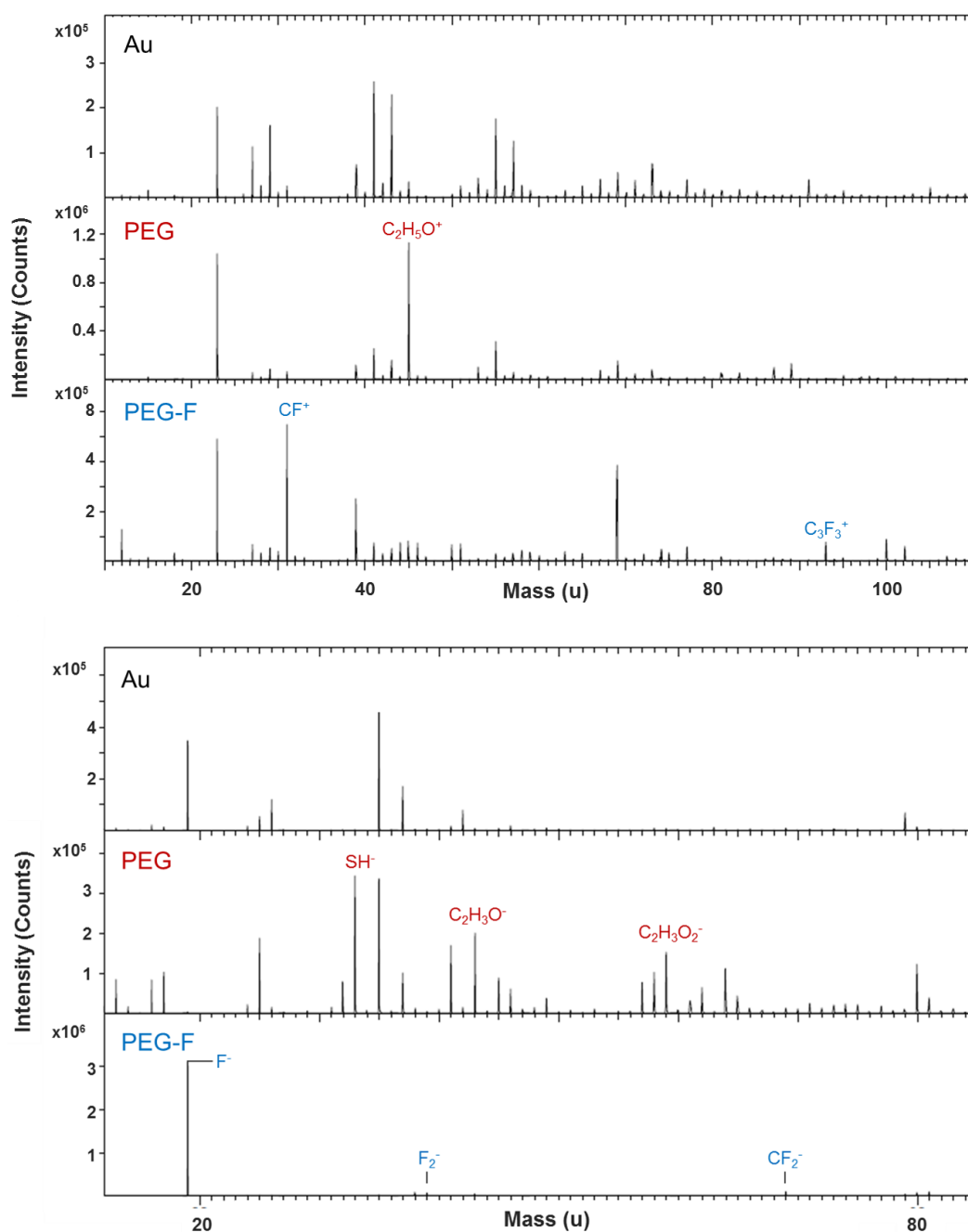
Figure 3.3.3[*] – Comparison on the positive (top) and negative (bottom) spectra of the three control samples in SIMS. Au – a clean gold substrate (Sample 1, Table 2.2.1), PEG – a complete PEG SAM on gold (Sample 2, Table 2.2.1) and PEG-F – a complete PEG-F SAM on gold (Sample 3, Table 2.2.1). Fragments that were found to be characteristic of samples 2 and 3 are labelled.

If PDMS had contaminated the gold surfaces during the µCP process, peaks that are characteristic for PDMS would appear in the spectra (with a strong signal in the negative spectra) [181]. Figure 3.3.4 displays both the positive and negative spectra for a gold surface that was stamped with a PDMS stamp that underwent no cleaning protocols (Sample 4, Table

---

[*] Data recorded by Claire Hurley at the Sheffield Surface Analysis Centre (SSAC).

2.2.1), with the location of the peaks characteristic for PDMS (*i.e.* silicon containing moieties such as siloxanes) labelled. As can be seen in Figure 3.3.4, significant levels of PDMS contamination are not observed. This is consistent with all of the recorded spectra, suggesting that even poly-dimethyl siloxane (PDMS) stamps that undergo no cleaning protocols do not significantly contaminate the gold surfaces with siloxanes when patterning PEG SAMs during µCP.
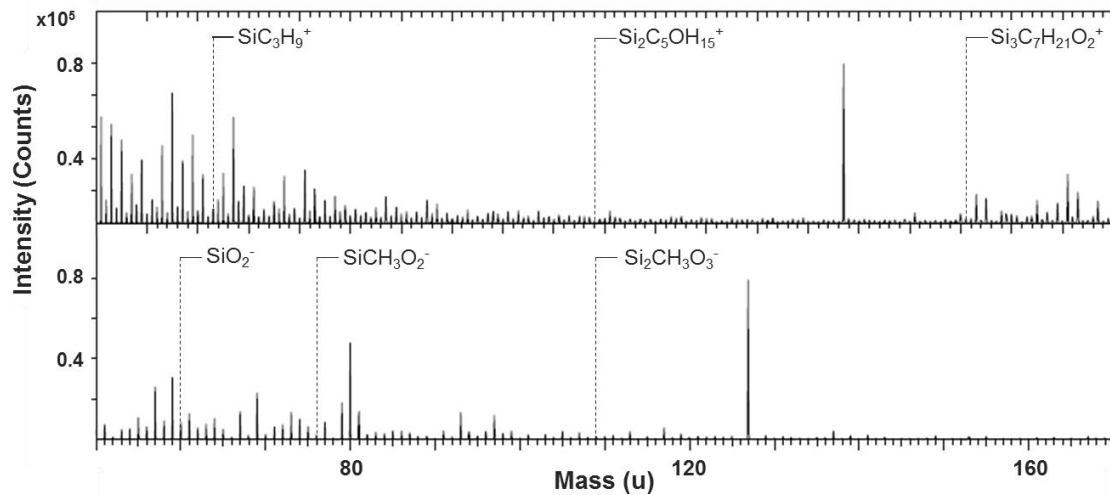
Figure 3.3.4[*] – Comparison of the positive (top) and negative (bottom) spectra of gold surrface µCP with PEG using a PDMS stamp that underwent no cleaning protocls, and was backfilled with PEG-F (Sample 4, Table 2.2.1).

Furthermore, peaks that were characteristic for PEG and PEG-F were used to map the location of these molecules in the samples that were patterned using the PDMS stamps. Figure 3.3.5 displays ion maps for the gold surface that were patterned with PEG *via* µCP with an uncleaned stamp (Sample 4, Table 2.2.1), which were again representative of all the samples imaged. It can clearly be seen in these images that PEG was successfully patterned onto the gold surfaces with microscale precision, forming a surface that is suitable for backfilling with PEG-F, and thus presumably also with biomolecules such as Mms6 and Mms6$_{Peptide}$.

---

[*] Data recorded by Claire Hurley at the Sheffield Surface Analysis Centre (SSAC).
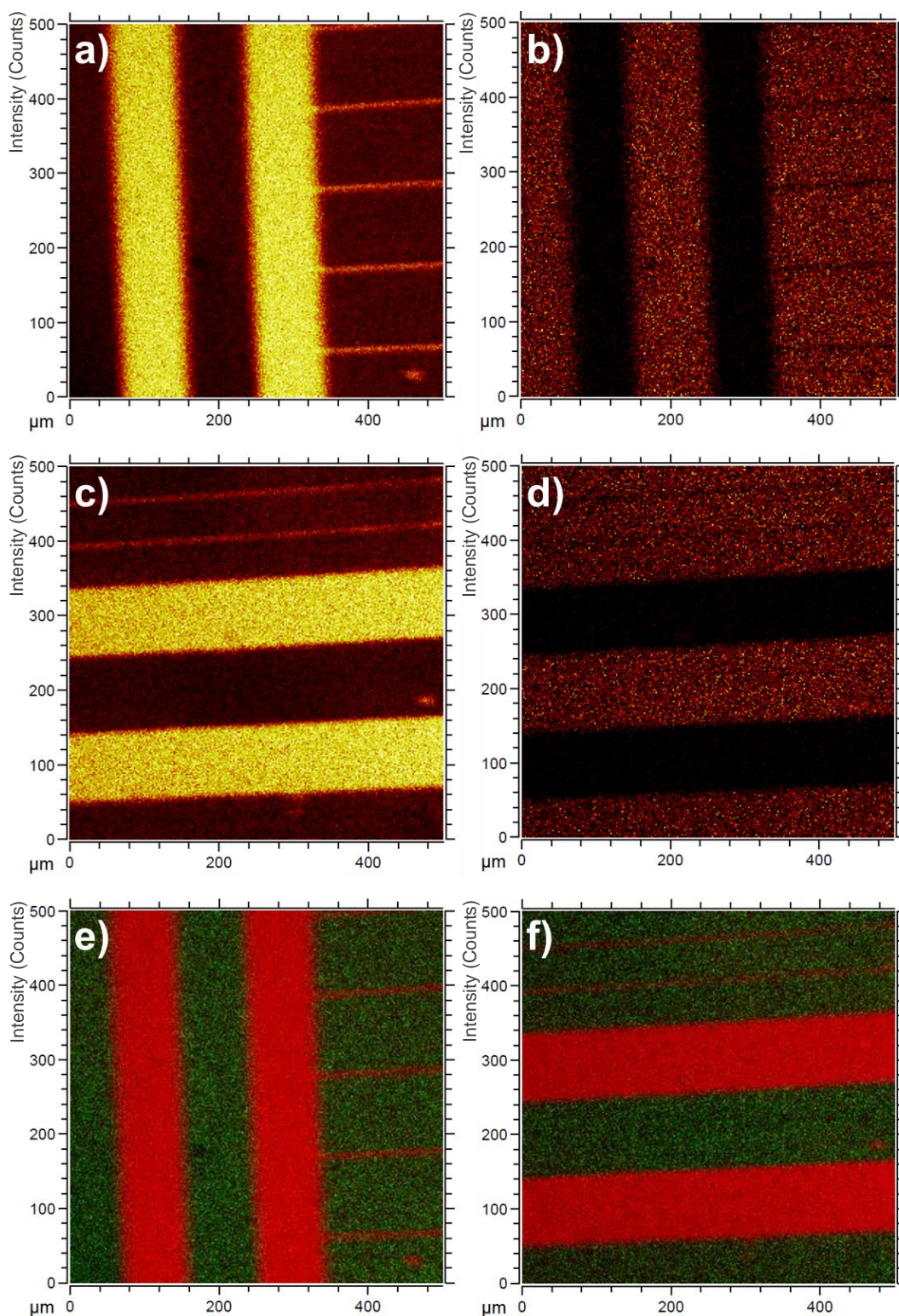
Figure 3.3.5[*] – Negative ion maps obtained for a gold surface μCP with PEG using PDMS stamps that underwent no cleaning protocols, and was backfilled with PEG-F (sample 4). Maps of fragments with an atomic mass of 19 (F⁻) (a and c), and with an atomic mass of 33 (SH⁻) (b and d). Overlay of maps a and b (e), and c and d (f).

---

[*] Data recorded by Claire Hurley at the Sheffield Surface Analysis Centre (SSAC).

3.5 Attachment of Cysteine-Tagged Mms6 and Mms6$_{Peptide}$ to Gold

If the cysteine-tagged biomolecules of Mms6 and Mms6$_{Peptide}$ are to be used effectively to biomineralise MNP arrays, it is vital that they form a correctly orientated and functional layer on a gold surface, and do not bind to the protein resistant PEG SAM. Therefore, the binding of both these biomolecules to clean and PEG coated gold crystals was monitored with QCM-D. Figure 3.5.1 displays the adsorption profile of the 7th overtone recorded with QCM-D when exposed to Milli-Q water, a PBS buffer containing 10 µg mL^{-1} solution of cysteine-tagged Mms6 for 1 hour, and finally back to Milli-Q water. It is immediately evident that there is a much greater frequency shift (Δf) for the clean gold crystal than the PEG coated crystal after application of the protein, corresponding to a greater adsorbed mass.
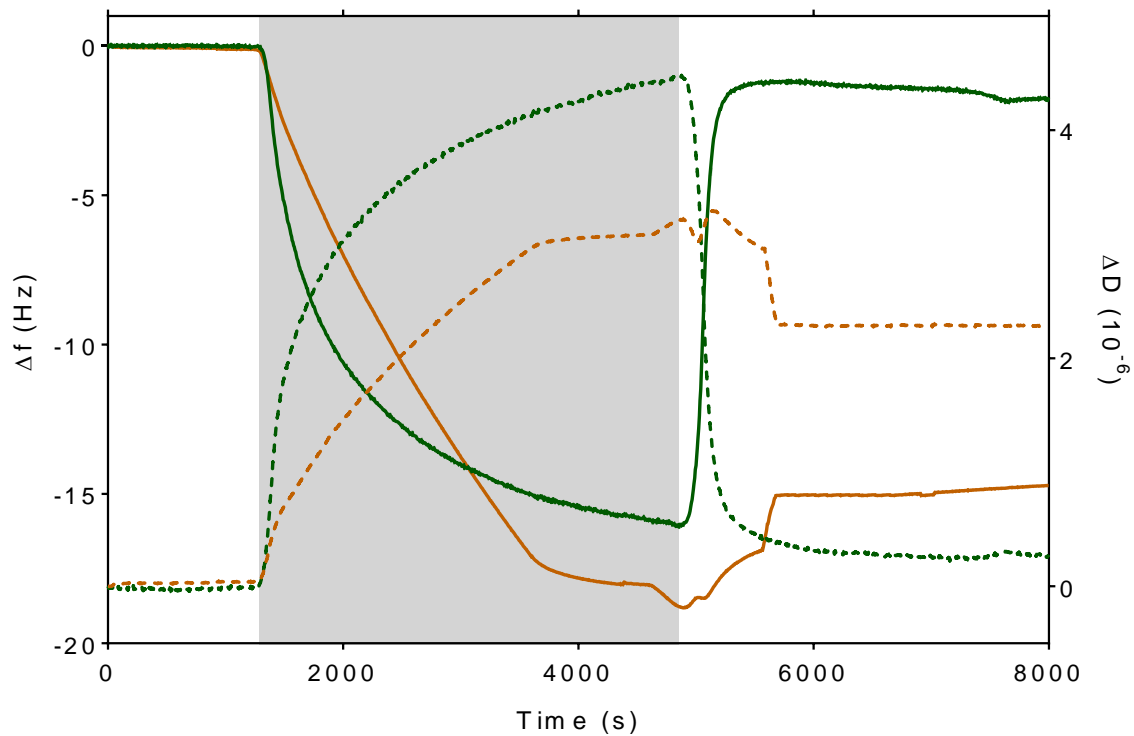
Figure 3.5.1 - Frequency (Δf, solid lines) and dissipation (ΔD, dotted lines) changes of the 7th overtone recorded with QCM-D during adsorption of cysteine-tagged Mms6 onto clean (gold) and PEG coated (green) gold coated quartz crystals. White regions show when a Milli-Q water was applied, and the grey region shows when a PBS buffer containing cys-Mms6 at a concentration of 10 µg mL^{-1} was applied (flow rate 50 µL min^{-1}).

The mass adsorbed onto the crystals was calculated through the use of the Sauerbrey equation (Equation 2.3.1) [182], and the Voight model [183] was applied to determine the viscoelastic properties of the adsorbed protein layer (Table 3.5.1). However, the Sauerbrey equation only provides a good estimate for the adsorption of rigid, thin and evenly distributed layers, and not for thicker adsorbed layers that act as a coupled resonator such as the Mms6 protein studied here [182]. Therefore, this model can only be used to provide an estimate of the

mass of the Mms6 protein that adsorbed onto the gold-coated QCM-D crystals. In addition, during the QCM-D experiment solvent may couple by direct hydration, drag or entrapment to the protein layer [182]. In reality it is more accurate to describe the adsorbed protein layer as a hydrogel. So in this study an estimate of the amount of the gold surface covered by the Mms6 protein was obtained by assuming a molecular weight of 11 kDa (including a 25% mass increase that takes into account the average water content of hydrated proteins [184]). Using a model of the Mms6 protein built on the Quark server [91], the length (33.66 Å) and width (20.27 Å) of the folded protein was also estimated. This allows an estimate of the molecular coverage of a complete layer of the protein on the gold surface (ideally bound *via* its *N*-terminal cysteine to the gold surface so that its *C*-terminus points directly away from the surface) to be calculated, which corresponds to approximately 24 pmol cm^{-2} (summarised in Table 3.5.1 below).

Table 3.5.1 - Mass coverage and viscoelastic properties of cys-Mms6 adsorbed onto the clean and PEG coated gold QCM-D crystals.

Sauerbrey Values	Clean Gold Crystal	PEG Coated Crystal
Mass (ng cm^{-2})	258	30
Coverage (pmol cm^{-2})	23	3
Complete Monolayer (pmol cm^{-2})	≈24	≈24
Coverage (%)	≈96	≈13
Voight Values		
Viscosity (kg m^{-1} s^{-1})	0.0015	—
Shear (MPa)	2.2	—
Thickness (nm)	2.8	—

These data displayed in Table 3.5.1 suggest that the protein layer that formed was approximately 96% of the thickness expected for a full monolayer of hydrated cys-Mms6 on the clean gold quartz crystals, with only 13% of monolayer thickness seen on the gold crystals protected by a PEG SAM. Voight modelling shows the protein adsorbs onto the gold surface to form a layer with a thickness of 2.8 nm, which again fits well with what is expected if the model produced on the Quark server is assumed to be correct. It should be noted that the Voight model is based on a number of assumptions, and many parameters can effect the accuracy of the model during a QCM-D experiment including; the viscosity and density of the buffer, the temperature and pressure, the electrode surface roughness and wettability and the topology, homogeneity and elasticity of the bound layer [183]. Therefore, these data can not be used to determine accurate values for the properties of the adsorbed protein layer, but overall suggests that the cysteine-tagged protein forms an almost complete monolayer on a gold surface (if

bound *via* its cysteine at the *N*-terminal region so that the *C*-terminal is exposed) that would be well suited for biomineralisation with only limited binding to the PEG SAM.

This experiment and analysis was repeated with Mms6$_{Peptide}$, with Figure 3.5.2 displaying the adsorption profile of the 7th overtone recorded with QCM-D, this time in a PBS buffer containing 10 µg mL^{-1} solution of Mms6$_{Peptide}$ for 1 hour. Once more there was a much greater frequency shift (Δf) when the peptide was exposed to the clean gold crystal when compared to the PEG SAM. The mass adsorbed onto the crystals and the Voight model were applied in the same way as described for the full Mms6 protein. The peptide itself was found to have limited structure when built on the Quark server [91]. Mms6$_{Peptide}$ was assumed to have a length, width and hydrated mass of approximately 10 Å, 20 Å and 2.6 kDa respectively, with complete molecular coverage calculated to be 84 pmol cm^{-2}.
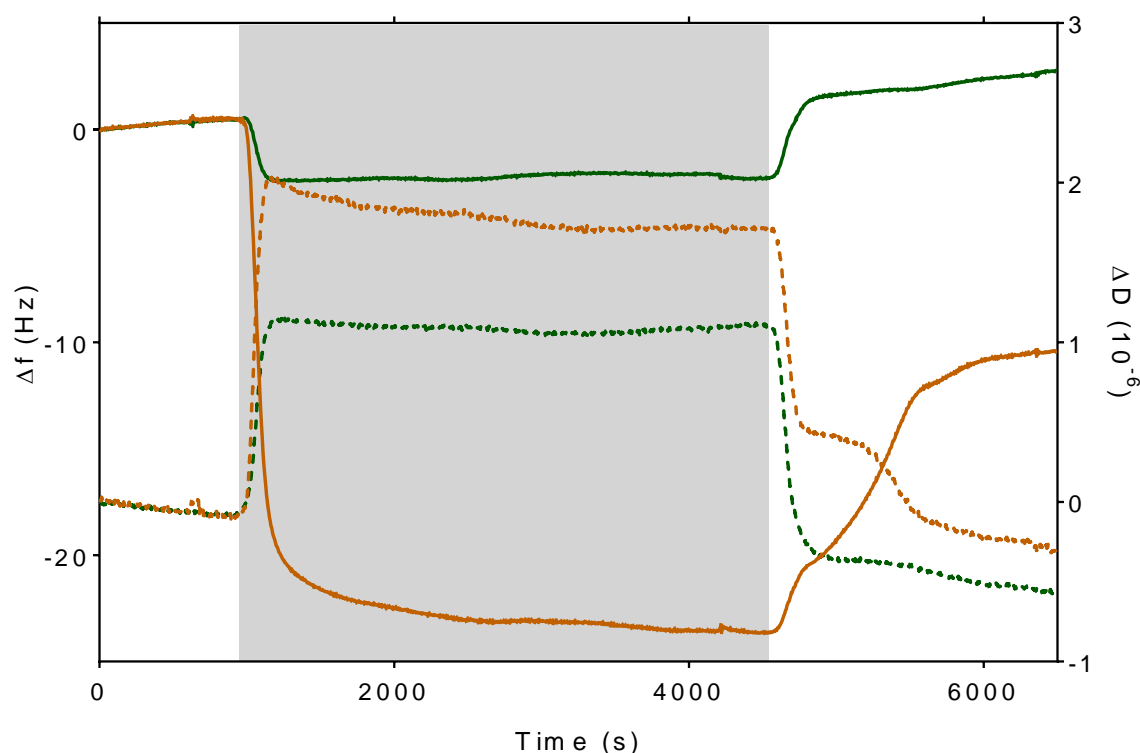
Figure 3.5.2 - Frequency (Δf, solid lines) and dissipation (ΔD, dotted lines) changes of the 7th overtone recorded with QCM-D during adsorption of Mms6$_{Peptide}$ onto clean (gold) and PEG coated (green) gold coated quartz crystals. White regions show when a Milli-Q water buffer was applied, and the grey region shows when a PBS buffer containing Mms6$_{Peptide}$ at a concentration of 10 µg mL^{-1} was applied (flow rate 50 µL min^{-1}).

Table 3.5.2 - Mass coverage and viscoelastic properties of Mms6$_{Peptide}$ adsorbed onto the clean and PEG coated gold QCM-D crystals.

Sauerbrey Values	Clean Gold Crystal	PEG Coated Crystal
Mass (ng cm^{-2})	182	-19.63
Coverage (pmol cm^{-2})	70	-7.55

Complete Monolayer (pmol cm^{-2})	≈83	≈83
Coverage (%)	≈84	≈-9
Voight Values		
Viscosity (kg m^{-1} s^{-1})	0.0012	—
Shear (MPa)	2.56	—
Thickness (nm)	8.6	—

The data displayed in Table 3.5.2 shows that the mass of the PEG coated crystals reduced after it was exposed to Mms6$_{Peptide}$. However, this is probably a result of frequency drift during the measurement process, and it can clearly be seen in Figure 3.5.2 that there is a gradual increase in the recorded frequency. Therefore it is far more likely that, as with the full Mms6 protein, there is only limited binding to the PEG SAM. Using the estimated length and width of Mms6$_{Peptide}$, ordered on the gold surface so that it is bound via its *N*-terminal cysteine and its *C*-terminus points directly away from the surface, these data suggest that the peptide forms with a thickness of approximately 84% of a full hydrated monolayer of Mms6$_{peptide}$ on the gold surface. This value is likely to also be reduced by the gradual increase seen in the recorded frequency, suggesting that Mms6$_{Peptide}$ forms an almost full thickness layer on gold.

Unlike the dissipation recorded after the full Mms6 protein bound to clean gold crystals in QCM-D (Figure 3.5.1), the dissipation recorded for Mms6$_{Peptide}$ returned back to the baseline value (Figure 3.5.2). This is consistent with other examples of small and rigid biopolymers, whose adsorption have been monitored with QCM-D [185]. The less rigid the adsorbed layer, the more it deforms on the vibrating surface. As a result, the coupled mass deviates more from the rest mass, leading to a greater dissipation value. Therefore, the larger Mms6 protein deforms more than the smaller, more rigid Mms6$_{Peptide}$ during the QCM-D experiment. In addition, Voight modelling suggests that the peptide forms a thick 8.6 nm layer on the gold crystals [183]. It is possible that the peptide is not structured in this way, and the model is not able to accurately fit the thickness of rigid peptide layer that was adsorbed onto the gold crystals [183]. The Mms6$_{Peptide}$ could be ≈8.4 nm if it is assumed that it forms one long linear chain.[*] When compared to the full Mms6 protein, which is predicted to fold so as to shield hydrophobic sections, the peptide is more likely to be unstructured. Hence, despite being a smaller subunit Mms6$_{Peptide}$ is more likely to form a linear deformable tethered chain when immobilised onto the gold surface and pack together more closely to form a thicker layer. It is also impossible to rule

---

[*] Average length of an amino acid assumed to be 3.5 Å.

out the fact that the peptide layer does not form in this way and could bind to gold the surface by lying flat, forming what could be described as a mesh network on the gold surface.

3.6 Formation of Biomineralised MNP Arrays with Cysteine-Tagged Mms6

Gold surfaces were patterned with a PEG SAM with the use of µCP, before being backfilled with cysteine-tagged Mms6 and placed into a POFHK reaction. When patterned and immobilised onto gold *via* an *N*-terminal cysteine, Mms6 biotemplates the formation of MNPs with narrow size distribution to form what appears to be a single layer, with negligible mineralisation on the PEG background (Figure 3.6.1). Consistent patterns of biomineralised nanoparticles were formed over wide areas, with feature sizes on the limit of what is achievable with µCP using conventional s-PDMS stamps (<1 µm, Section 2.2.3.4). Biotemplated arrays containing features with nanoscale dimensions (such as the ≈500 nm wide lines shown in Figure 3.6.1d) were occasionally produced, but these were only ever seen to form over small areas and could not be routinely reproduced. Therefore, these are probably a result of fortunate deformations of the PDMS stamp during is manufacture or the µCP process, or the stamp not contacting the surface uniformly.

Grainsize analysis shows that the MNPs that are biotemplated onto the surface by Mms6 (Figure 3.6.1f) have a larger mean size and smaller size distribution (≈87±18 nm) than those that form in the control POFHK reaction (Figure 3.2.1b, ≈60±21 nm). From the SEM images, the MNPs biotemplated by Mms6 on the surface also all appear to have a cubic-like morphology, and large numbers of long needle shaped particles are not seen. This is reflected in the aspect ratio recorded for the particles that were grainsized (Figure 3.6.1g). In this case, this dual distribution is not observed as was seen from the control particles (Figure 3.2.1c). This suggests that acicular iron oxide impurities were not formed by the surface immobilised Mms6 protein, which is able to biotemplate the formation of more equidimensional MNPs. Overall, these data suggests that Mms6 not only initiates MNP growth on the surface and anchors these MNPs onto the gold surface, but also has a strong effect on increasing the size and narrowing the size distribution of the MNPs.
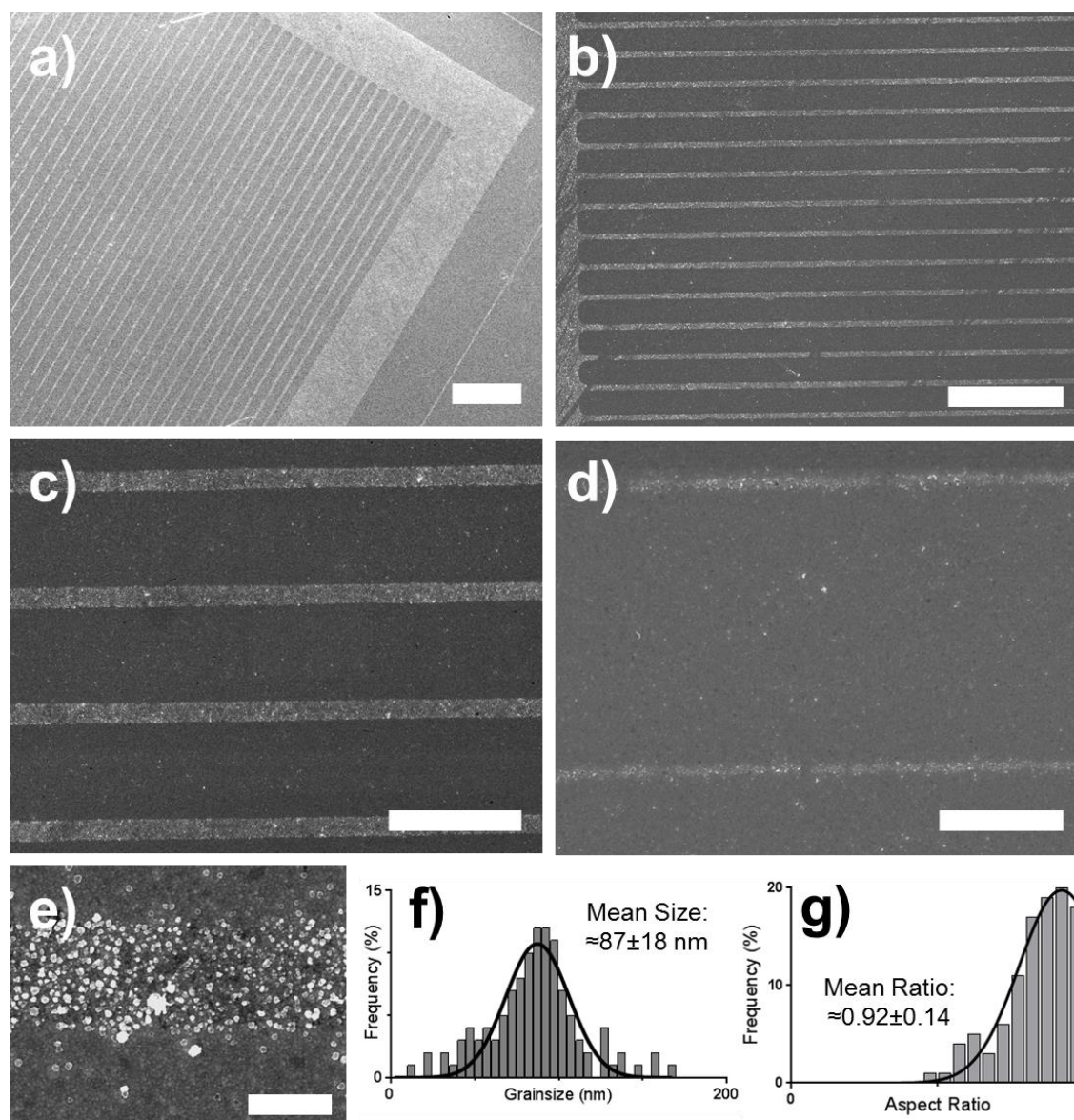
Figure 3.6.1 – SEM images (a – e), grainsize analysis (f) and aspect ratio (g) of MNP arrays formed on Mms6 surfaces patterned by µCP after a POFHK reaction. Scale bars: a – 100 µm, b – 50 µm, c – 25 µm, d – 5 µm and e – 2.5 µm.

In the work done previously, arrays of magnetite MNPs were biotemplated onto gold surfaces by Mms6 that was immobilised by its *N*-terminal region to a SAM containing carboxylic acid residues, after activation by EDC and NHS [97, 98, 154]. This aimed to correctly orientate the protein so that the *C*-terminal region was exposed for efficient biomineralisation, and space the protein from the gold surface. However, the SEM analysis shown here (Figure 3.6.1) suggests that the immobilisation of Mms6 directly to gold *via* an *N*-terminal sulphur did not adversely affect the functionality of the immobilised Mms6 protein. Highly uniform MNPs are biotemplated on the protein patterned regions, with only negligible mineralisation on the PEG background. This removes the need for the attachment SAM, resulting in the loss of a step that simplifies synthesis of biotemplated MNP arrays.

3.6.1 Chemical Composition

Evidence for the presence of magnetite on the regions patterned with Mms6 was confirmed with EDXA. Figure 3.6.2 displays two spectra obtained for different areas on the biomineralised arrays; one on the antibiofouling PEG background, and one on a dense region of particles that formed on an area patterned with Mms6. As expected, peaks corresponding to gold (e.g. Au Mα_1 at 2.142 keV), silicon (Si Kα at 1.740 keV) from the substrate, and carbon from the SAM and/or protein (C Kα at 0.277 keV) can be seen in both spectra. Excitingly, peaks for iron (FeLα at 0.705 keV) and oxygen (O Kα at 0.525 keV) only appear in the spectrum recorded from the particles formed on the protein patterned region. This can be seen more clearly in an EDXA map (Figure 3.6.3), which show significantly higher levels of iron and oxygen were detected on areas that are biomineralised.
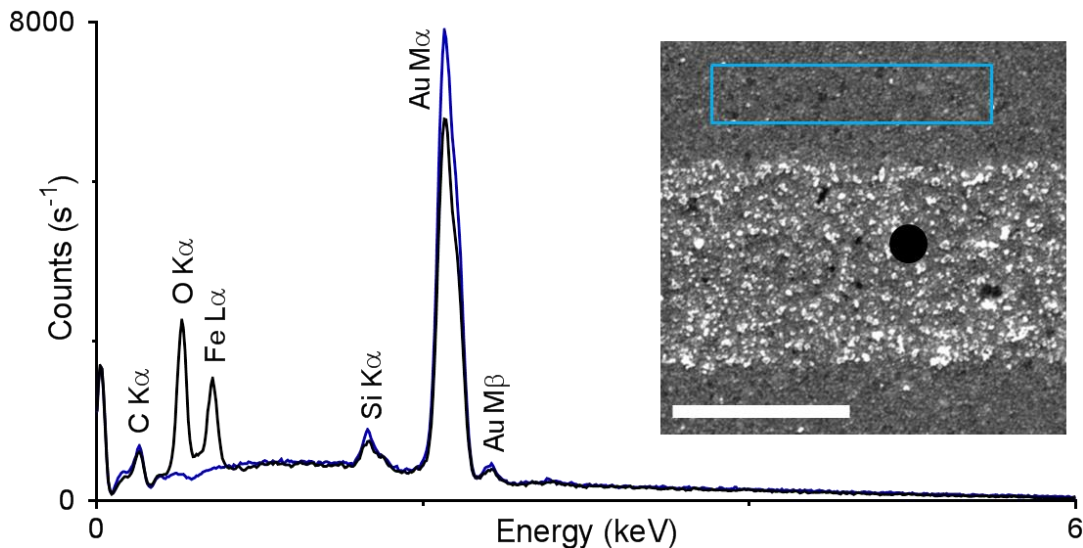
Figure 3.6.2 - EDXA spectra and corresponding SEM image (scale bar 1 μm) of nanoparticles biotemplated by Mms6 onto gold during a POFHK reaction. X-rays were collected over the wide anti-biofouling PEG SAM background area marked by the blue box on the SEM image (blue spectrum), and where a dense region of particles formed indicated by the black circle (black spectrum).
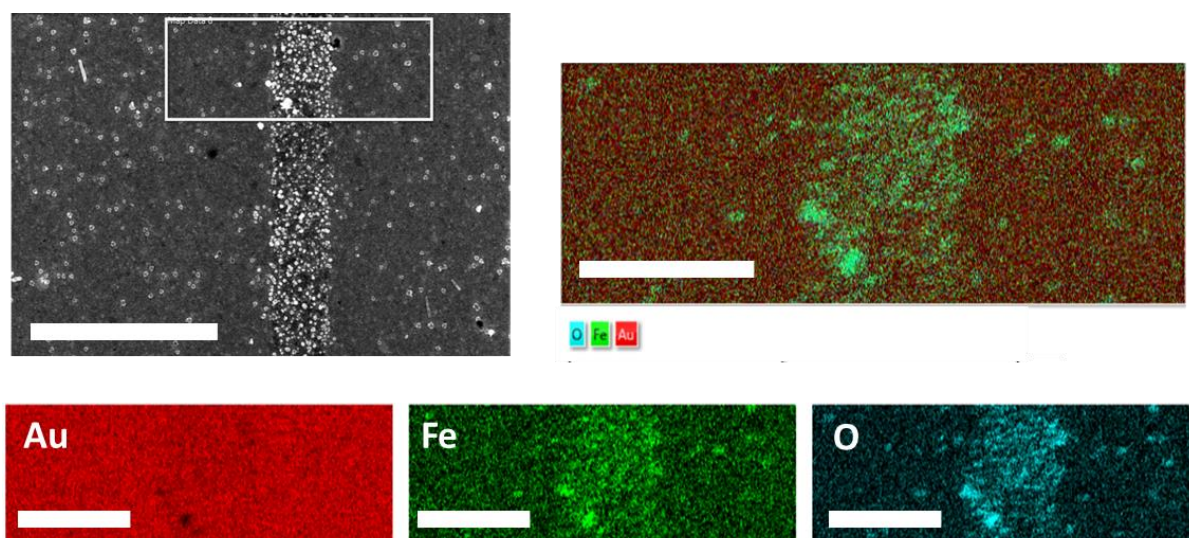
Figure 3.6.3 - SEM image and corresponding EDXA maps of gold (red), iron (green), oxygen (blue) and these maps overlaid (top right) of magnetite nanoparticles biotemplated by Mms6 onto gold during a POFHK reaction. Scale bars: SEM image 5 µm, EDXA maps 2 µm.

3.6.1 Crystallographic Analysis

Crystallographic analysis of the biomineralised surfaces was performed using XRD (Figure 3.6.4), and the position of the peaks were converted to *d*-spacings (using Equation 2.5.1, Table 3.6.1). As described in Section 3.2 for the control sample of MNPs produced in a POFHK reaction, the XRD data recorded for the MNP arrays biotemplated by Mms6 was compared to the known values (from the JCPDS crystallographic data base) for maghemite and goethite as well as magnetite. The XRD data (Figure 3.6.4) shows peaks at 2θ = 30.15°, 35.50°, 43.10°, 53.50°, 57.00°, 62.60° and 74.05° which are all a closer fit to the magnetite (220), (311), (400), (422), (511), (440) and (533) peaks respectively than the peaks for maghemite (Table 3.6.1). The peaks which can be seen in Figure 3.6.1 at 2θ = 38.25°, 44.45° and 77.65° correspond to the Au (111), (200) and (311) reflections from the gold film onto which the Mms6 protein is patterned, with the (111) peak obscuring the (222) peak for magnetite. However, these data strongly suggest that it is magnetite that is biotemplated onto the gold surfaces by Mms6.

As with the XRD data for the MNPs formed in the control POFHK reaction (Section 3.2), the 311 peak was fitted to the Debye-Scherrer equation (Equation 2.5.2) to determine the grainsize of the particles [178]. This fitting found that MNPs formed on the surface with a mean size of ≈ 83 nm. Unlike the fitting discussed in Section 3.2 for the MNPs formed in a control POFHK reaction, this is a close fit to the ≈87±18 nm size obtained from SEM images. This closer

agreement in size could be a result of a tighter size distribution, coupled with better crystallinity, and lack of acicular MNPs that are biotemplated by the surface immobilised Mms6.
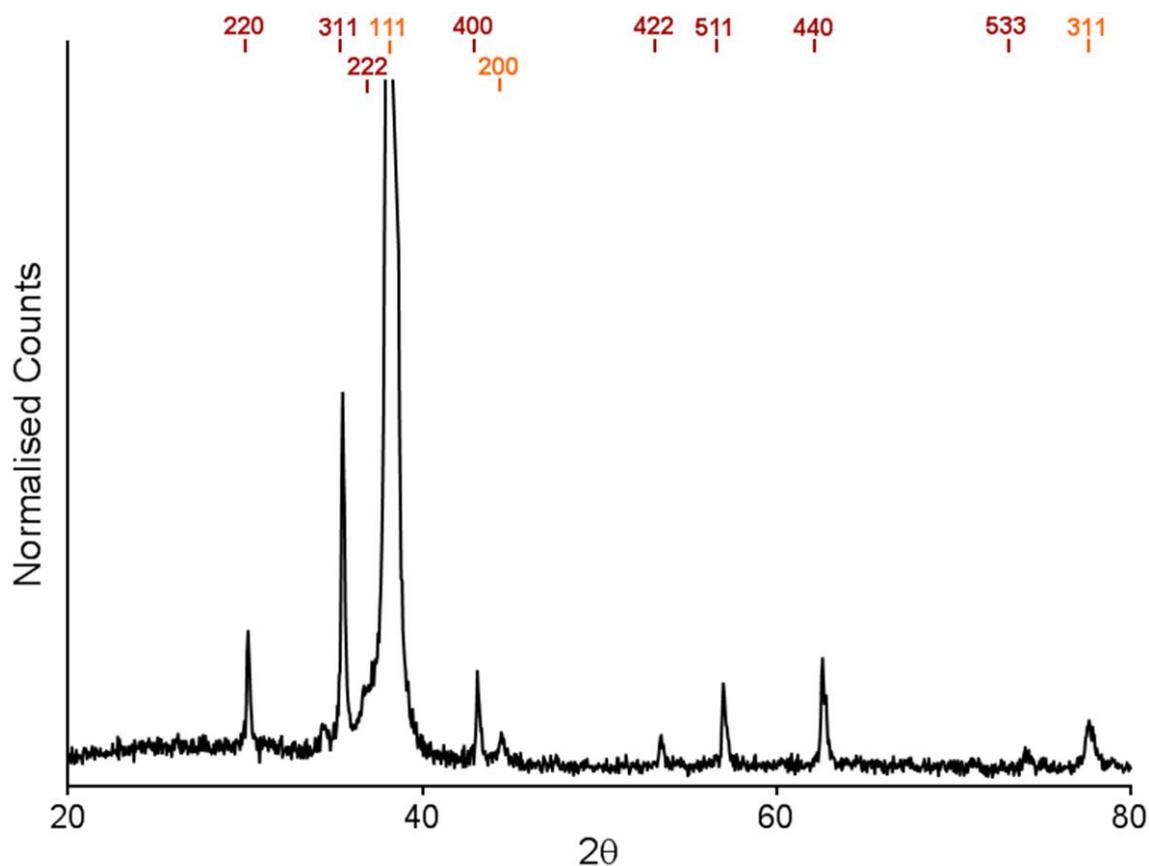
Figure 3.6.4 - XRD diagram of a biomineralised MNP surface, synthesised by Mms6 immobilised onto a gold surface *via* a POFHK reaction. The expected peak positions for magnetite (red) and gold (gold) are highlighted.

Table 3.6.1 - Summary of the d-spacings for maghemite, goethite and magnetite, and from the MNPs formed on an Mms6 patterned gold surface in a POFHK reaction shown in Figure 3.6.4 (all measured in Å). Maghemite values are from JCPDS card 00-039-1346, magnetite from 00-019-0629 and goethite from 01-081-0464. The value which is the closest match to the POFHK peak is highlighted in green, and only those plains on the JCPDS card that are the nearest to the peak are shown.

Peak	Maghemite	Magnetite	Goethite	Mms6 Surface
(220)	2.950	2.966		2.965
(130)			2.693	
(311)	2.520	2.530		2.529
(101)			2.527	
(111)			2.449	—*
(222)	2.410	2.419		
(220)			2.190	2.099
(400)	2.080	2.096		

---

* This peak is obscured by the dominant Au (111) peak.

(221)			1.719	1.713
(422)	1.700	1.712		1.713
(511)	1.610	1.614		1.616
(231)			1.603	1.616
(440)	1.480	1.483		1.484
(241)			1.475	1.484
(042)			1.292	1.280
(533)	1.270	1.279		1.280

3.6.3 Bulk Magnetic Properties of Biotemplated Magnetite from Vibrating Sample Magnetometry (VSM)

Many factors affect the magnetic properties of a MNP, including the type of material, and the size, the shape and crystallinity of the particles [27]. To be used successfully within technologies, the MNPs on the biomineralised MNP arrays are required to be highly uniform, which ensures that the magnetic response is also uniform. As the magnetisation of superparamagnetic nanoparticles is constantly thermally reordered, they could not be used within a magnetic HDD, as they would be unable to maintain their magnetisation and any stored data would be lost. Particles that are above the single domain size and form multi-domain particles have lower saturation magnetisation than single domain particles, as energy is lost in the creation of domain walls in multi-domain particles. Therefore, single domain magnetic nanoparticles are highly desirable for magnetic data storage.

As shown previously, Mms6 is seen to exert control over the magnetite nanoparticles that are biotemplated onto the gold surfaces, forming MNPs with a narrower size distribution and larger mean size than those that form in a control bulk POFHK reaction (Figure 3.2.1 and Figure 3.6.1). Below ≈85 nm, spherical magnetite nanoparticles are single domain, becoming superparamagnetic below ≈25 nm [186, 187]. The majority of the surface biotemplated particles are around the single to multi-domain boundary for magnetite (70-100 nm), with the number of smaller particles (<50 nm) being significantly reduced when compared to the control POFHK reaction. Relatively few nanoparticles formed on the surfaces in the superparamagnetic size range (<25 nm). Therefore, the surface biotemplated magnetite MNPs should be in the single domain size range for magnetite, and thus show single domain magnetic behaviour.

Figure 3.6.5 displays the hysteresis loops recorded for MNPs formed in a POFHK reaction and on a MNP array biomineralised by Mms6[*] at room temperature. The magnetisation of the loops was normalised, as the mass or volume of the MNPs that formed on the Mms6 patterned surface could not be quantified. So, although the saturation magnetisation for these two samples cannot be compared, the coercivities can. It can been seen in Figure 3.6.5 that both the MNPs that formed in solution and those on the biomineralised surface display a typical hysteresis loop expected for a soft ferrimagnetic material, with a uniform magnetic switching behaviour.
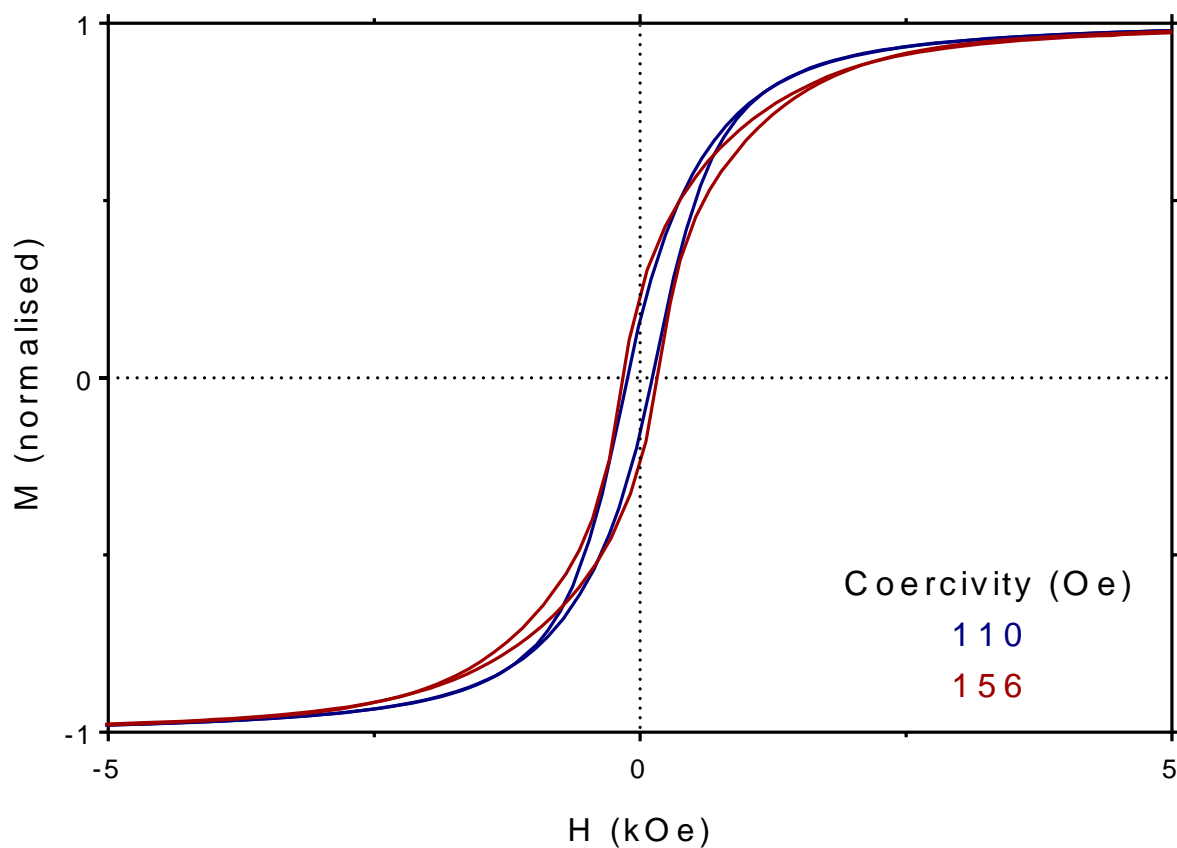
Figure 3.6.5[†] - Magnetic hysteresis loops were recorded using VSM at 295 K of the MNPs that form in a POFHK reaction (blue), and the MNPs biotemplated onto a gold surface by Mms6 (red).

Figure 3.7.5 shows that the coercivity of the particles that formed in solution during a POFHK reaction (black loop Figure 3.6.5) is 110 Oe at 295 K, which is within published values for magnetite nanoparticles [188]. However, the larger coercivity of 156 Oe recorded for the biotemplated surfaces at 295 K (blue loop Figure 3.7.5) is not [188]. It can also be seen that the

---

[*] A complete surface of Mms6 (without any PEG or patterning) was used to ensure a greater coverage of Mms6, and hence the formation an extensive layer of surface biotemplated MNPs maximising the signal.
[†] Data recorded by Johanna Galloway.

particles that formed in the bulk solution display a steeper slope, and hence have a more uniform switching behaviour. This could be a feature of the larger mean size of the MNPs that were biomineralised by Mms6 onto the surfaces when compared to those that formed in the control POFHK reaction. This larger size would result in a greater number of multi-domain particles, which (when coupled with the single domain and pseudo single domain particles) are likely to have a less uniform switching behaviour than seen for single domain particles. Furthermore, the densely packed arrays of MNPs that formed a planar assembly on the gold surfaces patterned with Mms6 could be exchanged coupled [26]. This may provide an explanation for not only the more gradual switching behaviour, but also the increased coercivity recorded.

Although the MNP array of magnetite biotemplated by Mms6 onto gold have many of the properties required for use as the recording medium within a magnetic HDD, unfortunately the coercivity of these surfaces is too low and are unsuitable for this technology. Current magnetic HDDs use a recording medium that have coercivities in the kOe range [41]. This ensures that the magnetic information written into the devices is stable and not easily reoriented, which is something that would result in the catastrophic loss of data. However, the coercivity recorded with VSM for the MNP arrays of magnetite biomineralised by Mms6 is much lower than this range. Even though the biotemplated MNP arrays of magnetite present a significant step towards developing a new bioinspired approach to data storage, ultimately magnetite is too magnetically soft to be used as the recording medium within a magnetic HDD. Any data stored on MNP array of magnetite that were biomineralised by Mms6 would be too prone to being lost due to the soft magnetic hysteresis of magnetite.

3.6.4 Magnetic Force Microscopy (MFM) of Surface Biotemplated Magnetite

Topographic images of the MNP arrays biomineralised by Mms6 were imaged with tapping mode AFM (Figure 3.6.6a). When a magnetised tip is used, this topography was then retraced at a specified lift height. Magnetic interactions between the tip and the surface cause the cantilever to deflect, allowing the nanomagnetic properties of the samples to be probed (Figure 3.6.6b-d). Attractive forces result in a negative shift in the phase of the cantilever, and repulsive forces in a positive shift. The magnitude of this phase shift is not only dependent on the strength and orientation of the magnetisation of the MNPs on the surface, but also many other factors including the strength of the magnetisation of the tip and the distance between the tip and the surface. This is shown in Figure 3.6.6b-d, where the magnitude of the recorded

phase shift reduces as the lift height is increased. It was not possible to quantify the magnetisation of the tip used to probe the biotemplated magnetite surfaces, so comparisons between different samples are purely qualitative.

Combined 3D plots displaying both the topographic information recorded with tapping mode AFM, and the MFM measurements in lift mode were rendered in 'R' (Figure 3.6.5e-g). In these images, positive phase shifts appear blue, with negative phase shifts appearing as red. As it can be seen in Figure 3.6.6 the same magnetic signal was recorded as the lift height was increased from 50-200 nm, with the magnitude of this signal reducing as the lift height increases and the magnetic tip is further from the sample surface. Therefore, a lift height of 50 nm was used during MFM measurements throughout this study, as this resulted in the strongest signal without the tip colliding with the surface. To further confirm that the cantilever deflections recorded during a lift scan was a result of magnetic interactions between a magnetised tip and the MNP surface, MFM measurements were performed in exactly the same way with a non-magnetic tip (TESPA-V2, Bruker). In this case even when a lift height of 50 nm the magnetic phase shift recorded was significantly reduced, and this is shown in the composite image rendered in 'R' (Figure 3.6.7). The phase shift recorded also appears to be the same on both the biotemplated MNPs and the PEG ground regions where no particles formed, suggesting that no magnetic information was recorded when a non-magnetic-tip was used.
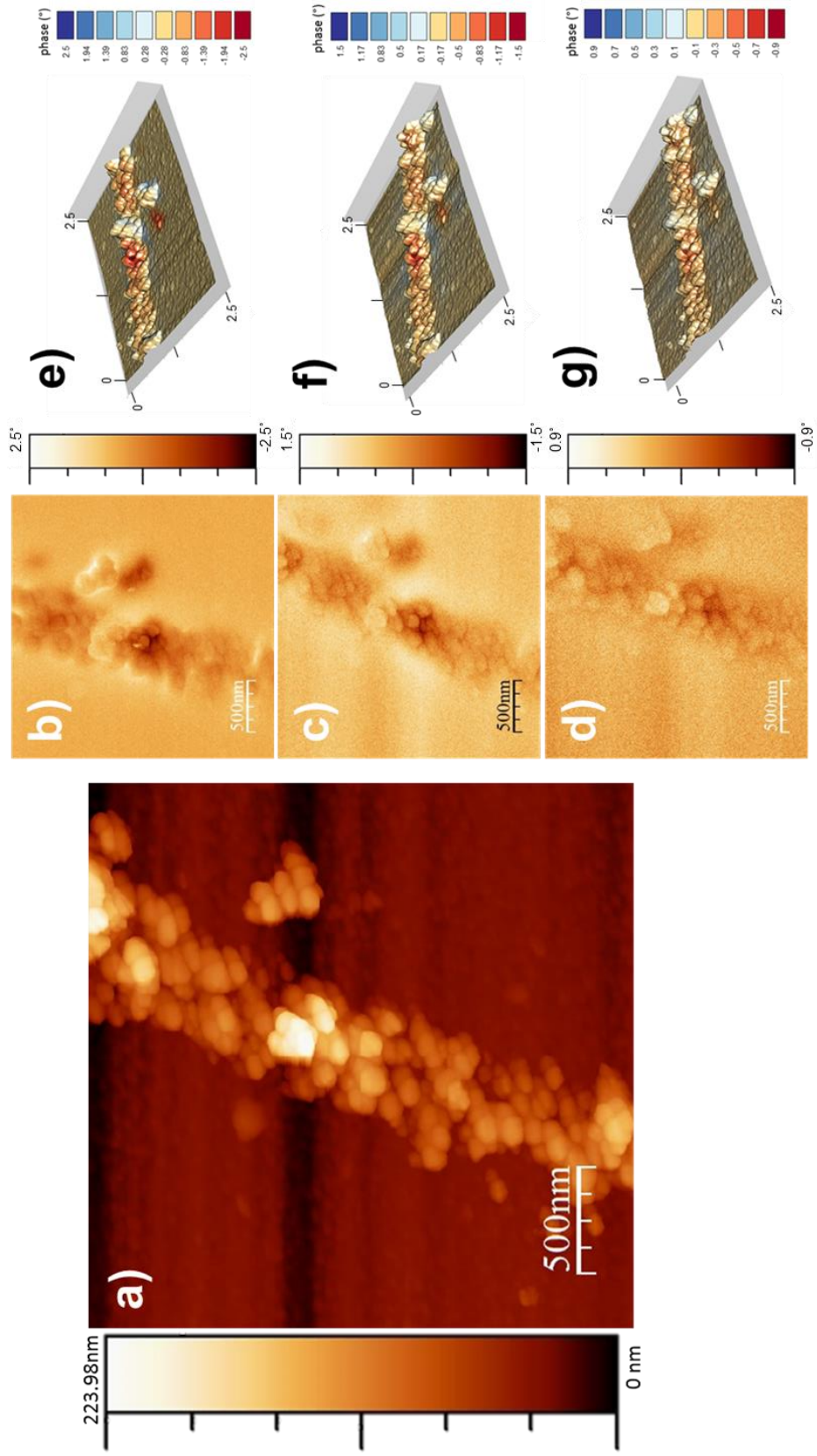
Figure 3.6.6 – Tapping mode AFM (a), lift mode MFM (b-d) and composite images rendered in 'R' (e-g) of a biomineralised MNP array. Light height of; 50 nm (b and e), 100 nm (c and f) and 200 nm (d and g). Scales in µm (e-g).
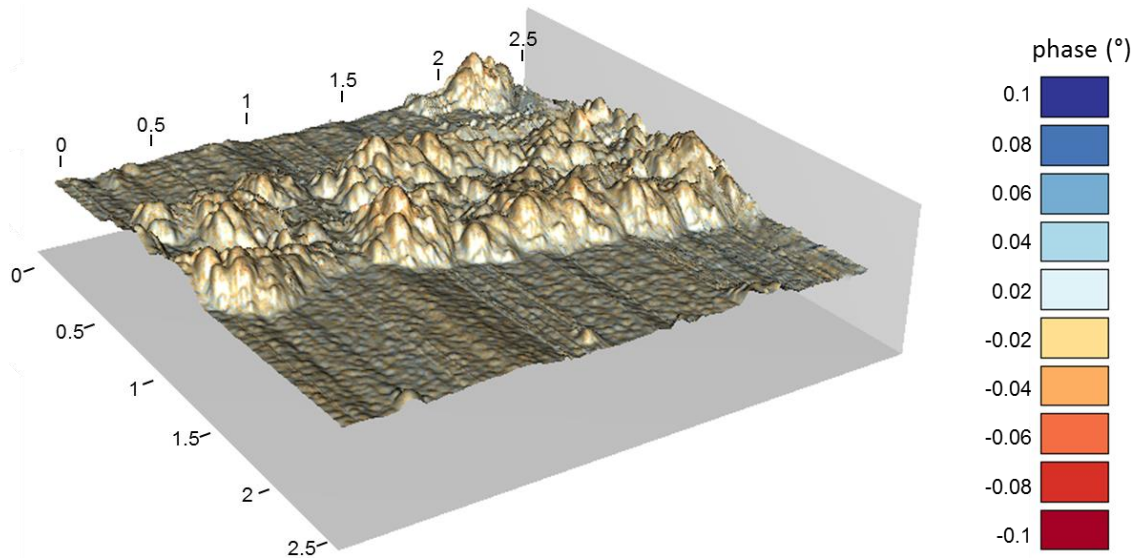
Figure 3.6.7 – Composite image of tapping AFM and MFM phase shift of a biomineralised MNP array at a lift height of 50 nm using a non-magnetic magnetic TESPA-V2 tip (Bruker). Scales in μm.

Figure 3.6.8 and Figure 3.6.9 display MFM plots of MNP arrays biomineralised onto gold surfaces by patterned and immobilised Mms6. Once more it is immediately evident that a layer of MNPs formed onto the protein patterned arrays, with minimal mineralisation on the PEG background. These MFM plots also show that zones of attraction and repulsion (red and blue areas respectively) are detected. These were also found to be stable and unchanging when the same area was recorded with a scan direction rotated by 90˚. As the MNPs maintain their magnetic orientation at room temperature, this suggests that they are ferrimagnetic at this temperature, and that the zones of attraction and repulsion are not altered by scanning the magnetised tip across the surface. This supports previous MFM measurements on MNP arrays biomineralised by Mms6 attached to gold *via* a SAM containing carboxylic acid moieties [97, 98, 154].

To be used successfully in technologies such as magnetic data storage, the biomineralised MNPs are required to be able to maintain their magnetic orientation long term, so that any stored data is not lost. Although the zones of attraction and repulsion recorded in these MFM studies show that they were stable as different scan directions were used, it was not possible to determine how long this stability was maintained. The stability of the magnetic orientation of the biomineralised nanoparticles could be tested by repeatedly recording the same area of the sample over a long period of time. However, it is incredibly difficult to locate the same area of the sample with absolute certainty using current AFM systems. The densely packed MNPs also make it difficult to probe the nanomagnetism of individual MNPs with MFM. For this to become possible, the magnetic complexity would have to be reduced. One way to do

this would be to pattern the biomolecule (e.g. Mms6) on the nanoscale to try and biotemplate individual MNPs. Nanoscale patterning of biomolecules would also be desirable to enable the development of biotemplated MNP arrays to be used to form bit-patterned media.
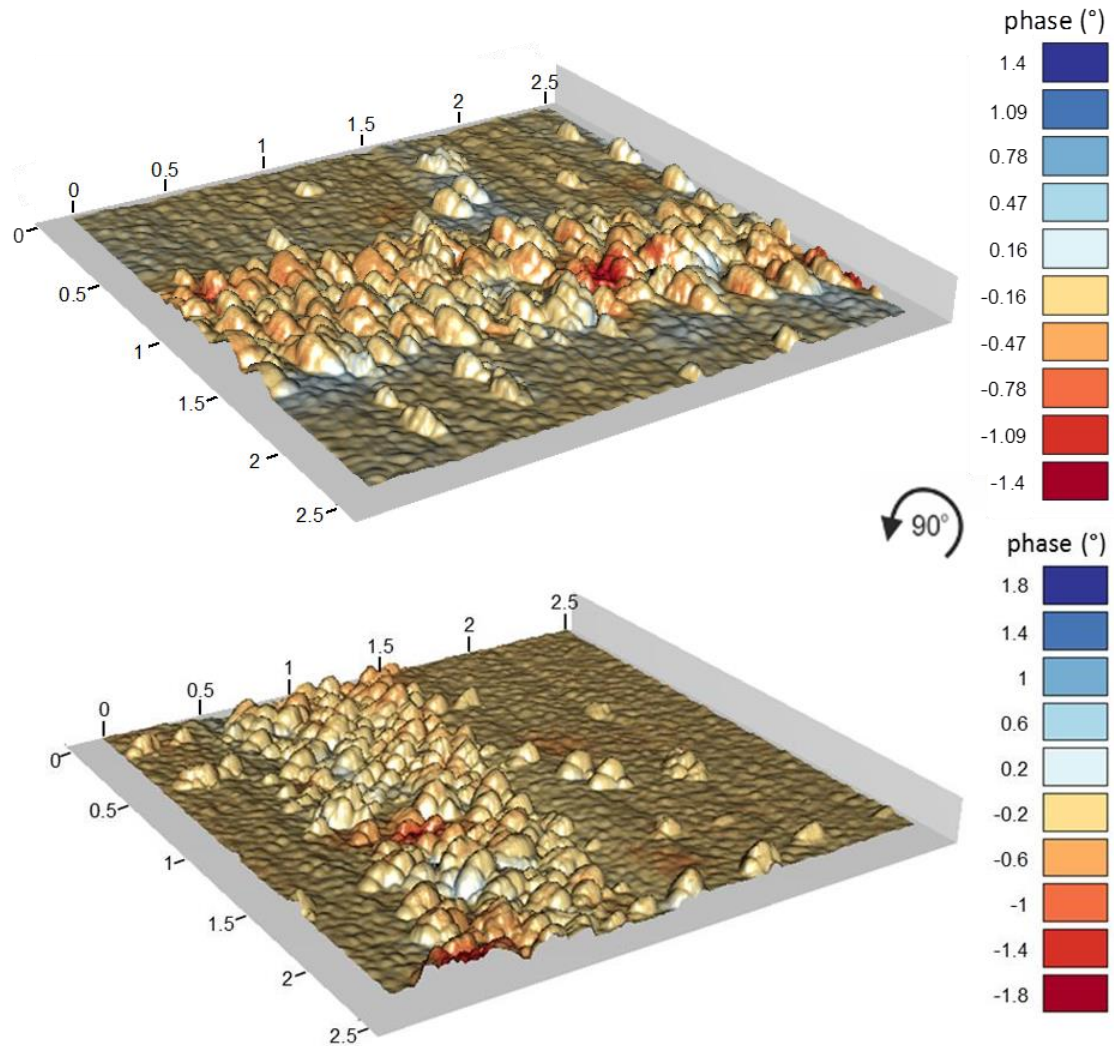
Figure 3.6.8 - Composite images of tapping mode AFM and MFM phase shift of a biomineralised MNP array at a lift height of 50 nm. The images are of the same area, but the scan direction has been rotated by 90˚ between recording each image and shows that the areas of attraction and repulsion remain in the same places. Scales in μm.
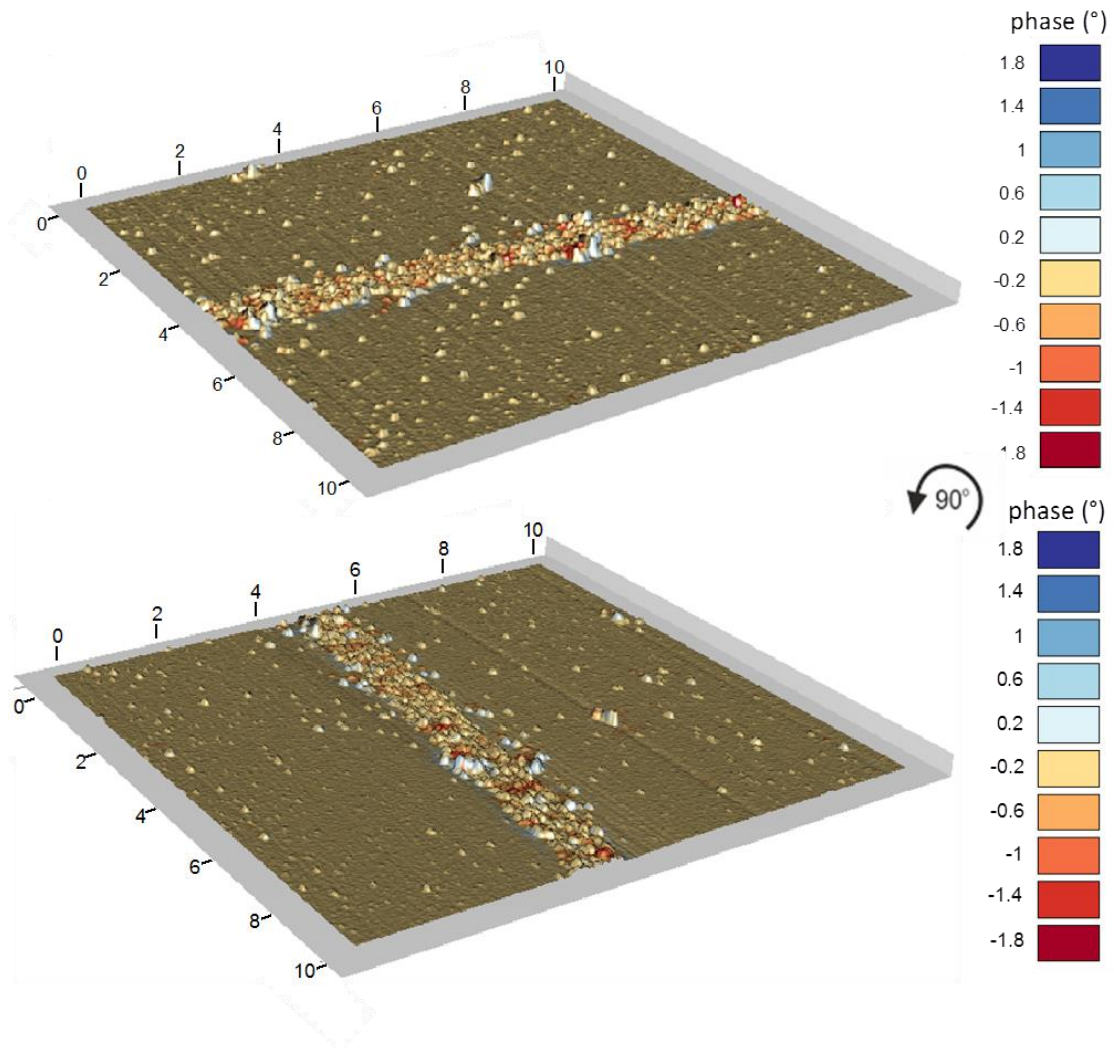
Figure 3.6.9 - Composite images of tapping mode AFM and MFM phase shift of a biomineralised MNP array at a lift height of 50 nm. The images are of the same area, but the scan direction has been rotated by 90˚ between recording each image and shows that the areas of attraction and repulsion remain in the same places. Scales in µm.

3.7 Alternative Routes to Forming MNP Arrays of Magnetite with Biomolecules Based on Mms6

This chapter examines some alternative approaches to using biomolecules to form patterns of MNPs on gold surfaces with cysteine-tagged Mms6 and a peptide derivative based on the *C*-terminal region of Mms6 (Mms6_{Peptide}). It was thought that Mms6 would be able to bind to MNPs that were pre-formed in a POFHK reaction. Therefore, MNP arrays could be formed by supplying a surface patterned with Mms6 with pre-formed MNPs, without having to be subjected to a POFHK reaction (Figure 3.1.1b). So in this Section, this approach is compared to the biotemplated MNP arrays formed by placing Mms6 patterned surfaces into a POFHK reaction (Figure 3.1.1a, Section 3.6). These two approaches were also trialled with the simpler Mms6_{Peptide}, which is cheaper and easier to produce than the full-length protein, and comparisons are drawn against the pre-formed MNP arrays formed by the full Mms6 protein.

3.7.1 SEM Images and Grainsize Analysis of Mms6 Protein and Mms6_{Peptide} Biomineralised and MNP binding Surfaces

Gold surfaces were patterned with PEG using µCP, and backfilled with either Mms6 or Mms6_{Peptide}. These patterned surfaces were then either immersed into a POFHK reaction (*i.e.* biomineralised, Figure 3.1.1a), or placed into a solution containing pre-made magnetite nanoparticles (*i.e.* magnetite binding, Figure 3.1.1b). A wide view of the four different MNP surfaces produced is displayed in Figure 3.7.1. There is a consistent and densely packed single layer of MNPs on the Mms6 protein surfaces after mineralisation with the POFHK reaction (Figure 3.7.1a). When pre-made nanoparticles are supplied to this surface immobilised Mms6 protein (Figure 3.7.1b) there is a more sparse distribution of particles on the patterned biomolecules. The gold surfaces that are patterned with the Mms6_{Peptide} have fewer particles attached to the biomolecule patterns, both when placed into a POFHK reaction (*i.e.* biomineralisation, Figure 3.7.1c) and when magnetite MNPs that were pre-made were supplied (*i.e.* magnetite binding, Figure 3.7.1d).
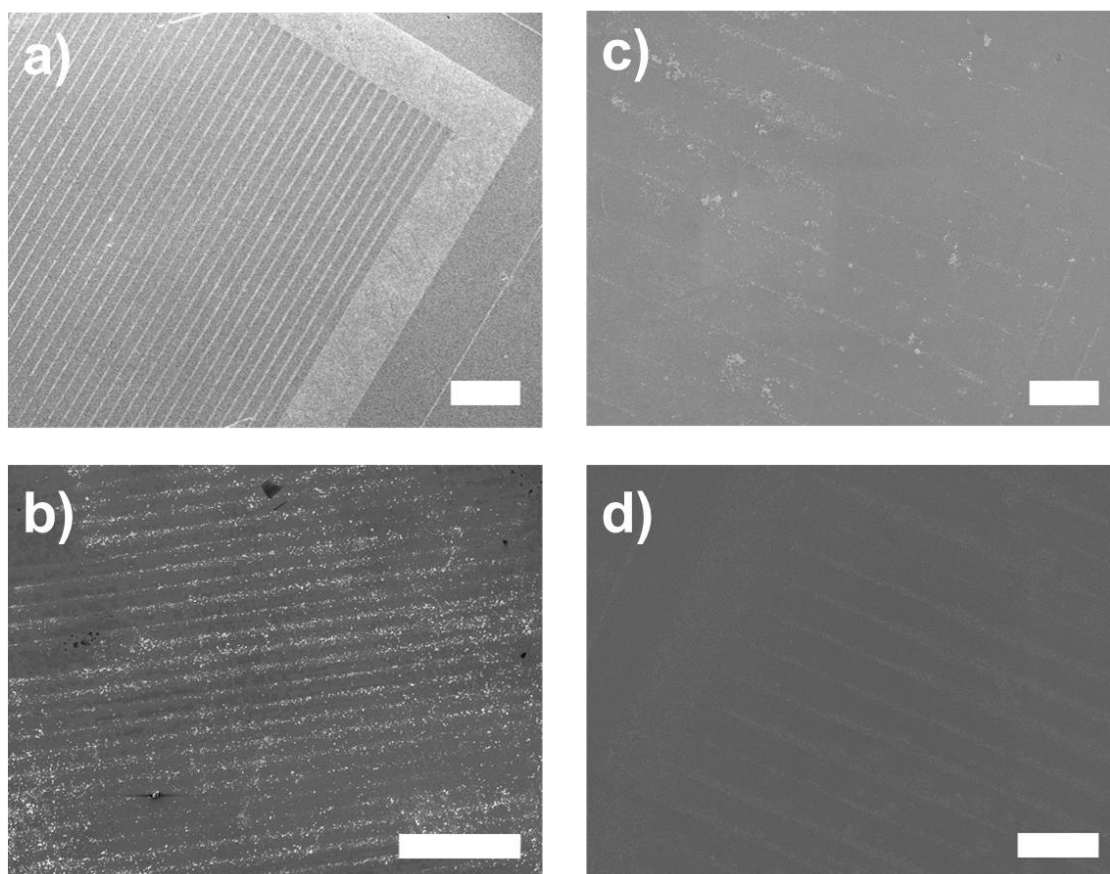
Figure 3.7.1 – SEM images of MNP arrays formed on gold surfaces patterned with either Mms6 (a and b) or Mms6$_{Peptide}$ (c and d) after a POFHK reaction (a and c) or MNP washing (b and c). All scale bars 100 μm.

The resulting surfaces are compared in more detail in Figure 3.7.2, and grainsizing was performed. When the surfaces patterned with the full Mms6 protein are compared, many more MNPs can be seen to form on the biomineralised surfaces that were placed into a POFHK reaction. This suggests that fewer nanoparticles were adsorbed onto the protein pattern surfaces when the nanoparticles were simply washed over. The full protein also shows no selectivity in binding the pre-formed MNPs. When placed into a POFHK reaction, the Mms6 protein biotemplates the formation of MNPs with a larger mean size (≈87±19 nm) than those that form in the control POFHK reaction (Figure 3.2.1). However, the grainsize analysis of the MNPs that bound when the particles are washed over the immobilised Mms6 were found to have a smaller mean size (≈67±23 nm), with a size distribution that is a close match to the MNPs that formed in the POFHK control reaction (Figure 3.2.1). This suggests that the protein may not selectively bind to nanoparticles of a certain size, but simply binds to the particles that are present, possibly through non-specific binding with the MNPs in the suspension. However, when surfaces patterned with Mms6 were placed into POFHK reactions not only do the patterns of

MNPs appear more densely packed, but the particles are formed with a larger mean size and narrower size distribution.
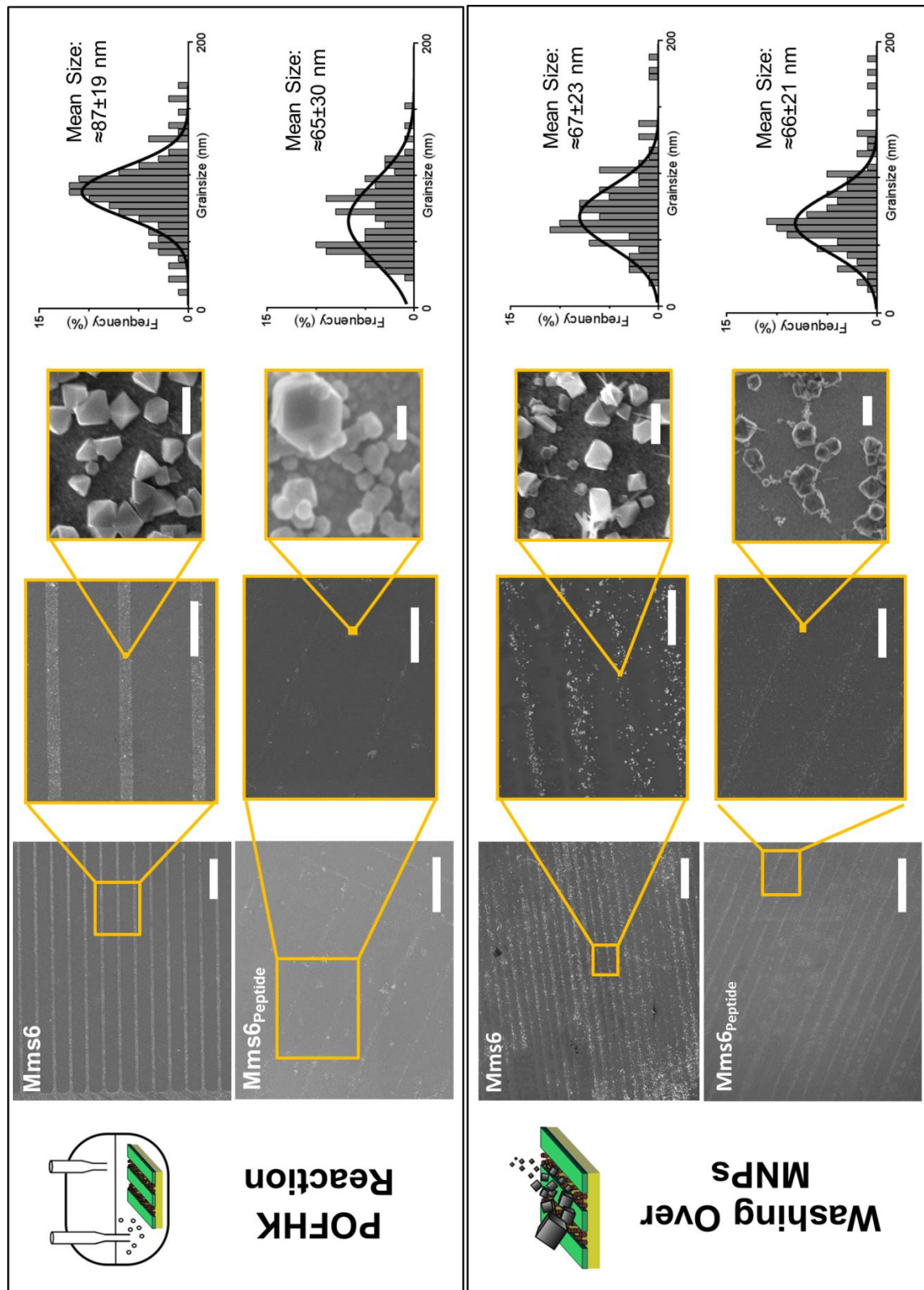
Figure 3.7.2 - SEM and grainsize analysis of Mms6 and Mms6$_{Peptide}$ surfaces after a POFHK reaction or MNP washing. Scale bars: 100 μm left, 20 μm centre, 100 nm right.

Additionally, SEM of the Mms6$_{peptide}$ surfaces reveals that much fewer MNPs formed on the biomineralised surfaces, when both the surfaces immersed into a POFHK reaction and when pre-formed magnetite nanoparticles were supplied. Grainsize analysis once again revealed that the MNPs formed with a mean size (biomineralisation; ≈65±30 nm, magnetite binding; ≈66±21 nm) close to those that formed in the POFHK control reaction (Figure 3.2.1). This suggests that the peptide did not template the formation of MNPs during a POFHK reaction, and the MNPs that formed on the surface may just be a result of non-specific binding.

3.7.2 MNP Density on Mms6 Protein and Mms6$_{Peptide}$ Patterns

The density of MNPs that formed on the four different biomineralised surfaces shown in Figure 3.7.3 were quantified by recording the number of particles in five randomly selected areas of SEM images of the surfaces.[*] This highlights how approximately four times as many particles formed on Mms6 patterned surfaces that underwent a POFHK reaction than any of other the other samples. This is despite these surfaces being subjected to 80°C and extremes of pH during the POFHK biomineralisation reaction, compared to simple immersion into a water solution containing pre-formed nanoparticles. This is probably a result of Mms6 binding and concentrating iron ions, before nucleating and stabilising a growing MNP. Therefore the protein mediates more contacts with the growing nanoparticles, than if pre-formed MNPs are just supplied. As a result the strong attachment of Mms6 to magnetite is most probably a by-product of its nucleation function.

---

[*] These areas were all on the areas patterned with either Mms6 or Mms6$_{Ppetide}$, and not the antibiofouling PEG regions.
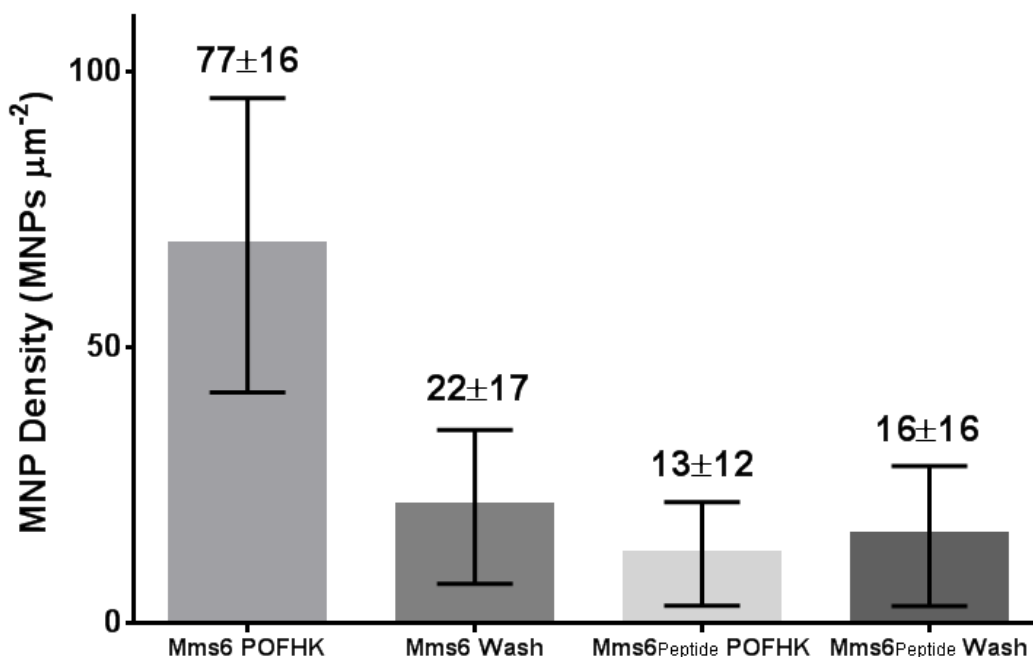
Figure 3.7.3 – Particle density measurements and standard deviation of five selected areas of the samples displayed in Figure 3.6.1.

3.7.3 Comparison of MNPs bound to Mms6 Protein and Mms6$_{Peptide}$ Patterns

In summary, these results suggest that only the full Mms6 protein is able to control the growth of magnetite MNPs when the biomolecule is immobilised onto a gold surface during a POFHK reaction. This leads to the formation of denser packed MNPs on the Mms6 protein patterns. These biotemplated MNPs also have a larger mean size and narrower size distribution than the non-biotemplated MNPs that form in a control POFHK reaction. However, the Mms6 protein only shows limited binding to pre-formed MNPs of magnetite, and appears to be unable to selectively bind to MNPs with certain properties (e.g. size, shape, crystal face specific). Additionally, Mms6$_{Peptide}$ appears unable to biotemplate the formation of magnetite MNPs during a POFHK reaction, and also only shows unselective binding to pre-formed MNPs of magnetite. Together, these results help to build a picture of the differences between the Mms6 protein and Mms6$_{Peptide}$, and inform on how Mms6 may function.

Mms6$_{Peptide}$ seems to not only be less effective at binding nanoparticles than the full Mms6 protein, but also does not seem to control the size or shape of the nanoparticles that form *in situ*. It is possible that the shorter peptide may be inaccessible on the gold surfaces patterned by PEG, so complete surfaces of Mms6$_{Peptide}$, without any patterning or PEG, were subjected to both a POFHK reaction and immersed in a water suspension of pre-formed nanoparticles. These surfaces are displayed in Figure 3.7.4 and 3.7.5, and the same low density

coverage can be seen. Once more, the peptide seems to offer little to no control over the MNPs that formed, with grainsize analysis once again being a good match for the control POFHK reaction (Figure 3.2.1). Therefore, it is unlikely that the ineffectiveness of the peptide is a result of it being buried or masked by the PEG SAM, and it could be that the Mms6 peptide crowds itself by packing more closely than the full Mms6 protein.
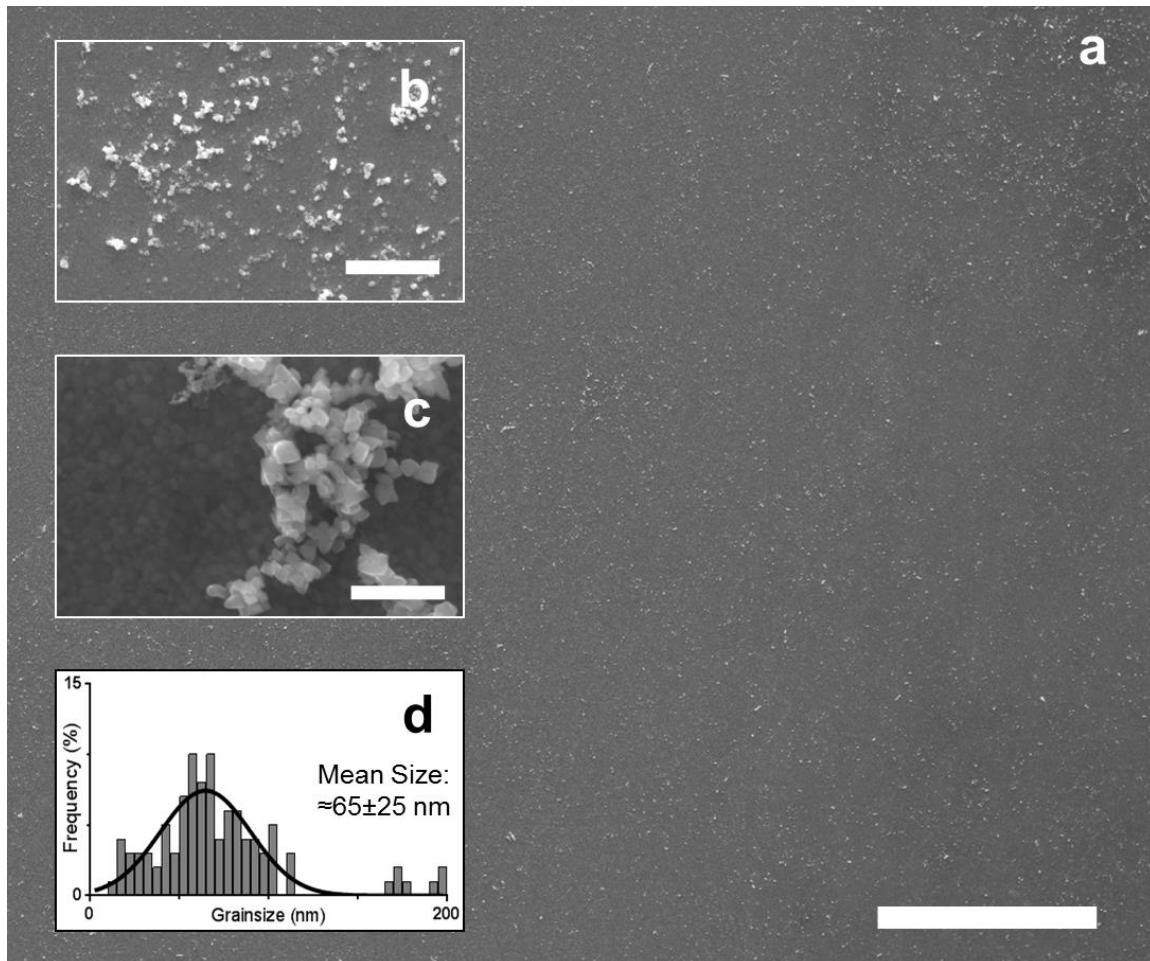
Figure 3.6.4 - SEM (a-c) and grainsize analysis (d) of a complete surface of Mms6$_{Peptide}$ (without any patterning or PEG) after a POFHK reaction. Scale bars: a – 50 μm, b – 2 μm, c – 250 nm.

Mms6$_{Peptide}$ is based on the *C*-terminal region of Mms6, containing the acidic residues that are considered essential for biomineralising magnetite [189]. Previous studies of an Mms6 *C*-terminal peptide in solution phase POFHK magnetite formation show modest particle size effects [95], however under the conditions used here the peptide fails to show activity that is comparable to the full Mms6 protein. One key difference between the full Mms6 protein and the Mms6$_{Peptide}$ is that the full protein contains a repeating sequence of glycine and leucine amino acids in its *N*-terminal region. This glycine-leucine (G-L) repeat motif is common to many self-assembling proteins such as silk fibroins, and a peptide based on the *C*-terminal region of Mms6 with the additional G-L repeat section has been shown to display greater activity [190].

The G-L motif (Figure 3.7.6a) could have a key role in organising the protein so that it is packed into a highly ordered assembly onto the gold surface for efficient biomineralisation. It may also space the protein away from the gold surface, and ensure the correct geometry and position of iron binding residues for the binding and nucleation of magnetite.
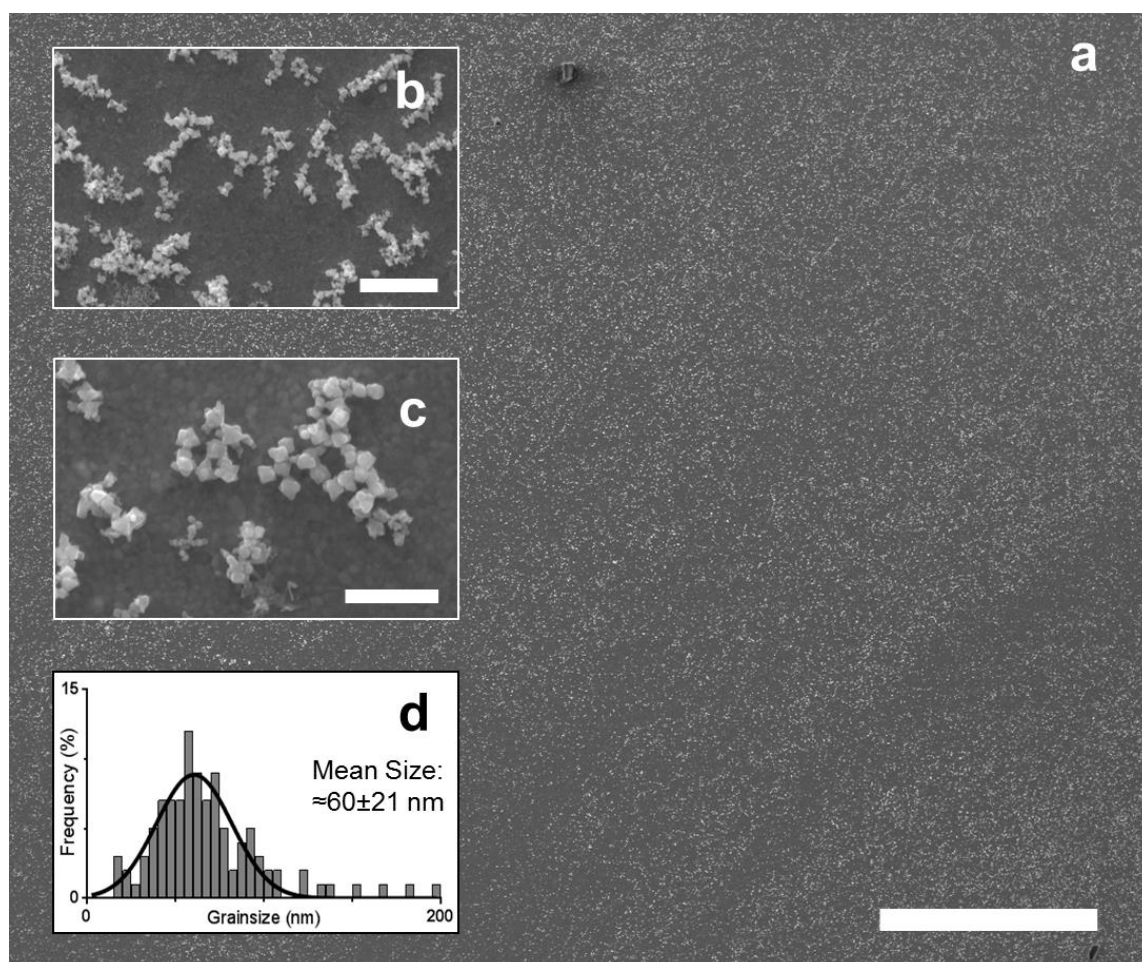
Figure 3.7.5 - SEM (a-c) and grainsize analysis (d) of a complete surface of Mms6$_{Peptide}$ (without any patterning or PEG) after MNP washing. Scale bars: a – 100 µm, b – 2 µm, c – 500 nm.

The possibility of such a self-assembly motif was investigated by modelling the G-L motif in Swiss-PdbViewer [191], which then allowed for analysis in Pymol [92]. It was found that it was possible for the sequence to form both a helix and a beta strand, with the glycine residues in both cases forming holes that could interlock with leucine sidechains that form knobs. Therefore, it is possible that when bound onto a surface two or more Mms6 proteins might interlock *via* knobs-into-holes packing, resulting in a parallel arrangement of the helices [192]. This was shown to be possible when the G-L region was modelled as a helix using the HexServer[*]

---

[*] http://hexserver.loria.fr/

[193], that was used to dock two monomers together resulting in 100 dimer models that had a parallel arrangement (Appendix 2). A parallel assembly of the Mms6 protein may allow precise packing of multiple protein molecules, forming a *C*-terminal surface of iron ion binding residues. Close packing may also control the geometry and spacing of the *C*-terminal iron binding residues on adjacent Mms6 proteins, ensuring the precise geometry and spacing of key iron binding residues to facilitate iron ion coordination and the nucleation of a magnetite nanoparticle.

The Mms6$_{Peptide}$ does not contain the G-L repeat motif, and the potentially uncontrolled surface packing of the peptide may result in its reduced ability to biotemplate the formation of MNPs of magnetite. Furthermore, it is also not possible to rule out the fact that the short Mms6$_{Peptide}$ sequence is more readily denatured during the POFHK reaction, which is run at 80˚C. If this is the case, this further highlights the importance of the structure of the full Mms6 protein, and the fact that the short Mms6$_{Peptide}$ sequence is unable to replicate the biotemplating function of the full protein under the same conditions.

3.7.4 Magnetite Formation by Mms6

In summary, the full Mms6 protein bound to gold via an *N*-terminal cysteine produced denser packing of MNPs, with a larger mean size and narrow size distribution than when pre-made MNPs of magnetite were simply washed over the surfaces or a simpler peptide based on the *C*-terminal region of Mms6 (Mms6$_{Peptide}$) was used. However, it should be noted that the Mms6 patterned surfaces biotemplated the formation of MNPs from a POFHK reaction that were approximately 50% larger ($\approx 87 \pm 19$ nm) than the particles formed in a control POFHK reaction in the absence of a biotemplating biomolecule ($\approx 60 \pm 21$ nm). This is in contrast to natural magnetosomes within magnetotactic bacteria that are approximately 50 nm in size [60], and to experiments were Mms6 controlled the formation of magnetite nanoparticles in solution to produce MNPs approximately 23 nm in diameter [189].

These differences could be an effect of curvature (Figure 3.7.7). When free in solution, Mms6 self-assembles into soluble micelles (Figure 3.7.7a). The convex surface of the micelle may provide a smaller nucleation surface than when Mms6 is assembled onto a flat surface (Figure 3.7.7b). Therefore, when assembled onto a surface a larger expanse of the active *C*-terminal region may well lead to increased nucleation and the formation of larger crystals. Additionally, when the Mms6 protein is assembled onto a surface it is only able to contact that the growing nanoparticle from one side (as shown in Figure 3.7.7b). Conversely, when in solution multiple

proteins may be able to bind to one nanoparticle, and this may drastically alter the size and the shape of the MNPs that form. Yet, neither of these two approaches are perfect matches for the concave assembly of Mms6 inside a magnetosome (Figure 3.7.7c), which also contains many other biomineralisation proteins and ultimately has a lipid membrane that may restrict crystal size.
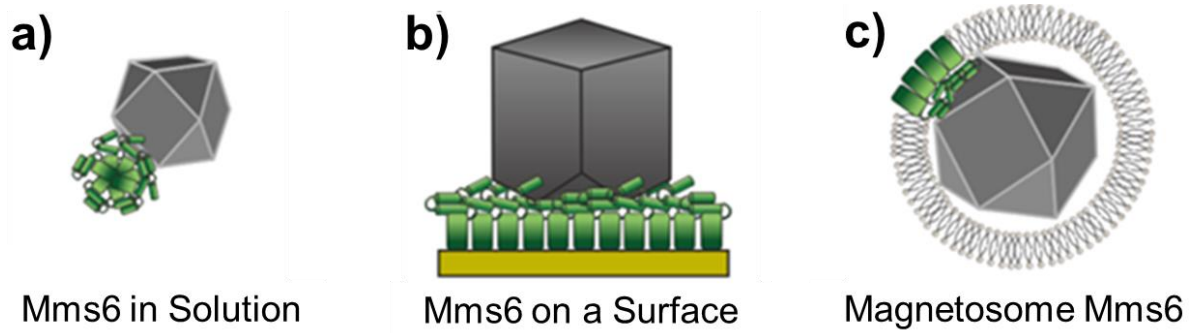
Figure 3.7.6 - The assembly of Mms6 under different conditions (the *N*-terminal region of Mms6 is represented by a green rectangle and the iron binding *C*-terminal region by two green cylinders).

4. Patterning on the Nanoscale

"If something's hard to do, then it's not worth doing."

One of Homer J. Simpson's many anti-quotes.

4.1 Overview: Different Patterning Techniques

The arrays of magnetite MNPs biomineralised by the biomineralisation protein Mms6 in Chapter 3 present a novel approach to the challenge of forming surfaces containing the billions of uniform nanomagnetic islands that would be ideal for BPM [41]. However, the microscale patterns that were generated are a long way from being able to meet this challenge. What is needed is a new approach to patterning, with the ability to control the location of Mms6 with nanoscale precision. Therefore, in this section several different ways of patterning the antibiofouling PEG SAM or Mms6 protein are explored, with the aim of reducing the feature sizes of the biomineralised MNP patterns formed to the nanoscale dimensions required for BPM.

Although it is able to pattern wide areas (on the cm scale), μCP with traditional s-PDMS stamps cannot be used to routinely generate patterns on surfaces with dimensions < 1 μm (as discussed in Section 1.5.4.2) [139]. μCP with the use of composite stamps, consisting of a thin rigid layer of h-PDMS reinforced by a supporting layer such as glass, has been shown to pattern SAMs with a resolution of 50 nm [138]. Therefore, in Section 4.2 the use of μCP with h-PDMS was explored as an alternative route to patterning Mms6 onto gold surfaces.

It is unlikely that the type of μCP used in Chapter 3 could ever be scaled up for the mass production of a BPM recording disk. Achieving faultless and nanoscale precision is essential, and it is apparent that laying a PDMS stamp onto a surface by hand will never be able to achieve this. As a result PPL (discussed in Section 1.5.4.4), which controls a PDMS stamp with nanoscale precision through the use of a piezoelectric system, is explored as an alternative in Section 4.3 [145, 146]. PPL does require the use of a specialised system, and a short collaboration with the Dip-Pen Nanolithography Group at the Karlsruhe Institute of Technology (KIT) in Germany allowed access to this equipment and this approach to be trialled. DPN has been shown to routinely pattern SAM surfaces with nanoscale resolution (as discussed in section 1.4.4.3), and the collaboration at KIT also allowed access to a DPN system [140]. This technique was also trialled, and is discussed in Section 4.4.

Finally, Section 4.5 outlines work done with the use of IL (as discussed in Section 1.5.4.5) [150]. IL has the ability to pattern wide areas (of a few cm^2), has been shown to produce features in SAM surfaces with dimensions of 30 nm and once exposure conditions are established offers excellent reproducibility [150]. It does require the use of a laser and a specialised optical system, but collaboration with The Nanoscale Analytical Science Group at

the University of Sheffield allowed this work to take place with regular access to the equipment.

4.2 μCP with Nanoscale Precision

4.2.1 Stamp Masters with Nanoscale Features

The generation of stamp masters with patterns on the nanoscale is a lot more challenging than the well-established photolithography of SU-8, which was used to form stamp masters with microscale features (that the s-PDMS stamps used to pattern Mms6 in Chapter 3 were cast over) [158]. Traditional photolithography (and the equipment that was available) was not able to achieve the nanoscale patterning resolution required [194]. Therefore, stamp masters with nanoscale features were generated by the EBL of an electron-sensitive ZEP520A resist [161]. ZEP520A was applied to a silicon substrate with 1 μm of thermally grown oxide, which after the EBL process was followed by a reactive ion etch (RIE) and lift off (as outlined in Chapter 2.2.4.1).

It is well known that stamp masters have to meet certain design criteria, even when the more rigid h-PDMS is used [138]. To avoid forming stamps with problems such as lateral collapse and sagging, masters should be designed to strict guidelines as shown in Figure 4.2.1. This guideline was taken into account during the design process.
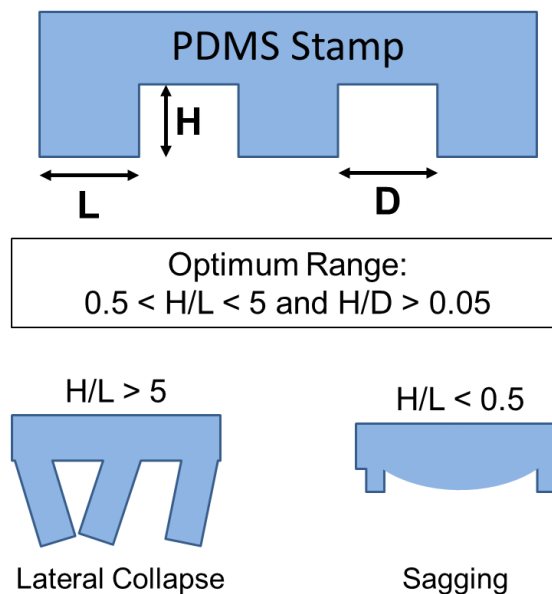
Figure 4.2.1 – A simple diagram highlighting the main problems that should be considered when designing a master for PDMS stamps (adapted from Figure 3 in ref. [138]). Lateral collapse can take place when L/H > 5, and sagging can occur when H/L < 0.5. Both of these would ruin any patterns during a stamping process.

The production of stamp masters with nanoscale features was undertaken at the University of Leeds, but due to continuous problems with the EBL system and ultimately the loss of regular access after relocation to Sheffield only three trials were run. Example SEM images of the three samples that were formed are shown in Figure 4.2.2, and the formation of line and square patterns can be seen. Each of samples underwent a RIE process for different times; 150, 270 and 540 seconds. The sample etched for the shortest time of 150 seconds resulted in an measured etch depth of ≈210 nm into the silicon oxide, with the 270 second etch measured to reach ≈390 nm and the longest 540 second etch found to reach ≈680 nm. If the size of features and the optimum ratios displayed are considered the shorter etch times result in features that are on the lower end of the optimum ratio for H/L, with the greater etch depth preferable.

As can be seen in Figure 4.2.2e and f the longest etching time resulted in the formation of a rough oxide surface. This is probably a result of the ZEP520A resist, which acts as an etch mask, being completely eroded. The resit mask becomes roughened during the etch process, and as a result this roughness is transferred to the oxide surface as it is completely removed in a RIE process. Therefore, this long etch time could not be used to form suitable stamp masters. This problem may have been heightened by further issues in ensuring that the base vacuum level of the etcher was sufficient, leading to poor etch selectivity between the resist and the oxide [195]. It can be seen that this process was able to generate patterns with feature sizes down to ≈200 nm (Figure 4.2.2d). Although, in most cases the resist structure was not accurately transferred into the oxide film, a particular issue at 90˚ corners that are pinched (not 90˚). Furthermore, the etch profile does not look vertical, but is probably tapered. Again these issues are probably a result of the poor etch selectivity, and oxide material being eroded and re-deposited leading to distortion [195].

It was hoped that these problems could be rectified with the deposition of a chrome layer after the EBL of the ZEP520A resist. This would form a more robust hard mask that would offer better selectivity during the etching process, allowing for deeper and more uniform etching [196]. Patterning would be achieved by the removal of the resist (and the chrome on top of it) in ZDMAC developer solution, to form an inverse of the patterns shown in Figure 4.2.2. This would actually be preferred as the masters shown in Figure 4.2.2 would produce stamps with the smaller patterns that would touch the surface during a stamping process. The stamps that were produced from the masters shown in Figure 4.2.2 have to be used to directly print Mms6 onto the surface, to from nanoscale patterns of the protein. With

the preferred approach being the process used in Chapter 3, patterning of the antibiofouling PEG SAM followed by backfilling with the biomineralisation protein from a buffer solution.
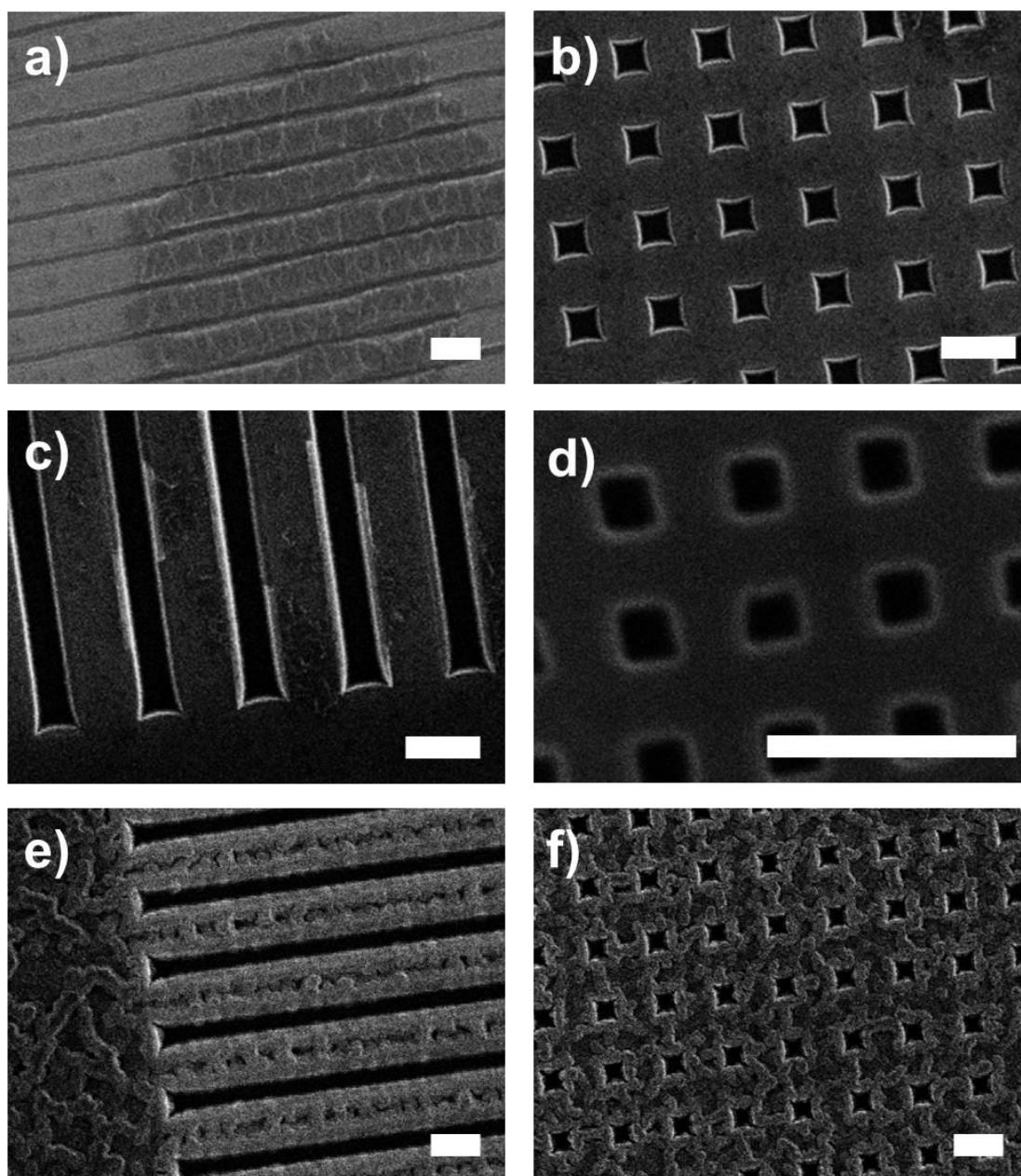
Figure 4.2.2[*] – SEM images of stamp masters with nanoscale features manufactured by the EBL of ZEP520A resist on a silicon substrate with 1 μm thick layer of thermally grown oxide and a RIE for; 150 seconds (a and b), 270 seconds (c and d) and 540 seconds (e and f). All scale bars 1 μm.

---

[*] Electron beam lithography was performed by Mark Rosamond at the University of Leeds.

4.2.2 Biomineralised MNP Arrays with Nanoscale Dimensions formed by μCP with h-PDMS Stamps

PDMS stamps consisting of a layer of h-PDMS supported by a glass back panel were cured over the silicon masters displayed in Figure 4.2.2. As discussed in Section 4.2.1 the stamps cast over these masters had to be used to pattern Mms6 directly on to the gold surfaces, so as to generate patterns of Mms6 with nanoscale dimensions. This is the opposite approach to the traditional μCP with s-PDMS stamps that was used in Chapter 3 to form microscale patterns of biomineralised magnetite MNPs. During the previous μCP process with s-PDMS stamps an antibiofouling PEG SAM was printed onto the gold surfaces, with the remaining clean gold backfilled with Mms6 by immersing the PEG patterned substrates in a buffer solution containing the protein. Conversely, to pattern Mms6 with nanoscale precision the h-PDMS stamps were inked with a PBS solution containing Mms6, before the being placed in conformal contact with the gold surfaces. The protein patterned surfaces were then immersed in a solution of PEG in ethanol to backfill the remaining clean gold with a PEG SAM, before being subjected to a POFHK reaction (process outlined in Figure 4.2.3). Unlike the patterning performed in Chapter 3 the PEG SAM is not being used to control the location of the protein on the gold surface, but is still essential as it prevents MNPs settling on and binding to the clean gold areas during the POFHK reaction.
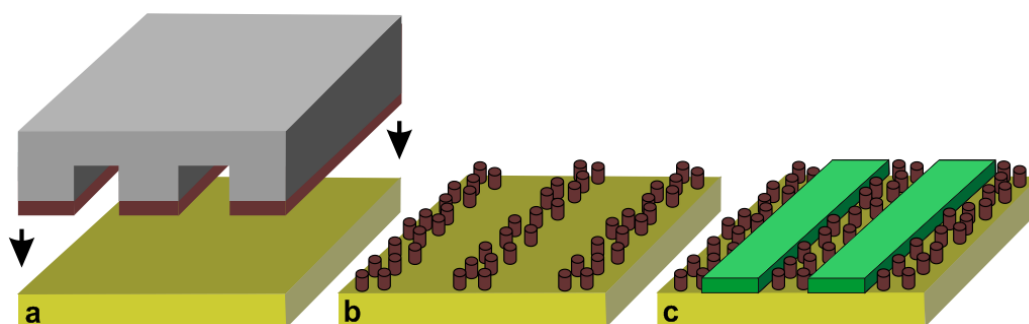
Figure 4.2.3 - Schematic of the process used to pattern gold with Mms6 *via* μCP using h-PDMS stamps. a) A stamp inked with a PBS buffer containing Mms6 is placed in contact with a clean gold surface. b) The stamp is then removed, with the protein (brown cylinders) binding to the gold surface at the points were the stamp was in contact with gold. c) The remaining clean gold space is then backfilled with a PEG SAM (green), before being subject to a POFHK reaction.

The patterning of Mms6 with the h-PDMS stamps was found to be far less successful than the patterning achieved with s-PDMS stamps analysed in Chapter 3. In Figure 4.2.4 SEM images that show some evidence for the formation of MNPs biomineralised by Mms6 into lines that are ≈250 nm wide is displayed, but the patterns of MNPs appear much less dense and uniform than the MNP patterns formed with s-PDMS stamps (Figure 3.6.1). The MNPs that formed on the protein patterned regions appear to have a cubic-like morphology and

grainsize analysis (Figure 4.2.4d) shows that the MNPs formed on the surface with a mean size of ≈80±24 nm. This larger mean size than those that formed in a control POFHK reaction (Figure 3.2.1, 60±21 nm), and is similar to the MNPs that were biotemplated by Mms6 after patterning with s-PDMS stamps in Chapter 3 (Figure 3.6.1, ≈87±19 nm). This suggests that the Mms6 protein was patterned onto the surface, and biomineralised MNPs that have a larger mean size than those that form in solution during a POFHK reaction as in Chapter 3.
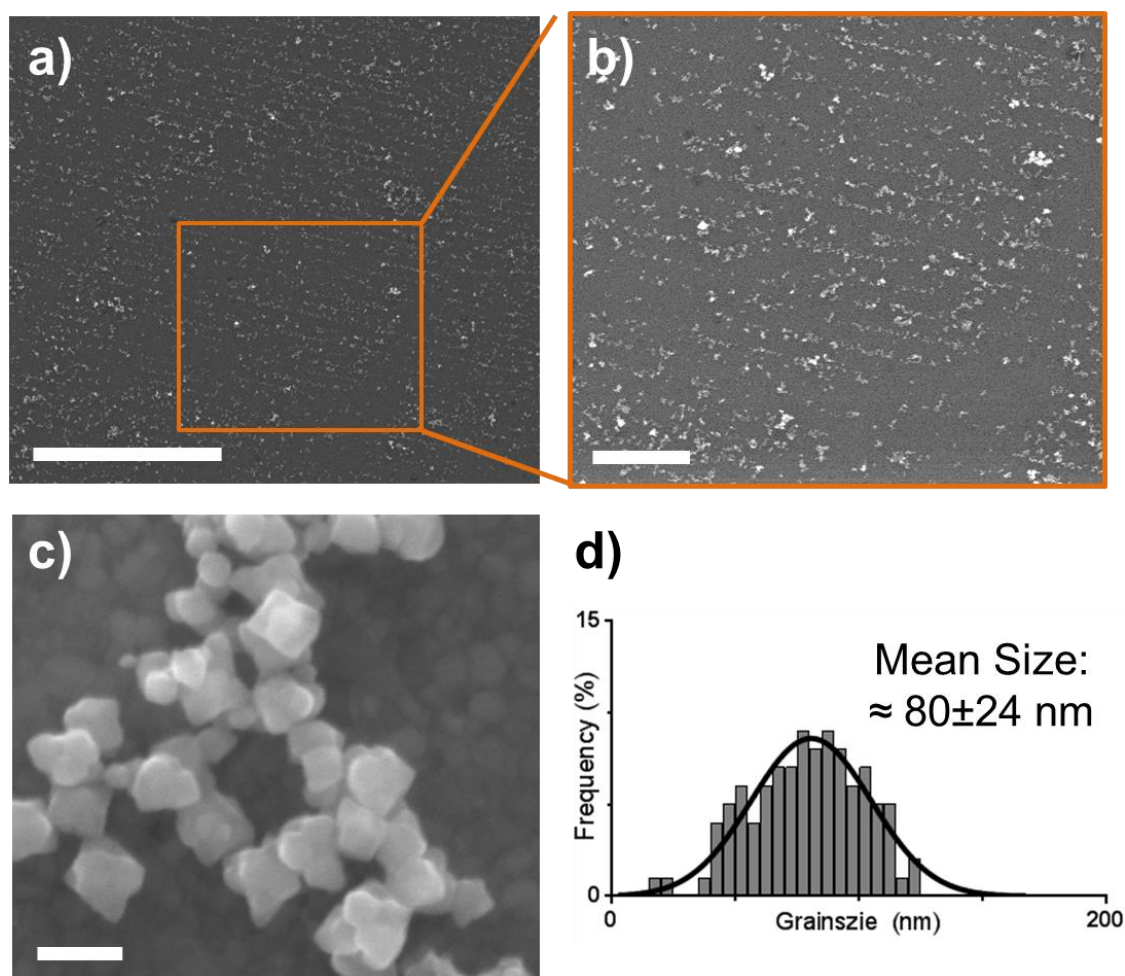
Figure 4.2.4 – SEM images (a-c) and grainsize analysis (d) of a gold surface patterned with Mms6 using μCP with h-PDMS stamps after a POFHK reaction. Scale bars: a – 10 μm, b – 2 μm, c – 100 nm.

Not only did patterning Mms6 with h-PDMS stamps lead to MNP arrays with a poorer uniformity of MNP patterns than the microscale arrays patterned with s-PDMS stamps in Chapter 3. The process was also found to be far less reproducible, and in most cases the expected pattern could not located in an SEM analysis. This could be a result of Mms6 not being delivered correctly to the gold surfaces during the stamping processes. The flexible s-PDMS are much more suited to being laid onto the gold substrates in conformal contact with the surface than the rigid layer of h-PDMS supported by a glass back panel. It also remains

unclear how the immersion of the Mms6 patterned gold surfaces into a solution of PEG in ethanol effects the protein.

It is possible that when binding to clean gold from solution Mms6 forms a more ordered, higher density layer to result in a more efficient biomineralising surface. It is also possible that when the gold surfaces patterned with Mms6 were placed into an ethanol solution containing PEG that the protein is reordered or outcompeted by the PEG SAM. It has been reported that competitive adsorption is an issue for alkanethiols with bulky or complex head groups, leading to the blocking of the close packed alkane chains that reduces the driving force for adsorption [197]. Therefore, it is likely that when a gold surface patterned with Mms6 is placed into a PEG SAM solution, the protein pattern could be disrupted or outcompeted as the PEG SAM is driven to form a highly ordered and close packed layer on the gold surface.

In addition, the poor quality of the stamp masters that were produced could also have led to the poor quality patterns that were formed. This work could have been continued after the relocation from the University of Leeds to Sheffield (and the loss of access to the EBL system at Leeds) to produce stamp masters that were more suitable and of a better quality. This would have required the optimisation of the process around the equipment and facilities that were available at Sheffield. However, it was decided that due to the time and cost involved, and the fact that μCP is unlikely to ever be used for the mass production of MNP arrays suitable for use in BPM, that other more suitable patterning techniques would be explored.

4.3 Polymer Pen Lithography (PPL)

In the process of PPL a PDMS stamp is controlled with the use of a piezoelectric stage, with the potential to vastly increase the resolution and reproducibility that is achievable with μCP [145]. As discussed in Section 2.2.5, the h-PDMS stamps used contained a regular array of pyramid tips. Therefore, in this case unlike the μCP used in Chapter 3 and like the h-PDMS discussed in the previous chapter cysteine-tagged Mms6 had to be stamped directly onto the gold surfaces. First attempts to pattern Mms6 onto gold surfaces with PPL involved inking the stamp with a PBS solution containing Mms6, before stamping the gold surface to pattern Mms6 into regular arrays of dots.

The surfaces were then backfilled with a PEG SAM, by placing the Mms6 patterned surfaces into a PEG in ethanol solution for one hour. As discussed in the previous chapter in this case the PEG SAM does control the location of the protein on the gold surface, but is required to prevent MNPs settling on the clean gold areas during the next mineralisation step. After backfilling with a PEG SAM the surfaces were placed into a POFHK reaction, with the aim of forming a biotemplated MNP array. However, this process was found to be ineffective. Mms6 was attempted to be patterned into a regular and repeating array of dots across the gold surfaces, but no evidence of this type of pattern was ever found with SEM studies after a POFHK reaction. It remained unclear whether the Mms6 was being delivered to the surface correctly or at all, as it was not possible to image or test for this with the time and resources available during the short collaboration with KIT.

The PPL process was repeated with stamps that were inked with a mixture of PBS and glycerol containing the Mms6 protein in a concentration 10 μg mL^{-1}. In this case the glycerol was used as a carrier to deliver the protein to the surface during the stamping process, and has the advantage that glycerol forms dots that are visible on the gold surface in an optical microscope (this process is outlined in Figure 4.3.1). This allowed the stamping process to be assessed before the glycerol was rinsed away and the surfaces were backfilled with a PEG SAM (Figures 4.3.2 and 4.3.3). During this analysis the dwell time (the time the stamp is in contact with the gold surface during the stamping process) could also be optimised. Figure 4.3.2 shows optical images of gold surfaces immediately after patterning by PPL, with a dwell time of 5 seconds (Figure 4.3.2a) and 2 minutes (Figure 4.3.2b).
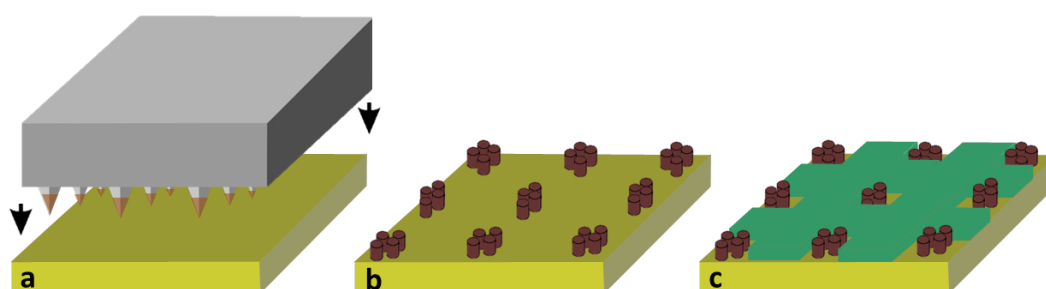
Figure 4.3.1 - Schematic of the process used to pattern gold with Mms6 via PPL. a) A stamp inked with a PBS-glycerol buffer containing Mms6 is placed in contact with a clean gold surface. b) The stamp is then removed, with the protein (brown cylinders) binding to the gold surface at the points were the stamp was in contact with gold, forming an array of dots. c) The remaining clean gold space is then backfilled with a PEG SAM (green), before being subject to a POFHK reaction.
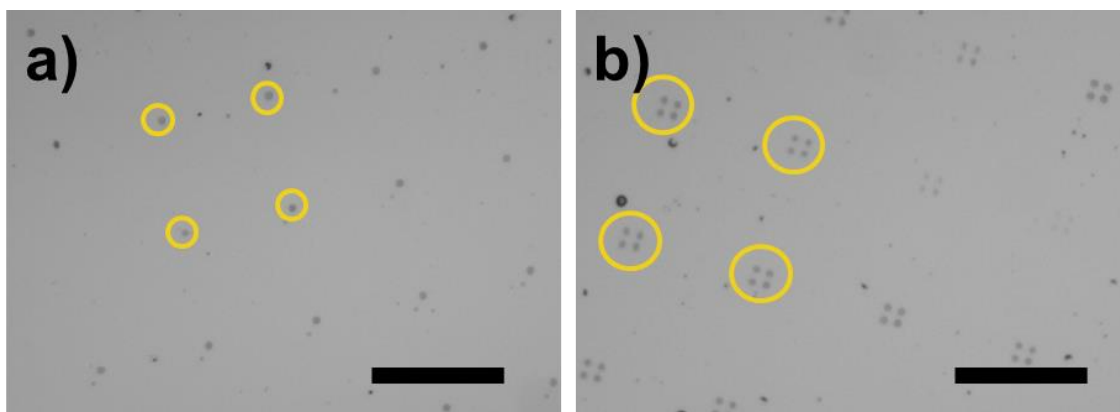
Figure 4.3.2 – Optical microscopy images of gold surfaces after the patterning of Mms6 with PPL in a 2x2 dot array with a 5 second dwell time (a) and 2 minute dwell time (b). Example areas of where the location of Mms6 in a PBS-glycerol carrier solution can be seen are circled. Scale bars are 50 µm.

When the stamp is first brought into contact with the gold surface, it is checked to make sure that it uniformly contacts the whole gold surface (a process that takes a few minutes). This process results in approach dots that are clearly visible in both images displayed in Figure 4.3.2. The stamp was then raised and lowered a further three times with the aim of producing a 2x2 pattern of dots. When a short dwell time of 5 seconds was used, further glycerol dots are not visible (Figure 4.3.2a), suggesting that the ink containing Mms6 was not transferred to the surface. On the other hand, when a longer dwell time of 2 minutes was used a much more uniform array of 2x2 glycerol dots was formed on the surface (Figure 4.3.2b). When dwell times longer than 2 minutes were used more ink was found to be delivered to the surface, and the glycerol dots were found to coalesce. Therefore, a dwell time of 2 minutes was found to be optimum.

Figure 4.3.3 displays a typical image of a gold surface directly after it was patterned with PPL, using a stamp that was inked with the PBS-glycerol mixture. When wide areas of the gold surface were imaged it was found that although the desired patterned formed over some areas the pattern was not uniform and large drops of glycerol were always found to coalesce in certain areas. This was found to be unavoidable, with shorter dwell times leading to smaller areas that were stamped with a uniform pattern, and longer dwell times resulting in the formation of an increased number and larger areas of the large glycerol drops. Consequently, achieving patterning uniformity across wide areas on the cm-scale, something that is required for bit-patterned media, remained unachievable.
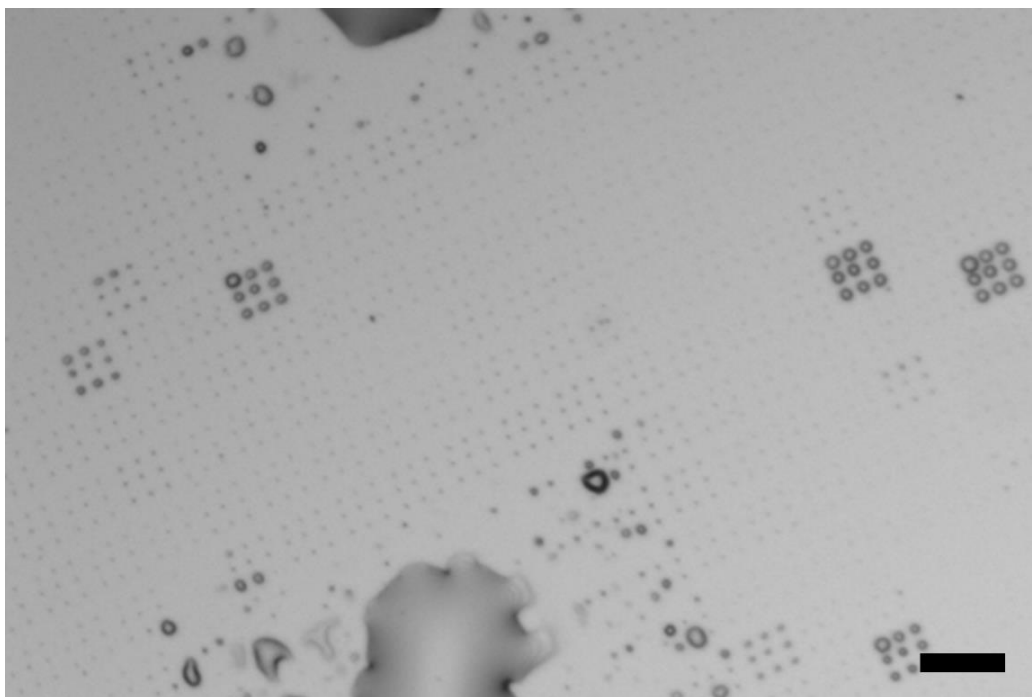
Figure 4.3.3 – Optical microscopy image of a gold surface after the patterning of Mms6 with PPL in a PBS-glycerol carrier solution into 3x3 dot arrays, with each dot spaced 15 µm apart. Scale bar 50 µm.

The gold surfaces patterned with PPL were incubated for 1 hour to allow the Mms6 protein to order onto the gold surface, before being rinsed with PBS to remove the excess glycerol and placed into a PBS solution overnight. The Mms6 patterned surfaces were then placed into a solution of PEG in ethanol, and then subject to a POFHK reaction. Some evidence of patterning was found with SEM analysis, such as a region patterned with the ≈3 µm diameter dots shown in Figure 4.3.4. The particles that formed all appear to have a uniform cubic-like morphology. In addition, grainsize analysis shows that these MNPs that formed with a larger mean size (82±22 nm) than those that formed in a control POFHK reaction (Figure 3.2.1, 60±21 nm), similar to the MNPs that were formed on the gold surfaces that were patterned with Mms6 using conventional µCP after a POFHK reaction (Figure 3.6.1, ≈87±19 nm). This suggests that the Mms6 protein was patterned onto the surface in these regions, and acts to biotemplate the formation of MNPs with a larger mean size than those that form in solution during a POFHK reaction.

When the MNP arrays that were biotemplated by Mms6 patterned with PPL (Figure 4.3.4) are compared with those that were formed using conventional µCP (Figure 3.6.1), the MNPs appear to form with a much lower density on the regions patterned with Mms6. This could be a result of there being less Mms6 present, or the protein may not be orientated correctly with an exposed *C*-terminal region for efficient biomineralisation. Patterning was also not achieved with the same level of consistency. In some areas high

density collections of MNPs were seen to have formed on the surface, which could be a result of the large drops of coalesced glycerol that were seen to form on the surface (Figure 4.3.3). Though, in most cases a low density layer of MNPs formed and no evidence of patterning could be found.
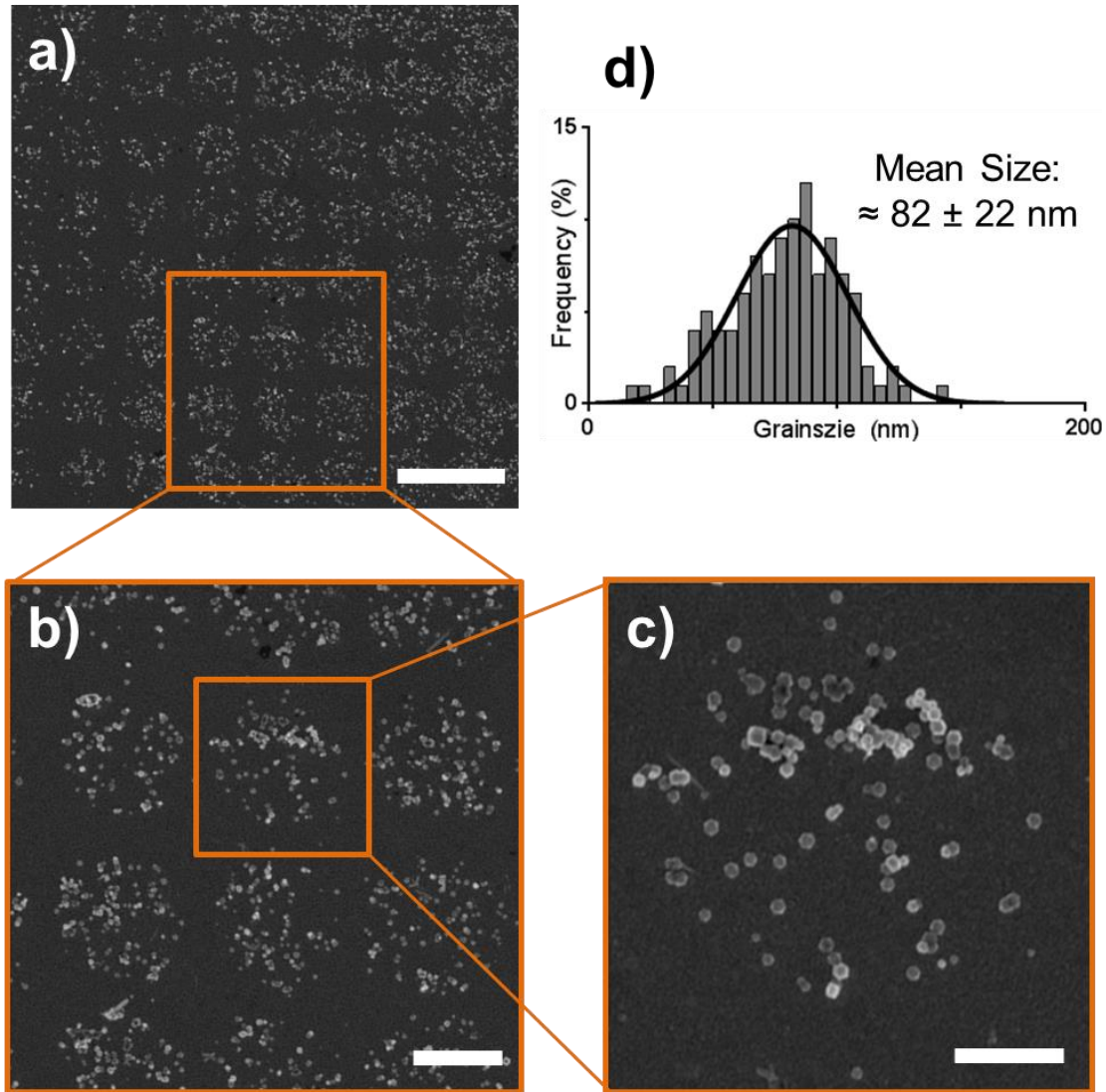
Figure 4.3.4 – SEM images (a-c) and grainsize analysis (d) of a gold surface patterned with Mms6 using PPL after a POFHK reaction. Scale bars: a- 5 µm, b – 2.5 µm, c – 1 µm.

Figure 4.3.5a displays an SEM image of a high density region of MNPs that formed after a POFHK reaction, which is probably a result of the coalescence of the PBS-glycerol ink on the gold surface during the PPL stamping process. Whereas, Figure 4.3.5b is an SEM image that is far more representative of the majority of the samples that were imaged, with no clear patterning visible on the surface. In summary, it appears that the PPL process developed was far less effective at patterning Mms6 onto gold surfaces for the efficient biomineralisation of MNP arrays of magnetite than the conventional µCP process that used in Chapter 3. It remains unclear what the main reason for this is, but could be a result of the PPL process not

delivering the Mms6 protein to the surface during stamping. It could also be due to the fact that (as with the use of the h-PDMS stamps discussed in the previous section) the Mms6 protein has to be patterned directly onto gold during the PPL process, before the remaining clean gold was backfilled with a PEG SAM.
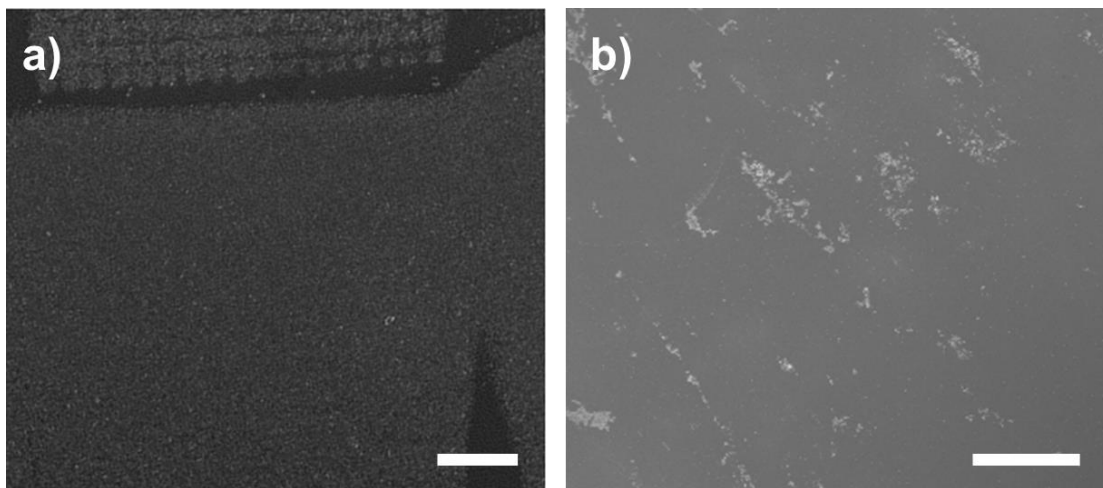
Figure 4.3.5 – SEM images of gold surfaces patterned with Mms6 using PPL after a POFHK reaction. a) A region where a high density layer of MNPs formed. b) A typical example of a sample where MNPs could not be found ordered into the regular pattern that was stamped onto the surface. Scale bars: a – 10 µm, b – 100 µm.

4.4 Dip-Pen Nanolithography (DPN)

DPN has been shown to form patterns on surfaces with a resolution <50 nm, and the collaboration with KIT allowed access to a DPN system [140, 162]. As with PPL, DPN had to be used to write the Mms6 protein directly onto the gold surface before backfilling the remaining clean gold with a PEG SAM. DPN is a slow serial writing process, so attempting to write the PEG SAM over wide areas of a gold surface is not feasible. Therefore, attempts were made to write a mixture of PBS and glycerol containing the Mms6 protein on to the gold surface. After patterning the surfaces were immersed in a solution of PEG in ethanol, and were then subject to a POFHK reaction (the process is outlined in Figure 4.4.1).
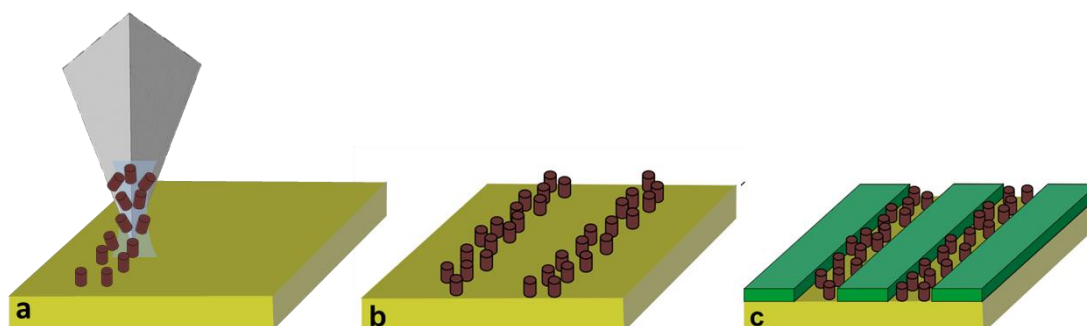
Figure 4.4.1 - Schematic of the process used to pattern gold with Mms6 via DPN. a) An AFM tip is used to write Mms6 directly onto a clean gold surface. b) The Mms6 protein (brown cylinders) forms an ordered array. c) The remaining clean gold space is then backfilled with a PEG SAM (green), before being subject to a POFHK reaction.

Example SEM images of surfaces patterned with Mms6 by DPN after a POFHK reaction are shown in Figure 4.4.2. It is clear in these images that the protein was not patterned onto the gold surfaces, and instead the tips scratched the desired pattern into the gold film. MNPs can be seen to form around the scratched pattern in the images shown in Figure 4.4.2, and this could be a result of the Mms6 protein ink being sprayed over the gold film during the writing process.
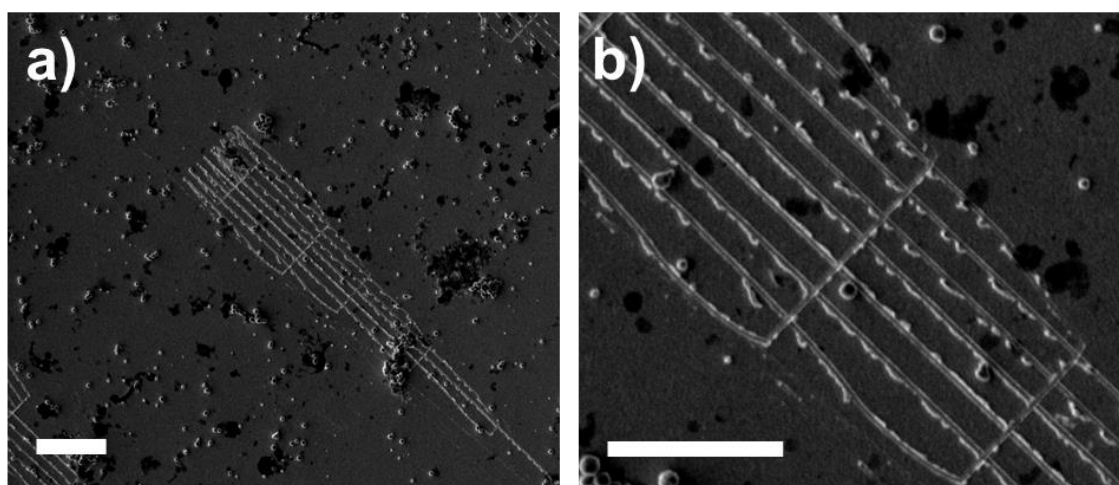
Figure 4.4.2 – SEM images of a gold surface patterned with Mms6 using DPN after a POFHK reaction (scale bars 5 µm). Unfortunately these images show that Mms6 was not delivered to the surface, and instead the tip just scratched the gold.

Further trails could have been run, and by varying parameters such as the humidity during writing, tip-surface contact and inks used Mms6 could have been patterned more effectively [162]. Unfortunately, time did not allow for the patterning conditions to be optimised. DPN could have been a useful approach to test the patterning resolution achievable for the MNPs biomineralised by Mms6, but ultimately this slow serial writing process cannot be scaled up for the cost-effective mass production of biomineralised surfaces for use in magnetic HDDs. In addition, this approach requires the remaining clean gold on the

Mms6 patterned surfaces to be backfilled with a PEG SAM, something that was found to be a potential issue with the patterning techniques discussed in Sections 4.2 and 4.3. As a result, more suitable patterning techniques were explored.

4.5 Interferometric Lithography (IL)

IL has been shown to form patterns in SAMs with 30 nm resolution [150, 152, 153]. In addition, IL is also capable of patterning wide areas (on the cm scale) in one exposure, and once exposure conditions are established forms patterns that are extremely reliable and reproducible [150]. Therefore, IL not only forms a lithographic approach that can achieve the patterning resolution required for the production of BPM, but could also lends itself well to being scaled-up for high throughput mass production. Collaboration with The Nanoscale Analytical Science Group at the University of Sheffield allowed for access to an IL system, and Mms6 to be patterned with nanoscale precision with this approach.

Clean gold substrates were immersed in a solution of PEG in ethanol, to form a complete PEG SAM on a gold surface. These surfaces were then exposed to laser light in a Lloyd's mirror configuration, forming a diffraction pattern of bright and dark fringes over the surface (as discussed in Section 1.5.4.5). This led to spatially selective photo-oxidation in regions exposed to a maximum in the interferogram (formed by constructive interference), while minimal modification of the surface occurred in regions exposed to minima in the interferogram (corresponding to destructive interference). The result is the formation of a periodic array of uniformly aligned bands occupied by the PEG SAM, separated by regions in which the adsorbate has been photo-oxidised. The photo-oxidised adsorbates are susceptible to displacement from the surface, either by a contrasting adsorbate or, as here, by solvent rinsing to expose the underlying gold surface. The protein cys-Mms6 was adsorbed onto the gold regions formed between the bands of intact PEG adsorbates. These Mms6 patterned surfaces were then immersed in a POFHK reaction to form a biomineralised MNP array of magnetite (the patterning process is outlined in Figure 4.5.1).
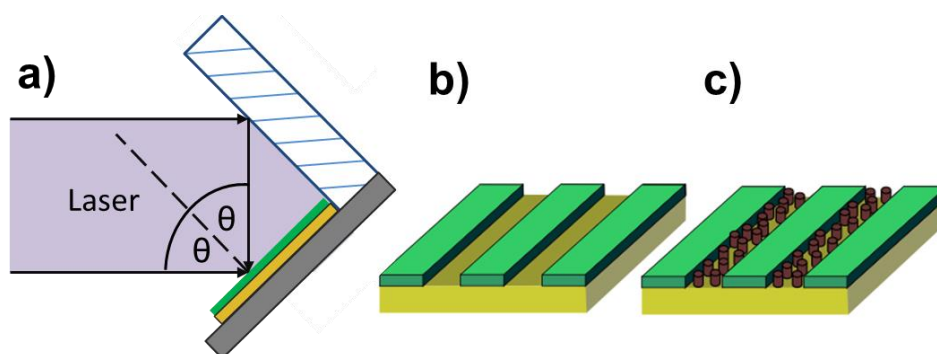
Figure 4.5.1 - Schematic of the process used to pattern gold with Mms6 *via* IL. a) A gold surface with a complete PEG SAM (green) is exposed to laser light in a Lloyd's mirror configuration. A diffraction pattern of bright and dark fringes is formed over the surface, with the areas of SAM exposed to the bright fringes being degraded more quickly. b) The degraded SAM can be rinsed away to form a regular line array of clean gold and PEG SAM. c) The remaining clean gold space is then backfilled with the cysteine-tagged Mms6 protein (brown cylinders), before being subject to a POFHK reaction.

4.5.1 Optimising the Patterning Conditions

The exposure dose delivered to the complete PEG SAM layer on the gold substrates is proportional to the laser power and the exposure time. Therefore, before each exposure the power of the laser at the SAM surface was recorded, and the exposure time was adjusted so that a consistent dose was applied. To determine the optimum exposure in the lithographic process, gold surfaces covered in a mixed SAM of PEG and carboxylic acid terminated thiols were exposed for a range of different times, and hence doses. After exposure, the surfaces were backfilled with a CH_3 terminated thiol, and characterised by friction force microscopy (FFM). The CH_3 terminated SAM provides good contrast in FFM, because it exhibits a much lower coefficient of friction than the polar adsorbates [198], allowing the pattern generated to be readily observed. It was found that an exposure of 20 J cm^{-2} (equivalent to a few minutes at usual operating powers) was sufficient to create clear features with well-defined contrast in the PEG in the SAM, and this dose was selected for the subsequent Mms6 experiments (Figure 4.5.2). The use of higher doses leads to the blurring and thinning of the pattern formed in the SAM. This is because the diffraction pattern formed over the surface consists of a periodic series of fringes representing intensity minima and maxima (Equation 2.2.1). Hence, longer exposure times lead to regions of lower intensity photo-oxidising the PEG SAM, resulting in broader and less defined areas of clean gold that would be suitable for backfilling with Mms6.
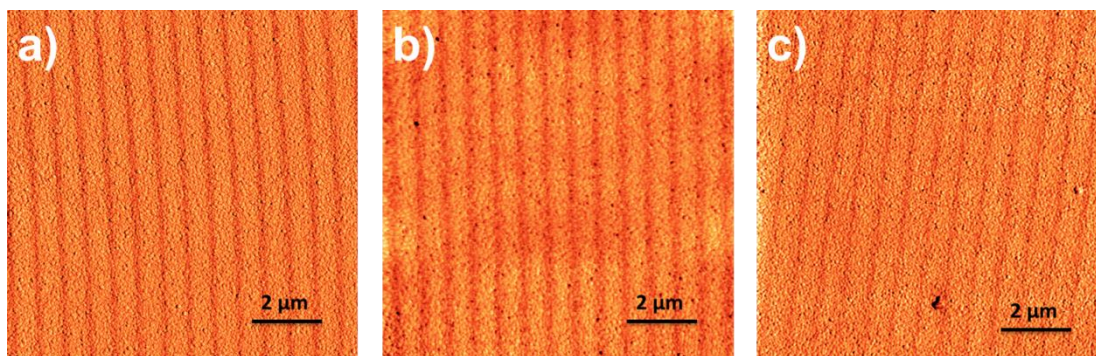
Figure 4.5.2[*] – Friction force microscopy (FFM) image of a mixed SAM containing PEG and a carboxylic acid terminated thiol that was patterned by IL at a dose of 20 J cm^{-2} (a), 30 J cm^{-2} (b) or 40 J cm^{-2} (c), before being backfilled with a CH$_3$ terminated thiol SAM to provide contrast in FFM (regions patterned with the CH$_3$ terminated thiol appear lighter).

4.5.2 Biomineralised MNP Line Arrays

Biomineralised line arrays of magnetite MNPs were formed through the patterning of a complete PEG SAM on gold with IL at an exposure dose of 20 J cm^{-2} and angle of $2\theta=20°$. The PEG patterned surfaces were then backfilled with cysteine-tagged Mms6, and the protein patterned surfaces was subjected to a POFHK reaction. As can be seen in Figure 4.5.3 biomineralised line arrays of MNPs were formed over a wide area, with dimensions of a few nanometres. As with the biomineralised MNPs formed when Mms6 was patterned on the microscale a high density layer of MNPs can be seen to have formed on the protein patterned regions, with only limited MNP formation on the areas patterned with the antibiofouling PEG SAM.

[*] FFM was performed by Osama El-Zubir.
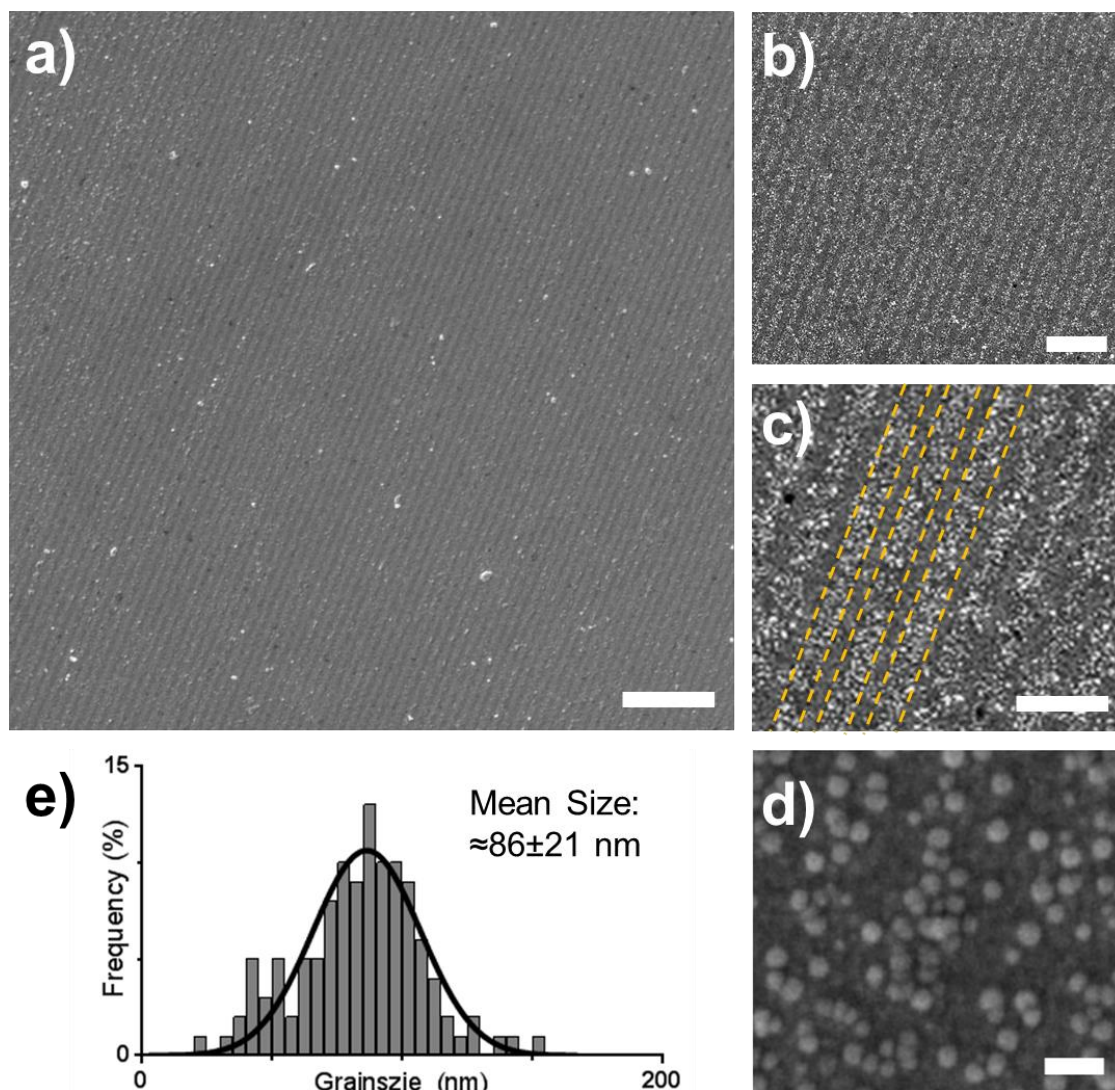
Figure 4.5.3 – SEM images (a-d) and grainsize analysis (e) of Mms6 surfaces patterned by IL after a POFHK reaction. The yellow dotted lines in image c highlight the approximately 250 nm line pattern that was formed in this case. Scale bars: a – 2 µm, b – 1 µm, c – 500 nm and d – 200 nm.

Mms6 was seen to exert similar control over the formation of MNPs, compared to the MNPs formed when patterned with µCP into microscale arrays (Chapter 3). When compared with the control MNPs formed in solution during the POFHK reaction (Figure 4.5.4), grainsize analysis (Figure 4.5.3e and Figure 4.5.4b) found that the MNPs biomineralised onto the surface formed with a larger mean size (≈86±21 nm) and smaller size distribution than the control MNPs (≈64±24 nm). The fact that these results are comparable to those in Chapter 3 (Figure 3.2.1 and 3.6.1) suggests that Mms6 was successfully patterned and ordered onto the gold surface. These results also provide further evidence to support Mms6 nucleating iron ions, templating the growth of larger and more consistent MNPs of magnetite on the gold surface than the control MNPs that form in a POFHK reaction.
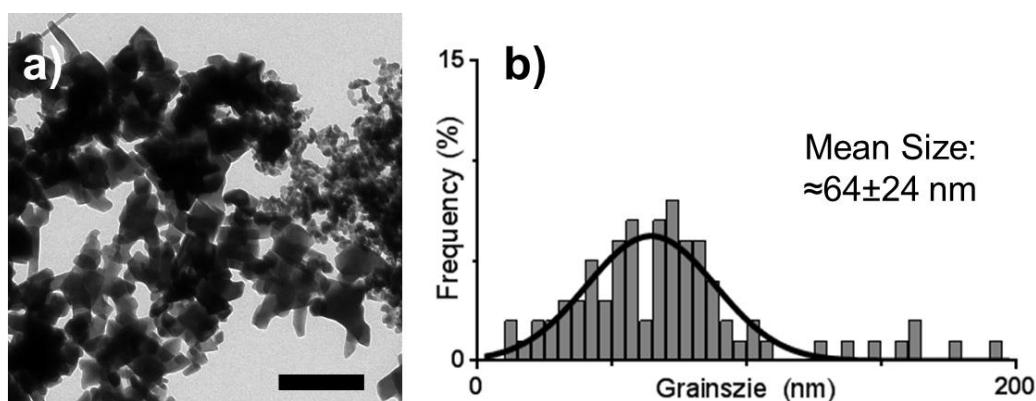
Figure 4.5.4 - TEM image (a) (scale bar 250 nm) and grainsize analysis (b) of the control MNPs that formed in solution during the POFHK reaction, which the surface displayed in Figure 4.5.1 was placed into.

4.5.3 Crystallographic Analysis

Crystallographic analysis of the biomineralised surfaces, and the particles that formed in solution during the POFHK reaction was performed using XRD (Figure 4.5.5). The positions of the peaks were then converted to *d*-spacings (using Equation 2.5.1, Table 4.4.1). As described in Section 3.2 the sample was compared to the known values (from the JCPDS crystallographic database) for magnetite as well as maghemite. For the particles that formed in solution during the POFHK reaction (black data, Figure 4.4.5) the XRD diagram shows peaks at 2θ = 30.09°, 35.34°, 37.10°, 43.10°, 53.40°, 56.80°, 62.51° and 73.50°. Similarly, for the MNPs biomineralised onto the gold surface the XRD data (gold data, Figure 4.5.5) shows peaks at 2θ = 30.15°, 35.45°, 42.95°, 53.40°, 57.20°, 62.65° and 74.05°. These were all a good fit to the magnetite (220), (311), (400), (422), (511), (440) and (533) peaks respectively, and a closer fit than the peaks for maghemite or goethite (with one exception being the (511) peak actually being a fit for maghemite instead of magnetite for the MNPs biotemplated onto the gold surface by Mms6, Table 4.4.1). The additional peaks at 2θ = 38.25°, 44.45° and 77.65° correspond to the Au (111), (200) and (311) reflections from the gold substrate that the Mms6 protein is patterned on, with the Au (111) peak obscuring the (222) peak for magnetite. However, once again this analysis provides strong evidence that magnetite was the majority product formed during the POFHK reaction and biotemplated onto the gold surfaces by Mms6.
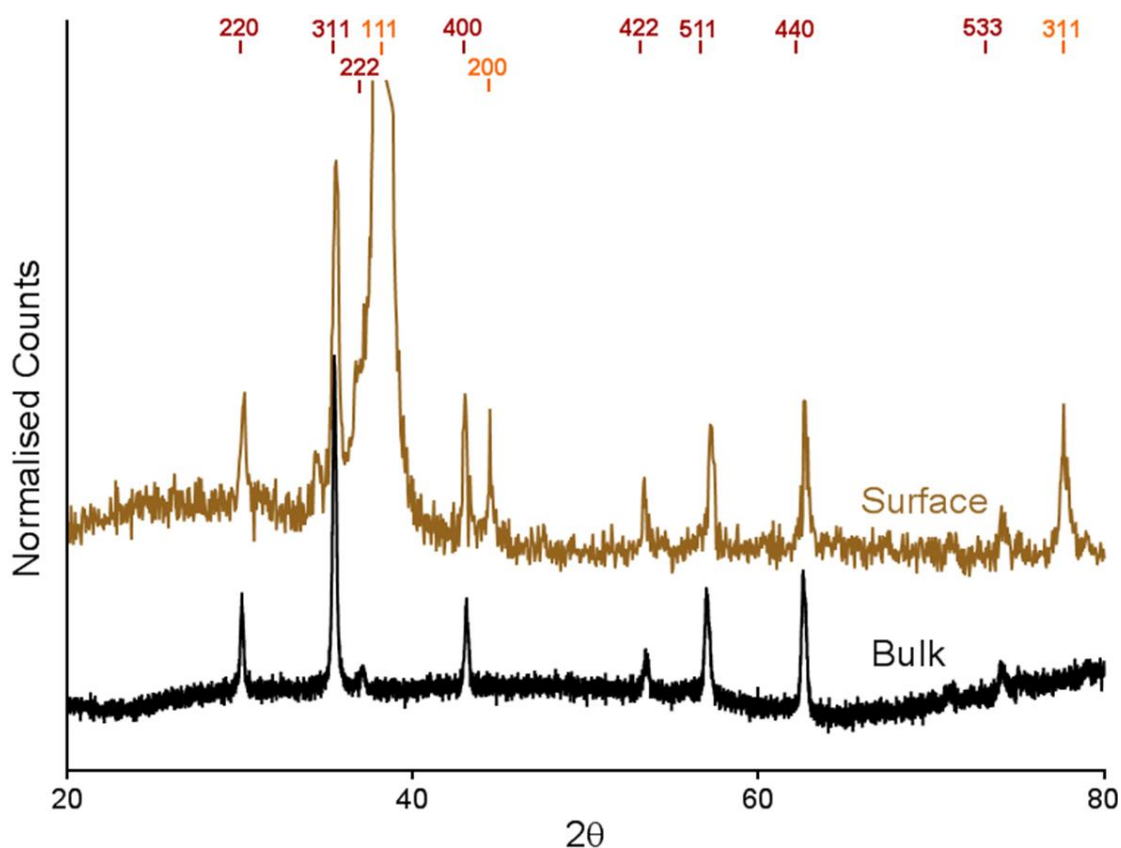
Figure 4.5.5 - XRD diagram of the MNPs biomineralised by Mms6 onto gold (gold) and of the particles that form in solution (black) during a POFHK reaction. The expected peak positions for magnetite (red) and gold (gold) are highlighted.

Table 4.5.1 – Summary of the *d*-spacings for maghemite, goethite and magnetite, and the bulk MNPs formed in a POFHK reaction and the MNPs biotemplated on to the gold surface shown in Figure 4.5.5 (all measured in Å). Maghemite values are from JCPDS card 00-039-1346, magnetite from 00-019-0629 and goethite from 01-081-0464. The value which is the closest match to the MNPs that formed in solution during the POFHK retraction or were biotemplated onto the gold surface are highlighted in green and orange respectively, and only those plains on the JCPDS card that are the nearest to the peak are shown.

Peak	Maghemite	Magnetite	Goethite	Bulk	Surface
(220)	2.950	2.966		2.970	2.964
(130)			2.693		
(311)	2.520	2.530		2.540	2.532
(101)			2.527		
(111)			2.449	2.423	—*
(222)	2.410	2.419			
(220)			2.190	2.099	2.106
(400)	2.080	2.096			
(221)			1.719	1.716	1.716
(422)	1.700	1.712			
(511)	1.610	1.614		1.621	1.610

---

* Peak obscured by the dominant Au (111) peak.

(231)			1.603		
(440)	1.480	1.483		1.486	1.483
(241)			1.475		
(042)			1.292	1.285	1.280
(533)	1.270	1.279			

The 311 peak was fitted to the Debye-Scherrer equation (Equation 2.5.2), to determine the grainsize of the MNPs that were biomineralised onto the surfaces and those that formed in solution during the POFHK reaction [178]. This fitting suggested that the nanoparticles that formed in solution had a mean size of ≈72 nm, while the MNPs biomineralised onto the gold surfaces by Mms6 had a mean size of ≈89 nm. These values confirm the general trend that MNPs were biomineralised onto the gold surfaces by Mms6 with a larger mean size than those that form in solution during a POFHK reaction. The mean sizes calculated are slightly larger than the mean sizes calculated for these particles from TEM images in the last chapter (≈64±24 nm for the particles that formed in solution and ≈86±21 nm), but analysis with the Debye-Scherrer equation assumes the particles are perfectly crystalline with a narrow grainsize distribution [179]. Discrepancies may be explained by the fact that the control nanoparticles were seen to form with a large size distribution (as shown in Figure 4.4.3 and 4.4.4), and with a crystallinity that was not uniform.

4.5.4 Magnetic Force Microscopy (MFM)

Figure 4.5.6 displays a tapping mode AFM image and MFM plots of MNP arrays, which were biomineralised onto gold surfaces by Mms6 that was immobilised onto gold surfaces after a PEG SAM was patterned by IL. It is immediately evident that a high density layer of MNPs formed onto the protein patterned arrays, with only limited mineralisation on the PEG background. The composite AFM and MFM plots also show that zones of attraction and repulsion (red and blue areas respectively). As with the MFM data recorded for the MNP arrays biomineralised by Mms6 after patterning with μCP (Chapter 3.6.4) and previous measurements when Mms6 was bound to a SAM containing carboxylic acid moieties [97, 98, 154], this suggests that the biotemplated MNPs are ferrimagnetic and able to maintain magnetic orientation at room temperature.

These images also help to show the clarity and uniformity of patterning that was achieved. A regular line array consisting of a high density layer of MNPs and regions with no MNP formation can be seen to have formed, corresponding to the regions patterned with

Mms6 and the PEG SAM respectively. Figure 4.5.6b displays an example height profile across the tapping mode AFM image (Figure 4.5.6a), showing that the regular line patterned formed with an average period of 357 nm. This includes lines of biotemplated MNPs with an average width of ≈274 nm, and a PEG SAM background spacing region with an average width of ≈83 nm. Although, this period can be adjusted by varying the angle at which the PEG SAM layer is exposed during the IL patterning process (Equation 2.2.1).
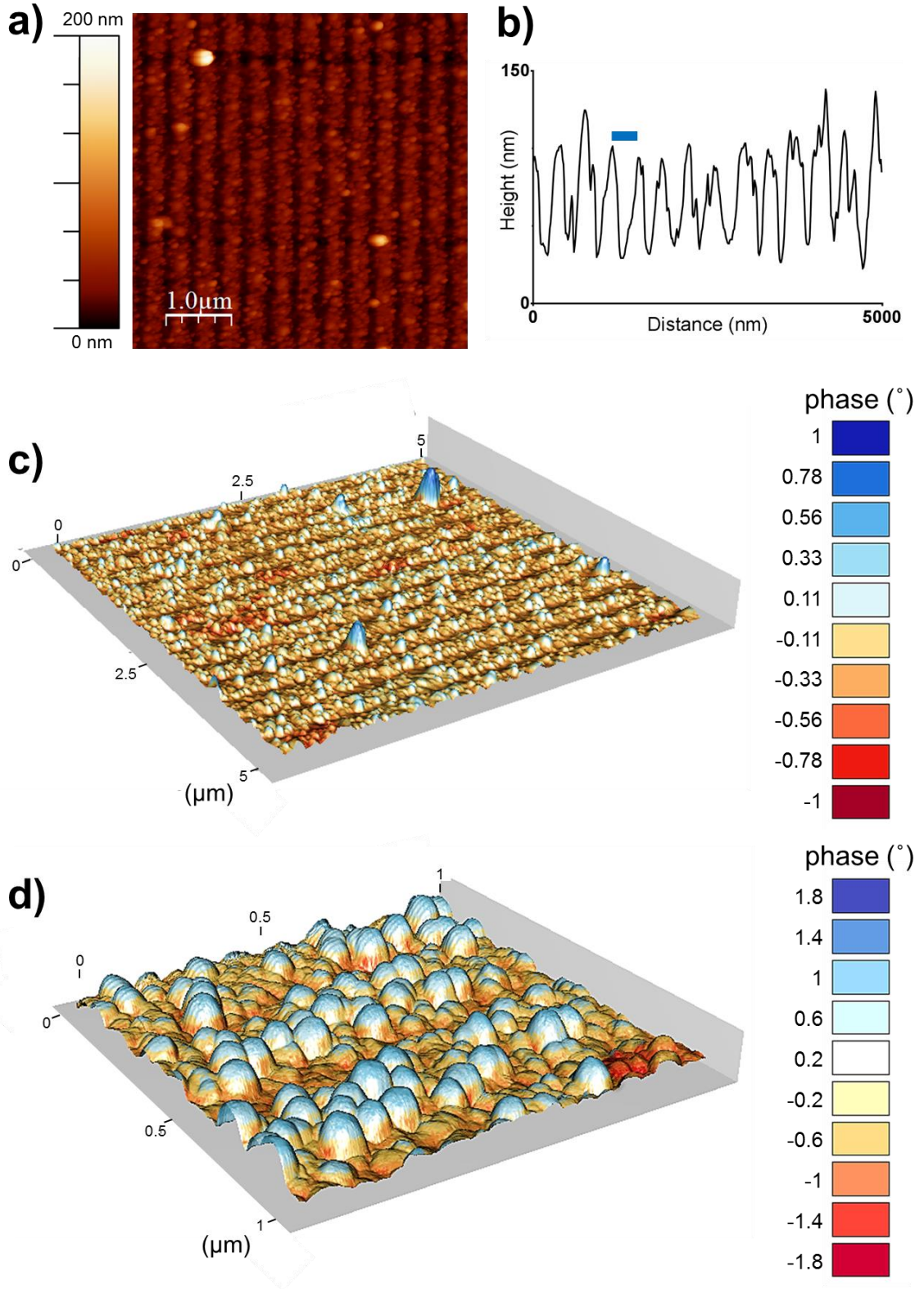
Figure 4.5.6 – Tapping mode AFM image (a), an example height profile across a section of the tapping mode AFM image (b, blue bar represents the average period 357 nm) and composite images of tapping mode AFM and MFM phase shift at a lift height of 50 nm (c and d, scales in μm) of a MNP array biotemplated by Mms6 after patterning by IL.

4.5.5 Forming Dot Arrays of Biomineralised Magnetite MNPs

For the first time, with the use of IL, Mms6 has been used to produce uniform lines of magnetite MNPs with nanoscale precision. This proof of principle experiment demonstrates that nanostructured arrays of magnetite nanoparticles can be biotemplated. Clearly, future work will be needed to address the geometry of the patterns formed, and optimise these for specific applications such as BPM. However, previous work has shown that a very wide range of packing geometries and particle morphologies is readily accessible by the IL patterning of SAMs [152, 153]. IL has been shown to generate dot arrays with nanoscale precision in SAMs, through the application of two identical exposures at 90˚ angles [150]. This approach could not be applied to the scheme followed in Section 4.5.2 (Figure 4.5.1) to generate dot arrays of Mms6. In this case a complete PEG SAM would be exposed twice at 90˚ angles to form dots of the PEG SAM, with the gold surface then backfilled with Mms6. The PEG SAM is used to block the attachment of the Mms6 protein, and control the location of the protein on the surface. Therefore, this approach would lead to the majority of the surface being covered by Mms6, the opposite configuration to what is required.

As a result, clean gold surfaces were immersed in a PBS buffer containing Mms6, so that a complete layer of Mms6 formed onto the surface. These surfaces were then taken through exactly the same process to the gold surfaces coated in a PEG SAM in Section 4.4.2, with the anticipation that the Mms6 protein exposed to the bright fringes formed over the surface would be photo-degraded. The surface could then go through the same exposure at a 90˚ angle to generate dot arrays of Mms6 on the gold surface, before being backfilled with a PEG SAM and a POFHK reaction (this process is outlined in Figure 4.5.7).
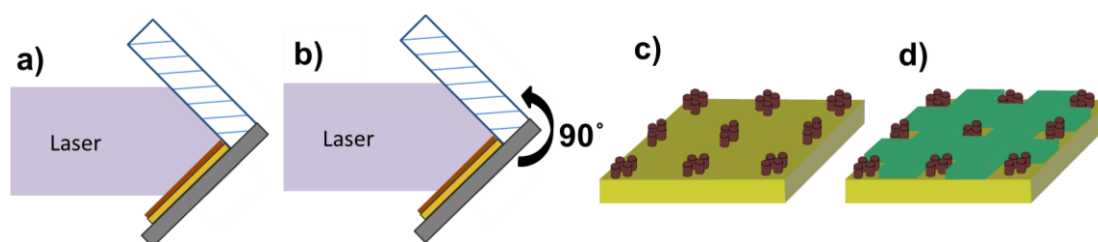
Figure 4.5.7 - Schematic of the process used to pattern gold with a dot array of Mms6 *via* IL. a) A gold surface with a complete layer of Mms6 protein (brown cylinders) is exposed to laser light in a Lloyd's mirror configuration. A diffraction pattern of bright and dark fringes is formed over the surface, with the areas of SAM exposed to the bright fringes being degraded more quickly. b) This exposure is then repeated at a 90˚angle. c) The Mms6 can be rinsed away to form a regular dot array of clean gold and Mms6 protein. d) The remaining clean gold space is then backfilled with a PEG SAM (green), before being subject to a POFHK reaction.

The approach outlined in Figure 4.5.7 could not be used to successfully pattern Mms6, simply because photodegrading the protein is much more difficult, and requires much more

energy than the simpler PEG. The Mms6 protein was found to remain stable on the surface even at IL doses as high as 100 mJ cm^{-2}. During these experiments the laser was operating at reduced power and with low stability, resulting in this type of exposure usually taking well in excess of an hour. Occasionally what appears to be blurred line patterns of MNPs could be seen in surfaces that underwent the process shown in Figure 4.5.7 without a second exposure at 90° (*i.e.* without step b in Figure 4.5.8), but surfaces containing uniform dot arrays of biomineralised magnetite MNPs were never formed.
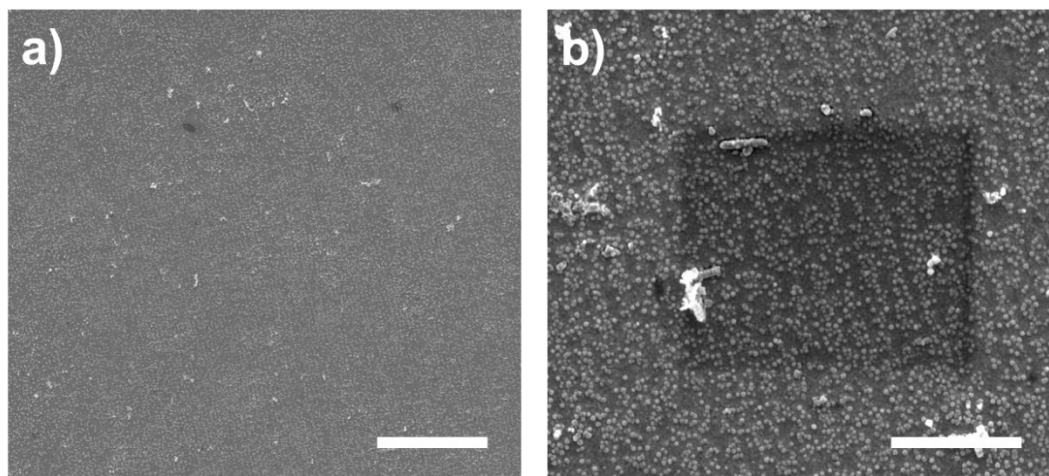
Figure 4.5.8 - SEM images of Mms6 surfaces patterned by IL, before being backfilled with a PEG SAM and subjected to a POFHK reaction. Scale bars: a – 19 μm and b – 2 μm.

In addition, this approach is also likely to suffer from the same problems discussed in Sections 4.2 and 4.3, where the backfilling of an Mms6 patterned gold surface leads to the disruption of the protein layer. Therefore, it is unlikely that this approach could be used to pattern Mms6 for the biomineralisation of uniform islands with nanoscale dimensions of magnetite MNPs using the approach outlined in Figure 4.5.7. Clearly, future work will be needed to address the geometry of the patterns formed, and optimise these for specific applications such as BPM. However, previous work has shown that a very wide range of packing geometries and particle morphologies is readily accessible by the IL patterning of SAMs [152, 153], and alternative strategies are discussed in Chapter 7.

5. Magnetite Nanoparticle Arrays formed with an Artificial Magnetite Binding Protein

"Physics is the only real science. The rest are just stamp collecting."

Ernest Rutherford

(I wonder what Rutherford would make of the interdisciplinary nature of this thesis)

5.1 Overview: Magnetite Interacting Adhiron 1 (MIA-1)

Within nature a wide range of different biomineralisation proteins have evolved, capable of controlling the formation of many different biomaterials [199]. However, they are not always suitable for use within technology, and the types of material they can biotemplate and the conditions in which they can be used are not exhaustive. These proteins can also be expensive and hard to manufacture, and restricts us to the materials available in nature. Recently, biopanning has uncovered many novel peptide sequences, capable of interacting with materials that are not found in nature (as discussed in Section 1.4.8) [105]. Building on this Rawlings *et al*. [114] combined this approach with a robust protein scaffold called Adhiron [115], which displays two peptide loops of variable sequence. A diverse library of different Adhirons were successfully screened for binding to the [100] face of magnetite. One artificial magnetite binding protein from this library, termed 'magnetite interacting Adhiron 1' (MIA-1), was found to be able to interact with forming magnetite nanoparticles during room temperature co-precipitation reactions and direct them towards a cubic morphology [114]. During QCM-D analysis MIA-1 was also found to form an ordered monolayer on a gold surface *via* a cysteine, and interact with MNPs magnetite when immobilised in this way [114].

In this section MIA-1 was immobilised onto gold surfaces *via* attachment through a cysteine residue, which is present at the *C*-termini of the protein [114]. This provides a potentially new route to forming biomineralised arrays of magnetite MNPs. Firstly, in each case, gold surfaces were patterned with a PEG SAM with the use of μCP (using an identical method to that used to pattern Mms6 in Chapter 3). Following this, a range of different methods were used to investigate the action of MIA-1, to determine the best route for forming MNP arrays (these schemes are summarised in Figure 5.1.1 and the key differences and similarities are highlighted in Table 5.1.1):

Scheme I) The unmodified gold areas of the gold surfaces patterned with PEG were backfilled with MIA-1, and these surfaces were then subjected to a POFHK reaction (in the same way that surfaces patterned with Mms6 were in Chapter 3). The MIA-1 was previously shown to direct the formation of MNPs of magnetite towards a cubic morphology during a room temperature co-precipitation (RTCP) reaction [114]. As the Adhiron protein scaffold itself was designed to be very robust and is known to be stable up to 100°C, it should also be stable under the mild heating to 80°C involved in a POFHK reaction [115]. Therefore, it was anticipated that MIA-1 would direct the growth of MNPs of magnetite with a cubic morphology onto the patterned surfaces. Previously, an RTCP reaction was found to be unsuitable for forming MNP arrays with

Mms6 [98, 154]. It was unclear whether this would be the case when MIA-1 was used. Therefore, MIA-1 patterned surfaces were also subjected to a RTCP reaction and these were compared to those that formed in a POFHK reaction.

Scheme II) MIA-1 was previously selected for binding to the [100] face of magnetite. Therefore, it was considered that this protein may be better suited to binding to pre-formed magnetite nanoparticles than Mms6 is. Gold surfaces patterned with MIA-1 were supplied with MNPs of magnetite, which were pre-formed in POFHK and RTCP reactions, with the aim that the protein would bind the magnetite MNPs that were present. Also, a more uniform subset of MNPs may bind to the MIA-1 patterned surface, as MIA-1 may act to filter out MNPs with certain properties (*i.e.* by only binding to MNPs of magnetite, or to a particular crystallographic face).

Scheme III) Instead of the first step being the immobilisation of MIA-1 onto the unmodified gold areas of a PEG patterned gold surface, in this scheme the protein was added directly to solution during POFHK and RTCP magnetite mineralisation reactions. It was anticipated that the protein would direct the growth of cubic MNPs of magnetite, before binding to these MNPs. The PEG patterned substrates were then added after the mineralisation reactions, so that MIA-1 (bound to MNPs of magnetite) would then be immobilised on the clean gold areas of the surface *via* the cysteine residue.

Scheme IV) As with Scheme III, MIA-1 was not initially immobilised on the unmodified gold areas of the PEG patterned gold surfaces. Instead, the protein was incubated in a solution containing MNPs that were pre-formed in POFHK or RTCP reactions, with the intention that the protein would bind to MNPs. Gold surfaces patterned with PEG were then added to the solution, so that the protein would order these MNPs onto the clean gold arrays to form a MNP array.
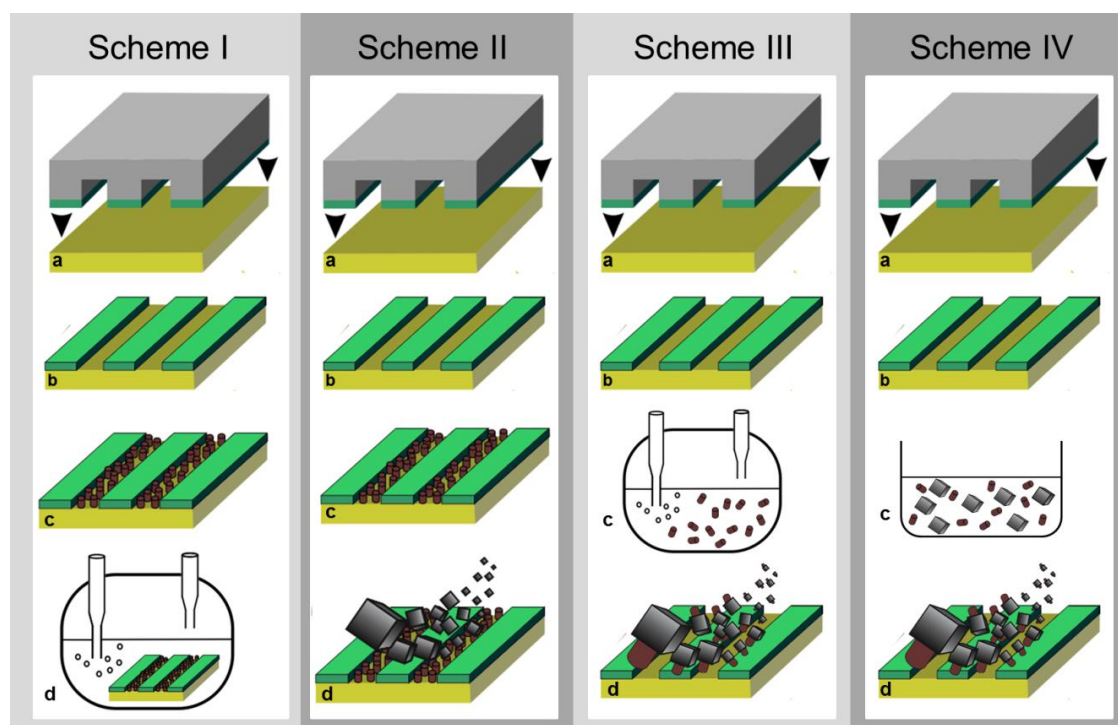
Figure 5.1.1 - Schematic of the experimental schemes. In each of the schemes a PEG SAM (green) is printed onto a gold surface with the use of μCP (a-b). In Scheme I the remaining space is than backfilled with MIA-1 (c), and the protein patterned surface is subjected to a mineralisation reaction (d). In Scheme II the remaining space is also backfilled with MIA-1 (c), but in this case pre-formed MNPs are supplied to the surface. In Scheme III a mineralisation reaction is performed in the presence of MIA-1 (c), the magnetic nanoparticle-protein composites are then supplied to the PEG patterned surface (d). In Scheme IV MIA-1 is mixed with pre-formed nanoparticles (c), with these magnetic nanoparticle-protein composites supplied to the PEG patterned surfaces (d).

Table 5.1.1 – A summary of the key differences and similarities between the four schemes.

	Scheme I	Scheme II	Scheme III	Scheme IV
MIA-1 exposure to magnetite	Added to a mineralisation reaction.	Supplied with pre-formed MNPs	Added to a mineralisation reaction.	Supplied with pre-formed MNPs
Point of MIA-1 immobilisation	Before mineralisation reaction	Before exposure to pre-formed MNPs	After mineralisation reaction	After exposure to pre-formed MNPs

5.2 Comparison of RTCP and POFHK Mineralisation Reactions

RTCP and POFHK reactions were used to form MNPs of magnetite. When added to the reaction solution MIA-1 was previously shown to direct a RTCP reaction towards the formation of cubic magnetite [114]. A RTCP was found to be unsuitable for the production of MNPs using surfaces patterned with Mms6 [97, 98, 154] (as in Chapter 3), but it remained unclear whether this would be the case for MIA-1 and for all of the different schemes trialled in this Chapter. Therefore, both RTCP and POFHK reactions were used in Schemes I-IV (Figure 5.1.1), to determine which reaction would form the best route to synthesising MNP arrays of

magnetite with the use of MIA-1. The formation of iron oxides is complex, and many intermediates or other iron minerals can be formed during the course of a mineralisation reaction [27, 200]. Therefore, the pH traces of the RTCP and POFHK reactions used in this study are compared here (Figure 5.2.1), which allows the reaction process to be analysed.
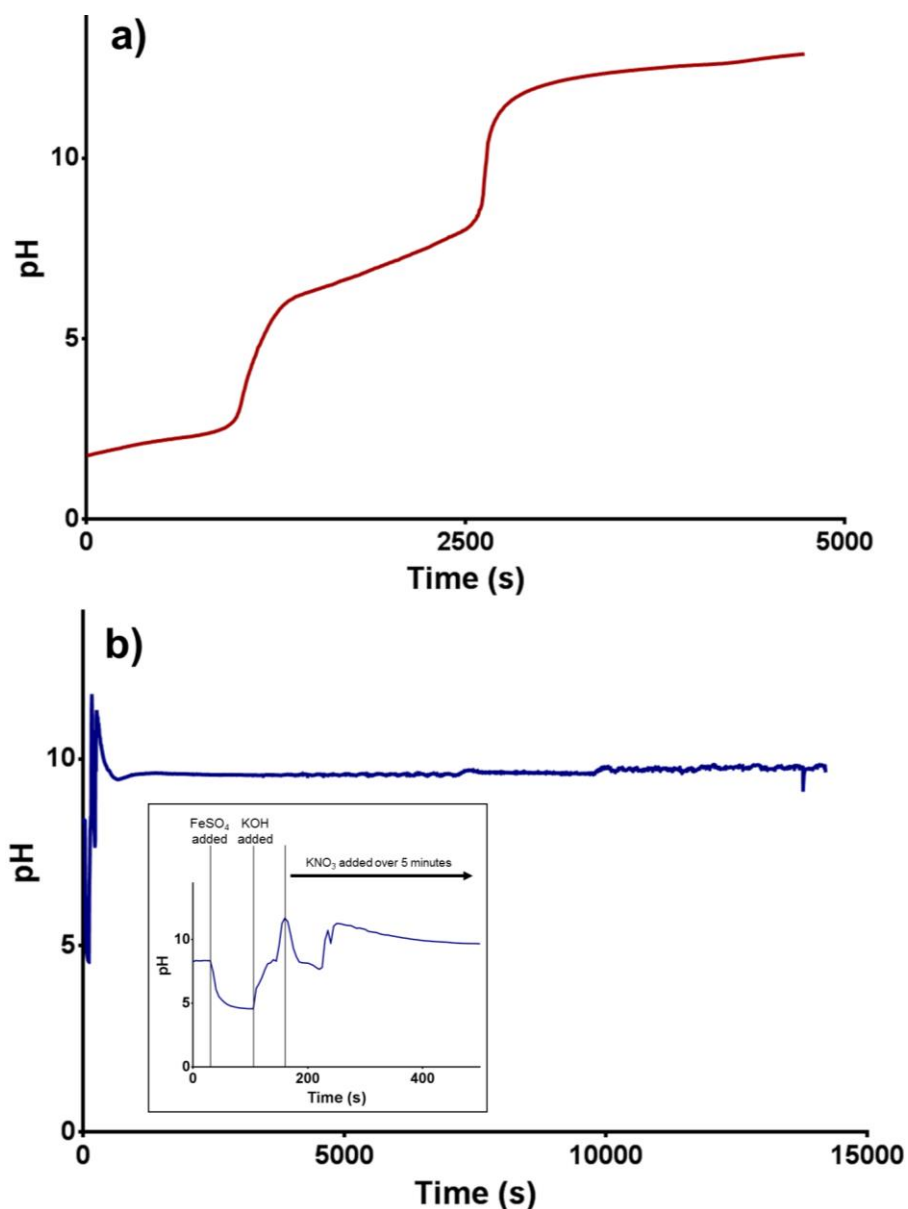
Figure 5.2.1 – pH traces recorded for the RTCP (a) and POFHK (b) mineralisation reactions used to form MNPs of magnetite (inset in (b) is a zoom in on the start of the POFHK reaction, where the different reactants were added).

Figure 5.2.1 displays pH traces recorded during the RTCP and POFHK mineralisation reactions (full experimental details for these two reactions can be found in Chapter 2.4) that were used to generate MNPs of magnetite in Schemes I-V (Figure 5.1.1). During the RTCP reaction ferrous and ferric iron salts are dissolved in aqueous solution, after which base is added at a constant rate over approximately 80 minutes. The pH increases from approximately 2 to 13 over the duration of the reaction (Figure 5.2.1a). The processes that

take place during the reaction have been well documented, with an in depth analysis performed by Ruby *et al*. [200]. Initially, the pH remains almost constant as base is added, as the ferric iron is converted to ferric basic salts (e.g. ferric oxyhydroxide). After all of the ferric iron is consumed the pH increases rapidly as the base is added, explaining the rise in the recorded pH after approximately 900 seconds (Figure 5.2.1). As addition of base increases the ferrous iron is precipitated after approximately 1200 seconds, resulting in a second plateau in the recorded pH trace (Figure 5.2.1). This generates the formation of unstable green rusts, which, with continued base addition, quickly convert to magnetite.

On the other hand the POFHK reaction goes through a smaller range of pH values, whilst remaining at a stable pH of approximately 9 for the majority of the 4 hour reaction (Figure 5.2.1b). During this reaction ferrous hydroxide is formed shortly after the mixing of a ferrous iron salt and potassium hydroxide. This is then partially oxidised by potassium nitrate [169]. Initially, a ferrous iron salt is dissolved into an aqueous solution, resulting in a decrease in pH to approximately 5. After less than 1 minute the pH then rises above 10 as the base is added. Potassium hydroxide is then added over 5 minutes, as the pH quickly stabilises to approximately 9 for the remainder of the reaction.

When compared to the POFHK reaction, the RTCP reaction has the advantage of not requiring mild heating to 80˚C. However, it does experience a wider range of pH values. The MNPs that were formed in each of these two reactions were then analysed with TEM (Figure 5.2.2). It can immediately be seen by comparing the TEM images in Figure 5.2.2 that the large number of elongated needle shaped MNPs that formed in the POFHK reaction were not seen to form in the RTCP reaction. However, a large amount of material, which appears with less contrast in the TEM images, can be seen to have formed in the RTCP reaction. This is probably green rust phases that did not convert to magnetite, and due to their lack of contrast in the TEM images, could not be included in the grainsize analysis.

Grainsize analysis (Figure 5.2.2) reveals that the MNPs formed in the RTCP reaction feature a smaller mean size ($\approx 54 \pm 21$ nm) than in the POFHK reaction ($\approx 63 \pm 27$ nm). The measured aspect ratio of the MNPs confirms that the large number of acicular nanoparticles (long needle shaped crystals that can be seen in Figure 5.2.2b) that formed during the POFHK reaction did not form during the RTCP reaction. As discussed previously (Section 3.2) these needle shaped structures are probably another iron mineral and not magnetite, leading to a bimodal distribution in the measured aspect ratio of the MNPs (Figure 5.2.2f).
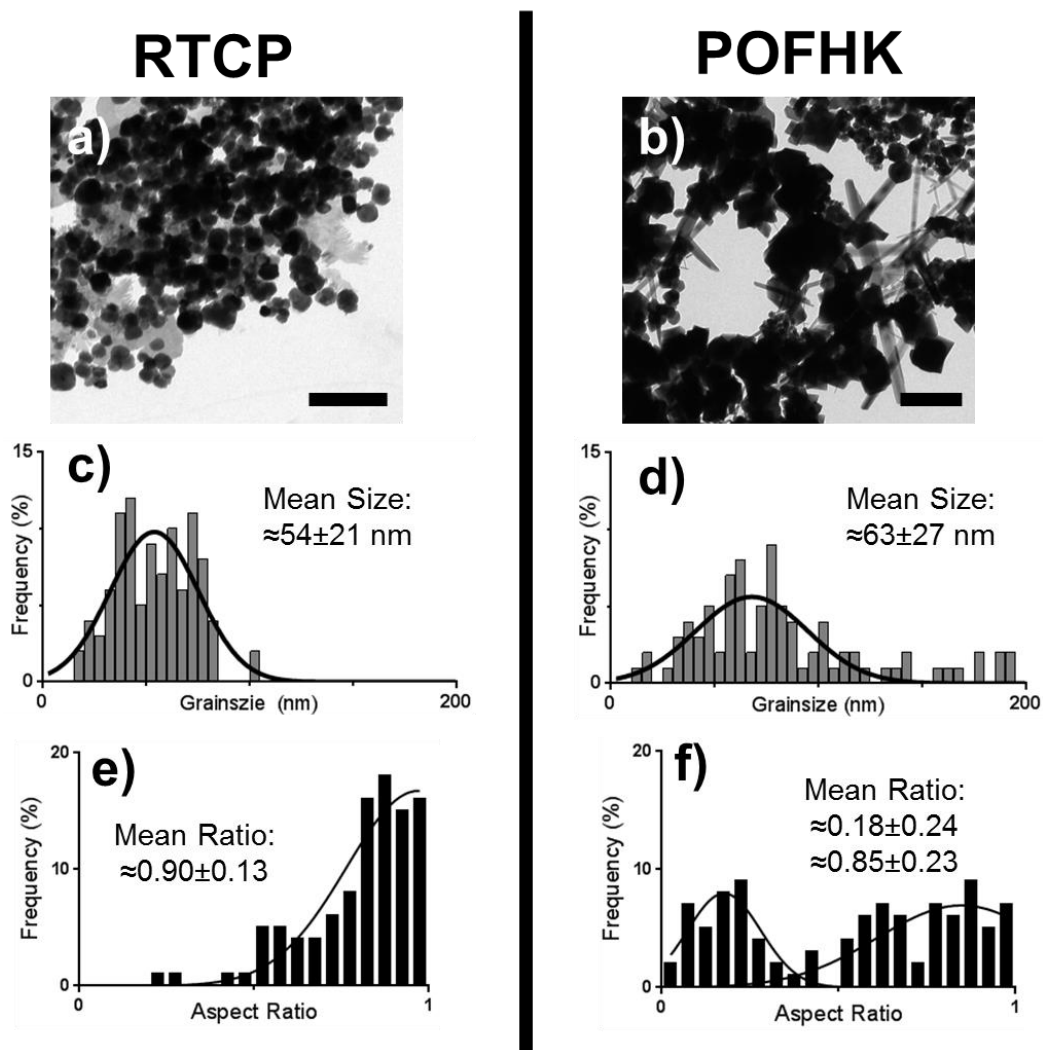
Figure 5.2.2 – TEM images (a and b, scale bars 200 nm), grainsize analysis (c and d) and aspect ratio (e and f) of the MNPs that formed in a RTCP (a, c and e) and POFHK (b, d and f) reaction.

To provide further confirmation that magnetite was formed in the RTCP and POFHK reactions, crystallographic analysis was performed using XRD (Figure 5.2.3). The positions of the peaks were then converted to *d*-spacings (using Equation 2.5.1, Table 5.2.1). As described in Section 3.2 these values were compared to the known values (from the JCPDS crystallographic database) for magnetite as well as maghemite and goethite.
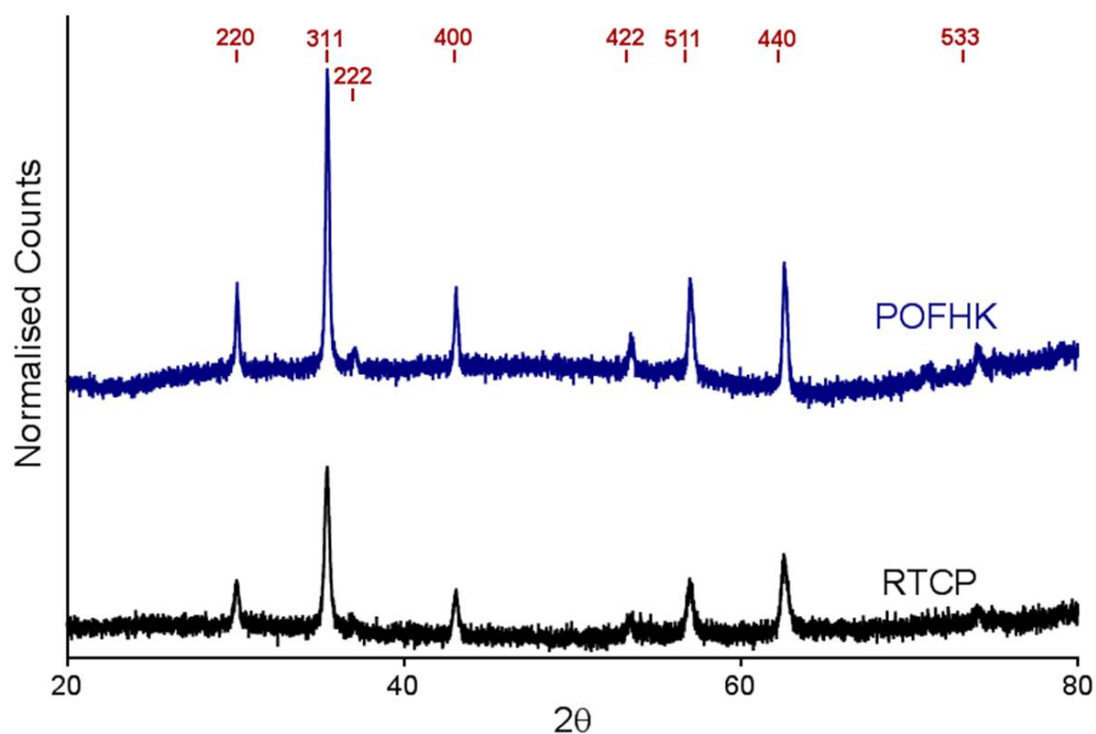
Figure 5.2.3 - XRD diagram of MNPs synthesised in a RTCP (black) and a POFHK (blue) reaction. Peaks are offset for clarity, and the expected peak positions for magnetite (red) are highlighted.

Table 5.2.1 – Summary of the *d*-spacings for maghemite, goethite and magnetite, and the MNPs formed in a RTCP and a POFHK reaction shown in Figure 5.2.3 (all measured in Å). Maghemite values are from JCPDS card 00-039-1346, magnetite from 00-019-0629 and goethite from 01-081-0464. The value which is the closest match to the MNPs that formed in solution during the RTCP or POFHK retraction are highlighted in green and orange respectively, and only those plains on the JCPDS card that are the nearest to the peak are shown.

Peak	Maghemite	Magnetite	Goethite	RTCP	POFHK
(220)	2.950	2.966		2.969	2.966
(130)			2.693		
(311)	2.520	2.530		2.530	2.534
(101)			2.527		
(111)			2.449	2.426	2.423
(222)	2.410	2.419			
(220)			2.190	2.099	2.097
(400)	2.080	2.096			
(221)			1.719	1.713	1.711
(422)	1.700	1.712			
(511)	1.610	1.614		1.615	1.615
(231)			1.603		
(440)	1.480	1.483		1.483	1.483
(241)			1.475		
(042)			1.292	1.280	1.280
(533)	1.270	1.279			

The XRD diagram (Figure 5.2.3) shows peaks at 2θ = 30.10°, 35.48°, 37.09°, 43.10°, 53.49°, 57.01°, 62.63° and 74.05°, and 2θ = 30.13°, 35.42°, 37.10°, 43.13°, 53.55°, 57.01°, 62.62° and 74.07° for the MNPs that were formed in RTCP and POFHK reactions respectively. All the peaks were a close fit to the magnetite (220), (311), (222), (400), (511), (440) and (533) peaks and a closer fit than for maghemite or goethite (Table 5.2.1). This suggests that in the most part magnetite was formed in both the RTCP and POFHK reactions, and that the MNPs that were formed were not subjected to heavy oxidisation.

The dominant (311) peak was then fitted to the Debye-Scherrer equation (Equation 2.5.2) to determine the grainsize of the particles [178]. This fitting found that MNPs had a mean size of ≈59 nm and ≈79 nm for the MNPs that were formed in RTCP and POFHK reaction respectively. This analysis provides further confirmation that the MNPs formed in the POFHK reaction with a larger mean size. However, this analysis assumes the particles are perfectly crystalline with a narrow grainsize distribution [179]. Discrepancies between these values and the mean size calculated from the grainsize analysis (Figure 5.2.2) may be a result of the nanoparticles forming with a large size distribution, and with a crystallinity that was not uniform.

5.3 SEM Analysis of the Biomineralised MNP Arrays

The MNP arrays synthesised following Schemes I-IV (Figure 5.1.1) were analysed by SEM, and the results are displayed in Figures 5.3.1 and 5.3.2 for MNPs that were synthesised by RTCP and POFHK reactions respectively. Unlike the surfaces patterned with Mms6 (Chapter 3), SEM analysis showed Scheme I was the least successful approach. When a MIA-1 patterned surface was placed into a RTCP reaction the surfaces were covered in a layer of MNPs, both on regions patterned with the protein and the PEG SAM. On the other hand, when Scheme I was combined with a POFHK reaction only a limited number particles were seen to form on the surface, including the protein patterned regions.
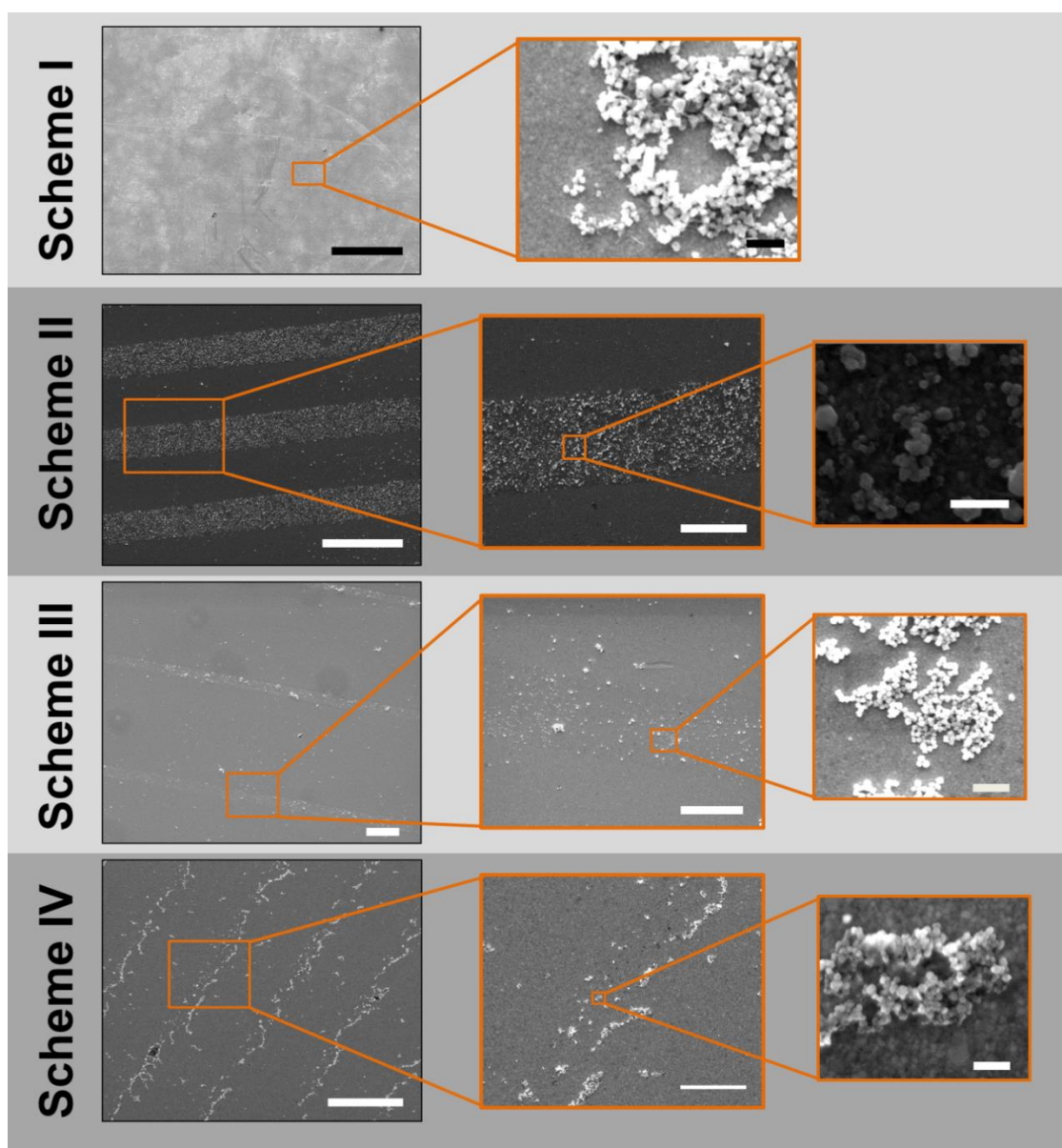
Figure 5.3.1 – SEM images of the biomineralised MNP arrays formed by MIA-1 using MNPs synthesised in a RTCP reaction, following the four experimental schemes outlined in Figure 5.1.1. Scale bars: Scheme I – 20 µm left, 200 nm right, Scheme II, III and IV – 20 µm left, 5 µm centre and 200 nm left.

Of the other three schemes trialled, Scheme II appears to result in the production of the most dense and clearest MNP patterns. When surfaces patterned with MIA-1 were supplied with MNPs that were performed separately in both RTCP and POFHK reactions, a dense layer of nanoparticles were found to bind to the protein patterned regions with only limited binding to the PEG SAM. It can be seen in Figures 5.3.1 and 5.3.2 that Schemes III and IV also formed patterns of MNPs, but these patterns look to be much less consistent and less populated with nanoparticles.
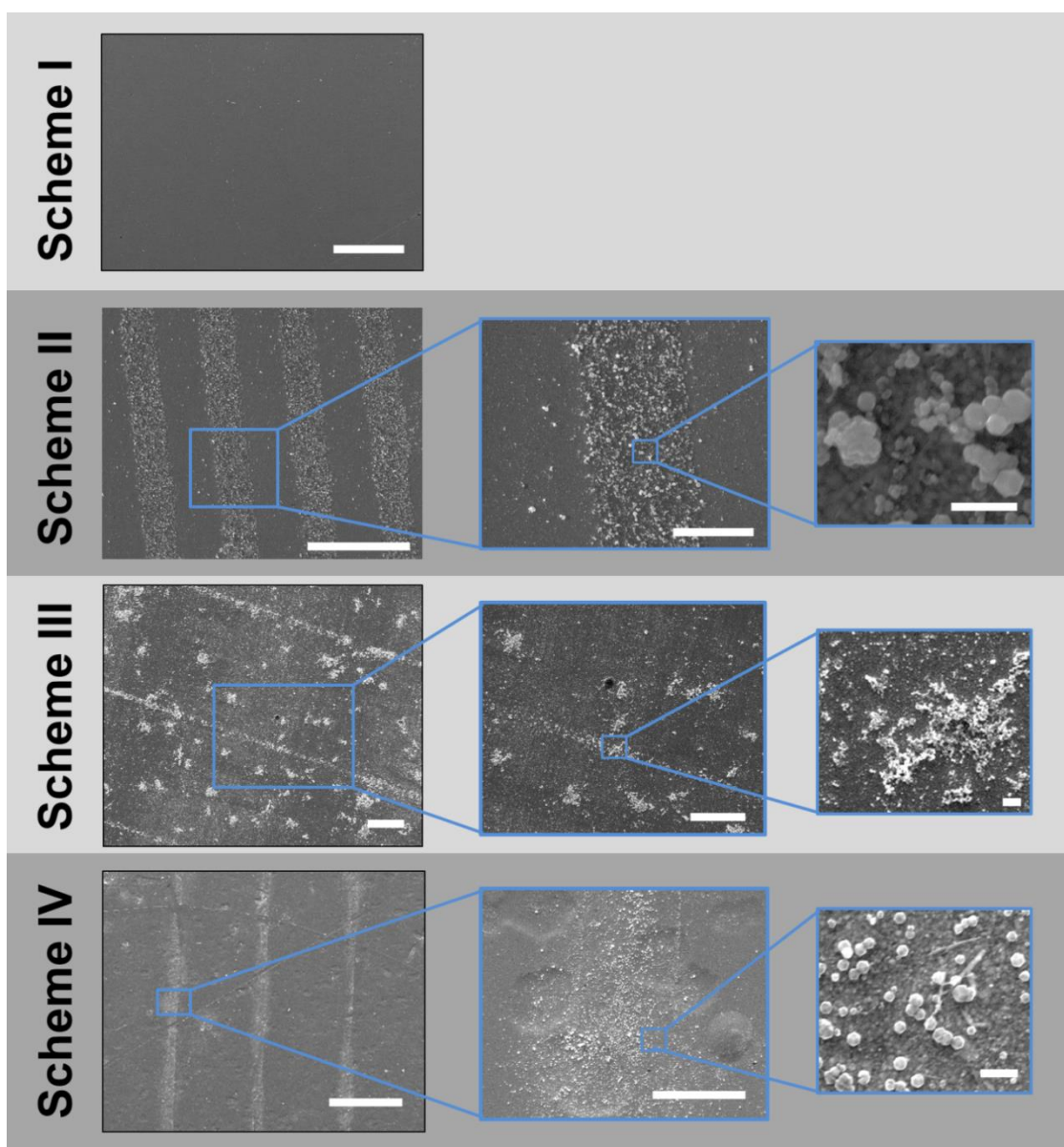
Figure 5.3.2 – SEM images of the biomineralised MNP arrays formed by MIA using MNPs synthesised in a POFHK reaction, following the four experimental schemes outlined in Figure 5.1.1. Scale bars: Scheme I – 100 μm, Scheme II, III, and IV - 20 μm left, 5 μm centre and 200 nm left.

The MNPs found to form on the MNP surfaces using Schemes III and IV can be seen to have collected into high density regions on the gold surface, separated by regions sparsely populated with nanoparticles. This is in much the same way that MNPs have been previously found to form on clean gold surfaces (Figure 3.3.1). The density of MNPs that formed on the MNPs surfaces produced with Schemes II-IV were quantified by recording the number of particles in five randomly selected areas of SEM images of the surfaces (Figure 5.3.3).[*] This

---

[*] These areas were all on the areas patterned with MIA-1, and not the antibiofouling PEG regions.

analysis confirmed that a greater number of MNPs formed on the surfaces with the use of Scheme II, when either the products from RTCP or POFHK reactions were used.
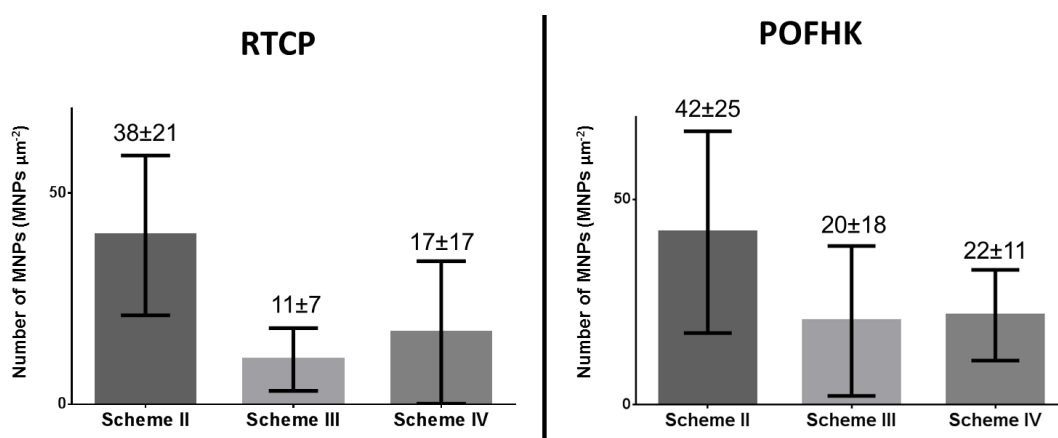
Figure 5.3.3 - Particle density measurements and standard deviation of MNPs on surfaces using Schemes II-IV with RTCP (left) and POFHK (right) reactions.

5.4 Comparison of Schemes I-IV

The surface from Scheme I showed a layer of MNPs was present on the gold surface during a RTCP reaction, on both the regions patterned with MIA-1 and the PEG SAM background. It was previously shown that after a POFHK reaction, MNPs are not present on a PEG SAM (Figure 3.3.2). The presence of MNP over all regions of the surface in Scheme I suggests that the antibiofouling SAM may have been removed during the RTCP reaction. The RTCP is carried out through a large range of pH (Figure 5.2.1), which could lead to the PEG SAM and MIA-1 being degraded or completely removed from the surface. MNPs could then bind to the exposed gold surface. To determine if this was the case, gold surfaces covered in a complete PEG SAM (without any patterning with μCP and backfilling with MIA-1) were placed into a RTCP reaction. SEM analysis (Figure 5.4.1) revealed that MNPs formed on these surfaces in the same way as the MIA-1 patterned surfaces, suggesting that the PEG SAM was degraded or removed from the surface during a RTCP reaction.
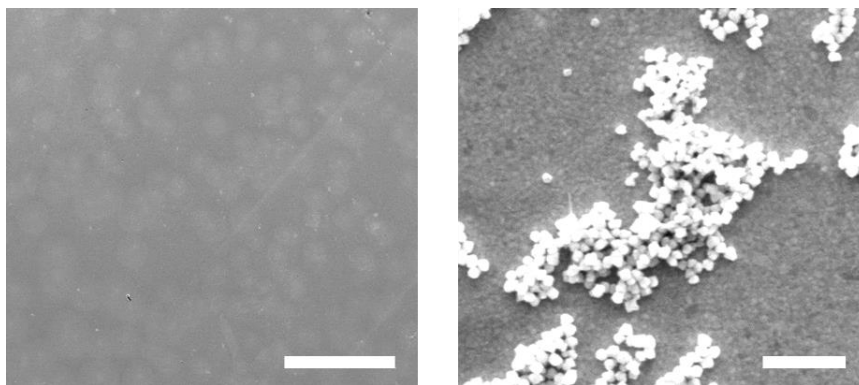
Figure 5.4.1 – SEM images of gold surfaces covered with a complete PEG SAM after a RTCP reaction. Scale bars: 250 µm (left) and 1 µm (right).

Conversely, when a POFHK reaction was combined with Scheme I, only a negligible number of MNPs formed on the surface. As MNPs have been shown to form on an unmodified gold surface during a POFHK reaction (Figure 3.3.1), this suggests that MIA-1 remained on the surface during this reaction. The reason for the lack of MNP formation on the MIA patterned regions could be explained by considering how the protein functions. MIA-1 displays two peptide loops, which interact strongly with the [100] face of magnetite [113]. Unlike the active *C*-terminal region of Mms6 that contains a large number of acidic amino acids, the first binding loop of MIA-1 is dominated by basic amino acids. In particular there are a large number of lysine residues, which are believed to form strong interactions with the [100] face of magnetite [113]. The second loop remains basic overall, but does contain some acidic and hydrophobic amino acids. Therefore, unlike Mms6, that is believed to nucleate iron irons, MIA-1 appears to be unable to bind the MNPs of magnetite that form under the basic conditions of POFHK reaction (Figure 5.2.1b).

A layer of MNPs forms on MIA-1 patterned regions in Scheme II, when MNPs formed in both RTCP and POFHK reaction were supplied. The peptide loops displayed on MIA-1 were selected to interact strongly with magnetite. The SEM analysis suggests that the surface immobilised MIA-1 was able to bind to the MNPs that were supplied in aqueous solution. During schemes III and IV MIA-1 was not initially immobilised onto the gold surface, but instead the protein was added to the mineralisation reaction or placed into a solution of pre-formed MNPs prior to gold surface immobilisation. However, these two Schemes were found to be less effective at forming an MNP array than Scheme II, resulting in fewer MNPs forming on the surface.

It remains unclear from analysis of surfaces from Schemes III and IV whether all the MNPs bound to MIA-1, and it was not possible to separate the MNPs that were bound to the

protein from those that were not. Therefore, it remains possible that protein free MNPs could stick to the unmodified areas on the PEG patterned gold surfaces that were supplied. It is also probable that multiple proteins could interact with the same MNP, and this could have an effect on the density of the MNP array formed. However, it is clear that Schemes III and IV were less successful at forming biotemplated MNP arrays than Scheme II. As a result, Scheme II was taken forward for further analysis.

5.5 Grainsize Analysis

The MNPs that bound to MIA-1 patterned surfaces following Scheme II were compared to the MNPs from RTCP and POFHK reactions that had been supplied to them (Figure 5.5.1). As discussed in Section 5.2, the control MNPs in a RTCP reaction had a smaller mean size (≈54±21 nm) compared to the product of a POFHK reaction (≈63±27 nm). The large number of acicular particles that were found to form in a control POFHK reaction was not present in the sample product from a control RTCP reaction. However, a large amount of amorphous material was seen to form.
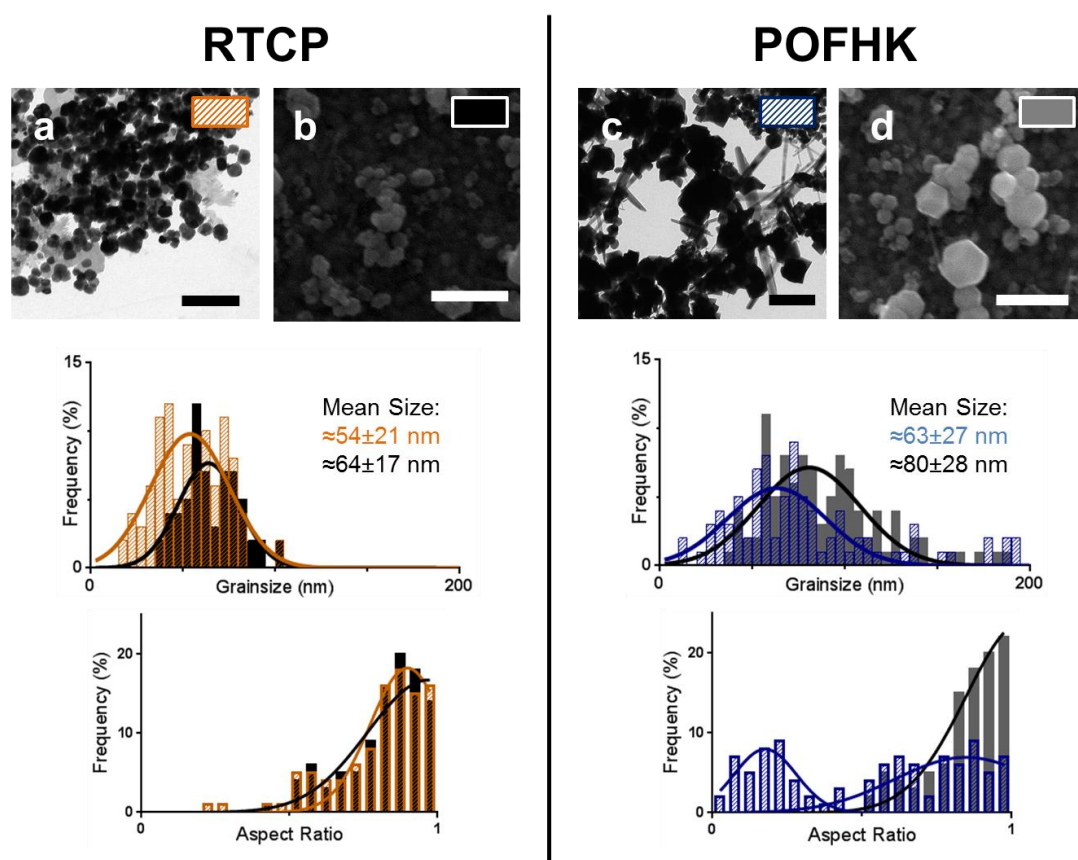
Figure 5.5.1 – TEM images (scale bars 200 nm), grainsize analysis and the measured aspect ratio of MNPs formed in a RTCP reaction (a, orange) and a POFHK reaction (c, blue), and of particles pre-formed in a RTCP (b, black) and POFHK (d, grey) reactions that bound to MIA-1 patterned surface following Scheme II.

When MNPs that were pre-formed in an RTCP reaction were supplied to MIA-1 patterned surfaces, they were found to have a larger mean size (≈64±17 nm) and similar distribution with respect to aspect ratio (Figure 5.5.1) when compared to the characteristics of the MNPs formed in a control RTCP reaction. The amorphous material, which was seen to form in the control RTCP reaction, was not found on the MIA-1 surface. Therefore, this suggests that the protein did not bind to this material, and, as this material is probably not magnetite, provides evidence that suggests the protein is selective for magnetite. MIA-1 was also selective for the larger MNPs that formed during the RTCP reaction, with the number of smaller particles (<35 nm) significantly reduced compared to the MNPs that formed in a control RTCP reaction. This could be an effect of batch to batch variation in the size of the MNPs formed during the RTCP (for example a warmer day can lead to an increase in the reaction temperature), or a result of larger MNPs mediating more contacts with a greater number of MIA-1 proteins that act to stabilise them onto the surface more quickly.

Similarly, when particles produced in a POFHK reaction were supplied to the surfaces patterned with MIA-1, once again the smallest particles formed in the reaction did not bind to MIA-1 reflecting in a larger mean size (≈80±28 nm). The large number of acicular particles that formed in the control POFHK reaction was not seen to bind to the MIA-1 patterned surface, reflecting in the measured aspect ratio that was no longer bimodal. As these needle shaped crystals are unlikely to be magnetite, this provides further evidence to suggest that MIA-1 is selective for the MNPs of magnetite that were formed in the control POFHK reaction, and not the acicular MNPs that are most probably another iron mineral.

5.6 Crystallographic Analysis

Crystallographic analysis of the MNP surfaces produced with Scheme II was performed using XRD (Figure 5.6.1), and the position of the peaks were converted to *d*-spacings (using Equation 2.5.1, Table 5.6.1). As described in Section 3.2 the sample was compared to the known values (from the JCPDS crystallographic database) for maghemite and goethite as well as the expected magnetite.
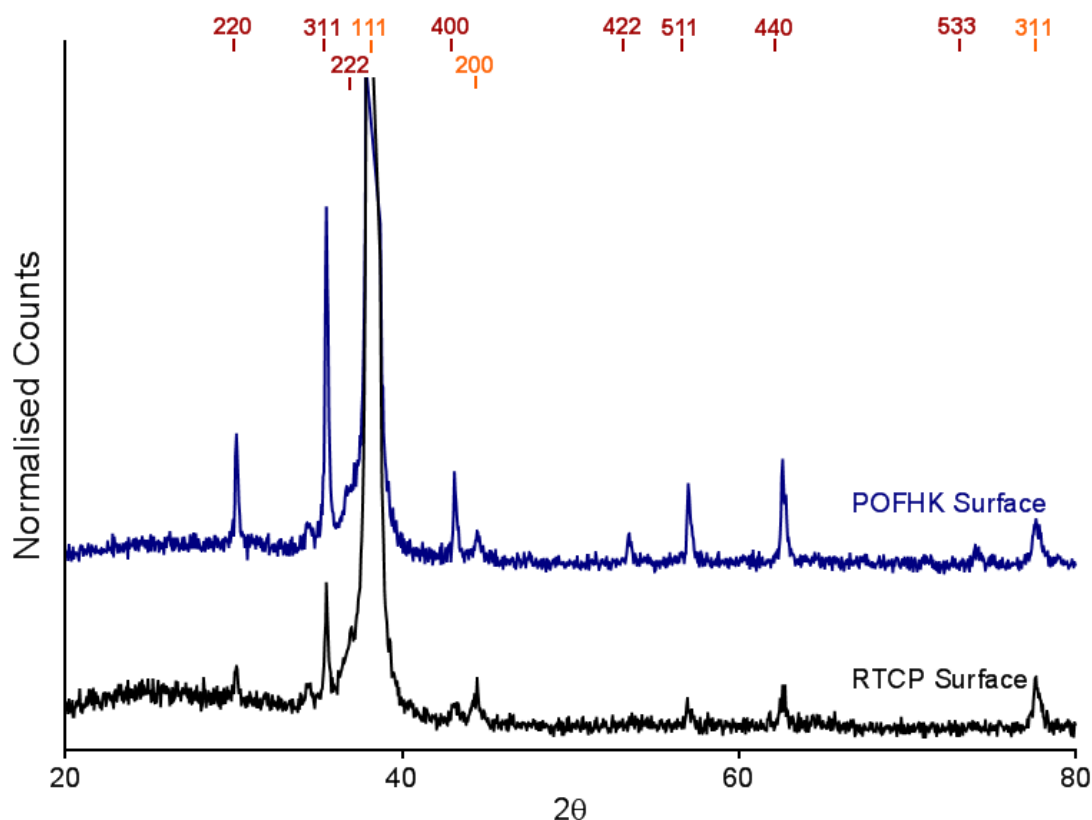
Figure 5.6.1 - XRD diagram of the biotemplated MNP surfaces formed by supplying a gold surface patterned with MIA with pre-formed MNPs produced by RTCP (black) and POFHK (blue). Peaks are offset for clarity, and the expected peak positions for magnetite (red) and gold (gold) are highlighted.

Table 5.6.1 - Summary of the *d*-spacings for maghemite, goethite and magnetite, and the MNPs formed with Scheme II when MNPs pre-formed in a RTCP and a POFHK reaction were supplied shown in Figure 5.6.1 (all measured in Å). Maghemite values are from JCPDS card 00-039-1346, magnetite from 00-019-0629 and goethite from 01-081-0464. The value which is the closest match to the RTCP or POFHK surface are highlighted in green and orange respectively, and only those plains on the JCPDS card that are the nearest to the peak are shown.

Peak	Maghemite	Magnetite	Goethite	RTCP Surface	POFHK Surface
(220)	2.950	2.966		2.962	2.962
(130)			2.693		
(311)	2.520	2.530		2.529	2.529
(101)			2.527		
(111)			2.449	_*	_*
(222)	2.410	2.419			
(220)			2.190	2.093	2.097
(400)	2.080	2.096			
(221)			1.719	_†	1.711
(422)	1.700	1.712			
(511)	1.610	1.614		1.614	1.614
(231)			1.603		

---

* Obscured by the dominant Au(111) peak.
† Peak not distinguishable.

(440)	1.480	1.483		1.479	1.483
(241)			1.475		
(042)			1.292		1.276
(533)	1.270	1.279		-†	

The XRD diagram (Figure 5.6.1) shows peaks at 2θ = 30.17°, 35.52°, 43.24°, 57.05°, 62.85° and 2θ = 30.17°, 35.52°, 43.14°, 53.56°, 57.06°, 62.64° and 74.33° for the MNP arrays formed with Scheme II after RTCP or POFHK particles were supplied respectively. These are all a close fit to the magnetite (220), (311), (222), (400), (422), (511), (440) and (533) peaks and a closer fit than the peaks for maghemite (Table 5.6.1). There is one exception, the (440) peak was found to be a closer fit for maghemite than magnetite when RTCP MNPs were supplied. Additionally, the (222) peak for magnetite is not visible on the data recorded for the MNP arrays formed on the gold surfaces, as the dominant (111) peak for gold obscures this peak. The (422) and (533) peaks were also not distinguishable in the XRD data recorded for the MNP surfaces. It can be seen in Figure 5.6.1 that the XRD signal recorded for the Scheme II RTCP MNP arrays is not as strong as the POFHK system. This is most probably a result of there being less MNPs present (grainsize analysis also found MNPs formed in a RTCP reaction with a smaller mean size). During SEM analysis it did not appear that less MNPs bound to the MIA-1 patterned regions. It could be that the patterned region was less extensive on the sample that was analysed with XRD due to a less efficient stamping process during µCP. However, in general these data strongly suggest that in the most part MNPs of magnetite bound to the MIA-1 patterned surfaces.

As with the MNPs that were supplied to the MIA-1 patterned surfaces (Section 5.2), the dominant (311) peak was then fitted to the Debye-Scherrer equation (Equation 2.5.2) to measure the grainsize of the particles [11]. In this case the fitting found that the MNPs that bound to the MIA-1 patterned surfaces had a mean size of 75 nm (RTCP) and 87 nm (POFHK). This analysis confirms the slightly larger mean size of the MNP that bound to the MIA-1 patterned surfaces. Differences between the mean sizes calculated from the grainsize analysis (Figure 5.5.1) could be due to the nanoparticles forming with a large size distribution, a crystallinity that was not uniform, or a combination of these factors [12].

5.7 Nanoscale Patterns

In the previous section it was shown that MNP arrays of magnetite can be formed on gold surfaces patterned with MIA-1 *via* Scheme II. Gold surfaces are first patterned with an

antibiofouling PEG SAM, before the remaining clean gold space is backfilled with MIA-1. MNPs of magnetite bind to the protein patterned regions when MNPs that were pre-formed in either RTCP or POFHK reactions are supplied. This forms an alternative approach to that which was developed for Mms6 and discussed in Chapter 3 (in that case the most efficient route to forming arrays of magnetite MNPs was found to be by using Mms6 in a POFHK reaction). Therefore, with the aim of forming nanoscale MNPs with MIA-1 the first step of Scheme II, the patterning of a protein resistant PEG SAM to gold with μCP, was replaced by patterning the PEG SAM layer with IL (as discussed in Chapter 4). A complete PEG SAM layer formed on a gold surface was exposed to laser light (λ=244 nm) in a Lloyd's mirror configuration, so that a dose of 20 J cm^{-2} at a mirror-surface angle of 2θ=20° was applied. This generates a regular line array of PEG SAM and unmodified gold, with dimensions on the nanoscale. The unmodified gold space was then backfilled with MIA-1, and MNPs that were pre-formed in an RTCP reaction were then washed over these surfaces.
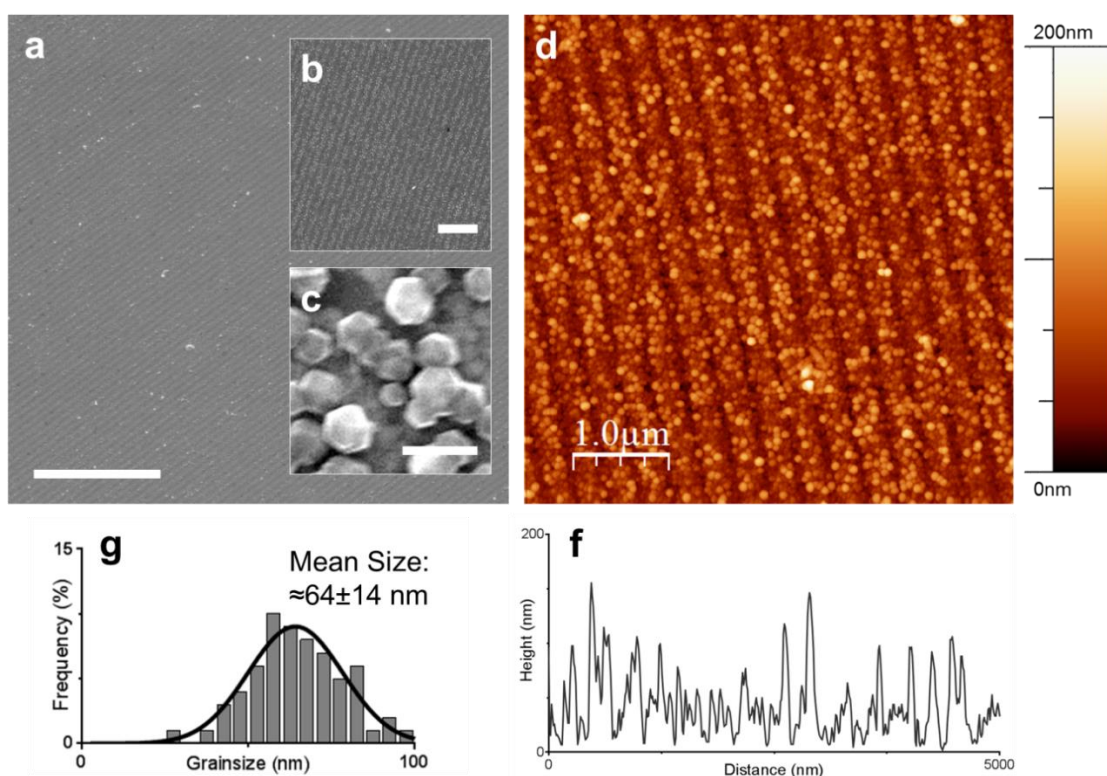
Figure 5.7.1 – SEM images (a-c) and AFM image (d) of MNP arrays formed via MIA-1 patterned surfaces after patterning by IL. Along with grainsize analysis (g), and an example height profile across a section of the AFM image shown (f). Scale bars (a-c): a – 5 μm, b – 2 μm, c – 100 nm.

Figure 5.7.1 displays SEM and a tapping mode AFM image of the biotemplated MNP arrays that were formed. The clarity of the patterning can clearly be seen, with MNPs binding to the protein patterned regions, and, as expected, only limited MNP binding on the PEG background. Grainsize analysis (Figure 5.7.1g) reveals that the MNPs on the surface have a

mean size of ≈64±14 nm, which is comparable with the mean size and distribution of particles on the µCP surface analysed previously in this Chapter (Figure 5.5.1). Figure 5.7.1f displays a height profile across a section of the AFM height image. This analysis reveals that the lines of biotemplated MNPs were successfully formed with an average period of ≈313 nm, including the width of the line and the PEG background spacing. Therefore, this approach forms a viable alternative to that developed with Mms6 (binding pre-formed particles to surfaces rather than manufacturing them *in situ*), opening up a new strategy to generate biotemplated MNP arrays with nanoscale precision.

6. Alternative Materials

"The Force is strong with this one."

Darth Vader

6.1 Overview: Alternative Materials to Magnetite

Magnetite is a magnetically soft material that would not be well suited to applications such as data storage. Current magnetic HDDs record data onto magnetic materials that have coercivities in the kOe range, but as shown previously (Section 3.7.3) the MNP arrays biotemplated onto gold surfaces by Mms6 were found to have coercivities approximately 10 times smaller [41]. Hence, the magnetisation of magnetite nanoparticles is too prone to being reoriented, and if used as the recording medium in a HDD would lead to the catastrophic loss of data. In this section alternative materials are explored, with the aim of developing a biotemplated magnetic surface that would be more suitable for use within data storage technologies.

It has previously been shown that Mms6 is able to template the formation of magnetically harder cobalt-doped magnetite in POFHK reactions, with cobalt-doping in the range of 0-15% [99, 154]. This was found to increase the coercivity of the biomineralised nanoparticles from 53-622 Oe, but decrease the magnetic saturation from 91-28 emu g^{-1} [99]. Therefore, cobalt can be doped into the biomineralised MNPs of magnetite to alter their coercivity and magnetic saturation. In this work it was also found that a doping level of 6% cobalt resulted in the largest increase in coercivity, with only a small effect on the saturation magnetisation [99]. In the first part of this Chapter the use of Mms6 to biotemplate MNPs of magnetite onto surfaces with the addition of 6% cobalt is explored, as a route to tuning the magnetic properties of the system.

Platinum alloys of cobalt and iron in the $L1_0$ phase are considered to have the ideal properties for use in BPM [24]. When correctly aligned on a surface, $L1_0$ phase CoPt is well suited for magnetic recording due to their extremely high out-of-plane magnetic anisotropy [24]. MNPs of CoPt remain magnetically stable at dimensions of a few nanometres, making them the ideal candidates for forming the nanoscale magnetic islands required for BPM [24]. However, manufacturing ordered films of $L1_0$ phase CoPt nanoparticles has remained elusive, requiring the use of high temperature annealing to generate the $L1_0$ phase that leads to the agglomeration and sintering [23]. To date an industrially viable approach capable of generating a highly consistent layer of CoPt nanoislands with an ordered $L1_0$ phase has yet to be developed [41]. Therefore, in the second part of this chapter the use of a CoPt binding peptide to biotemplate the formation of MNPs of CoPt onto gold surfaces is explored as a novel and green approach to this significant challenge.

6.2 Cobalt-Doped Magnetite

6.2.1 SEM Analysis of MNP Arrays of Biotemplated 6% Co-Doped Magnetite

Biomineralised arrays of cobalt-doped magnetite nanoparticles were formed on gold surfaces in exactly the same way as described in Chapter 3, except in this case the magnetite mineralisation reaction was performed with the addition of 6% cobalt. A PEG SAM was patterned onto gold surfaces with the use of µCP, before the surface was backfilled with Mms6 that was engineered to contain an *N*-terminal cysteine. These protein patterned surfaces were then placed into a POFHK reaction (with the addition of a ratio of 6% Co^{2+} to Fe^{2+}). As can been seen in Figure 6.2.1, the MNP arrays that formed in the process are comparable to those that formed without the addition of cobalt (Figure 3.7.1). A layer of MNPs can be seen to have formed on to the areas of the gold patterned with Mms6, with only a limited number of particles forming on the anti-biofouling PEG background.
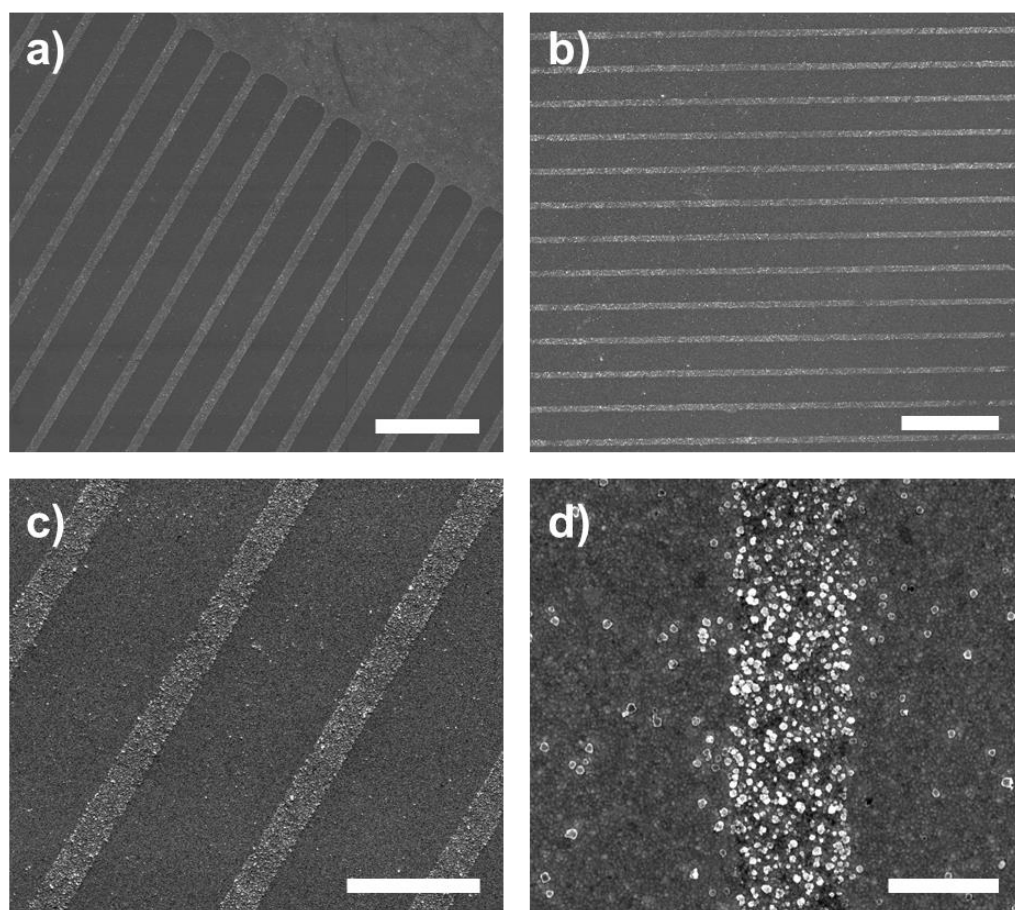
Figure 6.2.1[*] - SEM images of Mms6 surfaces patterned by µCP after a POFHK reaction with the addition of 6% cobalt. Scale bars: a and b – 50 µm, c – 20 µm, d – 1 µm.

[*] SEM images recorded at the University of Leeds.

In this chapter the cobalt-doped magnetite MNP arrays that were biomineralised by Mms6 are compared to those that were formed without the addition of cobalt (Chapter 3). The biomineralised arrays formed without the addition of cobalt are hereby referred to as $Fe_{Surface}$, with the MNP arrays that were biotemplated with the addition of 6% cobalt referred to as 6% $Co_{Surface}$. The MNPs that were biotemplated onto the gold surfaces are also compared to those that formed in solution during the mineralisation reactions, with the particles that formed in a POFHK reaction without the addition of cobalt referred to as Fe_{Bulk} and with the addition of 6% cobalt as 6% Co_{Bulk}.

6.2.2 Grainsize Analysis of MNP Arrays of Biotemplated 6% Co-Doped Magnetite

Grainsize analysis (Figure 6.2.2) shows that the MNPs that were biotemplated onto the gold surfaces by Mms6 ($Fe_{Surface}$: ≈90±15 nm and 6% $Co_{Surface}$: ≈84±14 nm) were not only significantly larger than those that formed in solution during the POFHK reactions (Fe_{Bulk}: ≈68±35 nm and 6% Co_{Bulk}: ≈61±53 nm), but also formed with a narrower size distribution. In particular the number of smaller particles (<50 nm) that were seen to form in the mineralisation reaction is considerably reduced in comparison to those that were biotemplated onto the surfaces by Mms6, with and without cobalt-doping. This provides further evidence to suggest that Mms6 nucleates iron ions and templates the formation of larger nanoparticles, reducing the number of smaller particles that are seen to form in the bulk POFHK reactions.

When the MNPs that formed on the $Fe_{Surface}$ are compared to those of the 6% $Co_{Surface}$, they can be seen to have formed with a slight reduction in mean size and with a tighter size distribution. The smaller mean size of the cobalt doped samples is also seen when the Fe_{Bulk} and 6% Co_{Bulk} samples are compared, but in this case the cobalt-doped particles were seen to form with a wider size distribution. It is also evident that there is a bimodal distribution of 6% Co_{Bulk} MNP sizes, with a noticeable drop in the number of particles that form in the 40-60 nm range. However, this trend is not found in the 6% $Co_{Surface}$ MNPs that were biotemplated onto the surfaces. In general, the MNPs that were biotemplated onto the gold surfaces with and without the addition of cobalt appear to be highly crystalline, with a cubic morphology and form with a larger mean size and smaller distribution of sizes than those that for form in the control POFHK reactions.
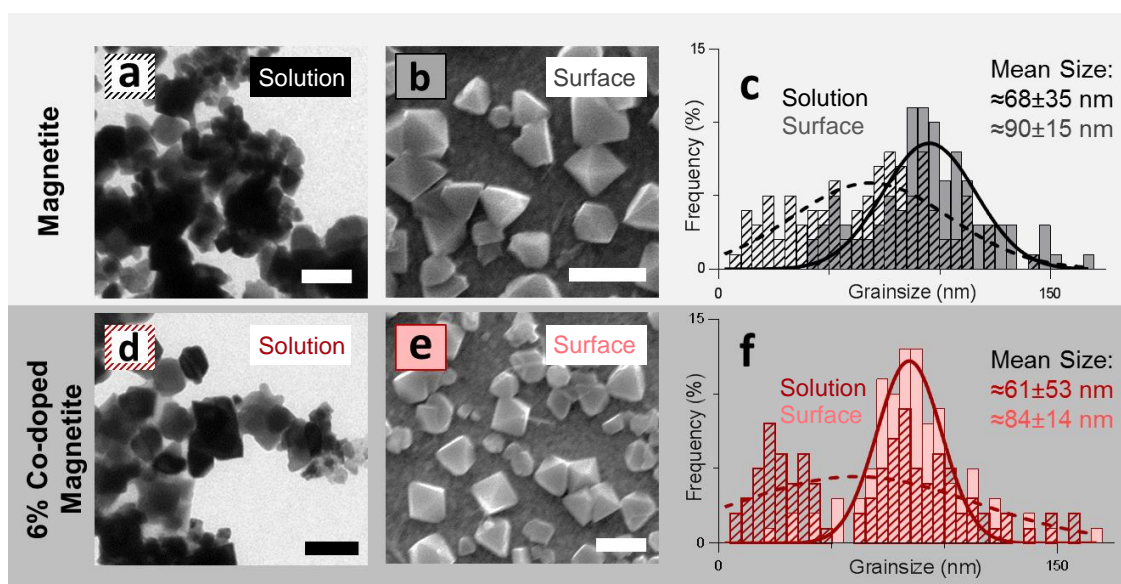
Figure 6.2.2[*] – TEM images (a and d) of MNPs that formed in solution (Fe_{Bulk} and 6% Co_{Bulk}), SEM images (b and e) of MNPs biotemplated onto gold by immobilised Mms6 ($Fe_{Surface}$ and 6% $Co_{Surface}$), and grain size analysis (c and f) during a POFHK reaction designed to form magnetite (a,b and c) or 6% cobalt-doped magnetite (d, e and f). Scale bars are 100 nm.

6.2.3 Elemental Analysis of MNP Arrays of Biotemplated 6% Co-Doped Magnetite

Elemental Analysis was performed with EDXA, and Figure 6.2.3 shows two spectra obtained for different areas on the biomineralised arrays; one on the antibiofouling PEG background, and one on a dense region of particles that formed on an area patterned with Mms6 during a POFHK reaction with the addition of 6% cobalt. Peaks corresponding to gold (e.g. Au Mα1 at 2.142 keV) and silicon (Si Kα at 1.740 keV) from the substrate, and carbon from the SAM or protein (C Kα at 0.277 keV) can be seen in both spectra. Peaks for iron (Fe Lα at 0.705 keV) and oxygen (O Kα at 0.525 keV) only appear in the spectrum recorded on the protein patterned region, corresponding to the particles that have formed. However, it was not possible to resolve a peak for cobalt, as the Co Lα (776 eV) peak significantly overlaps with that of Fe Lα (705 eV).

---

[*] SEM images recorded at the University of Leeds.
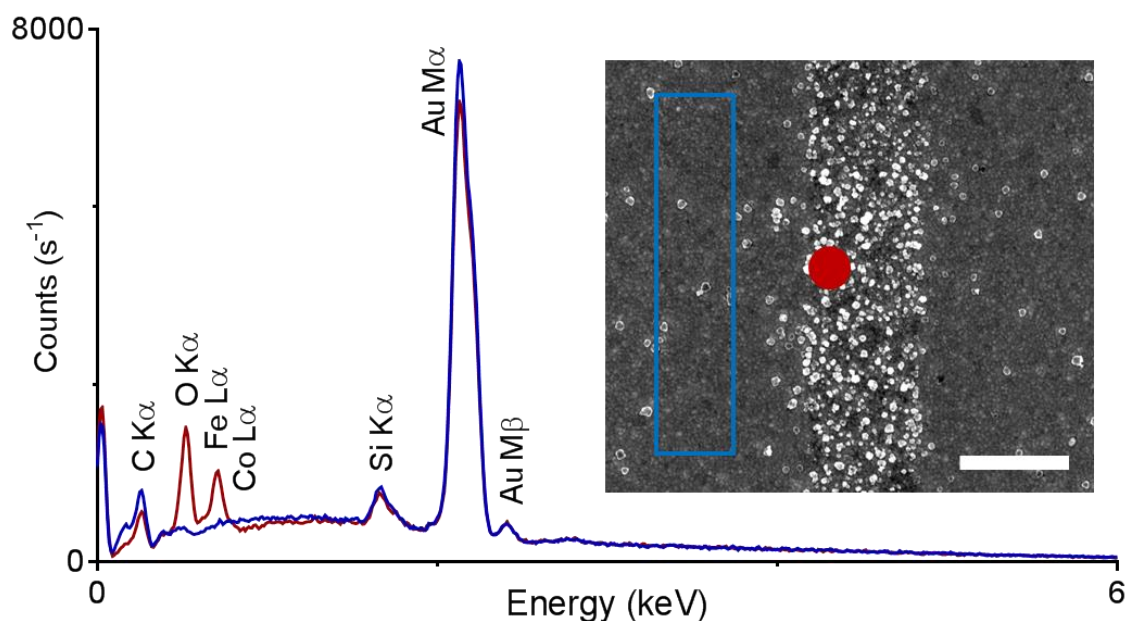
Figure 6.2.3[*] - EDXA spectra and corresponding SEM image (scale bar 1 μm) of nanoparticles biotemplated by Mms6 onto gold during a POFHK reaction designed to form 6% cobalt-doped magnetite. X-rays were collected over the wide anti-biofouling PEG SAM background area marked by the blue box on the SEM image (blue spectrum), and where a dense region of particles formed indicated by the red circle (red spectrum).

In light of the EDXA analysis, it was considered possible that the Mms6 protein was selective in only biotemplating the formation of magnetite onto the surfaces, with MNPs of cobalt-doped magnetite only forming in solution during the POFHK reactions. Therefore, each of the surfaces ($Fe_{Surface}$ and 6% $Co_{Surface}$) and the particles that formed in solution (Fe_{Bulk} and 6% Co_{Bulk}) were dissolved in aqua regia and analysed with ICP-ES, to determine the total levels of iron and cobalt present and to ensure that there was no significant bias for iron or cobalt enrichment in the biomineralised nanoparticles.

Table 6.2.1 – MNP composition determined by ICP-ES.[†]

Sample	Fe (ppm)	Co (ppm)	% of Co
Blank	0.16±0.01	<0.01	0
Fe_{Bulk}	922±19.8	<0.01	0
6% Co_{Bulk}	905±18.1	57±1.1	5.9±0.1
$Fe_{Surface}$	231±4.6	<0.01	0
6% $Co_{Surface}$	216±4.3	13±0.3	5.7±0.1

The ICP-ES data (Table 6.2.1) reveals that as expected cobalt was not detected in a control sample of just aqua regia (Blank, Table 6.2.1) or in MNPs produced without the

[*] Data recorded at the University of Leeds.
[†] Data collected by Neil Bramall.

addition of cobalt (Fe$_{Surface}$ and Fe$_{Bulk}$). Cobalt was detected in an approximately 6% ratio in both samples when cobalt was added in a 6% ratio of cobalt to iron (6% Co$_{Surface}$ - 5.7 ± 0.1% and 6% Co$_{Bulk}$ - 5.9 ± 0.1%). These data suggest that Mms6 is able to biotemplate the formation of cobalt-doped magnetite when patterned and immobilised onto a surface, and that there was no significant bias for iron.

6.2.4 Crystallographic Analysis of MNP Arrays of Biotemplated 6% Co-Doped Magnetite

Crystallographic analysis of the biomineralised surfaces (Fe$_{Surface}$ and 6% Co$_{Surface}$) and the particles that formed in solution during the POFHK reactions (Fe$_{Bulk}$ and 6% Co$_{Bulk}$) was performed using XRD (Figure 6.2.4). The position of the peaks was then converted to *d*-spacings (using Equation 2.5.1, Table 6.2.2). As described previously (Section 3.2) the samples were then compared to the known values (from the JCPDS crystallographic data base) for maghemite, magnetite and cobalt ferrite.

The Fe$_{Bulk}$ sample (black data, Figure 6.2.4) shows peaks at *2θ* = 35.52°, 57.00° and 62.80°, which are a closer fit to the magnetite (311), (511) and (440) peaks respectively than the peaks for maghemite. Likewise, the 6% Co$_{Bulk}$ sample (dark red data, Figure 6.2.4) shows reflections at *2θ* = 35.52°, 57.00° and 62.70°, which again are a closer fit to the (311), (511) and (440) peaks of magnetite than those for maghemite. Both the Fe$_{Surface}$ (grey data Figure 6.2.4) and 6% Co$_{Surface}$ (light red data Figure 6.2.4) samples show peaks at *2θ* = 38.35° and 43.15° that correspond to the Au (111) and (200) reflections from the gold film on the substrate. The Fe$_{Surface}$ sample also shows peaks at 2θ = 18.35°, 30.15°, 35.55°, 57.00° and 62.80°, which are a closer fit to the magnetite rather than maghemite (111), (220), (311), (511) and (440) peaks respectively. The 6%Co$_{Surface}$ sample displays peaks at 2θ = 18.35°, 30.25°, 35.55°, 57.00° and 62.70°, with the majority of these peaks being a closer fit to the magnetite (111), (220), (311), (511) and (440) peaks respectively than maghemite (with the only exception being the (220) peak, which is a slightly closer match to maghemite rather than magnetite).

Overall, these XRD data strongly support that the crystal structure of the surface biotemplated samples, and the particles that formed in the bulk solutions, are all a good match for magnetite or cobalt-doped magnetite, rather than maghemite or other iron mineral species. The relative intensities of the peaks are as expected (for example the (311) peak is the most intense). Unfortunately it was not possible to resolve the (200) or (111) peaks in the

data of the MNPs that formed in solution, highlighting the strong crystallinity of both the Fe$_{Surface}$ and 6% Co$_{Surface}$ biotemplated MNPs when compared to the particles that were not biotemplated onto the surface. These crystallographic data also suggest that the MNPs are stable against oxidation, as there is no strong indication of maghemite or other oxidation products present.
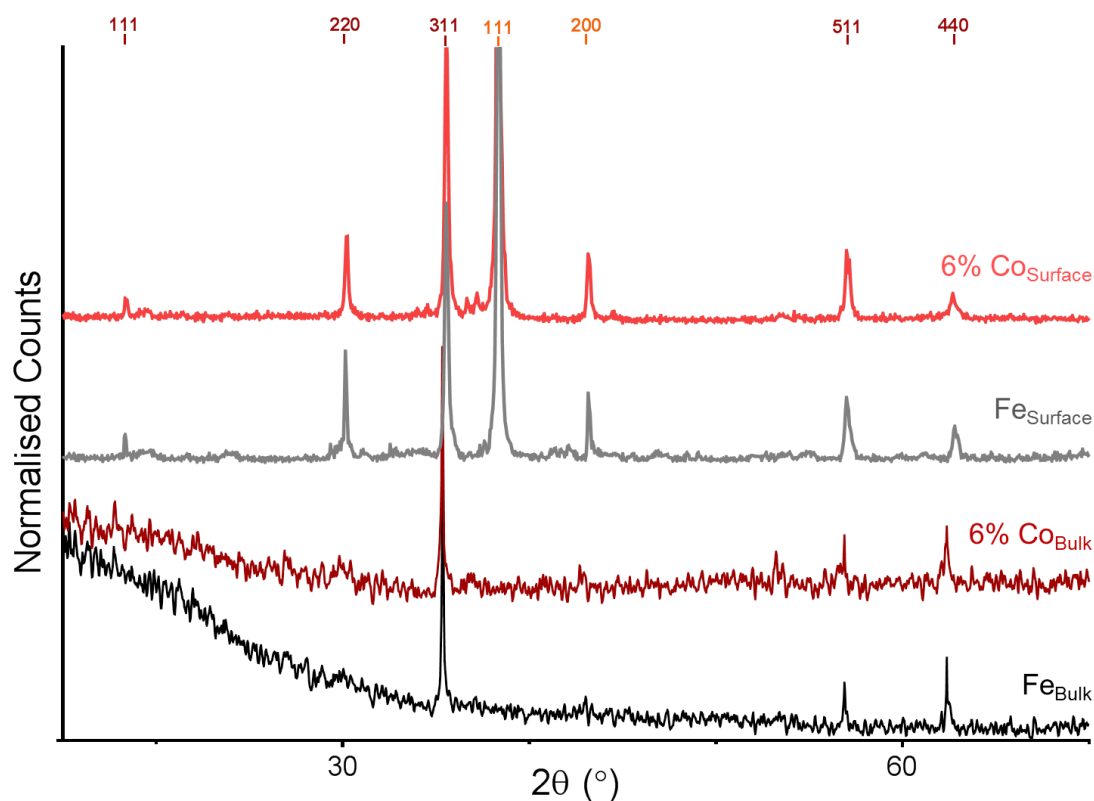
Figure 6.2.4 - XRD diagram of MNPs that formed in solution (black and red) and biomineralised MNP surfaces synthesised by Mms6 immobilised onto gold (grey and pink) *via* a POFHK reaction designed to form magnetite (black and grey) or 6% cobalt-doped magnetite (red and pink). The expected peak positions for magnetite (red) and gold (gold) are highlighted.

Table 6.2.2 - Summary of the *d*-spacings for maghemite, magnetite and cobalt-ferrite, and peak positions from the MNPs formed in solution and on an Mms6 patterned gold surface in POFHK reactions designed to form magnetite and 6% cobalt-doped magnetite shown in Figure 6.2.4 (all measured in Å). Maghemite values are from JCPDS card 00-039-1346, magnetite from 00-019-0629 and cobalt ferrite from 00-022-1086. The value which is the closest match to the POFHK peak is highlighted in green, and only those plains on the JCPDS card that are the nearest to the peak are shown.

Peak	Maghemite	Magnetite	Cobalt Ferrite
(111)	4.822	4.850	4.847
(220)	2.953	2.966	2.968
(311)	2.518	2.530	2.531
(511)	1.607	1.614	1.615
(440)	1.476	1.483	1.483

Peak	Fe$_{Bulk}$	6% Co$_{Bulk}$	Fe$_{Surface}$	6% Co$_{Surface}$
(111)	—	—	4.835	4.835
(220)	—	—	2.964	2.954
(311)	2.527	2.527	2.525	2.525

(511)	1.616	1.616	1.616	1.616
(440)	1.480	1.482	1.480	1.482

Based on the standard spectrum for magnetite and the data shown in Figure 6.2.4, the (311) peak is the most intense and distinguishable. Therefore, this peak was fitted to the Debye-Scherrer equation (Equation 2.5.2) to measure the grainsize of the particles in the same way as described in Section 3.2 [178]. Using this analysis the size of the particles that formed in solution during the POFHK reactions (Fe_{Bulk} ≈91 nm and 6% Co_{Bulk} ≈84 nm) were found to be larger than the particles that were biotemplated onto the surfaces ($Fe_{Surface}$: ≈83 nm and 6% $Co_{Surface}$: ≈66 nm). This poor agreement may be a result of the nanoparticles forming with a large distribution with respect to size and crystallinity. It should also be noted that two different spectrometers were used to collect the data for the biotemplated surfaces and the MNPs that formed in solution. As a result of this, different scan times were used, and the data recorded for the bulk particles was much noisier. Therefore, the particle size calculated for the MNPs biotemplated onto surfaces cannot be directly compared to those that formed in solution during the mineralisation reaction. However, these data supports the general trend that cobalt-doping results in a slight decrease in the mean size of the nanoparticles that form.

6.2.5 Hysteresis Loops of MNP Arrays of Biotemplated 6% Co-Doped Magnetite

Doping cobalt into magnetite alters the magnetic properties, and it was anticipated that this could be used to biomineralise MNPs more suitable for use within technologies such as data storage. A prefered axis of magnetisation is introduced, leading to an increase in coercvity and hense magnetic hardness. Spherical MNPs of pure cobalt ferrite are known to maintain a single domain in a decreased size range when compared to magnetite, becoming superparmagnetic below ≈5 nm [201] and single domain below ≈70 nm [202]. An exact literature value for 6% cobalt-doped magnetite is not published, but if a linear relationship is assumed it is expected that these particles will maintain a single domain above approximately 18 nm in diameter [99, 154].

From the grainsize analysis (Figure 6.2.2) it can be seen that both the Fe_{Bulk} and 6% Co_{Bulk} particles that form in solution during the POFHK reactions are synthesised with a range of sizes, covering the superparamagnetic, single domain and multi-domain size range. The $Fe_{Surface}$ and 6% $Co_{Surface}$ nanoparticles that were biotemplated by Mms6 onto gold show an

increase in the mean size, decrease in the size distribution and a significant reduction of nanoparticles that would be in the superparamagentic size range and unsuitable for data storage. Therefore, hysteresis loops were recorded with VSM for the biomineralised 6% Co$_{Surface}$ at room temperature, allow for a comparison with a Fe$_{Surface}$ (Figure 6.2.5) and the 6% Co$_{Bulk}$ particles that formed in solution during mineralisation (Figure 6.2.6).[*]
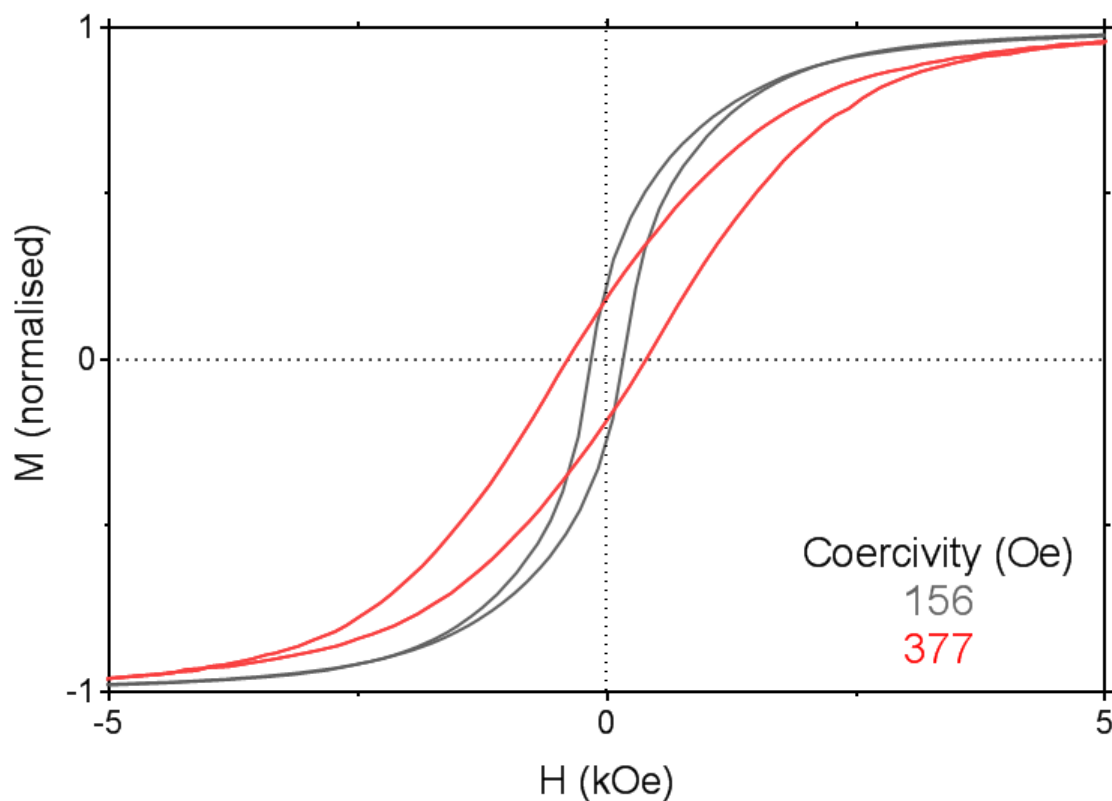
Figure 6.2.5[†] - Magnetic hysteresis loops recorded using VSM at 295 K of MNP arrays biomineralised by Mms6 onto gold during a POFHK reaction designed to form magnetite (grey) and 6% cobalt-doped magnetite (pink).

It is immediately evident in Figure 6.2.5 that the 6% Co$_{Surface}$ displays a wider hysteresis, and hence is magnetically harder than the undoped Fe$_{Surface}$. As with previous VSM data (Section 3.7.3) the magnetisation of these two samples was normalised, as the mass or volume of the MNPs that formed on the surfaces could not be quantified. Both of these samples (Fe$_{Surface}$ and 6% Co$_{Surface}$) display a typical hysteresis loop for a soft ferrimagnetic material with a uniform switching behaviour. As expected, 6% cobalt doping resulted in an increase in coercivity from 156 Oe to 377 Oe [99, 154, 203], however this increase in

---

[*] A complete surface of Mms6 (without any PEG or patterning) was used to ensure a greater coverage of Mms6, and hence the formation an extensive layer of surface biotemplated MNPs maximising the signal.
[†] Data collected by Johanna Galloway.

coercivity is still much smaller than what is required for use within a working magnetic HDD [41].

It can also be seen in Figure 6.2.5 that the undoped $Fe_{Surface}$ has a steeper hysteresis curve, displaying more uniform magnetic switching. The majority of the MNPs of both of the $Fe_{Surface}$ and 6% $Co_{Surface}$ samples formed in the single to multi-domain crossover size region, but the introduction of a preferred axis of magnetisation could lead to greater exchange coupling on the densely packed planar MNP arrays on the 6% $Co_{Surface}$. This could explain the shallower hysteresis loop that was recorded for this sample.
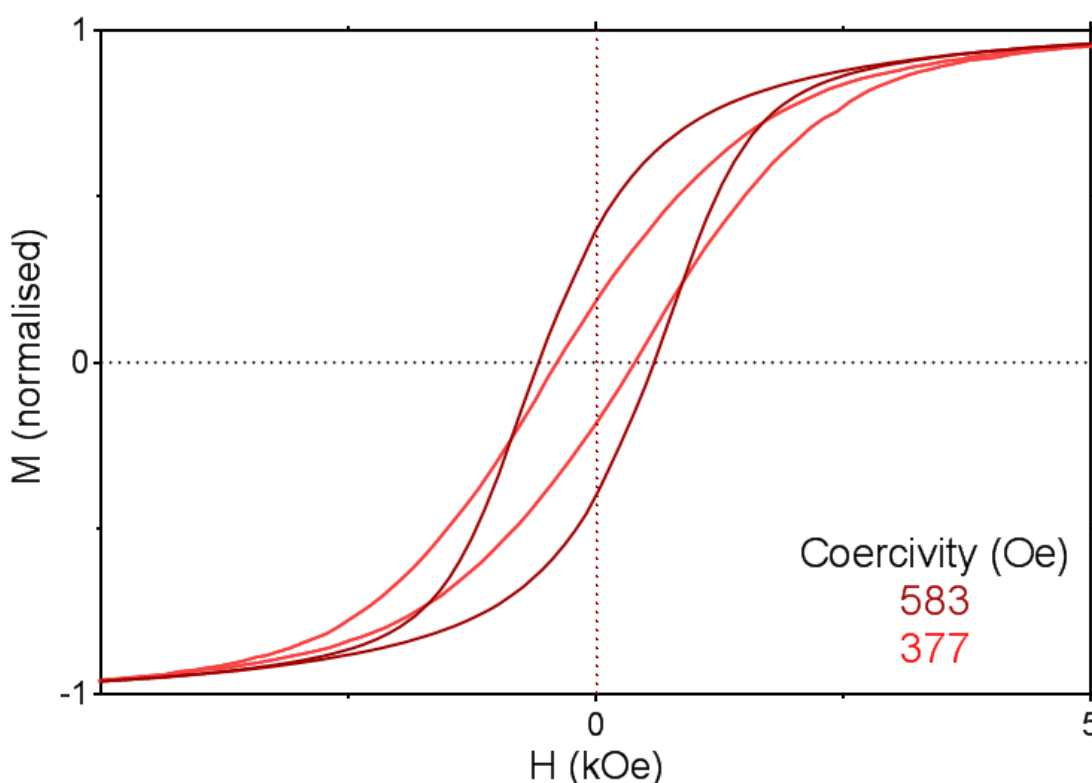
Figure 6.2.6[*] - Magnetic hysteresis loops recorded using VSM at 295 K of the MNPs that form in solution (red), and the MNPs biotemplated onto a gold surface by Mms6 (pink) during a POFHK reaction designed to form 6% cobalt-doped magnetite.

Figure 6.2.6 displays the hysteresis loops recorded at room temperature for MNPs biomineralised onto the surface by Mms6 and the particles that formed in solution during a POFHK reaction with the addition of 6% cobalt. It can be seen that the coercivity recorded increases from 377 Oe for the 6% $Co_{Surface}$ to 583 Oe for the 6% Co_{Bulk} sample. This increased coercivity may be a result of different size distributions of the MNPs in these two samples (Figure 6.2.2). A greater number of smaller MNPs in the single domain size range were found

[*] Data collected by Johanna Galloway.

in the 6% Co_{Bulk} sample, with the MNPs biotemplated by Mms6 found to form with a larger mean size and tighter size distribution. The coercivity of cobalt ferrite nanoparticles reaches a maximum in the single domain size range at ≈25 nm, before reducing with particle size [204]. As a greater number of smaller single domain nanoparticles were found in the 6% Co_{Bulk} sample, this may provide an explanation to the increased coercivity that was recorded. This is also supported by the steeper hysteresis loop recorded for the 6% Co_{Bulk} sample, suggesting a more uniform switching behaviour and hence a greater number of single domain particles.

6.2.6 Magnetic Force Microscopy (MFM) of MNP Arrays of Biotemplated 6% Co-Doped Magnetite

Figure 6.2.7 displays composite tapping mode AFM and MFM phase plots of 6% cobalt-doped MNP arrays biomineralised onto gold surfaces by Mms6. The clarity of patterning that was achieved can be seen in these images. A high density layer of biotemplated MNPs can be seen to have formed on the protein patterned regions, with little mineralisation of the PEG background regions. As with the MFM data recorded for the pure magnetite MNP arrays biomineralised by Mms6 (Chapter 3.6.4), zones of attraction and repulsion (red and blue areas respectively) extending over multiple MNPs can be seen to have formed. This suggests that the biotemplated MNPs are able to maintain magnetic orientation at room temperature and are ferrimagnetic.

Previously, MFM measurements performed on MNP arrays of cobalt-doped magnetite have showed that the magnetic zones of attraction and repulsion extended over larger distances than undoped magnetite samples (Figure 6.14 in [154]). This is most likely an effect of the cobalt doping, which increases the coercivity of the doped MNPs making the direction of magnetisation more difficult to perturb at room temperature. Therefore, the biotemplated 6% cobalt-doped MNPs could be able to form more stable interactions on the 2D surface.
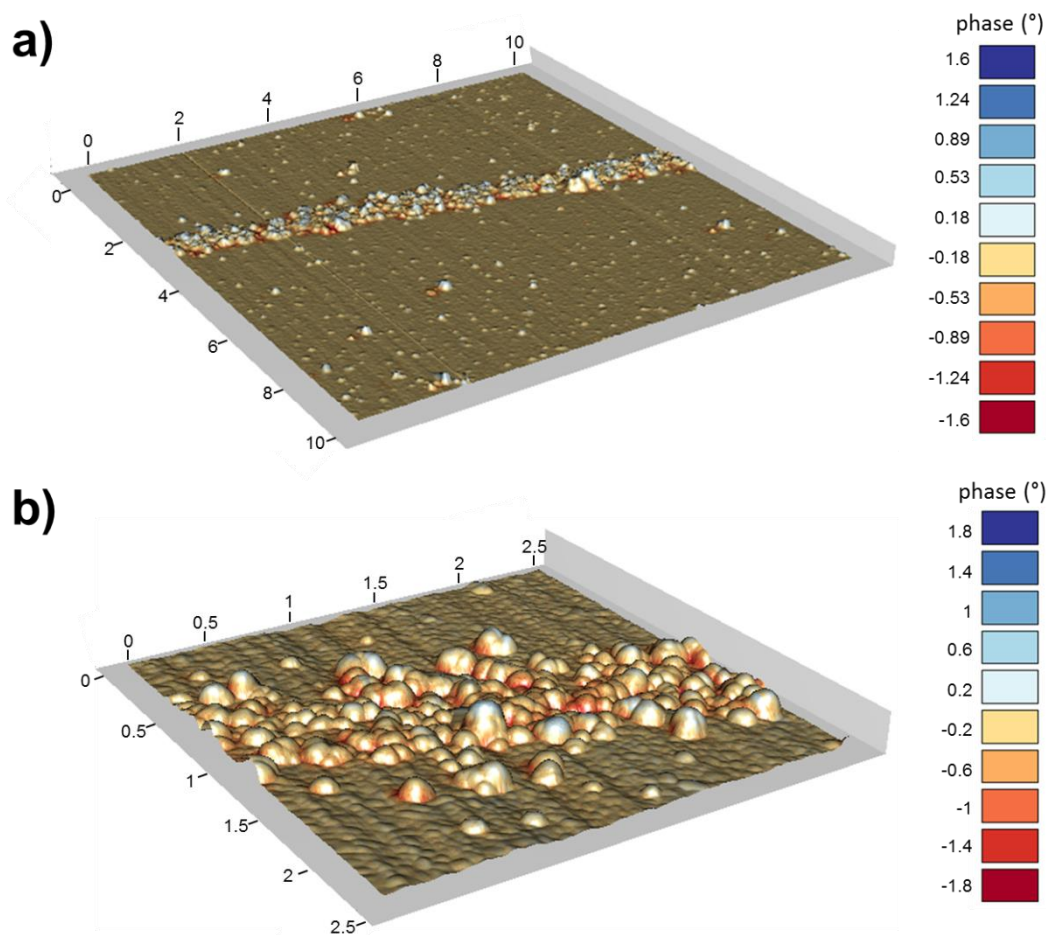
Figure 6.2.7 - Composite images of tapping mode AFM and MFM phase shift of a biomineralised 6% cobalt-doped magnetite MNP array at a lift height of 50 nm. Scales in μm.

6.3 Cobalt-Platinum (CoPt)

Recently, Galloway *et al*. [11] showed that a dual affinity peptide (with one half the peptide sequence designed to bind to SiO_2, and the other half the CoPt binding sequence displayed in Table 2.1.1) could be used to biotemplate MNPs of $L1_0$ phase CoPt onto a SiO_2 surface during a simple room temperature mineralisation reaction [156]. MNPs of CoPt were found to form in a control mineralisation reaction, without the addition of any peptide or patterned surfaces, with a mean size of ≈5±5 nm and measured aspect ratio of ≈0.84±0.11 [156]. Further analysis, with techniques such as XRD, found evidence to suggest that MNPs of $CoPt_3$ formed during these control reactions, and not the $L1_0$ phase that is required for high-density data recording [156].

Surfaces patterned with a complete layer of the dual affinity peptide was found to lead to the mineralisation of MNPs onto the SiO_2 surface that were both larger and more equidimensional, suggesting that the peptide exerts control over the size and shape of the

MNPs that form [156]. More importantly, XRD analysis suggested that these biotemplated MNPs formed in $L1_0$, probably by lowering the activation energy for the formation of this phase [156]. Therefore, for the first time, MNPs of CoPt were formed on a surface in the $L1_0$ phase from aqueous solution, without the need for high temperature annealing. Unfortunately, magnetic measurements suggested that the *c*-axis of the biotemplated $L1_0$ phase CoPt MNPs was not uniformly aligned parallel with the surface [156], something which is required for data recording [41]. Coupled with this, patterning the dual affinity peptide on the SiO_2 surface with μCP was challenging [156]. Therefore, in this section a modified version of the dual affinity peptide, which contains a cysteine and a glycine linker in place of the SiO_2 binding region, is patterned and immobilised onto gold surfaces with the use of IL, as a route to forming patterned biotemplated MNP arrays of $L1_0$ phase CoPt under mild aqueous reaction conditions.

6.3.1 SEM Analysis of Biotemplated MNP Arrays of CoPt

MNP arrays of CoPt were successfully biotemplated onto functionalised gold surfaces with nanoscale precision (Figure 6.3.1). A complete antibiofouling PEG SAM was formed on a gold surface, before an IL exposure (using the conditions described in Chapter 4; applied dose of 20 J cm^{-2}, *2θ* =20˚) to form a regular line array of PEG SAM and clean gold. The clean gold space was then backfilled with the CoPt binding peptide, which bound to the gold surface *via* an *N*-terminal cysteine. These surfaces were then subjected to a CoPt mineralisation reaction, before being characterised with SEM (Figure 6.3.1). As can be seen in Figure 6.3.1 MNPs of CoPt formed on the regions patterned with the peptide (corresponding to the bright fringes formed during the IL exposure), with negligible mineralisation on the PEG background (corresponding to the dark fringes formed during the IL exposure).
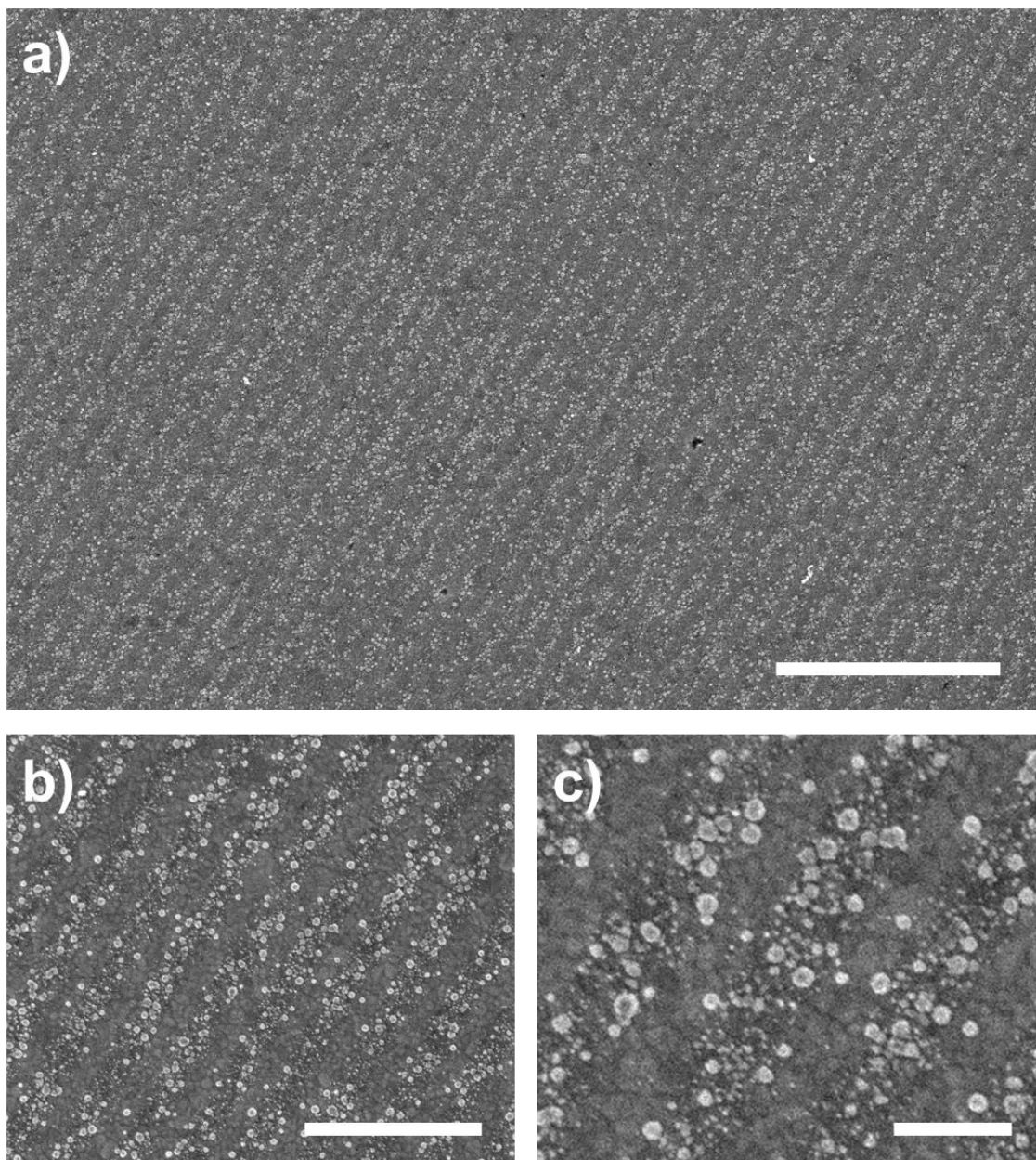
Figure 6.3.1[*] - SEM images of surfaces of the CoPt binding peptide patterned by IL after a CoPt mineralisation reaction. Scale bars: a – 2.5 μm, b – 1 μm and c – 250 nm.

Grainsize analysis (Figure 6.3.2a) reveals that the MNPs formed on the patterned gold surfaces with a mean size of ≈12±3 nm. The majority of the MNPs were found to form in the 10-20 nm range, but some larger crystals were also seen to form. The particles were also found to be highly equidimensional, and this is reflected in the aspect ratio recorded for the MNPs (≈0.90±0.14, Figure 6.3.2b). The MNPs of CoPt have been shown previously to form in a control mineralisation with a much smaller size (≈5±5 nm) and with a less equidimensional morphology (≈0.84±0.11) [156]. This suggests that the CoPt binding peptide exerts control

---

[*] Images were recorded by Johanna Galloway at the University of Leeds.

over the MNPs that form on the surface, leading to the formation of particles that are more equidimensional and with a larger mean size. Unfortunately, the MNPs that form in the CoPt mineralisation collect into supra-particle clumps. So it is not possible to form a MNP array by washing pre-formed MNPs over surfaces patterned with the CoPt binding peptide.
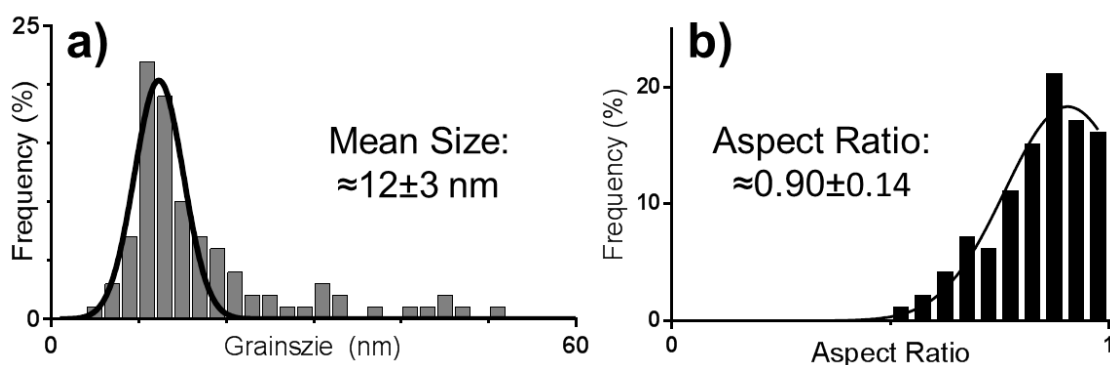
Figure 6.3.2 – Grainsize analysis (a) and measured aspect ratio (b) of the MNPs biotemplated onto the gold surfaces by the CoPt binding peptide.

6.3.2 AFM Analysis of Biotemplated MNP Arrays of CoPt

Tapping mode AFM images (Figure 6.3.3) further highlight the nanoscale patterning that was achieved, again showing that MNPs formed on the regions of the gold surface patterned with the CoPt binding peptide with limited mineralisation in the regions patterned with the antibiofouling PEG SAM. A height profile across the AFM image displayed in Figure 6.3.3b is shown in Figure 6.3.4, showing that a regular line pattern of biotemplated MNPs and PEG Background was formed with an average period of 312 nm. This highlights how the surface patterning methods developed in this thesis can be combined with any desired biotemplating biomolecule, to target materials other than just magnetite.
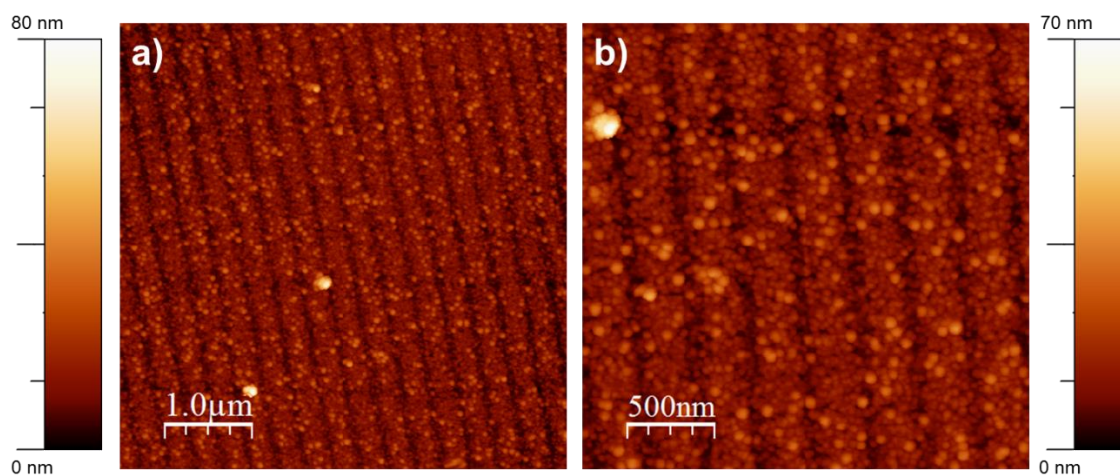
Figure 6.3.3 – Tapping mode AFM images of surfaces of the CoPt binding peptide patterned by IL after a CoPt mineralisation reaction.
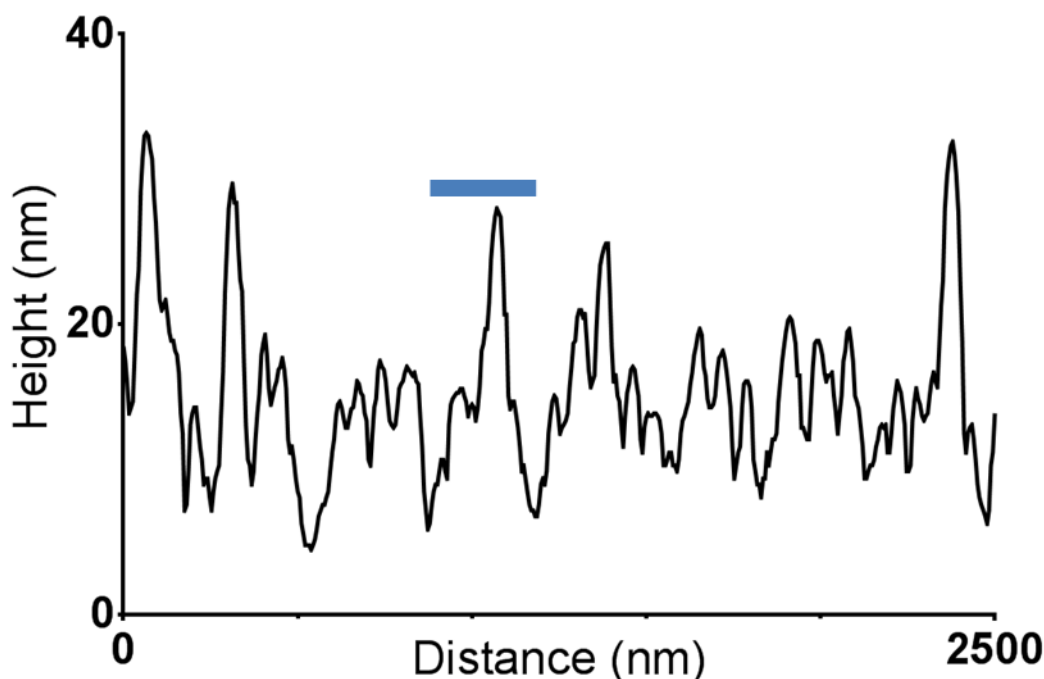
Figure 6.3.4 – Height profile across a section of the AFM tapping mode image displayed in Figure 6.3.2b. Blue bar indicates average period of 312 nm.

6.3.3 Biotemplated MNP Arrays of CoPt suitability for BPM

Work is currently on going to further characterise the MNP arrays of CoPt that were biotemplated onto the gold surfaces. Preliminary data shows strong evidence to suggest that the biotemplated MNPs are $L1_0$ phase CoPt, but magnetic measurements reveal that, as with the MNPs biotemplated onto SiO_2 surfaces, the coercivity is much lower than expected. To achieve high out of plane coercivity for $L1_0$ CoPt, something that is required for magnetic data storage, the *c*-axis of all the MNPs must be uniformly aligned perpendicular to the surface [41]. However, it appears that although $L1_0$ CoPt was formed, the MNPs are not uniformly aligned. It currently remains unclear whether the MNPs are orientated randomly or consistently aligned with the *c*-axis in an undesirable orientation. In an attempt introduce order, the CoPt mineralisation reaction was performed in the presence of a strong magnetic field (0.2 T DC field) aligned perpendicularly and parallel with the surfaces. However, these fields were found to have no effect on the out of plane coercivity of the biotemplated MNP arrays, suggesting that the applied fields did not help to uniformly align the *c*-axis of the CoPt MNPs perpendicular the surface.

Another challenge remains to pattern the biotemplating biomolecule into a uniform array of dots, and not the lines displayed in Figure 6.3.1 and 6.3.3. Although previously unsuccessful (Section 5.X), gold surfaces covered in a complete layer of the CoPt binding

peptide were exposed in IL, before being backfilled with the PEG SAM and placed into a mineralisation reaction. It was anticipated that this approach might be more successful with the simpler peptide, which could be more readily photodegraded than the larger Mms6 protein. Two identical exposures at 90° angles could generate dot patterns of the CoPt binding peptide (as shown in Figure 4.5.7).

When a high exposure dose of 100 J cm^2 was applied to the CoPt binding peptide surfaces during IL exposure, MNP arrays were successfully formed after backfilling with a PEG SAM and subjecting the surfaces to a CoPt mineralisation reaction (Figure 6.3.5). However, at the time of production the IL laser was running with reduced power and low stability, and achieving this dose took in excess of 1 hour. Unfortunately, after samples were exposed in two identical IL exposures at 90° angles no evidence of MNP arrays in a dot pattern were found. In this case no mineralisation was found on the surfaces. This could be that due to the low stability of the laser resulting in the peptide layer being completely photodegraded and displaced by the PEG SAM. In addition, fewer MNPs seem to have formed on the array shown in Figure 6.3.5, which could be due some of the peptide layer being degraded in the dark fringes formed during the IL exposure. This could also be an effect of removing the peptide from solution during the exposure, and as discussed in Section 4.3 the peptide being outcompeted on the surface by the PEG SAM. It is also likely these effects may be more prevalent when the smaller dot features are formed, hence why this type of pattern could not be formed.
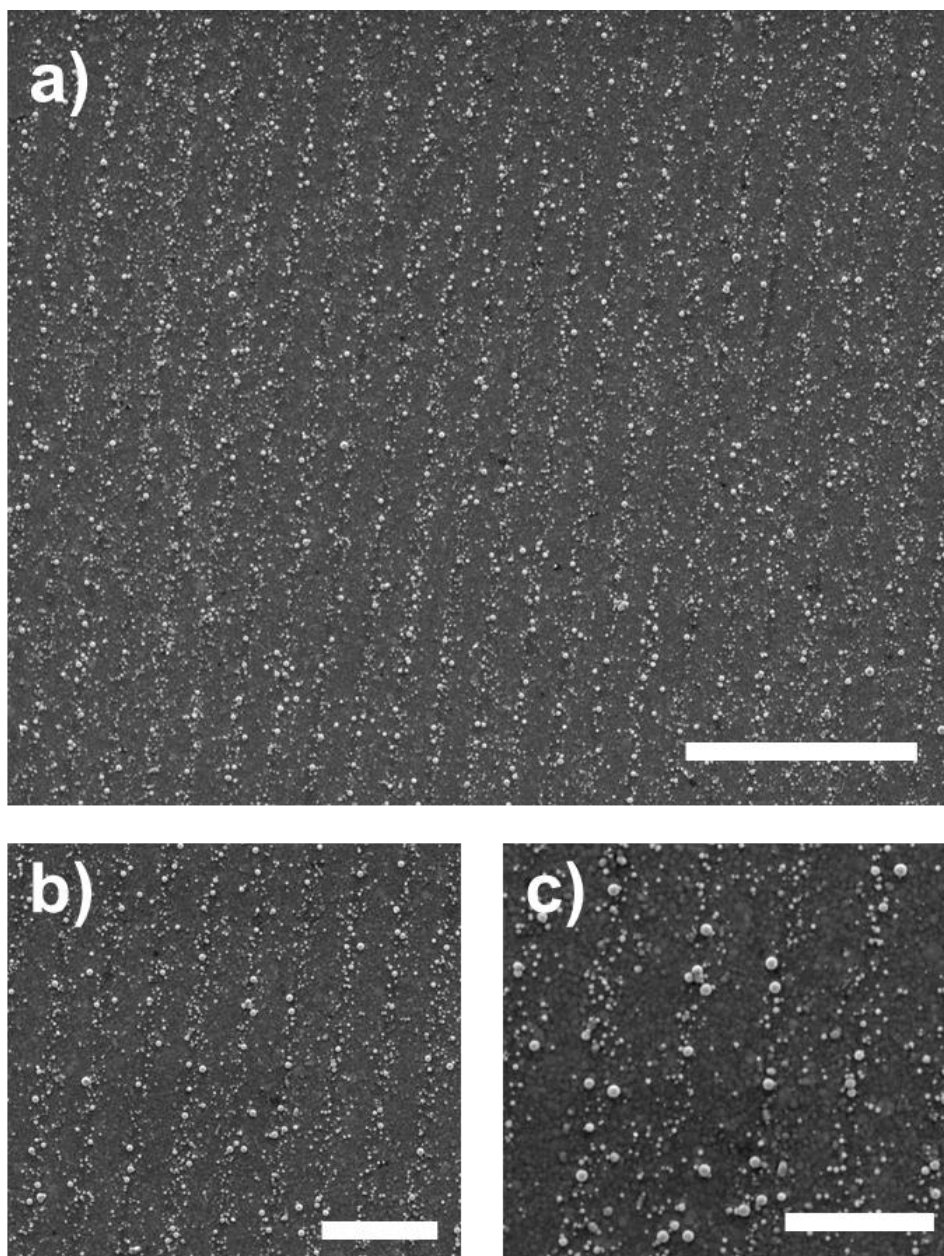
Figure 6.3.5 - SEM images of surfaces of the CoPt binding peptide patterned by IL after a CoPt mineralisation reaction. Scale bars: a – 2.5 µm, b – 1 µm and c – 250 nm.

The nanoscale lines of $L1_0$ CoPt MNP that were generated under mild aqueous reaction conditions are a significant step towards developing a new bioinspired and green route to forming BPM, but many challenges remain. These include uniformly aligning the *c*-axis of the MNPs on the surface to achieve a high out of plane coercivity, and addressing the pattern that is formed. It has already been stated that IL is capable of generating patterns suitable for BPM. It could be that biopanning against specific faces of $L1_0$ phase CoPt could generate new biomolecules capable of preferentially biotemplating the growth of these MNPs with a uniformly aligned *c*-axis perpendicular to the surface. This and other approaches that could be explored to achieve this goal are discussed in more detail in the following Chapter.

7. Summary, Conclusions and Future Directions

"I have not failed. I've just found 10,000 ways that won't work."

Thomas Alva Edison

(One of the world's most prolific inventors, during his life he amounted 1,093 US patents in his name, as well as many patents in the United Kingdom, France, and Germany. One wonders how many experiments he conducted.)

7.1 Chapter 3: Magnetic Nanoparticle Arrays Biotemplated with the Biomineralisation Protein Mms6

Previously, it has been shown that the biomineralisation protein Mms6, derived from the magnetosomes of the MTB AMB-1, is able to biotemplate the formation of MNPs of magnetite *in vitro* [86, 90, 189] and when immobilised onto functionalised gold surfaces [97, 98, 154]. Here, Mms6 was engineered to contain an *N*-terminal cysteine, which binds it directly onto a gold surface through a thiol-gold interaction. Surfaces were patterned with a protein resistant PEG SAM through the use of the soft lithographic approach of μCP, before being backfilled with the Mms6 protein. When immersed into a POFHK reaction MNPs of magnetite formed on the protein patterned regions of the surface with negligible mineralisation on the PEG background, suggesting that the immobilisation of cysteine-tagged Mms6 directly onto a gold surface did not affect its biotemplating function.

This forms a simple and green approach to generating MNP arrays of magnetite with microscale precision. The Mms6 protein itself was found to be dual purpose, both controlling the location of the MNP on the surface and biotemplating the formation of MNPs that have a larger mean size (≈87±18 nm) and tighter size distribution than those that form in a control POFHK reaction (≈60±21 nm). Magnetic measurements reveal that the magnetite nanoparticles are ferrimagnetic at room temperature, yet studying the nanomagnetic properties of individual MNPs with techniques such as MFM remains challenging with the densely packed microscale arrays that formed. The shape of a magnetite layer is known to have an effect on its magnetic properties [205], so patterning Mms6 with nanoscale precision (to form features such as high aspect ratio lines, squares, circles and ellipses) may allow for more insight into how this alters the magnetism of the biotemplated MNP arrays.

Before this study it remained unclear whether Mms6 was able to bind to magnetite, and whether washing MNPs of magnetite that were pre-formed in a mineralisation reaction over a Mms6 patterned surface rather than immersing the protein-patterned surfaces into a mineralisation reaction would be a more effective method for forming a MNP array. Therefore, gold surfaces that were patterned with Mms6 *via* μCP were placed into an aqueous solution of magnetite nanoparticles that were pre-formed in a POFHK reaction with gentle mixing. The MNP arrays formed were then compared to the MNP arrays formed when these surfaces were immersed into a POFHK reaction. It was found during SEM analysis that a clear defined pattern of magnetite nanoparticles was produced when the protein-patterned surfaces were immersed into a POFHK reaction, but this was not the case when pre-formed nanoparticles were supplied.

In this case the pattern was much less consistent and defined, and the particles were more sparsely distributed on the gold surface. Additionally, grainsize analysis found that the MNPs that bound to surface when pre-formed nanoparticles were supplied (≈65±30 nm) are a much closer fit in terms of mean size and morphology to the MNPs that form in a control POFHK reaction (≈60±21 nm). This is in contrast to the approximately 50% larger MNPs that formed on the surface when Mms6 patterned surfaces were immersed into a POFHK reaction (≈87±19 nm). Therefore, it appears that Mms6 acts to bind iron ions, nucleating and stabilising the formation of a growing MNP during a POFHK reaction. The *C*-terminal residues of Mms6 may mediate more contacts with the growing particle than if the MNP is supplied pre-formed. This may suggest that the strong attachment of Mms6 to magnetite is a by-product of its nucleating activity.

Short peptide sequences based on the *C*-terminal region of Mms6 have been previously shown to have an effect on the size and morphology of MNPs of magnetite when added to a mineralisation solution [96, 189]. As a result, it was hoped that a synthetic peptide based on the *C*-terminal region of Mms6 (termed in this thesis Mms6$_{Peptide}$), which is cheaper and easier to produce than the full Mms6 protein, that was engineered to contain an *N*-terminal cysteine would make the biotemplating properties of Mms6 more industrially amenable. Surfaces patterned with PEG by μCP were backfilled with Mms6$_{Peptide}$, and both immersed in a POFHK reaction and supplied with magnetite nanoparticles that were pre-formed in a POFHK reaction. However, when these surfaces were compared with the MNP surface formed when surfaces patterned with the full Mms6 protein were placed into a POFHK reaction, again the MNP pattern was much less consistent and densely populated. Once more the MNPs on the surface were found to be much closer to those that form in the control POFHK reaction (≈60±21 nm), both when the Mms6$_{Peptide}$ patterned surface was placed into a POFHK reaction (≈65±30 nm) and when nanoparticles that were pre-formed in a POFHK reaction were supplied (≈66±21 nm).

Mms6$_{Peptide}$ appears to offer no effect on controlling the size or shape of the MNPs produced, and also sequesters fewer nanoparticles than the full Mms6 protein. Previous studies of an Mms6 *C*-terminal peptide in solution during POFHK magnetite formation show a negligible effect on particle size [96]. It was considered that the shorter length of Mms6$_{Peptide}$ (when compared to the Mms6 protein) may mean it is not as accessible on the SAM patterned surface, which may limit its ability to function. However, surfaces containing a complete layer of the peptide (without any PEG SAM or patterning) were found to result in the same sparse nanoparticle coverage after immersion in a POFHK reaction or pre-formed nanoparticles were supplied. The reasons for this remain unclear, and it could be that the shorter peptide crowds

itself by packing more closely on the gold surface or is more prone to being destabilised during the conditions of the POFHK reaction. One important feature absent from the peptide is the distinctive glycine-leucine repeat motif, which has been shown to be important in oligomerisation and activity [96, 206]. This motif could play a crucial role in the assembly of the Mms6 complex on the gold surface, by packing and orientating the proteins to facilitate iron ion coordination, binding, and nucleation of the magnetite nanoparticle. This packing may arrange the acidic residues of the *C*-terminal that is able to support iron binding and crystallisation of magnetite, as opposed to the potentially disordered surface packing of Mms6$_{Peptide}$.

This study could be built upon to further the understanding of the mode of action of Mms6. For example, the Mms6 protein could be engineered so that it contains a scrambled version of the *C*-terminal, or so that the glycine-leucine repeat motif is replaced with an *N*-terminal section that promotes different protein aggregation. These modified Mms6 proteins could then be patterned onto gold surfaces in the same way and exposed to a POFHK reaction. This could provide further insight as to whether these modifications have an effect on the biotemplating function of Mms6, and help to identify the key elements of the protein.

7.2 Chapter 4: Patterning with Nanoscale Precision

The microscale patterns of Mms6 biotemplated MNPs formed in Chapter 3 present a novel approach to the challenge of generating the billions of nanoscale magnetic islands that are required to form a recording medium suitable for BPM. However, for this approach to become reality the patterning resolution achieved with μCP would have to be significantly reduced to reduce feature sizes [41]. μCP with traditional Sylgard s-PDMS stamps is limited to a resolution of ≈500 nm and, although it is a simple and adaptable approach, it is also unlikely that μCP by hand could ever be scaled for high throughput mass production [138]. Therefore, in Chapter 4 Mms6 was patterned onto gold surfaces with a variety of alternative techniques, with the aim of generating patterns of MNPs that were more suitable for BPM.

Firstly, h-PDMS stamps, which have been shown to be able to pattern SAMs with a resolution down to 50 nm, were combined with the approach developed in Chapter 3 in order to pattern Mms6 with nanoscale precision [138]. This approach required the manufacture of stamp masters manufactured by EBL, to form the nanoscale features required. These were successfully formed through the EBL of an electron sensitive ZEP520A resist on silicon oxide surfaces, which acted as an etch mask in a subsequent RIE [161, 195]. However, due to continuous problems

with the EBL system only a few initial trials were ever run and the process was never optimised. As a result, the h-PDMS stamps had to be used to pattern the surface directly with the Mms6 protein, before the surface was backfilled with the PEG SAM (the SAM was still required to stop MNPs forming on the gold surface during the subsequent mineralisation reaction). These patterned surfaces were then immersed into a POFHK reaction that was designed to form magnetite. This approach was found to only have limited success. Some evidence of Mms6 biotemplated MNP patterns with nanoscale dimensions was observed, but this was found to extend over much smaller areas of the gold surfaces and the MNP patterns were less densely packed. It remains unclear if useable stamps were formed from the masters, whether the protein was delivered effectively to the surface during the stamping process without being degraded, and if the subsequent backfilling by the PEG SAM outcompeted or re-orientated the Mms6 protein as it was driven to form an ordered monolayer on the gold surface. These problems could be alleviated, by evaporating a chrome hard mask after the EBL of the ZEP520A resist. This would result in the formation of the inverse pattern, and optimising RIE etching techniques would allow for the formation of h-PDMS stamps that could print the PEG SAM onto the gold surfaces whilst leaving nanoscale areas of unmodified gold that are suitable for backfilling with Mms6.

The previous section reiterated that μCP printing is unlikely to ever form an industrially viable manufacture approach due to lack of control and reproducibility. Collaboration with the DPN Group at KIT in Germany allowed for access to PPL, which is essentially a controlled μCP process [145]. In this approach a PDMS stamp is controlled with the use of piezoelectrics to vastly improve the resolution and reproducibility achievable with μCP. The h-PDMS stamps that were available for use contained a regular array of pyramid tips, so again these stamps were used to pattern Mms6 directly onto the gold surfaces to achieve nanoscale patterning. Initial attempts to pattern Mms6 onto gold with PPL involved inking the h-PDMS stamps with Mms6 in a PBS buffer solution, before backfilling with the PEG SAM and immersing the patterned surfaces into a POFHK reaction. However, no evidence of biotemplated MNPs arranged into the expected dot patterns was seen during SEM analysis, and it remained unclear whether this was due to Mms6 not being delivered to the surface during the stamping process or a result of the backfilling with the PEG SAM process.

It was not possible to determine if Mms6 was successfully patterned onto the gold surface during the PPL process, but inking the stamps with a carrier mixture of glycerol and PBS that contained the Mms6 protein allowed the pattern that was stamped onto the gold surface to

be observed in an optical microscope. This allowed the dwell time (the stamp-surface contact time) to be optimised at 2 minutes. Shorter dwell times resulted in poor ink delivery, and longer dwell times resulted in the surface being over saturated. Achieving a uniform pattern across the gold surface remained challenging, even with the use of the optimum dwell time. After patterning the surfaces were incubated for 1 hour, before the glycerol was rinsed away and the patterned surfaces were subjected to a POFHK reaction.

In most cases the expected dot array of biotemplated MNPs were never seen during SEM analysis. Occasionally the expected pattern of nanoparticles was located during SEM analysis, but the pattern was less extensive and more sparsely populated with nanoparticles than the MNP patterned formed with the patterning of Mms6 with µCP in Chapter 3. This could be a feature of the problems in patterning the Mms6 directly onto the gold surface during the PPL process, and the backfilling of the protein patterned surfaces with the PEG SAM. Therefore, a potentially more successful approach to forming consistent biotemplated MNP arrays could be developed if stamps were produced that allowed for the patterning of the PEG SAM onto the gold surface with PPL, which leaves nanoscale areas of unmodified gold available to be backfilled with Mms6. Although, the small features on these stamps may well be swamped by the PEG ink.

The collaboration at KIT also allowed for access to DPN, which has been shown to pattern SAMs on surfaces with nanoscale precision [141]. Once again this approach had to be used to pattern a glycerol-PBS ink containing Mms6 directly onto the gold surface, before the surfaces were backfilled with PEG and immersed into a POFHK reaction. Unfortunately the DPN probe was found in an SEM analysis to scratch the desired pattern into the gold surface. MNPs did not form on these patterns and Mms6 appeared to not be delivered to the gold surface. This process could be optimised to determine the ultimate resolution achievable, but ultimately DPN is a slow serial writing process that could never be scaled up to form a cost-effect manufacturing process for the production of biomineralised surfaces for use in magnetic HDDs.

IL is a patterning technique that has not only been shown to be able to achieve patterning resolutions suitable for BPM, but is also able to expose wide areas (on the cm scale) in one highly reproducible exposure process [150, 151]. In this work a complete PEG SAM layer formed on gold was exposed to laser light in a Lloyd's mirror configuration, forming a diffraction pattern of bright and dark fringes over the surface [150]. Areas exposed to a high intensity bright fringe were photodegraded more quickly, and rinsed away from the surface forming a line pattern of PEG SAM and clean gold. The patterned surfaces were then backfilled with Mms6, with the protein binding to the clean gold spaces before being immersed in a POFHK reaction.

When an exposure dose of 20 J cm^{-2} was applied to the PEG patterned gold surfaces at a mirror surface angle of *2θ*=20˚ a regular line array of PEG SAM and clean gold was formed with nanoscale precision. Analysis of the MNPs on the surface reveals that the nanoparticles that formed were predominately magnetite, and had a larger mean size (≈86±21 nm) and smaller size distribution than the control MNPs (≈64±24 nm) suggesting that Mms6 was successfully patterned onto the surface. AFM measurements found that the MNP pattern formed with an average period of 392 nm, including lines of biotemplated MNPs with an average width of ≈308 nm and a PEG SAM background spacing region with an average width of ≈84 nm.

For the first time Mms6 was patterned onto a gold surface with nanoscale precision, biotemplating the formation of a line array of magnetite nanoparticles. Adapting this approach to be to form surfaces suitable for BPM would require Mms6 to be patterned into an array of dots and not lines. Previous work has shown that a very wide range of packing geometries and particle morphologies is readily accessible by the IL patterning of SAMs, including dot arrays through the use of two identical exposures at 90˚ angles [152]. However, this approach cannot be used to pattern the PEG SAM before backfilling with Mms6, as this would lead to the majority of the surface being covered by Mms6 (the opposite configuration to what is required). Therefore, attempts were made to pattern a complete layer of Mms6 formed on a gold surface with IL. Unfortunately, the Mms6 protein was found to remain stable on the surface even at IL doses as high as 100 mJ cm^{-2}. Therefore, this approach could not be used to pattern the protein on the surface in this geometry.

Recently, IL has been shown to be able to produce highly consistent dot arrays of gold and titanium on silicon substrates with dimensions as small as 30 nm [152, 153]. Combining these patterning approaches with biomineralisation proteins such as Mms6 could form an industrially scalable route to generating MNP arrays that are suitable for BPM. It is unlikely that gold surfaces would ever be cost effective, but it has been shown that proteins can be immobilised onto the cheaper alternative of titanium oxide as shown in Figure 7.2.1 [153]. Biomineralisation proteins could also be engineered to contain a titanium binding region that could drive their assembly, or the titanium oxide dots could be functionalised with a SAM that promotes protein attachment. Combining top-down IL nanopatterning with bottom-up biomineralisation proteins such as Mms6 to create uniform MNPs of magnetite in precise nanoscale patterns forms a novel, scalable and green approach to the challenge of forming a recording medium for BPM.
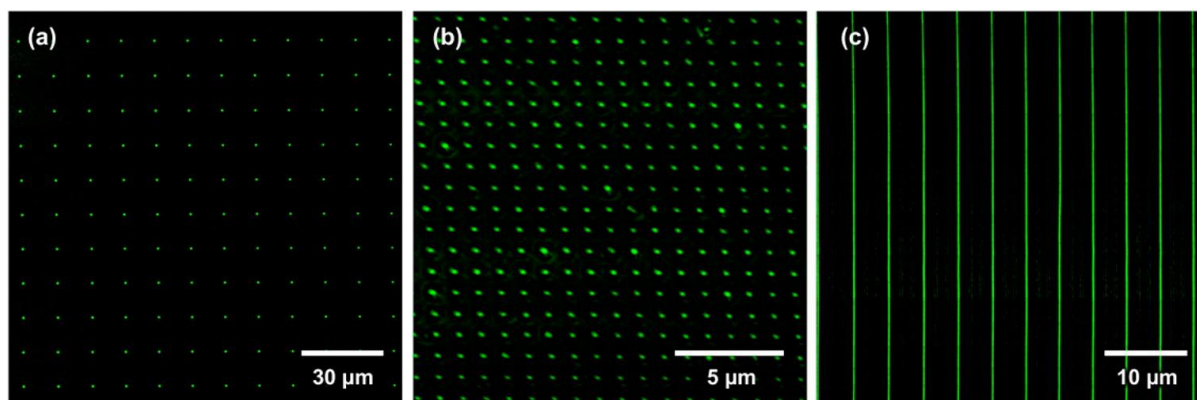
Figure 7.2.1 – Reprinted with permission from Figure 7 in Moxey, M., et al., Fabrication of Self-Cleaning, Reusable Titania Templates for Nanometer and Micrometer Scale Protein Patterning. ACS nano, 2015. 9(6): p. 6262-6270. Copyright © 2015 American Chemical Society. Confocal fluorescence microscopy images showing a fluorescent protein (fluorescein-conjugated wheat germ agglutinin, (FITC-WGA)) adsorbed to titanium oxide patterns formed through IL patterning consisting of (a) 0.6 µm dots, (b) 0.2 µm dots, and (c) 0.25 µm lines.

7.3 Chapter 5: Magnetite Nanoparticle Arrays formed with an Artificial Magnetite Binding Protein

Although a wide range of different biomineralisation proteins capable of controlling the formation of many different biomaterials have evolved in nature, they are not always suitable for use within technologies [199]. They can be expensive and difficult to manufacture, unusable in certain conditions and furthermore many technologically useful materials are not found in nature. However, we are no longer restricted by only the biomineralisation proteins that have evolved. The process of biopanning has uncovered many new peptide sequences that are capable of interacting with many different materials, including materials that are not found in nature [105]. Furthermore, this process has recently been extended to proteins, allowing for protein biopanning to be performed. Recently, Rawlings *et al*. [114] pioneered this approach to develop an artificial protein that interacted strongly with the [100] face of magnetite, termed 'magnetite interacting Adhiron 1' (MIA-1). In Chapter 5 MIA-1 was patterned onto gold surfaces that were functionalised with a PEG SAM *via* µCP, as an alternative to Mms6 for forming a biotemplated MNP array of magnetite. Four different schemes were trialled, with the use of magnetite nanoparticles that were formed in both RTCP and POFHK reactions, to determine the most efficient route to forming a MNP array with MIA-1.

When gold surfaces patterned with MIA-1 were placed into RTCP and POFHK reactions (Scheme I in Chapter 5), SEM analysis revealed that MNP arrays were not formed on the surface. When a RTCP reaction was used a complete layer of nanoparticles was seen to form on the

surface. As MNPs were previously shown not to form on areas of gold patterned with PEG this suggests that the PEG SAM was removed or damaged during the course of the RTCP reaction, which was found to go through a wide pH range of 2-13. This was confirmed when gold surfaces covered in a complete PEG SAM (without any patterning or protein) were immersed into a RTCP reaction, again resulting in a layer of MNPs forming on the gold surface. On the other hand when MIA-1 patterned surfaces were placed into a POFHK reaction, a negligible number of MNPs were found to form on the surfaces. This suggests that the PEG SAM and MIA-1 protein remain bound on the surface during this reaction, but the protein was unable to nucleate the formation of magnetite. The magnetite binding loops of MIA-1 contain a large number of basic amino acids. As a result, it is probable that MIA-1 is unable to bind to the magnetite nanoparticles that form under the basic conditions of a POFHK reaction, which was found to remain at a stable pH of approximately 9 for the majority of the 4 hour reaction.

Alternatively, MNPs were seen in SEM images to bind to the MIA-1 regions on the patterned gold surfaces when these surfaces were added to an aqueous solution at neutral pH containing MNPs that were pre-formed in both RTCP and POFHK after gentle mixing (Scheme II in Chapter 5). Patterns of MNPs were also found to form when variations of this scheme were trialled. MIA-1 was added to RTCP and POFHK reactions, with the aim of biotemplating and binding to MNPs of magnetite, before ordering these nanoparticles onto the unmodified gold areas of PEG patterned surfaces (Scheme III in Chapter 5). MIA-1 was also added to an aqueous solution of MNPs that were pre-formed in RTCP and POFHK reactions, again with the aim that the protein would bind to MNPs of magnetite before then binding to a PEG patterned surface to order these MNPs onto the gold surface (Scheme IV in Chapter 5). However, these two alternatives were found to produce patterns of MNPs that were found during SEM analysis to be less defined, consistent and contained fewer nanoparticles. Therefore, the most efficient route to forming biotemplated MNP arrays with MIA-1 was found to be first immobilising the protein onto a PEG patterned gold surface, before then supplying the protein patterned surfaces with a solution of pre-formed magnetite nanoparticles.

XRD and grainsize analysis suggests that the MNP patterns that bound to the gold surfaces during Scheme II were magnetite, with grainsize analysis finding that the MNPs bound to the surface had a mean size of ≈64±17 nm and ≈80±28 nm when MNPs that were pre-formed in RTCP and POFHK reactions respectively were supplied. These mean sizes are larger than the mean size of the particles found to form in control RTCP (≈54±21 nm) and POFHK (≈63±27 nm) reactions. This suggests that the protein is selective for the larger MNPs that form in the

mineralisation reactions, but the reason for this remains unclear. It is possible that this could be a result of larger MNPs mediating more contacts with the surface immobilised protein that stabilises the MNP on the surface more quickly, or could be selecting MNPs with certain cubic faces that have a larger mean size. Further studies that compare the size of the MNPs that were supplied to the surface with those that bind to a MIA-1 patterned surface and supplying MIA-1 patterned surfaces with magnetite MNPs of different and more consistent sizes may reveal the mechanism behind the size enhancement that was observed.

The use of MIA-1 demonstrates how artificial biomineralisation proteins can be identified, developed and used to form biotemplated MNP arrays. The use of MIA-1 over Mms6 also presents an alternative route to forming MNP arrays of magnetite, binding to preformed magnetite nanoparticles as opposed to biotemplating the growth of magnetite on the surface during a mineralisation reaction. MIA-1 was also shown to be patterned with nanoscale precision with the use of IL, leading to the production of nanoscale line arrays of magnetite nanoparticles. Therefore, this approach could be taken further, by combining MIA-1 patterned surfaces with magnetite mineralisation reactions that are not biocompatible such as thermal decomposition [27]. This approach could then be adapted to produce MNP arrays with properties that are more suitable for use in technologies.

7.4 Chapter 6: Alternative Materials

Magnetite has low coercivity and hence is a magnetically soft material that is unfortunately not suitable for use in magnetic data storage. The microscale arrays of Mms6 biotemplated MNPs that were produced in Chapter 3 were recorded to have a coercivity of 156 Oe at 295 K with VSM, orders of magnitude smaller than the magnetic materials that are currently used in magnetic HDDs [41]. Therefore, the magnetisation of magnetite is too prone to being reordered, which in a working HDD would lead to the catastrophic loss of data [41]. Therefore, in Chapter 6 biotemplated MNP arrays were formed with alternative materials, which are more suitable for use within magnetic data storage.

Previously, Mms6 has been shown to be able to template the formation of the magnetically harder material of cobalt-doped magnetite in the range of 0-15% [99]. This was found to result in a coercivity increase from 53-622 Oe, but decrease the magnetic saturation from 91-28 emu g^{-1} [99]. When a doping level of 6% cobalt was used, this was found to result in the largest increase in coercivity with only a minor effect on the saturation magnetisation [99].

Therefore, the use of Mms6 patterned gold surfaces to biotemplate the formation of MNPs of 6% cobalt-doped magnetite was explored, and the MNP arrays produced were compared to the Mms6 biotemplated MNP arrays formed without the addition of cobalt.

Gold surfaces were patterned with a PEG SAM with the use of μCP, before being backfilled with cysteine-tagged Mms6. These surfaces were then subjected to a POFHK reaction, with the substitution of 6% Co^{2+} to Fe^{2+}. MNPs were found to form on the protein patterned regions with limited mineralisation on the PEG SAM regions, and the biotemplated MNP arrays were comparable to those that formed in Chapter 3 during a POFHK reaction without the addition of cobalt. The MNPs that were biotemplated onto the surface formed with a larger mean size and tighter size distribution (≈84±14 nm) than those that formed in a control POFHK reaction with the addition of 6% cobalt (≈61±53 nm). XRD analysis confirmed that the biotemplated MNPs were predominantly magnetite or cobalt-doped magnetite, and ICP-ES analysis confirmed that the MNPs contained approximately 6% cobalt. When compared to the biotemplated nanoparticle array of pure magnetite the 6% cobalt-doped arrays were found to have a larger coercivity at 295 K, increasing from 156 Oe to 377 Oe. However, although this demonstrates how the magnetic properties of the biotemplated MNP arrays of magnetite can be tuned, this coercivity increase is still too low for this system to ever be used for data storage applications.

Galloway *et al.* [156] recently showed for the first time that MNPs of $L1_0$ phase CoPt, which would be well suited for BPM, can be biotemplated onto a surface under mild aqueous reaction conditions at room temperature. This was achieved through the use of a dual affinity peptide, with one half of the sequence designed to bind to a SiO_2 surface and the other a CoPt binding sequence [156]. In this work presented in this thesis the peptide sequence was modified, so that the SiO_2 binding region was replaced with a cysteine. Therefore, the patterning methods developed so far in this thesis could be combined with this peptide, as a route to forming a biotemplated surface that is suited for BPM.

A gold surface was coated with a PEG SAM, before exposed in IL to generate a line array of PEG SAM and clean gold with nanoscale dimensions. This surface was then backfilled with the CoPt binding peptide, before being subjected to a CoPt mineralisation reaction. MNPs were found to form on the surface on the regions patterned with the CoPt binding peptide, with a mean size of ≈12±3 nm. The MNPs were also found to be highly equidimensional and within the single domain size for CoPt. However, if this type of biotemplated surface is going to be used for BPM many challenges remain. Firstly, the biotemplated MNPs need to be in an array of dots and

not lines. Attempts were made to pattern a complete layer of the CoPt binding peptide into a dot array through the use of two identical IL exposures at 90˚ angles, but this was unsuccessful. As discussed previously, IL has been shown to be able to produce highly consistent dot arrays of gold and titanium on silicon substrates with dimensions as small as 30 nm (Figure 7.2.1) [152, 153]. Therefore, these patterning approaches could be combined with the CoPt binding peptide to form surfaces that are much more suitable for BPM, and this is something that is currently being explored by a new research student in the Staniland Group.

In addition, although the CoPt binding peptide has been shown to form $L1_0$ phase CoPt, to be used in data storage it is required that the *c*-axis of all the MNPs are uniformly aligned perpendicular to the surface. Magnetic measurements have found that this is not the case for the biotemplated CoPt nanoparticles formed with the CoPt binding peptide, and this problem was not rectified by performing the mineralisation step in the presence of a 0.2 T DC field aligned perpendicularly and parallel with the surfaces [156]. It could be that with a greater understanding of how the CoPt binding peptide interacts with the different facets of $L1_0$ phase CoPt, combined with biopanning to identify peptide sequences on Adhiron protein scaffolds that bind to specific faces of $L1_0$ phase CoPt could lead to the biomineralisation of a MNP array of CoPt with a uniformly aligned *c*-axis that is suitable for use in high-density data recording [156]. This has been achieved for gold [207] and platinum [208], so it could also be possible to achieve this for CoPt. The designed biomolecule could also be engineered to biotemplate the formation of soft magnetic under layers. For example, ruthenium is used to enhance the magnetic anisotropy of platinum surfaces, and a variation of this approach could also be combined with a CoPt binding peptide [209].

7.5 A Biologically Derived Magnetic Hard Disk and Beyond

It could be that a truly bioinspired approach to data storage is close to reality. The combination of the top-down patterning method of IL, with the bottom-up approach of biomineralisation could well be used to form a surface that is suitable for high-density data storage. However, there are still many obstacles to overcome, for example there remains challenges to the read/write head design and the suitability of a biotemplated MNP array in a working magnetic hard disk would have to be assessed.

There also remain many alternatives, in terms of the biomolecule and the patterning method used, to generate a surface suitable for BPM. For example, Klem *et al*. [155] developed a

heat shock protein from *Methanocooccus jainnaschii* that was modified to display a peptide with a $L1_0$ phase CoPt binding peptide within it. This forms a protein cage that contains a CoPt binding region. MNPs of CoPt were found to form inside the cage during a mild reaction of Co^{II} and Pt^{II} salts with a reducing agent [155]. The cage was found to have a mean cavity size of 6.5±1.3 nm (Figure 7.5.1), which could lead to the formation of highly consistent single domain CoPt nanoparticles as the cage acts to restrict the size of the MNPs that form [155]. In this work an annealing step was used to generate the $L1_0$ phase, but the cages could be adapted to display peptides that template the formation of $L1_0$ phase CoPt with a uniformly aligned c-axis. Along with a route to consistently immobilise the protein cage, such as modification of one of the subunits to contain a specific binding region, and while highly ambitious, this approach could form an alternative route to generating an array of MNPs with a highly uniform size and morphology that is suitable for BPM.
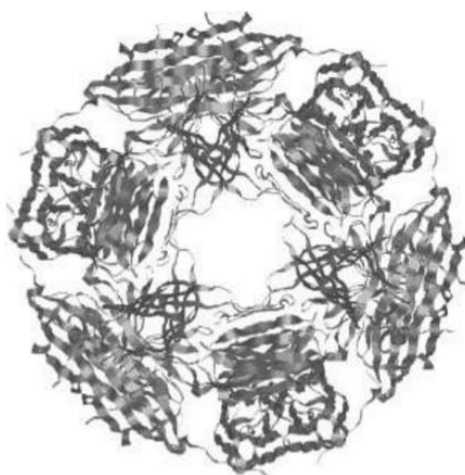
Figure 7.5.1 – Reprinted with permission from Fig. 1 in Klem, M.T., et al., Bio-inspired Synthesis of Protein-Encapsulated CoPt Nanoparticles. Advanced Functional Materials, 2005. 15(9): p. 1489-1494. Copyright © 2015 Advanced Functional Materials. Ribbon diagram of the heat shock protein from *Methanocooccus jainnaschii* looking down the threefold channel of the assembled protein cage.

There also remain many alternatives to the top-down patterning methods discussed so far in this thesis. There are a large number of self-ordered structures that are found in nature that could be adapted to form an etch mask or a template for the patterning of biomolecules, including; DNA origami [210], anodised alumina [211] and phase separation in block co-polymers [212]. One interesting approach could be the adaption of crystalline bacterial cell surface layers (S-layers), which are the cell envelope component in many bacteria and archaea. They form porous meshes with repeatable units in the range of 3-30 nm and pore sizes in the range of 2-8 nm [213]. More importantly they have been shown to self-assemble onto solid substrates, and could form a template for biomineralisation (Figure 7.5.2) [213]. Although these layers typically

only extend over micrometre size ranges, if this could be addressed the adaption of this layer to display a CoPt binding peptide could form a truly bioinspired and completely bottom-up self-assembly approach to BPM.
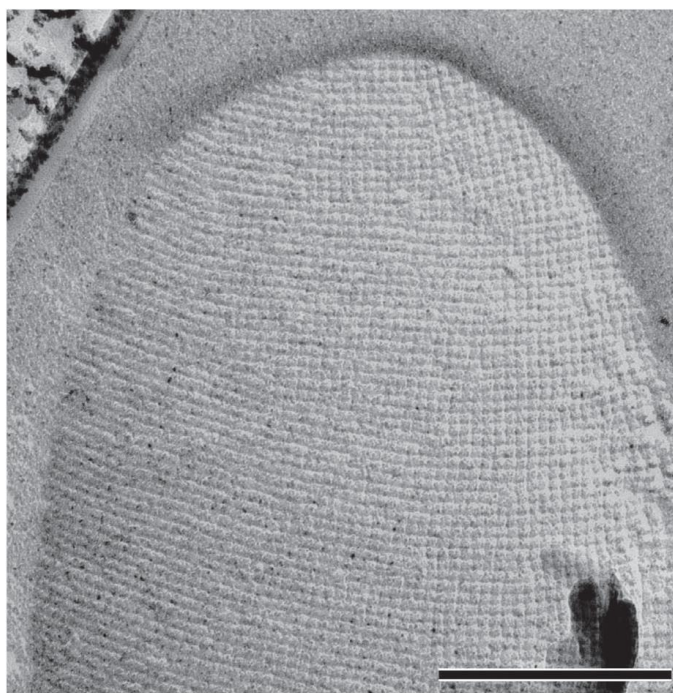
Figure 7.5.2 - Reprinted with permission from Figure 1 in Pum, D. and U.B. Sleytr, Reassembly of S-layer proteins. Nanotechnology, 2014. 25(31): p. 312001. Copyright © 2015 Nanotechnology. Transmission electron micrograph of a freeze-etched and metal-shadowed bacterial cell (*Desulfotomaculum nigrificans* strain NCIB 8706) revealing an S-layer with square lattice symmetry on its surface. Scale bar 200 nm.

In this thesis it has been shown that biomineralisation could be used as an alternative to traditional manufacturing to form devices, such as magnetic hard disks. The specificity of biomineralisation may also allow multi-material biotemplated devices to be fabricated, opening up a new route to building complex devices from the bottom up. There currently remain many challenges to developing the ability to control the location or formation of different types of biomaterials, but once these challenges are met biomineralisation could form a simpler, cheaper and more environmentally friendly alternative that could dominate the future of manufacturing and lead to a whole new range of bioinspired technologies.

References

1. Feynman, R.P., *There's plenty of room at the bottom.* Engineering and science, 1960. **23**(5): p. 22-36.
2. Milburn, C., *Nanovision: engineering the future*. 2010: Duke University Press.
3. Cullity, B.D. and C.D. Graham, *Introduction to magnetic materials*. 2 ed. 2011: John Wiley & Sons.
4. Keithley, J.F., *The story of electrical and magnetic measurements: from 500 BC to the 1940s*. 1999: John Wiley & Sons.
5. Oersted, H.C., *Electricity and magnetic needles.* Philosophy 1820. **16**(4): p. 273-276.
6. Maxwell, J.C., *A dynamical theory of the electromagnetic field.* Philosophical Transactions of the Royal Society of London, 1865: p. 459-512.
7. Thomson, J.J., *XL. Cathode rays.* The London, Edinburgh, and Dublin Philosophical Magazine and Journal of Science, 1897. **44**(269): p. 293-316.
8. Brown Jr, W., *Tutorial paper on dimensions and units.* Magnetics, IEEE Transactions on, 1984. **20**(1): p. 112-117.
9. Heering, P., *On Coulomb's inverse square law.* American journal of physics, 1992. **60**(11): p. 988-994.
10. Faraday, M., *On the physical character of the lines of magnetic force.* The London, Edinburgh, and Dublin Philosophical Magazine and Journal of Science, 1852. **3**(20): p. 401-428.
11. Spaldin, N.A., *Magnetic materials: fundamentals and applications*. 2010: Cambridge University Press.
12. Ampère, A.-M., *Théorie Mathématique des Phénomènes Électro-dynamiques Uniquement Déduite de l'Expérience (Éditions Jacques Gabay, Sceaux, 1990). Réimpression du Mémoire fondamental d'André-Marie Ampère paru en 1827 dans les.* Mémoires de l'Académie Royale des Sciences de l'Institut de France, année 1823, 1827. **6**: p. 175-388.
13. Bohr, N., *On the constitution of atoms and molecules.* The London, Edinburgh, and Dublin Philosophical Magazine and Journal of Science, 1913. **26**(151): p. 1-25.
14. Weiss, P., *L'hypothèse du champ moléculaire et la propriété ferromagnétique.* J. Phys. Theor. Appl., 1907. **6**(1): p. 661-690.
15. Bitter, F., *On inhomogeneities in the magnetization of ferromagnetic materials.* Physical review, 1931. **38**(10): p. 1903.
16. Cornell, R.M. and U. Schwertmann, *The iron oxides: structure, properties, reactions, occurrences and uses*. 2006: John Wiley & Sons.
17. Verwey, E., *Electronic conduction of magnetite (Fe3O4) and its transition point at low temperatures.* Nature, 1939. **144**(3642): p. 327-328.
18. Walz, F., *The Verwey transition-a topical review.* Journal of Physics: Condensed Matter, 2002. **14**(12): p. R285.
19. Sorescu, M., A. Grabias, D. Tarabasanu-Mihaila, and L. Diamandescu, *From magnetite to cobalt ferrite.* Journal of Materials Synthesis and Processing, 2001. **9**(3): p. 119-123.
20. Aboaf, J., S. Herd, and E. Klokholm, *Magnetic properties and structure of cobalt-platinum thin films.* Magnetics, IEEE Transactions on, 1983. **19**(4): p. 1514-1519.
21. Ford, L., *Platinum alloy permanent magnets.* Platinum Metals Rev, 1964. **8**(3): p. 82-90.
22. Laughlin, D.E., K. Srinivasan, M. Tanase, and L. Wang, *Crystallographic aspects of L1 0 magnetic materials.* Scripta Materialia, 2005. **53**(4): p. 383-388.
23. Wang, Y., X. Zhang, Y. Liu, Y. Jiang, Y. Zhang, and J. Yang, *Microstructure and magnetic properties of L10 CoPt nanoparticles by Ag addition.* Journal of Sol-Gel Science and Technology, 2014. **70**(3): p. 528-533.

24. Weller, D., A. Moser, L. Folks, M.E. Best, W. Lee, M.F. Toney, M. Schwickert, J.-U. Thiele, and M.F. Doerner, *High K u materials approach to 100 Gbits/in 2.* Magnetics, IEEE Transactions on, 2000. **36**(1): p. 10-15.

25. Brydson, R.M. and C. Hammond, *Generic methodologies for nanotechnology: classification and fabrication*, in *Nanoscale science and technology*, R.W. Kelsall, I.W. Hamley, and M. Geoghegan, Editors. 2005, John Wiley & Sons. p. 1-54.

26. Binns, C., *Nanomagnetism: Fundamentals and Applications*. Vol. 6. 2014: Newnes.

27. Lu, A.H., E.e.L. Salabas, and F. Schüth, *Magnetic nanoparticles: synthesis, protection, functionalization, and application.* Angewandte Chemie International Edition, 2007. **46**(8): p. 1222-1244.

28. Laurent, S., D. Forge, M. Port, A. Roch, C. Robic, L. Vander Elst, and R.N. Muller, *Magnetic iron oxide nanoparticles: synthesis, stabilization, vectorization, physicochemical characterizations, and biological applications.* Chemical reviews, 2008. **108**(6): p. 2064-2110.

29. Thomson, T. and B.D. Terris, *Patterned magnetic recording media: progress and prospects*, in *Developments in Data Storage: Materials Perspective*, S.N. Piramanayagam and T.C. Chong, Editors. 2012, John Wiley & Sons. p. 256-276.

30. Langevin, D., *Micelles and microemulsions.* Annual Review of Physical Chemistry, 1992. **43**(1): p. 341-369.

31. Deng, H., X. Li, Q. Peng, X. Wang, J. Chen, and Y. Li, *Monodisperse Magnetic Single-Crystal Ferrite Microspheres.* Angewandte Chemie, 2005. **117**(18): p. 2842-2845.

32. Papell, S.S., *Low viscosity magnetic fluid obtained by the colloidal suspension of magnetic particles*. 1965: US.

33. Raj, K., B. Moskowitz, and R. Casciari, *Advances in ferrofluid technology.* Journal of magnetism and magnetic materials, 1995. **149**(1): p. 174-180.

34. Tsang, S.C., V. Caps, I. Paraskevas, D. Chadwick, and D. Thompsett, *Magnetically Separable, Carbon-Supported Nanocatalysts for the Manufacture of Fine Chemicals.* Angewandte Chemie, 2004. **116**(42): p. 5763-5767.

35. Mornet, S., S. Vasseur, F. Grasset, P. Veverka, G. Goglio, A. Demourgues, J. Portier, E. Pollert, and E. Duguet, *Magnetic nanoparticle design for medical applications.* Progress in Solid State Chemistry, 2006. **34**(2-4): p. 237-247.

36. Zhang, D., S. Wei, C. Kaila, X. Su, J. Wu, A.B. Karki, D.P. Young, and Z. Guo, *Carbon-stabilized iron nanoparticles for environmental remediation.* Nanoscale, 2010. **2**(6): p. 917-919.

37. Lesser, M.L. and J. Haanstra. *The RAMAC data-processing machine: system organization of the IBM 305*. in *Papers and discussions presented at the December 10-12, 1956, eastern joint computer conference: New developments in computers*. 1956. ACM.

38. Poulsen, V., P.O. Pedersen, and C. Schou, *Telegraphone*. 1905: US789336.

39. Fritz, P., *Recording and reproducing device for magnetic sound writing*. 1941: US2247847.

40. Terris, B. and T. Thomson, *Nanofabricated and self-assembled magnetic structures as data storage media.* Journal of physics D: Applied physics, 2005. **38**(12): p. R199.

41. Piramanayagam, S.N. and T.C. Chong, *Developments in Data Storage: Materials Perspective*. 2012: John Wiley & Sons.

42. Richter, H., *The transition from longitudinal to perpendicular recording.* Journal of physics D: Applied physics, 2007. **40**(9): p. R149.

43. Ceruzzi, P.E., *A history of modern computing*. 2003: MIT press.

44. Weller, D. and A. Moser, *Thermal effect limits in ultrahigh-density magnetic recording.* Magnetics, IEEE Transactions on, 1999. **35**(6): p. 4423-4439.

45. Shi, L., R. Zhao, and T.C. Chong, *Phase change random access memory*, in *Developments in Data Storage: Materials Perspective*, S.N. Piramanayagam and T.C. Chong, Editors. 2012, John Wiley & Sons. p. 277-296.

46. Rausch, T., E. Gage, and J. Dykes, *Heat Assisted Magnetic Recording*, in *Ultrafast Magnetism I*, J.Y. Bigot, et al., Editors. 2015, Springer. p. 200-202.

47. Zhu, J.-G., X. Zhu, and Y. Tang, *Microwave assisted magnetic recording.* IEEE Transactions on Magnetics, 2008. **44**(1): p. 125-131.

48. Wollhofen, R., J. Katzmann, C. Hrelescu, J. Jacak, and T.A. Klar, *120 nm resolution and 55 nm structure size in STED-lithography.* Optics express, 2013. **21**(9): p. 10831-10840.

49. Driskill-Smith, A.A. *Electron-beam and emerging lithography for the magnetic recording industry*. in *Microlithography 2004*. 2004. International Society for Optics and Photonics.

50. Aranda, P. and J. Garcıa, *Porous membranes for the preparation of magnetic nanostructures.* Journal of magnetism and magnetic materials, 2002. **249**(1): p. 214-219.

51. Harrison, C., J.A. Dagata, and D.H. Adamson, *Lithography with self-assembled block copolymer microdomains* in *Developments in block copolymer science and technology* I.W. Hamley, Editor. 2003, John Wiley & Sons. p. 295-325.

52. Chou, S.Y., P.R. Krauss, and P.J. Renstrom, *Nanoimprint lithography.* Journal of Vacuum Science & Technology B, 1996. **14**(6): p. 4129-4133.

53. Kern, W., *Thin film processes II*. Vol. 2. 2012: Academic press.

54. Mann, S., *Biomineralization: principles and concepts in bioinorganic materials chemistry*. Vol. 5. 2001: Oxford University Press.

55. Kirschvink, J. and J. Hagadorn, *A Grand Unified Theory of Biomineralization.*, in *The biomineralization of nano-and microstructures*. 2000, Wiley-VCH Verlag: Weinheim, Germany. p. 139-150.

56. Arakaki, A., H. Nakazawa, M. Nemoto, T. Mori, and T. Matsunaga, *Formation of magnetite by bacteria and its application.* Journal of the Royal Society interface, 2008. **5**(26): p. 977-999.

57. Hildebrand, M., *Diatoms, biomineralization processes, and genomics.* Chemical reviews, 2008. **108**(11): p. 4855.

58. Lovley, D.R., S.J. Giovannoni, D.C. White, J.E. Champine, E. Phillips, Y.A. Gorby, and S. Goodwin, *Geobacter metallireducens gen. nov. sp. nov., a microorganism capable of coupling the complete oxidation of organic compounds to the reduction of iron and other metals.* Archives of microbiology, 1993. **159**(4): p. 336-344.

59. Frankel, R.B. and D.A. Bazylinski, *Biologically induced mineralization by bacteria.* Reviews in Mineralogy and Geochemistry, 2003. **54**(1): p. 95-114.

60. Komeili, A., *Molecular mechanisms of compartmentalization and biomineralization in magnetotactic bacteria.* FEMS microbiology reviews, 2012. **36**(1): p. 232-255.

61. Bellini, S., *On a unique behavior of freshwater bacteria.* Chinese Journal of Oceanology and Limnology, 2009. **27**(1): p. 3-5.

62. Bellini, S., *Further studies on "magnetosensitive bacteria".* Chinese Journal of Oceanology and Limnology, 2009. **27**(1): p. 6-12.

63. Blakemore, R., D. Maratea, and R. Wolfe, *Isolation and pure culture of a freshwater magnetic spirillum in chemically defined medium.* Journal of Bacteriology, 1979. **140**(2): p. 720-729.

64. Blakemore, R., *Magnetotactic bacteria.* Science, 1975. **190**(4212): p. 377-379.

65. Frankel, R.B. and R. Blakemore, *Navigational compass in magnetic bacteria.* Journal of Magnetism and Magnetic Materials, 1980. **15**: p. 1562-1564.

66. Frankel, R.B., D.A. Bazylinski, M.S. Johnson, and B.L. Taylor, *Magneto-aerotaxis in marine coccoid bacteria.* Biophysical Journal, 1997. **73**(2): p. 994-1000.

67. Alexandre, G., S. Greer-Phillips, and I.B. Zhulin, *Ecological role of energy taxis in microorganisms.* FEMS microbiology reviews, 2004. **28**(1): p. 113-126.

68. Simmons, S.L., D.A. Bazylinski, and K.J. Edwards, *South-seeking magnetotactic bacteria in the Northern Hemisphere.* Science, 2006. **311**(5759): p. 371-374.

69. Kopp, R.E. and J.L. Kirschvink, *The identification and biogeochemical interpretation of fossil magnetotactic bacteria.* Earth-Science Reviews, 2008. **86**(1): p. 42-61.

70. Byrne, J.M., N. Klueglein, C. Pearce, K.M. Rosso, E. Appel, and A. Kappler, *Redox cycling of Fe (II) and Fe (III) in magnetite by Fe-metabolizing bacteria.* Science, 2015. **347**(6229): p. 1473-1476.

71. Lefèvre, C.T., R.B. Frankel, and D.A. Bazylinski, *Magnetotaxis in prokaryotes*, in *eLS*. 2011, John Wiley & Sons, Ltd: Chichester.

72. Schleifer, K.H., D. Schüler, S. Spring, M. Weizenegger, R. Amann, W. Ludwig, and M. Köhler, *The genus Magnetospirillum gen. nov. Description of Magnetospirillum gryphiswaldense sp. nov. and transfer of Aquaspirillum magnetotacticum to Magnetospirillum magnetotacticum comb. nov.* Systematic and applied microbiology, 1991. **14**(4): p. 379-385.

73. Matsunaga, T., T. Sakaguchi, and F. Tadakoro, *Magnetite formation by a magnetic bacterium capable of growing aerobically.* Applied microbiology and biotechnology, 1991. **35**(5): p. 651-655.

74. Staniland, S.S., A. Rawlings, J. Bramble, J. Tolosa, O. Wilson, J.C. Garcia-Martinez, and C. Binns, *Novel Methods for the Synthesis of Magnetic Nanoparticles*, in *Nanomagnetism: Fundamentals and Applications*, C. Binns, Editor. 2014, Newnes. p. 85-101.

75. Gorby, Y.A., T.J. Beveridge, and R.P. Blakemore, *Characterization of the bacterial magnetosome membrane.* Journal of Bacteriology, 1988. **170**(2): p. 834-841.

76. Grünberg, K., E.-C. Müller, A. Otto, R. Reszka, D. Linder, M. Kube, R. Reinhardt, and D. Schüler, *Biochemical and proteomic analysis of the magnetosome membrane in Magnetospirillum gryphiswaldense.* Applied and Environmental Microbiology, 2004. **70**(2): p. 1040-1050.

77. Grünberg, K., C. Wawer, B.M. Tebo, and D. Schüler, *A large gene cluster encoding several magnetosome proteins is conserved in different species of magnetotactic bacteria.* Applied and Environmental Microbiology, 2001. **67**(10): p. 4573-4582.

78. Richter, M., M. Kube, D.A. Bazylinski, T. Lombardot, F.O. Glöckner, R. Reinhardt, and D. Schüler, *Comparative genome analysis of four magnetotactic bacteria reveals a complex set of group-specific genes implicated in magnetosome biomineralization and function.* Journal of Bacteriology, 2007. **189**(13): p. 4899-4910.

79. Fukuda, Y., Y. Okamura, H. Takeyama, and T. Matsunaga, *Dynamic analysis of a genomic island in Magnetospirillum sp. strain AMB-1 reveals how magnetosome synthesis developed.* FEBS letters, 2006. **580**(3): p. 801-812.

80. Ullrich, S., M. Kube, S. Schübbe, R. Reinhardt, and D. Schüler, *A hypervariable 130-kilobase genomic region of Magnetospirillum gryphiswaldense comprises a magnetosome island which undergoes frequent rearrangements during stationary growth.* Journal of Bacteriology, 2005. **187**(21): p. 7176-7184.

81. Komeili, A., H. Vali, T.J. Beveridge, and D.K. Newman, *Magnetosome vesicles are present before magnetite formation, and MamA is required for their activation.* Proceedings of the National Academy of Sciences of the United States of America, 2004. **101**(11): p. 3839-3844.

82. Kolinko, I., A. Lohße, S. Borg, O. Raschdorf, C. Jogler, Q. Tu, M. Pósfai, É. Tompa, J.M. Plitzko, and A. Brachmann, *Biosynthesis of magnetic nanostructures in a foreign organism by transfer of bacterial magnetosome gene clusters.* Nature nanotechnology, 2014. **9**(3): p. 193-197.

83. Tanaka, M., A. Arakaki, and T. Matsunaga, *Identification and functional characterization of liposome tubulation protein from magnetotactic bacteria.* Molecular microbiology, 2010. **76**(2): p. 480-488.

84. Okamura, Y., H. Takeyama, and T. Matsunaga, *A Magnetosome-specific GTPase from the Magnetic BacteriumMagnetospirillum magneticum AMB-1.* Journal of Biological Chemistry, 2001. **276**(51): p. 48183-48188.

85. Scheffel, A., M. Gruska, D. Faivre, A. Linaroudis, J.M. Plitzko, and D. Schüler, *An acidic protein aligns magnetosomes along a filamentous structure in magnetotactic bacteria.* Nature, 2006. **440**(7080): p. 110-114.

86. Arakaki, A., J. Webb, and T. Matsunaga, *A novel protein tightly bound to bacterial magnetic particles in Magnetospirillum magneticum strain AMB-1.* Journal of Biological Chemistry, 2003. **278**(10): p. 8745-8750.

87. Komeili, A., *Molecular mechanisms of magnetosome formation.* Annu. Rev. Biochem., 2007. **76**: p. 351-366.

88. Siponen, M., G. Adryanczyk, N. Ginet, P. Arnoux, and D. Pignol, *Magnetochrome: a c-type cytochrome domain specific to magnetotatic bacteria.* Biochemical Society Transactions, 2012. **40**(6): p. 1319.

89. Murat, D., V. Falahati, L. Bertinetti, R. Csencsits, A. Körnig, K. Downing, D. Faivre, and A. Komeili, *The magnetosome membrane protein, MmsF, is a major regulator of magnetite biomineralization in Magnetospirillum magneticum AMB-1.* Molecular microbiology, 2012. **85**(4): p. 684-699.

90. Amemiya, Y., A. Arakaki, S.S. Staniland, T. Tanaka, and T. Matsunaga, *Controlled formation of magnetite crystal by partial oxidation of ferrous hydroxide in the presence of recombinant magnetotactic bacterial protein Mms6.* Biomaterials, 2007. **28**(35): p. 5381-5389.

91. Xu, D. and Y. Zhang, *Ab initio protein structure assembly using continuous structure fragments and optimized knowledge-based force field.* Proteins, 2012. **80**: p. 1715-1735.

92. DeLano, W., *The PyMOL Molecular Graphics System; DeLano Scientific: San Carlos, CA.* 2009.

93. Arakaki, A., F. Masuda, and T. Matsunaga. *Iron oxide crystal formation on a substrate modified with the Mms6 protein from magnetotactic bacteria.* 2009. Cambridge Univ Press.

94. Tanaka, M., E. Mazuyama, A. Arakaki, and T. Matsunaga, *MMS6 protein regulates crystal morphology during nano-sized magnetite biomineralization in vivo.* Journal of Biological Chemistry, 2011. **286**(8): p. 6386-6392.

95. Prozorov, T., S.K. Mallapragada, B. Narasimhan, L. Wang, P. Palo, M. Nilsen-Hamilton, T.J. Williams, D.A. Bazylinski, R. Prozorov, and P.C. Canfield, *Protein-mediated synthesis of uniform superparamagnetic magnetite nanocrystals.* Advanced Functional Materials, 2007. **17**(6): p. 951.

96. Arakaki, A., F. Masuda, Y. Amemiya, T. Tanaka, and T. Matsunaga, *Control of the morphology and size of magnetite particles with peptides mimicking the Mms6 protein from magnetotactic bacteria.* Journal of colloid and interface science, 2010. **343**(1): p. 65-70.

97. Galloway, J.M., J.P. Bramble, A.E. Rawlings, G. Burnell, S.D. Evans, and S.S. Staniland, *Biotemplated Magnetic Nanoparticle Arrays.* Small, 2012. **8**(2): p. 204–208.

98. Galloway, J.M., J.P. Bramble, A.E. Rawlings, G. Burnell, S.D. Evans, and S.S. Staniland, *Nanomagnetic Arrays Formed with the Biomineralization Protein Mms6.* Journal of Nano Research, 2012. **17**: p. 127-146.

99. Galloway, J.M., A. Arakaki, F. Masuda, T. Tanaka, T. Matsunaga, and S.S. Staniland, *Magnetic bacterial protein Mms6 controls morphology, crystallinity and magnetism of cobalt-doped magnetite nanoparticles in vitro.* Journal of Materials Chemistry, 2011. **21**(39): p. 15244-15254.

100. Porath, J., J. Carlsson, I. Olsson, and G. Belfrage, *Metal chelate affinity chromatography, a new approach to protein fractionation.* Nature, 1975. **258**: p. 598-599.

101. Soong, R., S. Stelick, G. Bachand, and C. Montemagno. *Evaluating adhesion strength of biological molecules to nanofabricated substrates*. in *Technical proceedings of the Second International Conference on Modeling and Simulation of Microsystems*. 1999.

102. Marblestone, J.G., S.C. Edavettal, Y. Lim, P. Lim, X. Zuo, and T.R. Butt, *Comparison of SUMO fusion technology with traditional gene fusion systems: enhanced expression and solubility with SUMO.* Protein Science, 2006. **15**(1): p. 182-189.

103. Arnau, J., C. Lauritzen, G.E. Petersen, and J. Pedersen, *Current strategies for the use of affinity tags and tag removal for the purification of recombinant proteins.* Protein expression and purification, 2006. **48**(1): p. 1-13.

104. Jenny, R.J., K.G. Mann, and R.L. Lundblad, *A critical review of the methods for cleavage of fusion proteins with thrombin and factor Xa.* Protein expression and purification, 2003. **31**(1): p. 1-11.

105. Tamerler, C., S. Dinçer, D. Heidel, N. Karaguler, and M. Sarikaya. *Combinatorial Peptide Libraries for Selecting Inorganic-Binding Proteins: A Step in Molecular Biomimetics*. in *MRS Proceedings*. 2003. Cambridge Univ Press.

106. Seker, U.O.S. and H.V. Demir, *Material binding peptides for nanotechnology.* Molecules, 2011. **16**(2): p. 1426-1451.

107. Bratkovič, T., *Progress in phage display: evolution of the technique and its applications.* Cellular and molecular life sciences, 2010. **67**(5): p. 749-767.

108. Kim, J., Y. Rheem, B. Yoo, Y. Chong, K.N. Bozhilov, D. Kim, M.J. Sadowsky, H.-G. Hur, and N.V. Myung, *Peptide-mediated shape-and size-tunable synthesis of gold nanostructures.* Acta biomaterialia, 2010. **6**(7): p. 2681-2689.

109. Reith, F., B. Etschmann, C. Grosse, H. Moors, M.A. Benotmane, P. Monsieurs, G. Grass, C. Doonan, S. Vogt, and B. Lai, *Mechanisms of gold biomineralization in the bacterium Cupriavidus metallidurans.* Proceedings of the National Academy of Sciences, 2009. **106**(42): p. 17757-17762.

110. Liu, Y., J. Mao, B. Zhou, W. Wei, and S. Gong, *Peptide aptamers against titanium-based implants identified through phage display.* Journal of Materials Science: Materials in Medicine, 2010. **21**(4): p. 1103-1107.

111. Ruan, L., C.-Y. Chiu, Y. Li, and Y. Huang, *Synthesis of platinum single-twinned right bipyramid and {111}-bipyramid through targeted control over both nucleation and growth using specific peptides.* Nano letters, 2011. **11**(7): p. 3040-3046.

112. Mao, C., D.J. Solis, B.D. Reiss, S.T. Kottmann, R.Y. Sweeney, A. Hayhurst, G. Georgiou, B. Iverson, and A.M. Belcher, *Virus-based toolkit for the directed synthesis of magnetic and semiconducting nanowires.* Science, 2004. **303**(5655): p. 213-217.

113. Reiss, B.D., C. Mao, D.J. Solis, K.S. Ryan, T. Thomson, and A.M. Belcher, *Biological routes to metal alloy ferromagnetic nanostructures.* Nano letters, 2004. **4**(6): p. 1127-1132.

114. Rawlings, A.E., J.P. Bramble, A.A. Tang, L.A. Somner, A.E. Monnington, D.J. Cooke, M.J. McPherson, D.C. Tomlinson, and S.S. Staniland, *Phage display selected magnetite interacting Adhirons for shape controlled nanoparticle synthesis.* Chemical Science, 2015.

115. Tiede, C., A.A. Tang, S.E. Deacon, U. Mandal, J.E. Nettleship, R.L. Owen, S.E. George, D.J. Harrison, R.J. Owens, and D.C. Tomlinson, *Adhiron: a stable and versatile peptide display scaffold for molecular recognition applications.* Protein Engineering Design and Selection, 2014. **27**(5): p. 145-155.

116. Rusmini, F., Z. Zhong, and J. Feijen, *Protein immobilization strategies for protein biochips.* Biomacromolecules, 2007. **8**(6): p. 1775-1789.

117. Hadley, M.J., A.J. Wright, N.A. Rowson, and L.M. Grover, *Acicular nanoparticles formed through coprecipitation of iron salts in the presence of bovine serum albumin.* Journal of Materials Chemistry, 2011. **21**(36): p. 13769-13771.

118. Prime, K.L. and G.M. Whitesides, *Adsorption of proteins onto surfaces containing end-attached oligo (ethylene oxide): a model system using self-assembled monolayers.* Journal of the American Chemical Society, 1993. **115**(23): p. 10714-10721.

119. Love, J.C., L.A. Estroff, J.K. Kriebel, R.G. Nuzzo, and G.M. Whitesides, *Self-assembled monolayers of thiolates on metals as a form of nanotechnology.* Chemical reviews, 2005. **105**(4): p. 1103-1170.

120. Vericat, C., M. Vela, G. Benitez, P. Carro, and R. Salvarezza, *Self-assembled monolayers of thiols and dithiols on gold: new challenges for a well-known system.* Chem. Soc. Rev., 2010. **39**(5): p. 1805-1834.

121. Schreiber, F., *Self-assembled monolayers: from'simple'model systems to biofunctionalized interfaces.* Journal of Physics: Condensed Matter, 2004. **16**: p. R881.

122. Franklin, B., W. Brownrigg, and M. Farish, *Of the stilling of waves by means of oil. Extracted from sundry letters between Benjamin Franklin, LL. DFRS William Brownrigg, MDFRS and the Reverend Mr. Farish.* Philosophical Transactions, 1774. **64**: p. 445-460.

123. Langmuir, I., *The constitution and fundamental properties of solids and liquids. II. Liquids. 1.* Journal of the American Chemical Society, 1917. **39**(9): p. 1848-1906.

124. Blodgett, K.B. and I. Langmuir, *Built-up films of barium stearate and their optical properties.* Physical Review, 1937. **51**(11): p. 964.

125. Bigelow, W., D. Pickett, and W. Zisman, *Oleophobic monolayers: I. Films adsorbed from solution in non-polar liquids.* Journal of Colloid Science, 1946. **1**(6): p. 513-538.

126. Nuzzo, R.G. and D.L. Allara, *Adsorption of bifunctional organic disulfides on gold surfaces.* Journal of the American Chemical Society, 1983. **105**(13): p. 4481-4483.

127. Maoz, R. and J. Sagiv, *On the formation and structure of self-assembling monolayers. I. A comparative atr-wettability study of Langmuir—Blodgett and adsorbed films on flat substrates and glass microbeads.* Journal of Colloid and Interface Science, 1984. **100**(2): p. 465-496.

128. Schwartz, D.K., *Mechanisms and kinetics of self-assembled monolayer formation.* Annual review of physical chemistry, 2001. **52**(1): p. 107-137.

129. Schreiber, F., *Structure and growth of self-assembling monolayers.* Progress in surface science, 2000. **65**(5-8): p. 151-257.

130. Ulman, A., *Formation and structure of self-assembled monolayers.* Chemical reviews, 1996. **96**(4): p. 1533-1554.

131. Bain, C.D., E.B. Troughton, Y.T. Tao, J. Evall, G.M. Whitesides, and R.G. Nuzzo, *Formation of monolayer films by the spontaneous assembly of organic thiols from solution onto gold.* Journal of the American Chemical Society, 1989. **111**(1): p. 321-335.

132. Schneider, T.W. and D.A. Buttry, *Electrochemical quartz crystal microbalance studies of adsorption and desorption of self-assembled monolayers of alkyl thiols on gold.* Journal of the American Chemical Society, 1993. **115**(26): p. 12391-12397.

133. Xu, S., S.J.N. Cruchon-Dupeyrat, J.C. Garno, G.Y. Liu, G.K. Jennings, T.H. Yong, and P.E. Laibinis, *In situ studies of thiol self-assembly on gold from solution using atomic force microscopy.* The Journal of chemical physics, 1998. **108**: p. 5002.

134. Lavrich, D.J., S.M. Wetterer, S.L. Bernasek, and G. Scoles, *Physisorption and chemisorption of alkanethiols and alkyl sulfides on Au (111).* The Journal of Physical Chemistry B, 1998. **102**(18): p. 3456-3465.

135. Behm, J.M., K.R. Lykke, M.J. Pellin, and J.C. Hemminger, *Projection photolithography utilizing a Schwarzschild microscope and self-assembled alkanethiol monolayers as simple photoresists.* Langmuir, 1996. **12**(8): p. 2121-2124.

136. Zharnikov, M. and M. Grunze, *Modification of thiol-derived self-assembling monolayers by electron and x-ray irradiation: Scientific and lithographic aspects.* Journal of Vacuum Science & Technology B, 2002. **20**(5): p. 1793-1807.

137. Berggren, K.K., A. Bard, J.L. Wilbur, J.D. Gillaspy, A.G. Helg, J.J. McClelland, S.L. Rolston, W.D. Phillips, M. Prentiss, and G.M. Whitesides, *Microlithography by using neutral metastable atoms and self-assembled monolayers.* Science, 1995. **269**(5228): p. 1255-1257.

138. Qin, D., Y. Xia, and G.M. Whitesides, *Soft lithography for micro-and nanoscale patterning.* Nature protocols, 2010. **5**(3): p. 491-502.

139. Odom, T.W., J.C. Love, D.B. Wolfe, K.E. Paul, and G.M. Whitesides, *Improved pattern transfer in soft lithography using composite stamps.* Langmuir, 2002. **18**(13): p. 5314-5320.

140. Piner, R.D., J. Zhu, F. Xu, S. Hong, and C.A. Mirkin, *" Dip-pen" nanolithography.* science, 1999. **283**(5402): p. 661-663.

141. Ginger, D.S., H. Zhang, and C.A. Mirkin, *The Evolution of Dip-Pen Nanolithography.* Angewandte Chemie International Edition, 2004. **43**(1): p. 30-45.

142. Kelsall, R., I.W. Hamley, and M. Geoghegan, *Nanoscale science and technology*. 2005: John Wiley & Sons.

143. Hong, S., J. Zhu, and C.A. Mirkin, *Multiple ink nanolithography: toward a multiple-pen nano-plotter.* Science, 1999. **286**(5439): p. 523-525.

144. El Zubir, O., I. Barlow, G.J. Leggett, and N.H. Williams, *Fabrication of molecular nanopatterns at aluminium oxide surfaces by nanoshaving of self-assembled monolayers of alkylphosphonates.* Nanoscale, 2013. **5**(22): p. 11125-11131.

145. Huo, F., Z. Zheng, G. Zheng, L.R. Giam, H. Zhang, and C.A. Mirkin, *Polymer pen lithography.* Science, 2008. **321**(5896): p. 1658-1660.

146. Brinkmann, F., M. Hirtz, A.M. Greiner, M. Weschenfelder, B. Waterkotte, M. Bastmeyer, and H. Fuchs, *Interdigitated Multicolored Bioink Micropatterns by Multiplexed Polymer Pen Lithography.* Small, 2013.

147. Friebel, S., J. Aizenberg, S. Abad, and P. Wiltzius, *Ultraviolet lithography of self-assembled monolayers for submicron patterned deposition.* Applied Physics Letters, 2000. **77**(15): p. 2406-2408.

148. Hutt, D. and G. Leggett, *Dependence of rates of photo-oxidation of self-assembled monolayers on adsorbate alkyl chain length.* J Phys Chem, 1996. **100**: p. 6657.

149. Brewer, N.J., S. Janusz, K. Critchley, S.D. Evans, and G.J. Leggett, *Photooxidation of self-assembled monolayers by exposure to light of wavelength 254 nm: A static SIMS study.* The Journal of Physical Chemistry B, 2005. **109**(22): p. 11247-11256.

150. Tizazu, G., O. El-Zubir, S.R. Brueck, D.G. Lidzey, G.J. Leggett, and G.P. Lopez, *Large area nanopatterning of alkylphosphonate self-assembled monolayers on titanium oxide surfaces by interferometric lithography.* Nanoscale, 2011. **3**(6): p. 2511-6.

151. Brueck, S., *Optical and interferometric lithography-Nanotechnology enablers.* Proceedings of the IEEE, 2005. **93**(10): p. 1704-1721.

152. Tsargorodska, A., O. El Zubir, B. Darroch, M.L. Cartron, T. Basova, C.N. Hunter, A.V. Nabok, and G.J. Leggett, *Fast, Simple, Combinatorial Routes to the Fabrication of Reusable, Plasmonically Active Gold Nanostructures by Interferometric Lithography of Self-Assembled Monolayers.* ACS nano, 2014. **8**(8): p. 7858-7869.

153. Moxey, M., A. Johnson, O. El-Zubir, M. Cartron, S.S. Dinachali, C.N. Hunter, M.S. Saifullah, K.S. Chong, and G.J. Leggett, *Fabrication of Self-Cleaning, Reusable Titania Templates for Nanometer and Micrometer Scale Protein Patterning.* ACS nano, 2015. **9**(6): p. 6262-6270.

154. Galloway, J.M., *Biotemplating arrays of nanomagnets using the biomineralisation protein Mms6.* 2012, University of Leeds.

155. Klem, M.T., D. Willits, D.J. Solis, A.M. Belcher, M. Young, and T. Douglas, *Bio-inspired Synthesis of Protein-Encapsulated CoPt Nanoparticles.* Advanced Functional Materials, 2005. **15**(9): p. 1489-1494.

156. Galloway, J.M., J.E. Talbot, K. Critchley, J.J. Miles, and J.P. Bramble, *Developing Biotemplated Data Storage: Room Temperature Biomineralization of L10 CoPt Magnetic Nanoparticles.* Advanced Functional Materials, 2015. **25**(29): p. 4590-4600.

157. Bird, S.M., J.M. Galloway, A.E. Rawlings, J.P. Bramble, and S.S. Staniland, *Taking a hard line with biotemplating: cobalt-doped magnetite magnetic nanoparticle arrays.* Nanoscale, 2015. **7**: p. 7340 - 7351.

158. MicroChem. *SU-8 2000 Permanent Epoxy Negative Photoresist Processing Guidlines For: SU-8 2000.5, SU-8 2002, SU-8 2005, SU-8 2007, SU-8 2010 and SU-8 2015*. [cited 2013 3rd July]; Available from: http://microchem.com/pdf/SU-82000DataSheet2000_5thru2015Ver4.pdf.

159. Graham, D.J., D.D. Price, and B.D. Ratner, *Solution assembled and microcontact printed monolayers of dodecanethiol on gold: a multivariate exploration of chemistry and contamination.* Langmuir, 2002. **18**(5): p. 1518-1527.

160. Oechsner, H. and E. Stumpe, *Sputtered neutral mass spectrometry (SNMS) as a tool for chemical surface analysis and depth profiling.* Applied physics, 1977. **14**(1): p. 43-47.

161. Zeonex. *ZEP520A Technical Report* [cited 2013 3rd July]; Available from: http://www.zeonchemicals.com/pdfs/ZEP520A.pdf.

162. Chen, H.-Y., M. Hirtz, X. Deng, T. Laue, H. Fuchs, and J. Lahann, *Substrate-independent dip-pen nanolithography based on reactive coatings.* Journal of the American Chemical Society, 2010. **132**(51): p. 18023-18025.

163. Marx, K.A., *Quartz crystal microbalance: a useful tool for studying thin polymer films and complex biomolecular systems at the solution-surface interface.* Biomacromolecules, 2003. **4**(5): p. 1099-1120.

164. Zhang, Y., B. Du, X. Chen, and H. Ma, *Convergence of dissipation and impedance analysis of quartz crystal microbalance studies.* Analytical chemistry, 2008. **81**(2): p. 642-648.

165. Sauerbrey, G., *Use of quartz vibration for weighing thin films on a microbalance.* J. Physik, 1959. **155**: p. 206-212.

166. Q-Sense. *Quartz Crystal Microbalance With Dissipation (QCM-D)*. [cited 2015 1st August]; Available from: http://www.q-sense.com/file/qcm-d-technology-note.pdf.

167. Höök, F., B. Kasemo, T. Nylander, C. Fant, K. Sott, and H. Elwing, *Variations in coupled water, viscoelastic properties, and film thickness of a Mefp-1 protein film during adsorption and cross-linking: a quartz crystal microbalance with dissipation monitoring, ellipsometry, and surface plasmon resonance study.* Analytical chemistry, 2001. **73**(24): p. 5796-5804.

168. Krzemiński, Ł., S. Cronin, L. Ndamba, G.W. Canters, T.J. Aartsma, S.D. Evans, and L.J. Jeuken, *Orientational control over nitrite reductase on modified gold electrode and its effects on the interfacial electron transfer.* The Journal of Physical Chemistry B, 2011. **115**(43): p. 12607-12614.

169. Regazzoni, A.E., G.A. Urrutia, M.A. Blesa, and A.J.G. Maroto, *Some observations on the composition and morphology of synthetic magnetites obtained by different routes.* Journal of Inorganic and Nuclear Chemistry, 1981. **43**(7): p. 1489-1493.

170. Schneider, C.A., W.S. Rasband, and K.W. Eliceiri, *NIH Image to ImageJ: 25 years of image analysis.* Nat Meth, 2012. **9**(7): p. 671-675.

171. Horcas, I., R. Fernandez, J. Gomez-Rodriguez, J. Colchero, J. Gómez-Herrero, and A. Baro, *WSXM: A software for scanning probe microscopy and a tool for nanotechnology.* Review of Scientific Instruments, 2007. **78**: p. 013705.

172. Bennewitz, R., *Friction force microscopy.* Materials Today, 2005. **8**(5): p. 42-48.

173. Ul-Haq, E., S. Patole, M. Moxey, E. Amstad, C. Vasilev, C.N. Hunter, G.J. Leggett, N.D. Spencer, and N.H. Williams, *Photocatalytic nanolithography of self-assembled monolayers and proteins.* ACS nano, 2013. **7**(9): p. 7610-7618.

174. Watson, J.D. and F.H. Crick, *Molecular structure of nucleic acids.* Nature, 1953. **171**(4356): p. 737-738.

175. Bragg, W.L., *The diffraction of short electromagnetic waves by a crystal.* Proceedings of the Cambridge Philosophical Society, 1913. **17**(43): p. 4.

176. *Diffrac.Plus TOPAS: General Profile Structure and Analysis Software for Powder Diffraction Data.* Bruker AXS, Karlsruhe, Germany, 2000.

177. Patterson, A.L., *The Scherrer Formula for X-Ray Particle Size Determination.* Physical Review, 1939. **56**(10): p. 978-982.

178. Patterson, A., *The Scherrer formula for X-ray particle size determination.* Physical review, 1939. **56**(10): p. 978.

179. Langford, J.I. and A. Wilson, *Scherrer after sixty years: a survey and some new results in the determination of crystallite size.* Journal of Applied Crystallography, 1978. **11**(2): p. 102-113.

180. Thibault, C., C. Séverac, A.-F. Mingotaud, C. Vieu, and M. Mauzac, *Poly (dimethylsiloxane) contamination in microcontact printing and its influence on patterning oligonucleotides.* Langmuir, 2007. **23**(21): p. 10706-10714.

181. Briggs, D., A. Brown, and J.C. Vickerman, *Handbook of static secondary ion mass spectrometry*. 1989: John Wiley & Sons.

182. Sauerbrey, G., *Use of quartz crystal vibrator for weighting thin films on a microbalance.* Physics, 1959. **155**: p. 206-222.

183. Voinova, M.V., M. Rodahl, M. Jonson, and B. Kasemo, *Viscoelastic acoustic response of layered polymer films at fluid-solid interfaces: continuum mechanics approach.* Physica Scripta, 1999. **59**(5): p. 391-396.

184. Rodahl, M., F. Höök, C. Fredriksson, C.A. Keller, A. Krozer, P. Brzezinski, M. Voinova, and B. Kasemo, *Simultaneous frequency and dissipation factor QCM measurements of biomolecular adsorption and cell adhesion.* Faraday Discussions, 1997. **107**: p. 229-246.

185. Dixon, M.C., *Quartz crystal microbalance with dissipation monitoring: enabling real-time characterization of biological materials and their interactions.* Journal of biomolecular techniques: JBT, 2008. **19**(3): p. 151.

186. Dunlop, D., *Superparamagnetic and single-domain threshold sizes in magnetite.* Journal of Geophysical Research, 1973. **78**(11): p. 1780-1793.

187. Moskowitz, B.M. and S.K. Banerjee, *Grain size limits for pseudosingle domain behavior in magnetite: Implications for paleomagnetism.* Magnetics, IEEE Transactions on, 1979. **15**(5): p. 1241-1246.

188. Ma, M., Y. Wu, J. Zhou, Y. Sun, Y. Zhang, and N. Gu, *Size dependence of specific power absorption of Fe3O4 particles in AC magnetic field.* Journal of Magnetism and Magnetic Materials, 2004. **268**(1): p. 33-39.

189. Wang, L., T. Prozorov, P.E. Palo, X. Liu, D. Vaknin, R. Prozorov, S. Mallapragada, and M. Nilsen-Hamilton, *Self-assembly and biphasic iron-binding characteristics of Mms6, a bacterial protein that promotes the formation of superparamagnetic magnetite nanoparticles of uniform size and shape.* Biomacromolecules, 2011. **13**(1): p. 98-105.

190. Zhou, C.Z., F. Confalonieri, M. Jacquet, R. Perasso, Z.G. Li, and J. Janin, *Silk fibroin: structural implications of a remarkable amino acid sequence.* Proteins: Structure, Function, and Bioinformatics, 2001. **44**(2): p. 119-122.

191. Guex, N. and M.C. Peitsch, *SWISS-MODEL and the Swiss-Pdb Viewer: an environment for comparative protein modeling.* electrophoresis, 1997. **18**(15): p. 2714-2723.

192. Crick, F.H., *The packing of-helices: simple coiled-coils.* Acta crystallographica, 1953. **6**(8-9): p. 689-697.

193. Macindoe, G., L. Mavridis, V. Venkatraman, M.-D. Devignes, and D.W. Ritchie, *HexServer: an FFT-based protein docking server powered by graphics processors.* Nucleic Acids Research, 2010. **38**: p. W445-W449.

194.   Levinson, H.J. *Principles of lithography*. 2005. SPIE Bellingham.

195.   Jansen, H., H. Gardeniers, M. de Boer, M. Elwenspoek, and J. Fluitman, *A survey on the reactive ion etching of silicon in microtechnology.* Journal of micromechanics and microengineering, 1996. **6**(1): p. 14.

196.   Marty, F., L. Rousseau, B. Saadany, B. Mercier, O. Français, Y. Mita, and T. Bourouina, *Advanced etching of silicon based on deep reactive ion etching for silicon high aspect ratio microstructures and three-dimensional micro-and nanostructures.* Microelectronics journal, 2005. **36**(7): p. 673-677.

197.   Boeckl, M. and D.D. Graham, *Self-Assembled Monolayers: Advantages of Pure Alkanethiols.* Material Matters, 2006. **1**.

198.   Nikogeorgos, N., C.A. Hunter, and G.J. Leggett, *Relationship Between Molecular Contact Thermodynamics and Surface Contact Mechanics.* Langmuir, 2012. **28**(51): p. 17709-17717.

199.   Galloway, J.M., J.P. Bramble, and S.S. Staniland, *Biomimetic synthesis of materials for technology.* Chemistry-A European Journal, 2013. **19**(27): p. 8710-8725.

200.   Ruby, C., R. Aïssa, A. Géhin, J. Cortot, M. Abdelmoula, and J.-M. Génin, *Green rusts synthesis by coprecipitation of Fe II–Fe III ions and mass-balance diagram.* Comptes Rendus Geoscience, 2006. **338**(6): p. 420-432.

201.   Moumen, N., P. Bonville, and M. Pileni, *Control of the size of cobalt ferrite magnetic fluids: Mössbauer spectroscopy.* The Journal of Physical Chemistry, 1996. **100**(34): p. 14410-14416.

202.   Berkowitz, A., W. Schuele, and P. Flanders, *Influence of Crystallite Size on the Magnetic Properties of Acicular γ-Fe2O3 Particles.* Journal of Applied Physics, 1968. **39**(2): p. 1261-1263.

203.   Sorescu, M., A. Grabias, D. Tarabasanu-Mihaila, and L. Diamandescu, *Influence of cobalt and nickel substitutions on populations, hyperfine fields, and hysteresis phenomenon in magnetite.* Journal of applied physics, 2002. **91**(10): p. 8135-8137.

204.   Maaz, K., A. Mumtaz, S. Hasanain, and A. Ceylan, *Synthesis and magnetic properties of cobalt ferrite (CoFe2O4) nanoparticles prepared by wet chemical route.* Journal of Magnetism and Magnetic Materials, 2007. **308**(2): p. 289-295.

205.   Blundell, S., *Magnetism in condensed matter*. 2001: Oxford Univ. Press.

206.   Feng, S., L. Wang, P. Palo, X. Liu, S.K. Mallapragada, and M. Nilsen-Hamilton, *Integrated self-assembly of the mms6 magnetosome protein to form an iron-responsive structure.* International journal of molecular sciences, 2013. **14**(7): p. 14594-14606.

207.   Palafox-Hernandez, J.P., Z. Tang, Z.E. Hughes, Y. Li, M.T. Swihart, P.N. Prasad, T.R. Walsh, and M.R. Knecht, *Comparative Study of Materials-Binding Peptide Interactions with Gold and Silver Surfaces and Nanostructures: A Thermodynamic Basis for Biological Selectivity of Inorganic Materials.* Chemistry of Materials, 2014. **26**(17): p. 4960-4969.

208.   Ruan, L., H. Ramezani-Dakhel, C.-Y. Chiu, E. Zhu, Y. Li, H. Heinz, and Y. Huang, *Tailoring molecular specificity toward a crystal facet: a lesson from biorecognition toward Pt {111}.* Nano letters, 2013. **13**(2): p. 840-846.

209.   Lister, S., T. Thomson, J. Kohlbrecher, K. Takano, V. Venkataramana, S. Ray, M. Wismayer, M. de Vries, H. Do, and Y. Ikeda, *Size-dependent reversal of grains in perpendicular magnetic recording media measured by small-angle polarized neutron scattering.* Applied Physics Letters, 2010. **97**(11): p. 112503.

210.   Rothemund, P.W., *Folding DNA to create nanoscale shapes and patterns.* Nature, 2006. **440**(7082): p. 297-302.

211.   Metzger, R.M., V.V. Konovalov, M. Sun, T. Xu, G. Zangari, B. Xu, M. Benakli, and W. Doyle, *Magnetic nanowires in hexagonally ordered pores of alumina.* Magnetics, IEEE Transactions on, 2000. **36**(1): p. 30-35.

212. Harrison, C., J.A. Dagata, and D.H. Adamson, *Lithography with Self-Assembled Block Copolymer Microdomains*, in *Developments in Block Copolymer Science and Technology*, I.W. Hamley, Editor. 2004, John Wiley & Sons p. 295-320.

213. Pum, D. and U.B. Sleytr, *Reassembly of S-layer proteins.* Nanotechnology, 2014. **25**(31): p. 312001.

Appendix
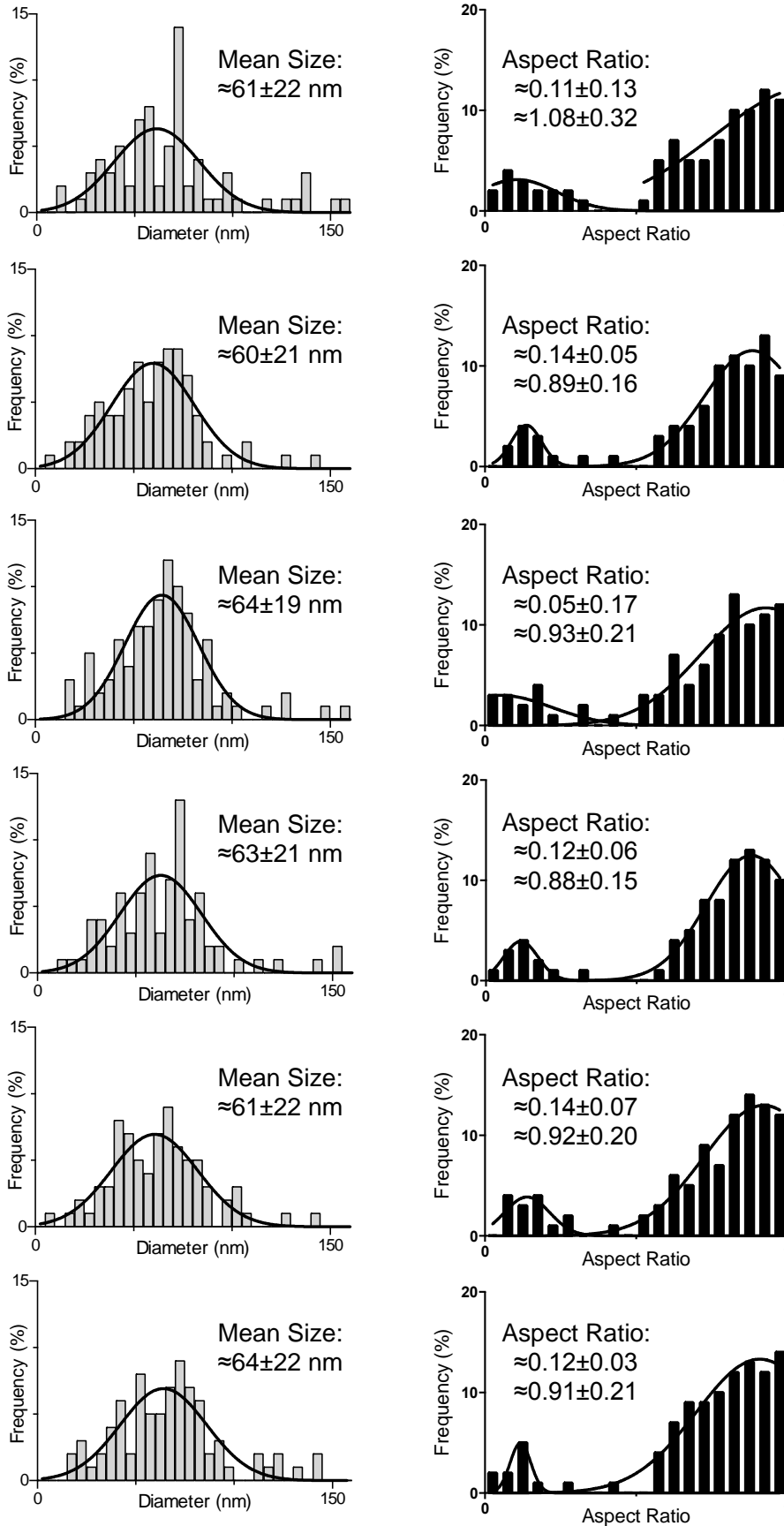
Appendix 1 – Grainsize analysis and measured aspect ratio from TEM images of MNPs formed in six different POFHK reactions.

Appendix 2[*] – a) Alignment of the amino acid sequence region containing the assembly motif of Mms6, and a similar sequence from fibroin (conserved residues are indicated with an asterisk). b) Views of the two faces of the putative assembly motif of Mms6 shown as a molecular surface representation of an ideal α-helix. Residues a-g coloured according to a. c) Model of parallel dimer of GL motif of Mms6. Side and end-on views respective of the dimer, represented as a ribbon with the alpha carbon atoms of the conserved glycine residues shown in solid molecular representation (left), and views of two faces of the dimer represented as a molecular surface (right). All colouring as labelled in a, except the hydrophobic side-chains of the two protomers (structural units of the protein) are shown in magenta and deep pink respectively.

---

[*] This analysis was performed by Steve Baldwin, with further input from Andrea Rawlings.

"A man does good work when he rids himself of shit."

Edward I (The Hammer of the Scots)